CASL-U-2017-1308-000

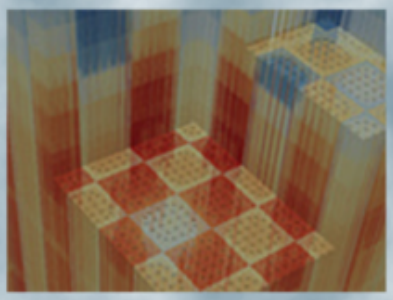

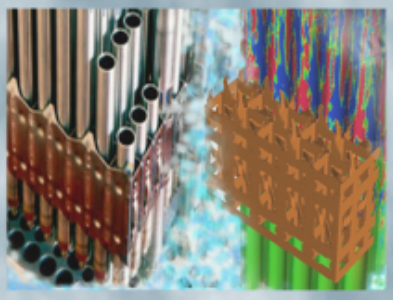

Development and Implementation of CFD-Informed Models for the Advanced Subchannel Code CTF

L3:PHI.CTF.P14.02

Taylor Blyth, Pennsylvania State University

Maria Avramova, North Carolina State University

04 April 2017

REVISION LOG

Revision	Date	Affected Pages	Revision Description
0	04/04/2017	All	Initial issuance

Document pages that are:

Export Controlled _____

IP/Proprietary/NDA Controlled_____

Sensitive Controlled_____

Requested Distribution:

To:

Copy:

ABSTRACT

The research described in this PhD thesis contributes to the development of efficient methods for utilization of high-fidelity models and codes to inform low-fidelity models and codes in the area of nuclear reactor core thermal-hydraulics. The objective is to increase the accuracy of predictions of quantities of interests using high-fidelity CFD models while preserving the efficiency of low-fidelity subchannel core calculations. An original methodology named Physics-based Approach for High-to-Low Model Information has been further developed and tested. The overall physical phenomena and corresponding localized effects, which are introduced by the presence of spacer grids in light water reactor (LWR) cores, are dissected in corresponding four building basic processes, and corresponding models are informed using high-fidelity CFD codes. These models are a spacer grid-directed cross-flow model, a grid-enhanced turbulent mixing model, a heat transfer enhancement model, and a spacer grid pressure loss model. The localized CFD-models are developed and tested using the CFD code STAR-CCM+, and the corresponding global model development and testing in sub-channel formulation is performed in the thermal-hydraulic subchannel code CTF. The improved CTF simulations utilize data-files derived from CFD STAR-CCM+ simulation results covering the spacer grid design desired for inclusion in the CTF calculation. The current implementation of these models is examined and possibilities for improvement and further development are suggested. The validation experimental database is extended by including the OECD/NRC PSBT benchmark data. The outcome is an enhanced accuracy of CTF predictions while preserving the computational efficiency of a low-fidelity subchannel code.

TABLE OF CONTENTS

List of Figures....vii

List of Tables....xiii

Acknowledgements....xv

REVISION LOG....iii

Chapter 1 Introduction....1

Heat Transfer in Rod Bundles....3
Statement of Objective....4
Method of Approach....6
Thesis Outline....7

Chapter 2 Literature Review....9

Spacer grid effects studied through experiment....9
Experimental studies on spacer grid pressure drop....9
Experimental studies on spacer grid-related heat transfer....11
Experimental studies on spacer grid effects on flow patterns and cross-flow....13
Spacer grid effects studied through numerics....15
Numerical studies on spacer grid pressure drop....15
Numerical studies on spacer grid-related heat transfer....17
Numerical studies on spacer grid effects on flow patterns and cross-flow....25
Spacer grid effects modelled in subchannel codes....35

Chapter 3 Methodology, Computer Codes, and Benchmark Experimental Data....37

Selected Low-Fidelity Subchannel Code, CTF....37
CTF conservation equations....38
CTF Spacer Grid Modelling....40
CTF Heat Transfer....41
Selected High-Fidelity CFD Code, STAR-CCM+....49
STAR-CCM+ background....49
STAR-CCM+ Heat Transfer....51
Introduction to the PSBT Benchmark....53
PSBT Test Series 1....54
PSBT spacer grid details....58
Modelling simplifications for the PSBT spacer grid in CFD simulations....61

Chapter 4 CFD-Informed Models for Spacer Grid-Enhanced Cross-flow in CTF....69

CFD-Informed Model for Spacer Grid-Enhanced Turbulent Mixing....69
CFD-Informed Spacer Grid-Directed Cross-flow Model....88

Chapter 5 CFD-Informed Model for Spacer Grid Loss Coefficient Calculations....116

Introduction 116
Background....116
Spacer grid loss coefficient calculations....119
Current form loss model in CTF....123
Current friction loss models in CTF 124
Form and friction losses in STAR-CCM+....127
CFD modelling details....128
CFD polyhedral mesh base size study 135
PSBT spacer grid loss coefficient calculations from 5x5 CFD simulations....138
Study on the effects of flow conditions on pressure loss coefficients....144
CTF and STAR-CCM+ pressure prediction comparison 146
Study on subchannels containing multiple spacer grid straps 149
PSBT Experiment 01-5343 CFD simulation 152
BFBT Single-Phase Pressure-Drop Experiment CFD simulations 154
Grid Convergence Index (GCI) Study....160
Summary and Conclusions 164

Chapter 6 CFD-Informed Spacer Grid-Enhanced Heat Transfer Model in CTF 166

Introduction 166
Background....167
Heat transfer coefficient factor calculations 175
CFD model description....176
HTC multiplier results for the 2x2 CFD simulations 180
HTC multiplier notes for full rod bundle geometry CFD simulations 192
Effects of varied flow inlet conditions on the CFD-predicted HTC....195
Application of CFD simulation results to CTF 198
CTF simulations with CFD-informed HTC data....200
Summary and Conclusions 205

Chapter 7 Conclusions and Future Work 207

Future Work....208
General....208
Spacer grid enhanced turbulent mixing 209
Spacer grid mixing vane-directed cross-flow 209
Spacer grid pressure loss coefficients....210
Spacer grid-enhanced heat transfer....210

BIBLIOGRAPHY 211

Appendix A 219

CTF data-files....219
Spacer grid-directed crossflow model data-files for CTF 219
Spacer grid-enhanced turbulent mixing model data-file for CTF....221
Spacer grid-enhanced heat transfer coefficient model data-file for CTF 223

LIST OF FIGURES

Figure 1: CTF flowchart for the HTC-related parameters....48

Figure 2: Normalized radial power profile for the PSBT Test Series 1 experimental cases....57

Figure 3: Top view of a spacer grid spring (left box) and a spacer grid dimple (upper box) ..58

Figure 4: Location of subchannel types within the PSBT A1 5x5 rod bundle....60

Figure 5: PSBT spacer grid and rod completely merged intersection....61

Figure 6: PSBT spacer grid and rod partially merged....62

Figure 7: PSBT SSG geometry details, top view....63

Figure 8: PSBT SSG geometry details, side view....63

Figure 9: PSBT SSG geometry details, isometric view....64

Figure 10: PSBT NMV geometry details, top view....64

Figure 11: PSBT NMV geometry details, side view....65

Figure 12: PSBT NMV geometry details, isometric view....65

Figure 13: PSBT MVG geometry details, top view....66

Figure 14: PSBT MVG geometry details, side view....66

Figure 15: PSBT MVG geometry, grid strap side view....67

Figure 16: PSBT MVG mixing vane geometry details....67

Figure 17: PSBT MVG geometry details, isometric view....68

Figure 18: Gap connection types for the PSBT A1 bundle....70

Figure 19: PSBT 2x1 MVG geometry layout for turbulent mixing simulations....72

Figure 20: PSBT 2x1 subchannel layout mesh overview....72

Figure 21: PSBT 2x1 SSG mesh overview in the region at the spacer grid straps....73

Figure 22: Flowchart of the spacer grid-enhanced turbulent mixing model in CTF....77

Figure 23: 2x1 subchannel layout used for the CFD determination of the mixing coefficient factor [2]....78

Figure 24: 2x1 subchannel geometry for the turbulent mixing CFD simulations....79

Figure 25: Single-phase mixing coefficient of the internal-internal gaps calculated from CFD simulation for the PSBT grids 81

Figure 26: Turbulent mixing multiplier of the internal-internal gaps calculated from CFD simulation for the PSBT grids 82

Figure 27: Turbulent mixing multiplier of the internal-side gaps calculated from CFD simulation for the PSBT grids 83

Figure 28: Turbulent mixing multiplier of the side-side gaps calculated from CFD simulation for the PSBT grids 84

Figure 29: Turbulent mixing multiplier of the corner-side gaps calculated from CFD simulation for the PSBT grids 84

Figure 30: Turbulent mixing multiplier results for each gap geometry in the PSBT NMV grid....85

Figure 31: Turbulent mixing multiplier results for each gap geometry in the PSBT SSG grid....86

Figure 32: CFD results of the NMV 2x1 CFD simulation at 45 mm axially (5 mm downstream from leading edge of spacer grid) 87

Figure 33: CFD results of the NMV 2x1 CFD simulation at 250 mm axially (210 mm downstream from leading edge of spacer grid) 87

Figure 34: Flowchart for the spacer grid-directed cross-flow scheme in CTF....90

Figure 35: PSBT MVG 2x2 CFD simulation interface connection geometry 91

Figure 36: Overall geometry of the PSBT MVG 2x2 CFD simulation....92

Figure 37: PSBT 2x2 subchannel layout mesh overview for directed crossflow simulations....93

Figure 38: PSBT detailed subchannel mesh view for directed crossflow simulations....93

Figure 39: Geometry of hypothetical PSBT MVG inter-assembly subchannels at the intersection of four rod bundles....96

Figure 40: PSBT MVG cross-flow directions, and gap/subchannel indices 97

Figure 41: Lateral convection factor calculated for the PSBT MVG spacer grid 98

Figure 42: Lateral convection factor for the PSBT MVG broken down by gap (gap geometry in Figure 35) 99

Figure 43: PSBT MVG lateral velocity magnitude visual at 200 mm from the flow inlet 100

Figure 44: PSBT MVG lateral velocity magnitude visual at 148 mm from the flow inlet 100

Figure 45: Calculated lateral convection factor for the PSBT MVG with a PSBT SSG located 229 mm 101

Figure 46: Lateral convection factor calculated for each type of PSBT spacer grid.....102

Figure 47: Directed cross-flow for a 5x5 bundle across only internal subchannel connections 103

Figure 48: PSBT MVG cross-flow directions over only internal subchannel gaps 105

Figure 49: Experimentally measured subchannel exit temperatures [°C] for PSBT Test 01-5343 106

Figure 50: Predicted – Experimental results averaged for PSBT Test Series 01, no CTF spacer grid models enabled, in Celsius.....106

Figure 51: Predicted – Experimental results averaged for PSBT Test Series 01, CTF directed cross-flow model enabled on all gaps, in Celsius.....107

Figure 52: Predicted – Experimental results averaged for PSBT Test Series 01, CTF directed cross-flow model enabled on internal gaps only, in Celsius.....108

Figure 53: Predicted – Experimental results averaged for PSBT Test Series 01, CTF turbulent mixing enabled, in Celsius 108

Figure 54: Predicted – Experimental results averaged for PSBT Test Series 01, both CTF directed cross-flow and turbulent mixing models enabled on all gaps, in Celsius.....109

Figure 55: Predicted – Experimental results averaged for PSBT Test Series 01, both CTF directed cross-flow and turbulent mixing models enabled on internal gaps only, in Celsius 110

Figure 56: Number of experimental measurements for subchannel in the model.....112

Figure 57: Normalized subchannel temperatures averaged over 21 cases with directed cross-flow modeling off.....113

Figure 58: Normalized subchannel temperatures averaged over 21 cases with directed cross-flow modeling on 113

Figure 59: Comparison of the average temperature difference by subchannel with the cross-flow model turned off 115

Figure 60: Comparison of the average temperature difference by subchannel with the cross-flow model turned on 115

Figure 61: CFD simulation geometry for the PSBT 5x5 spacer grid cases.....133

Figure 62: Flow volumes removed (red regions) from the PSBT 5x5 models 134

Figure 63: Detailed view of the PSBT grid's 0.7 mm protrusions from the nominal grid boundaries.....135

Figure 64: CFD Pressure predictions from the 2x2 meshing study with the PSBT MVG.....137

Figure 65: Detailed view of the line probe locations within an internal subchannel 140

Figure 66: Locations of the line probes used to extract subchannel-specific results from CFD simulations 140

Figure 67: Pressure vs. axial distance for the corner subchannels in the 5x5 PSBT MVG CFD simulation.....141

Figure 68: CFD results for the pressure profile 80 mm from the 4 MVG spacer grids' leading edges (~10 mm downstream from the vane tips).....150

Figure 69: Geometric details at the intersection of four PSBT MVG spacer grids.....150

Figure 70: Overall geometry at the intersection of four PSBT MVG spacer grids used in STAR-CCM+.....151

Figure 71: Full view of four PSBT MVG grids located with typical PWR fuel assembly spacing 151

Figure 72: BFBT CFD simulation geometry reduced with symmetry 155

Figure 73: BFBT general mesh overview 155

Figure 74: BFBT detailed mesh overview.....156

Figure 75: BFBT CFD simulation geometry, scaled to 10% axially 156

Figure 76: Nusselt number (HTC) multipliers calculated by the Yao-Hochreiter-Leech correlation and the Holloway et al correlation for a spacer grid with mixing vanes.....173

Figure 77: Nusselt number (HTC) multipliers calculated by the Yao-Hochreiter-Leech correlation and the Holloway et al correlation for a spacer grid with no mixing vanes...174

Figure 78: Numbering for the rod surfaces by subchannel, following CTF's numbering scheme on a 2x2 subchannel layout.....176

Figure 79: Near-wall prism mesh layers with a spacing ratio of 1.05.....179

Figure 80: Near-wall prism mesh layers with a spacing ratio of 1.20.....179

Figure 81: Near-wall prism mesh layers with a spacing ratio of 1.50.....180

Figure 82: STAR-CCM+ predicted local HTC values of the central rod surfaces in the PSBT MVG 2x2 simulation 181

Figure 83: Zoomed axial region of the STAR-CCM+ local HTC predictions in subchannel 1 of the 2x2 simulations....182

Figure 84: STAR-CCM+ predicted local HTC values of the central rod surfaces in the PSBT NMV 2x2 simulation 184

Figure 85: STAR-CCM+ predicted local HTC values of the central rod surfaces in the PSBT SSG 2x2 simulation 184

Figure 86: STAR-CCM+ predicted local HTC values of the central rod surfaces in the bare 2x2 simulation 185

Figure 87: STAR-CCM+ predicted HTC multipliers for each of the PSBT spacer grid types....186

Figure 88: STAR-CCM+ local HTC predictions for the PSBT MVG central rod, surfaces 3 and 1 (15% scaled axially)....187

Figure 89: STAR-CCM+ local HTC predictions for the PSBT MVG central rod, surfaces 4 and 2 (15% scaled axially)....187

Figure 90: STAR-CCM+ local HTC predictions of the PSBT MVG central rod surfaces showing the mixing vane downstream pattern 188

Figure 91: STAR-CCM+ local HTC predictions for the PSBT NMV central rod, surfaces 3 and 1 (15% scaled axially)....189

Figure 92: STAR-CCM+ local HTC predictions for the PSBT NMV central rod, surfaces 4 and 2 (15% scaled axially)....189

Figure 93: STAR-CCM+ local HTC predictions for the PSBT SSG central rod, surfaces 3 and 1 (15% scaled axially)....190

Figure 94: STAR-CCM+ local HTC predictions for the PSBT SSG central rod, surfaces 4 and 2 (15% scaled axially)....190

Figure 95: Comparison of HTC correlation predictions for the PSBT MVG spacer grid 191

Figure 96: Comparison of HTC correlation predictions for the PSBT NMV spacer grid 192

Figure 97: PSBT 5x5 rod bundle surfaces grouped by subchannel type....193

Figure 98: PSBT MVG spacer grid surface similarity generated by meandering flow patterns....195

Figure 99: STAR-CCM+ predicted local HTC results for the PSBT MVG 2x2 simulation with varying inlet flow 196

Figure 100: Flowchart for the spacer grid-enhanced HTC in CTF 199

Figure 101: STAR-CCM+ vs CTF prediction of surface temperatures at the central rod in a 2x2 bare simulation.....201

Figure 102: STAR-CCM+ vs CTF prediction of the bulk fluid temperature in a 2x2 bare simulation 202

Figure 103: Comparison of surface temperature predictions with the CFD-informed HTC multipliers vs the CTF YHL correlation.....203

Figure 104: Comparison of surface temperature predictions from CTF for the bare simulation and the PSBT MVG HTC multiplier simulation at the central rod 204

Figure 105: Surface temperature predictions of CTF and STAR-CCM+ with the PSBT MVG HTC multiplier applied in CTF at the central rod.....205

LIST OF TABLES

Table 1: CTF heat transfer coefficient calculations by regime 42

Table 2: PSBT Test Series 1 bundle geometry data [49] 54

Table 3: Details of the spacer grid placement in the PSBT Test Series 1 experiment 54

Table 4: Estimated accuracy in PSBT experimental conditions [49].....55

Table 5: PSBT DNB Test Series 1 experimental flow conditions [49].....56

Table 6: Details of the flow blockages for an internal subchannel in each PSBT spacer grid.....59

Table 7: Summary of geometry details for the internal subchannels with spacer grids in the PSBT A1 rod bundle.....60

Table 8: PSBT A1 bundle gap details 71

Table 9: Turbulent mixing CFD modelling details for the PSBT spacer grids 74

Table 10: CFD turbulent mixing model data extraction details 79

Table 11: Turbulent mixing CFD-determined parameters for the cold (300 C) bare subchannel 80

Table 12: Directed Cross-flow CFD modelling details for the PSBT spacer grids.....94

Table 13: Summary of CTF spacer grid modelling predictions for the PSBT Series 01 test cases.....111

Table 14: Spacer grid pressure loss coefficients calculated with Shiralkar and Radcliffe's method [59].....122

Table 15: PSBT MVG spacer grid loss coefficients calculated with Shiralkar and Radcliffe's method while ignoring the projected area of the mixing vanes 123

Table 16: PSBT MVG 2x2 subchannel meshing study CFD modelling parameters 130

Table 17: PSBT A1 bundle 5x5 CFD modelling parameters for the pressure study 132

Table 18: Results of the meshing study using the PSBT MVG in a 2x2 internal subchannel layout 137

Table 19: Details for the mesh sizes used in the 2x2 PSBT spacer grid mesh study 138

Table 20: PSBT A1 5x5 rod bundle pressure drop over axial distance with no spacer grid present.....142

Table 21: Form pressure drop across PSBT spacer grids, from CFD 143

Table 22: PSBT spacer grid loss coefficients as calculated for the 5x5 rod bundle, from CFD 143

Table 23: Pressure drop parameters for the 2x2 MVG varied flow CFD simulations 145

Table 24: Pressure drop results for the 2x2 MVG varied flow CFD simulations 146

Table 25: Frictional pressure losses calculated by CTF and STAR-CCM+ 147

Table 26: Form pressure losses for the 5x5 spacer grid geometry calculated by CTF and STAR-CCM+.....148

Table 27: Results from the PSBT 01-5343 CFD simulation with full A1 bundle geometry ...152

Table 28: BFBT Phase II Experiment 0 pressure tap location details.....157

Table 29: BFBT Test 70027 comparison of CFD results for pressure drop 158

Table 30: BFBT single-phase pressure drop CFD percent error by case 158

Table 31: CFD-calculated BFBT single-phase pressure drop spacer grid loss coefficients 159

Table 32: Relative root mean square error comparison of CTF and CFD results for BFBT single-phase pressure predictions 160

Table 33: GCI calculation mesh cell counts by base mesh size 163

Table 34: GCI calculation results from the pressure drop study with varied base mesh size ..164

Table 35: Details of the CFD 2x2 HTC simulations 178

Table 36: STAR-CCM+ predicted HTC ratios for rod surfaces relative to internal surfaces 194

Table 37: Inlet flow conditions used in the CFD 2x2 subchannel study of axial velocity effects.....196

Table 38: STAR-CCM+ HTC predictions with flow variations for the PSBT MVG 2x2 simulation 197

Table 39: CTF HTC predictions with flow variations for the PSBT MVG 2x2 simulation 198

Table 40: Sample HTC ratio data-file content for CTF simulations 199

ACKNOWLEDGEMENTS

This research is supported by and performed in conjunction with the Consortium for Advanced Simulation of Light Water Reactors (http://www.casl.gov), an Energy Innovation Hub (http://www.energy.gov/hubs) for Modeling and Simulation of Nuclear Reactors under U.S. Department of Energy Contract No. DE-AC05-00OR22725.

Chapter 1

Introduction

Simulations of flow through light water reactor (LWR) cores are complex and often computationally expensive. Analyses performed using subchannel codes must address the large scale and geometry of the reactor core components, and are prone to simplifications. These simplifications may take the form of reduced dimension (i.e. 3-dimensional to 2-dimensional), ignoring or smearing intricate geometric details, or in computational cell volume. By reducing the magnitude of the simulation, the computational time is decreased at the cost of prediction accuracy. Even with current computational resources these reductions are necessary if runs are to be completed in a timely fashion without the aid of large computer clusters.

The introduction of spacer grids into the simulations carries additional complexities. Spacer grids are used within LWRs in order to maintain the position of the rods during operation as well as to promote increased fluid motion, which in turn enhances cooling effects. Accounting for the detailed effects of spacer grids requires precise knowledge of the grid's geometry to be able to capture all of the grid-induced effects in the simulation. Spacer grids increase the turbulence within the flow and cause a form pressure loss due to their additional volume introduced into the subchannels. Depending on the type of grid, it may also impose some combination of inter-channel flow and intra-channel swirl. Spacer grids with vanes present on their trailing edges have the largest impact on the flow in terms of deviation from a non-gridded subchannel flow pattern. These vanes are often angled to divert flow in a certain pattern consistent with the type of LWR in which it they are placed. This pattern is generally a meandering pattern for cross-flow, which is good for thermal homogenization in a PWR, or a

swirling pattern for intra-channel mixing in a shrouded BWR assembly. In addition to their influence on coolant flow, spacer grids also have localized effects on the rod cladding. Grid-to-rod fretting occurs as vibrations create small motion at the springs and dimples which contact the rod surface. In addition to these rod-to-grid contact points causing wear on the cladding surface, they also can create areas of flow stagnation, which can offer increased likelihood of CRUD deposits [13]. The scale of these localized effects makes them difficult to place into subchannel codes and their predictions are generally better with CFD simulations.

Thermal-hydraulic subchannel codes, such as CTF [2], are computer codes which allow users to model flow scenarios with given boundary conditions and often specialize in geometries similar to those found within LWRs. These codes subdivide the flow domain, as well as certain solid regions, into mesh cells which contain data for each node, and solve for the system parameters with correlations relevant to the flow conditions experienced within an LWR. This method utilizes many constituent relations in order to solve for the cell-averaged fluid properties at each step in the solve process. Subchannel codes generally offer users flexibility with respect to the choice of relative correlations and methods to utilize during the code's solve procedure.

Computational fluid dynamics (CFD) codes seek to provide accurate representations of fluid flow using numerical methods. These codes, such as STAR-CCM+ by CD-adapco [50], differ from thermal-hydraulic subchannel codes in that they can employ a fine-mesh version of the Navier-Stokes equations in order to resolve the characteristics of the flow at the user-specified refinement. The numerical simulation is well-suited for fluid flow calculations and can be user-tuned with specific correlations as needed. Due to their inherent complexity, CFD codes have increased runtimes over subchannel codes. They do, however, offer the ability to capture more detailed geometries and provide results on a small scale. Lower-fidelity subchannel codes are less complex, but lack the flow domain resolution that a high-fidelity CFD code can provide [36].

Obtaining more accurate predictions from CTF simulations with improved models related to spacer grids can lead to an improvement of the safety margin and therefore an increase in the overall economics of an operating reactor. Utilizing correlations founded upon relevant data instead of correlations which may be extrapolated outside of their range of applicability will also improve the reliability and performance of CTF. Replacing outdated or improperly-applied correlations removes some uncertainty from the code. An example is CTF's option for the use of a simple pressure-loss-coefficient model to calculate the pressure drop, when relevant data can be extracted from an appropriate CFD simulation to provide grid-specific pressure-loss terms. Using more refined data on the spacer grids and the flow surrounding them from CFD analyses will help diminish some of the uncertainty in CTF simulations involving spacer grids.

Heat Transfer in Rod Bundles

The majority of the heat generation in an LWR occurs in the fuel pellets. The heat flux reaches the fuel rod's outer cladding surface where it meets the coolant flow. The Zircaloy cladding must be sufficiently cooled to maintain its structural integrity during operation. Conditions which negatively affect heat transfer such as departure from nucleate boiling (DNB) can be prevented with proper cooling [62].

The velocity of the fluid decreases as the distance to the surfaces such as fuel rods decreases. This region where the flow is not at the free-stream velocity is the boundary layer. The velocity of the fluid is assumed to be zero at the surface location, and it increases with distance away from the surface. The characteristics of flow inside of the boundary layer differ from those of the free-stream region. Turbulence in the boundary layer region causes greater mixing in all directions due to the eddy development and destruction of the more stratified laminar sub-layer. At flow conditions typical of an LWR, turbulence is expected within all the subchannels. There

are benefits to heat transfer due to this turbulence. A thermal boundary layer exists, which contains the largest portion of the thermal gradient in the heat transfer from the rod surfaces to the bulk coolant flow. The thermal boundary layer thickness is tied to the dimension of the momentum boundary layer, as the heat transfer is strongly influenced by local flow conditions [62].

Spacer grids provide enhanced heat transfer which can be attributed to several phenomena. The benefits can be attributed to the fluid acceleration due to the flow restriction caused by the spacer grid, and the destruction of the developed flow and additional turbulence generation. The effects on the turbulent boundary layers at the rod surfaces allow for a greater thermal gradient across the fluid in that region and therefore a stronger level of heat transfer from the surface.

Statement of Objective

The objective of this research is to develop a methodology for improving the subchannel code CTF's spacer grid modelling using CFD-informed models. The development of such methodology is supplemented by implementation, and verification and validation activities. This methodology includes a grid-directed cross-flow model, a grid-enhanced turbulent mixing model, as well as modelling of heat transfer enhancement and pressure losses utilizing CFD-based data. The CFD code, STAR-CCM+, a widely-used and well-supported package is utilized for this work. CTF, a thermal-hydraulic subchannel code, has been selected as the Consortium for Advanced Simulation of LWRs (CASL) thermal-hydraulic code and is coupled with other code packages within the Virtual Environment for Reactor Applications (VERA) suite which can benefit from its capabilities. STAR-CCM+ provides high-fidelity results to the subchannel code CTF, which can utilize the processed data from the CFD code via the developed methodology and

subsequently enhance models while still maintaining its computationally efficient predictive abilities.

The purpose of this research is to improve the spacer grid-related predictive capabilities of CTF without compromising its run time. By utilizing data from CFD simulations, CTF can be enhanced to better predict the effects of spacer grids on the subchannels. The CFD simulations must also be controlled in order to capture only the desired effects. The downstream heat transfer enhancement and pressure drops are parameters which are highly dependent upon the presence of spacer grids in the fluid's flow.

The methods for informing CTF with CFD-derived data utilizes a user-supplied input file which includes the relevant data corresponding to a specific grid. These data-files are read in and processed by CTF during its calculations. This file should be intuitive to produce, such that a user may generate his or her own data-file in similar fashion for any type of grid, and capable of holding all the information needed to specify the grid's properties as needed by CTF.

The Organisation for Economic Co-operation and Development (OECD) and Nuclear Regulatory Commission (NRC) PWR Subchannel and Bundle Tests (PSBT) benchmark data [49] is used for validation of CTF's models. The data of this benchmark are wide in scope, and they are open to the academic community for education and research. Contained in the benchmark are fluid mixing tests (exit fluid temperatures on a subchannel level); void fraction tests; and departure from nucleate boiling tests. Most of the PSBT test cases are already included in the CTF validation matrix. As this research deals with the single-phase liquid regime, the PSBT tests with exit temperature measurements with grids in place are helpful.

Method of Approach

Current CTF simulations which include spacer grid effects request the user to provide grid-related parameters, such as loss coefficients for the pressure loss calculation. The user may set these loss coefficients in a variety of manners; correlations to calculate values based upon spacer grid geometry exist, and it is also common to choose values which provide predicted results close to measured experimental results.

Currently there is a trend in nuclear reactor research and industry to use high-fidelity models and codes to inform low-fidelity models and codes. Due to their complexity, the high-fidelity codes are computationally expensive, and may take on the order of hours to days to complete a simulation run. This motivates the use of low-fidelity models, which are less comprehensive but provide numerical efficiency required for practical applications in design and safety evaluations. These low-fidelity codes have parameters or inputs which must be informed or calibrated using experimental data or simulations from validated high-fidelity codes. High-fidelity models can be used to predict physical behavior in regimes or on scales where physical data is not available. A number of methods have been proposed to address the integration of high-fidelity and low-fidelity codes to predict quantities of interests in an efficient manner. The first approach is based on non-linear multi-scale frameworks, which have been applied in reactor physics (neutronics) [3] and heat-transfer [4] simulations. This second type utilizes information theory in a Bayesian framework to use high-fidelity codes to calibrate low-fidelity codes [36]. The third approach, originally introduced in [2], is being utilized and further developed in this PhD thesis. In this methodology, the overall physical phenomena and corresponding effects are dissected in corresponding building basic processes, and corresponding models are informed using high-fidelity codes. This method is called a Physics-based Approach for High-to-Low Model Information.

The implemented and validated CFD-informed spacer grid models, which will be further detailed later, allow for the spacer-driven effects of turbulent mixing and vane-driven directed cross-flow across subchannels to be included in the CTF simulations. The current implementation of these models is examined and possibilities for improvement and further development are suggested. These simulations utilize data-files derived from CFD simulation results covering the spacer grid design desired for inclusion in the CTF calculation.

This research provides a method for developing loss coefficients using data from a CFD code. It will also utilize CFD results to provide heat transfer enhancement for single-phase liquid flow conditions in the presence of spacer grids. For the pressure loss coefficient calculations, CFD simulations are designed to capture the effects of the spacer grids on the surrounding fluid's pressure. Full spacer grid geometries are utilized to provide results for the various types of subchannel geometries within the model. A single spacer grid span is modelled with single-phase flow simulated both up- and downstream of the spacer grid location. The heat transfer enhancement effects are captured using CFD simulations which look at the effects of the spacer grid on downstream heat transfer coefficients of the rod surfaces. Spacer grid-caused variations in the CFD-calculated heat transfer coefficient are passed as information to CTF.

Thesis Outline

Chapter 2 details the literature review, covering research related to the topic presented in this paper. Spacer grid modelling in both subchannel and CFD codes, as well as heat transfer and pressure drop correlations are examined and discussed.

Chapter 3 contains descriptions of the codes utilized for this research. The subchannel code, CTF, and the CFD code, STAR-CCM+ are detailed, with information related to heat

transfer calculations and spacer grid models provided. The details of the experimental PSBT facility and spacer grids are included in this chapter as well.

Chapter 4 focuses on the previously-developed spacer grid models in CTF, their effects on CTF simulations, and an extension of their development for more thorough application.

Chapter 5 describes the heat transfer enhancement portion of this work, including the procedure for extracting data from the CFD code and its application within CTF.

Chapter 6 provides the details for the CFD-derived pressure loss coefficient determination and the associated effects on CTF.

Chapter 7 summarizes the research described in this paper and provides information as to the areas which would benefit from future research.

Chapter 2

Literature Review

This chapter presents a survey of past and current research articles related to spacer grid effects, modelling spacer grids in CFD and subchannel codes, and experimental and numerical studies of the effects of spacer grids on fluid flows.

Spacer grid effects studied through experiment

Experimental studies on spacer grid pressure drop

Rehme analyzed the effects of spacer grids on pressure losses in multi-rod fuel bundles using a variety of spacer grid designs [22]. Pressure drop measurements were taken during isothermal single-phase liquid experiments. The spacer grids in the study had blockage ratios ranging from 0.149 (tube-shaped spacer grid with no transverse connections) to 0.536 (thick coils wrapped around each rod). The heights of the spacer grids ranged from 5 mm to 14 mm. The total pressure drop along the bundle's height was defined as the sum of the frictional losses and the grid's pressure loss. With *n* identical spacer grids spaced along the bundle, this total pressure drop is given in Equation (1).

$$\Delta P_{total} = \Delta P_{fric} + n\Delta P_{grid} \tag{1}$$

The author related the pressure drop over the spacer grid to the fluid's axial velocity and density as shown in Equation (2).

$$\Delta P_{grid} = C_B \frac{\rho}{2} U_{ax}^2 \tag{2}$$

In Equation (2), C_B is the drag or loss coefficient of the spacer grid, caused by its geometry, and can be calculated from experimental results. The author proposes a method for relating the spacer grid's loss coefficient to its blockage ratio, ϵ, which is defined as the area of the flow blocked by the projected cross-section of the grid (as viewed perpendicularly to the flow direction) to the total flow area. A correlation for this modified grid loss coefficient, C_V, is proposed to be related to the grid's blockage ratio squared, as presented in Equation (3).

$$C_B = C_v \epsilon^2 \tag{3}$$

The author determined values of C_V for each grid and plotted the results against the Reynolds number of the experiment's flow conditions. The results for the square lattice grids show for Reynolds number flows of values from 3000 to 200000, the modified grid loss coefficient decreases slightly from approximately 12 to approximately 6. These results led the author to recommend a value of the modified grid loss coefficient for Reynolds numbers greater than 50000 as C_V between 6 and 7. Assuming a value of 6 would then transform Equation (2) to (4) using substitution from Equation (3).

$$\Delta P_{grid} = 3\epsilon^2 \rho U_{ax}^2 \tag{4}$$

Rehme does not make note of the projected area of the grid vanes, as vaned spacer grids were not included in the experiment. The height of the grid, which causes additional frictional drag, is not taken into account either.

Chun and Oh [23] proposed that the drag forces on the region where a spacer grid equipped with mixing vanes is located in a rod bundle is the sum of four components. These are the grid's form loss, the grid's frictional loss, the rods' frictional loss, and the mixing vane form loss. The frictional losses are estimated by calculating the losses over a flat plate of the same length as the region in consideration, which is the grid strap height. Their findings were compared with experimental results from spacer grids of blockage ratio 0.29 and non-split mixing vanes to

produce a loss coefficient of 1.60 at a Reynolds number of 30000. The mixing vane loss portion of the overall loss coefficient is reported as 20%.

Endo et al. [24] examined the effects of spacer grid mixing vane geometry on pressure drop in two-phase flow. Vane angles of 20° and 30° from the flow direction were considered, and results were compared with a spacer grid of the same geometry less the mixing vanes. The liquid droplet deposition rates were also compared between the spacer grids. The mixing vane angle of 30° produced the largest pressure drop of the three grids considered, and its deposition rate was also the greatest. The authors calculated a spacer grid loss coefficient of approximately 1.6 of the grid with the 30° vanes, and of approximately 1.4 of the grid with the 20° vanes. The spacer grid with no mixing vanes has a loss coefficient near 0.9, due to its lower blockage ratio. The pressure loss coefficients of two-phase experiments were compared with those of the single-phase experiments in order to draw a correlation between single- and two-phase pressure loss coefficients. The authors found that increasing the gas flow rate causes an increase in the spacer grid's loss coefficient, up to approximately twice the single-phase pressure loss coefficient when considering flow near $\beta = 0.008$, where β is defined as the gas volume flow rate fraction as shown in Equation (5).

$$\beta = \frac{j_{gas}}{j_{gas} + j_{liq}} \tag{5}$$

Experimental studies on spacer grid-related heat transfer

Using experiments with air as the working fluid and electrically-heated rods, Holloway et al. (2008) examined the effects of spacer grids on downstream heat transfer [13]. The experimental setup utilized typical PWR dimensions applied to a 5x5 bundle and flow conditions at a Reynolds number of approximately 30000. Temperature results were circumferentially

averaged around the central rod of the bundle using a moveable temperature sensor. The authors found that the Yao-Hochreiter-Leech correlation, Equation (14), tends to over-predict heat transfer downstream of the grids. For the vaned spacer grid, the experimental results did not decay as rapidly as the correlation predicts. Experimental results for the standard, un-vaned grid matched well with the correlation, however. The maximum reported heat transfer enhancement ratios were reported as 1.38 and 1.58, for the standard grid and the vaned grid, respectively. The peak values occurred at the downstream edge of the spacer grid. Experimental results show the heat transfer ratio returning to 1.0 after approximately 30 hydraulic diameters. Corresponding with this finding, Miller [17] also found the decay length of the Yao-Hochreiter-Leech correlation to be best suited for 20-30 hydraulic diameters downstream when comparing with experimental results [11].

Holloway et al. presented a grid blockage based Nusselt number correlation which was fit to their data over the first 5 hydraulic diameters downstream of the grids tested. This correlation, which is similar to the Yao-Hochreiter-Leech formula in its approach to exponential decay, is shown in Equation (6).

$$\frac{Nu_{avg}}{Nu_{fd}} = 1 + (0.8K_g - 0.4)\exp\left(-\frac{0.25z}{D_\infty}\right) \tag{6}$$

In Equation (6), K_g is the grid's loss coefficient. The authors note that the blockage ratio is not effective for capturing the effects on pressure drop for streamlined or blunt blockages, such as mixing vanes or disks.

The Nuclear Regulatory Commission (NRC) and the Pennsylvania State University (PSU) performed studies with the Rod Bundle Heat Transfer Test (RBHT) facility [51]. The facility is a full-length electrically-heated 7x7 array featuring mixing-vane style spacer grids. Steam is the working fluid, and relevant measured quantities include subchannel temperatures, rod temperatures, and pressure drops.

In the RBHT report, the authors discuss the calculation of the heat transfer coefficient (HTC) from the bulk fluid to the rod surface using the centerline vapor temperature measurement, the rod's electric heat flux, and the rod's surface temperature measurement. The grid loss coefficients are also calculated using the measure drop over the grid span and the flow conditions.

Experimental studies on spacer grid effects on flow patterns and cross-flow

McClusky et al. (2002) [40] performed experiments with a 5x5 bundle representative of a larger PWR fuel assembly. The single-phase water experiments are conducted at atmospheric pressure and ambient temperature, with a Reynolds number reported near 28000. Spacer grids were either of the split-vane geometry or contained swirl/twisted vanes. The lateral flow fields are analyzed at locations downstream of the mixing-vane grids using particle image velocimetry (PIV). The authors define two characteristic flow regions in the downstream zone based upon the lateral flow effects. The first region contains many vortices while the second (and further downstream) region generally contains a single vortex centered in the subchannel. The authors declare that the first region ends at 4.2 hydraulic diameters and the second region begins at 6.3 hydraulic diameters, and continues until 17 hydraulic diameters [39]. The differences in these regions illustrate the need to carefully account for downstream grid effects.

McClusky et al. (2002) note the strong variation in lateral velocity across the subchannel. The center of the subchannel may be the center of a strong vortex and therefore experience little lateral velocity in comparison to lateral velocities in the outer portions of the subchannel near the rod surfaces. These vortices were noted to migrate towards other subchannels as driven by the flow pattern direction of the vanes.

McClusky et al. (2002) reported that certain previous experimental studies do not do enough to account for the effects of walls when considering downstream spacer grid effects. They

note strong differences in lateral velocities measured downstream of a grid in similar subchannel geometries supposedly due to the wall effects. Several turbulence models were utilized, and subchannel geometry varied from a 5x5 subchannel layout to a single subchannel with appropriate boundary conditions and interfaces to make use of symmetry.

Holloway et al. (2006) [31] examined the flow downstream of a split-vane mixing spacer grid using a CFD code and comparing predictions of lateral velocities to experimentally-measured PIV results. Fine details in the spacer grid are analyzed by using a spacer grid with weld cutouts and a spacer grid without weld cutouts at its mixing vane split pair location. With water as the simulated fluid at ambient conditions and near a Reynolds number of 35000, very good agreements of the lateral flow fields were reported at locations just downstream (~1.5 hydraulic diameters) of the spacer grid. The vortex locations and swirl patterns are well-predicted, though the lateral velocities from CFD are noted to be about 12% larger in magnitude than those from the PIV measurements. Also, as distance downstream increases to 9 hydraulic diameters, the ability of the CFD code to predict lateral velocity profiles and magnitudes decreases significantly.

Hyvärinen studied the effects of spacer grids on two-phase flow using an experimental setup with partial rod bundle simulations [37]. The number of mixing vanes per spacer grid, the dimensions of the mixing vanes, as well as the orientation of the spacer grid were studied and the effects on the resulting void distribution was analyzed experimentally. Of the two spacer grid types, the egg-crate style spacer grid was found to have larger downstream impacts on most flow parameters, and the duct-style (ferrule type) spacer grid did not show the same magnitudes in the quantities of interest.

Ylönen [48] acknowledged the need for fine-scale experimental results and constructed a test loop capable of measuring details in single- and two-phase flow effects caused by spacer grids. CFD validation utilized the measured results and the Large Eddy Simulation (LES) and

Direct Numerical Simulation (DNS) results matched well with experiments. STAR-CCM+ was employed with its k-epsilon turbulence model and two-layer, all y^+ wall treatment options to model the flow downstream of the spacer grid. Velocity predictions from STAR-CCM+ matched well with experimentally-observed values at various axial locations downstream of the spacer grid's placement. Discrepancies arose in the predictions of the length of the swirl decay; the CFD simulations show a longer propagation of swirl downstream of the spacer than was measured during the experiments. The author attributes this to possible "instability-induced cross-flow" effects which are not modelled well with CFD codes, and states that LES simulations may expose the source of the errors in the predictions.

Spacer grid effects studied through numerics

Numerical studies on spacer grid pressure drop

Yao et. al [20] examined the effects of the spacer grids on pressure loss coefficients, and believed that the model proposed by Rehme [22] in Equation (7) could be improved.

$$K = C_v \epsilon^2 \tag{7}$$

In Equation (7), C_v is a grid drag term dependent upon the Reynolds number, though Rehme [22] suggests a constant value of 7.0 to be applied at relevant Reynolds numbers. K is the loss coefficient, and the ϵ parameter is the grid's blockage ratio. Yao et. al contend that this pressure loss coefficient correlation under-predicts pressure drops seen in experimental data and suggest a constant value of 10.5 instead of Rehme's 7.0 value. The authors also note that Rehme's method neglects skin friction effects which can be attributed to a portion of the difference from the experimental results.

Holloway et al. (2004) examined the effects of spacer grid features on the pressure loss coefficients and downstream heat transfer [12]. A correlation for the Nusselt number multiplier is introduced, and it depends on geometric characteristics of the spacer grid.

Holloway et al. (2004) [12] proposed that the geometric "flow-enhancing" features of the spacer grids can be separated into their own loss coefficient by examining the loss coefficient of a similar grid without any mixing features attached. This method is shown in Equation (8), where K_g is the loss coefficient of the grid with its flow-enhancing features and K_S is the loss coefficient of the same grid without its features.

$$K_{feat} = K_g - K_S \tag{8}$$

Although pressure drop is related to complex geometry relations, this feature loss coefficient provides a method for quantizes the effects of the spacer grid's vanes and other features on the pressure drop. The authors note that increased grid strap length causes additional form drag, and therefore two grids with the same blockage ratios may differ greatly depending on the grid's height. At a Reynolds number of 42000, grid loss coefficients reported in this study vary from 0.64 for a simple spacer grid with no flow-enhancing features to 1.60 for a grid with blunt disks at each strap intersection. The breakdown for the grid with the highest loss coefficient is reported to have 48% of its loss coefficient caused by the mixing features.

In et al. (2010) [27] utilized the CFD code CFX to calculate the pressure loss coefficient of several spacer grid geometries. The authors surmise a correlation for the total loss coefficient of a mixing vane spacer grid as the sum of several components, shown in Equation (9).

$$C_B = C_V\varepsilon^2 + C_{mv}\varepsilon_{mv}^2 + C_a\beta^2 \tag{9}$$

In Equation (9), C_V is the modified loss coefficient of the spacer grid, found by Rehme [22] to be near 6 to 7. For the other terms, C_{mv} is vane-dependent loss coefficient component, ϵ_{mv}

is the blockage ratio of the mixing vanes, C_a is the acceleration coefficient, and β is the relative increase of the fluid velocity caused by the spacer grid, as defined in Equation (10). U_{max} is the axial velocity at the location of the top of the spacer grid, and U_B is the nominal axial velocity.

$$\beta = \frac{U_{max}}{U_B} \tag{10}$$

The flow acceleration coefficient, C_a, is Reynolds number dependent and fitted using a polynomial shown in Equation (11).

$$C_a = 4.5668 - 1.7382\log(Re) + 0.1704\log^2(Re) \tag{11}$$

The effects of the spacer grid on the pressure drop were shown to abate by approximately 40 hydraulic diameters downstream of the top of the spacer grid. This decay is consistent for each of the Reynolds numbers of the surrounding flow tested; on a range of 12500 to 100000. The spacer grid's pressure loss coefficient is shown to drop with increasing Reynolds number, which is consistent with other research.

Numerical studies on spacer grid-related heat transfer

The effects of spacer grids on heat transfer and pressure drops have been studied and analyzed in many simulations. Various modelling approaches and CFD codes have been utilized to demonstrate the effects and compare predictions with relevant experimental results.

Yao, Hochreiter, and Leech led an investigation which compared the single-phase heat transfer effects of spacer grids with experimental data [20]. The authors attempted to expand upon the work of Marek and Rehme

[60] and account for the downstream dependence of heat transfer augmentation caused by grid spacers. Marek and Rehme developed a correlation for a Nusselt number multiplier based on

the grid's blockage ratio. This multiplier value is applied to a single point in the subchannel, as opposed to a correlation with downstream distance dependence. This correlation is presented in Equation (12).

$$\left(\frac{Nu}{Nu_0}\right)_{sp} = 1 + 5.55\epsilon^2 \tag{12}$$

Yao et al. [20] mention that rod bundles utilizing grids with swirl vanes or mixing vanes have a higher value for their critical heat flux than those bundles which utilize simple spacer grid designs. The authors also note that thermal radiation and fin cooling are other effects of the grid on local heat transfer, though these effects are small during normal operating conditions. Flow acceleration through the diminished flow area is also noted as aiding the augmentation. Further, Yao et. al [20] claim that the upstream heat transfer augmentation effects are present for a distance of 2 hydraulic diameters upstream of the grid's leading edge. In this upstream region, the heat transfer augmentation is treated as linear rising to the highest heat transfer value inside of the spacer region. The authors state "the exact functional form of the variation would depend upon the detail geometry of individual grid".

With experimental data of single-phase flow over simple egg-crate spacer grid designs without vanes, Yao et al. [20] proposed the correlation shown in Equation (13) as an update to Marek and Rehme's value of Equation (12) including downstream distance dependence.

$$\left(\frac{Nu}{Nu_0}\right)_{sp} = 1 + 5.55\epsilon^2 \exp\left(-0.13\frac{x}{D}\right) \tag{13}$$

As Yao et al. [20] did not have data from grids with vanes available to them, the authors analyzed a case which utilized a single-phase gas flowing around a swirling ribbon spacer. Based on these swirling ribbon data, the authors derived a de-coupled term to account for the presence of swirling vanes on the grid, presented in Equation (14).

$$\left(\frac{Nu}{Nu_0}\right)_{sp} = \left[1 + 5.55\epsilon^2 \exp\left(-0.13\frac{x}{D}\right)\right]\left[1 + A^2 \tan(\phi)^2 \exp\left(-0.034\frac{x}{D}\right)\right]^{0.4} \quad (14)$$

Yao et al. [20] state that in Equation (14), ϵ is the blockage ratio for both the grid and the vane, while A is the blockage ratio of just the vanes. ϕ is the angle of the vane with respect to the fluid flow and should be less than 45 degrees.

The heat transfer effects of the spacer grids are examined numerically, with Holloway et al. (2004) [12] stating the need for a correlation to account for specific geometric details of the grid, such as vane type. The authors propose to use the grid's pressure loss coefficient to calculate heat transfer just downstream of the grid. The authors note that the initial region of heat transfer enhancement is directly correlated to the grid's form losses and not its friction drag losses. The blockage ratio for only the grid's straps, ϵ_s, is used to define a Nusselt number multiplier with downstream dependence. Equation (15), which follows the form of the Yao-Hochreiter-Leech correlation, Equation (14), but includes dependence on the specific vanes is proposed.

$$\frac{Nu}{Nu_0} = 1 + \left[C_1\epsilon_s + C_2\left(\frac{K_{feat}}{K_g}\right)\right]\exp\left(-\frac{\alpha z}{D_h}\right) \quad (15)$$

In Equation (15), C_1, C_2, and α are constants which are calculated from curve fits of experimental data. Data from each grid design considered by the authors are combined, and the resulting values are $C_1 = 6.5$, $C_2 = 3.2$, and $\alpha = 0.8$. This leaves Equation (16), which then requires the feature and overall loss coefficients as well as the blockage ratio of the grids straps for the grid in question.

$$\frac{Nu}{Nu_0} = 1 + \left[6.5\epsilon_s + 3.2\left(\frac{K_{feat}}{K_g}\right)\right]\exp\left(-\frac{0.8z}{D_h}\right) \quad (16)$$

Equation (16) is stated to be valid on an axial distance range of 1.4 to 33.6 hydraulic diameters downstream of the grid, and data are set by experiments at Reynolds numbers of 28000

and 48000. The results of the heat transfer enhancement are compared with experimental values and are found to match much better than using the Yao-Hochreiter-Leech correlation, Equation (14). The decay length of the effect is much shorter with the model proposed by the authors than with Equation (14).

Holloway et al. also note a region downstream of the grid which is found to have a decreased level of heat transfer as compared to the un-gridded case. This region, with a Nusselt number multiplier less than unity, has been reported in other experiments [64] and demonstrates the difficulty in capturing heat transfer effects based solely on geometric grid parameters. Mills attributed the decrease to boundary layer transition downstream of the grid [64]. Holloway et al. note that the decreased was most pronounced for the split-vane pair grid design and is likely caused by axial velocity deficits or movement in the swirling vortices across the subchannel. The region of the decreased heat transfer lasts for approximately 10 hydraulic diameters in their experiments with the split-vane grid. This dip in the heat transfer enhancement is not covered by the model proposed by Holloway et al [12] or Equation (14) [20].

Cui and Kim used a CFD code, CFX-TASCflow, to analyze four different shapes of mixing vanes to study the effects on downstream heat transfer [10]. The authors applied various turbulence models within the CFD code and made comparisons with the results of the Yao-Hochreiter-Leech correlation, Equation (14). The authors name factors important to heat transfer enhancement as: a) production of turbulent kinetic energy, b) cross-flow mixing, and c) development of secondary flow. For their CFD simulations, the authors utilized a single subchannel with a single spacer grid. The effect of the vane's twist angle was studied while holding parameters such as the blockage ratio constant. This was accomplished by widening or narrowing the vane's base width as the angle of twist changed.

With rod surfaces at constant heat flux, typical PWR geometry, and a Reynolds number near 80000, the authors report that the heat transfer enhancement factor peaks at a twist angle of

45 degrees. The magnitude of the heat transfer enhancement, which is a ratio of the gridded Nusselt number to the case where no grid (bare subchannel) is present, reaches a maximum value of about 1.22 in this case. The authors compare results with the Yao-Hochreiter-Leech correlation's predictions, but note that the Yao-Hochreiter-Leech correlation, Equation (14), is unable to account for the vane's twist angle, instead factoring only the vane's bend angle with relation to the flow. Therefore, the authors saw a change in heat transfer effects with each grid geometry but its effects go unpredicted using Equation (14), illustrating one of this correlations' shortcomings when applied to detailed spacer grid geometries. The authors also note that the swirl produced by the vanes does not affect heat transfer as strongly as the cross-flow does.

Cui and Kim also examined the CFD turbulence models, selecting the standard k-epsilon model, the k-omega model, and the Reynolds stress model for comparison. By comparing lateral velocity predictions with experimental results, the authors recommend the k-epsilon model for both its accuracy and efficiency.

Using the CFD code CFX-5.6, Kim & Seo [15] examine the relationship between the swirl factor and heat transfer augmentation. The authors apply design optimization techniques to alter the base length and bend angle of a spacer grid vane and study the downstream effects in CFD. The authors used a 2x1 subchannel model layout, constant heat flux (at values much lower than typical PWR heat fluxes), and ignoring springs and dimples of the grid. The authors note that the fluid separation at the rod surface causes a recirculating flow inhibits cross-flow and, therefore, heat transfer enhancement. The results of their design study show that the bend angle of the vane has a much stronger impact on both the swirl and heat transfer enhancement than the vane's base width.

Serre et al. [66] modified the system code CATHARE 3, developed by France's Atomic Energy Commission (CEA) to account for increased heat transfer downstream of spacer grids. They utilized a turbulence model to account for increased turbulence downstream of the grid.

Their simulations were single-phase vapor flow through the rod bundle, in post-Critical Heat Flux (CHF) conditions. The authors introduced a k-epsilon turbulence model into CATHARE 3 in order to increase predictive performance in the areas downstream of spacer grids which generally have their surface temperatures conservatively estimated. The starting point for the heat transfer multiplier is the Nusselt number, which the authors calculate using the Dittus-Boelter correlation [54], which is represented in Equation (106). The proposed heat transfer multiplier is based upon the turbulent kinetic energy, which is calculated in both fully-established and downstream of a spacer grid conditions. During comparison with measured surface temperature data from single-phase vapor experiments, the authors determined that the multiplier for the Dittus-Boelter correlation is of the form shown in Equation (17), where k is the turbulent kinetic energy downstream of the grid and k_∞ is the turbulent kinetic energy in the fully-established flow.

$$Nu = 0.023Re^{0.8}Pr^{0.4}\left(\frac{k}{k_\infty}\right)^{0.5} \tag{17}$$

Navarro & Santos [18] note that while the grids have the same blockage ratio and number of vanes (for non-peripheral vane spacer grids), the arrangement of the vanes has a measurable effect on the downstream heat transfer without causing a noticeable difference in pressure drop. The authors also note the lack of good experimental measurements such as detailed subchannel velocity profiles as being a limiting factor in CFD simulation validation.

Jaeger & Sanchez [14] used the system code TRACE to predict the magnitude of heat transfer enhancement caused by a spacer grid. The TRACE code utilizes the Yao-Hochreiter-Leech correlation as a multiplier for the Nusselt number, and the authors tuned the parameters in this correlation's implementation within TRACE to obtain better predictions. With air as a working fluid and at a Reynolds number near 100000, the authors noted that TRACE predicted the magnitude of the heat transfer enhancement well, but that its decay took too long to return to

the nominal value. The experiment showed the effects returning to their nominal value near 10 hydraulic diameters.

With water as the working fluid and a PWR-like 5x5 bundle, four grids were examined and Jaeger & Sanchez noted a similar trend in the decay length of the Yao-Hochreiter-Leech correlation (Equation (14)). One grid was a simple (egg-crate) grid, two contained disks affixed to their downstream edges, and one was a split-vane mixing-style grid. The altering of the decay parameter in the Yao-Hochreiter-Leech correlation led the authors to determine that a value of 0.13 will return the correlation to a ratio of 1.0 after 50 hydraulic diameters, while a value of 0.20 will do the same in 40 hydraulic diameters, and a value of 0.25 will do the same in 30 hydraulic diameters. Jaeger & Sanchez suggest: "The factor B [of Equation (14)] of the exponential decay term should be increased from the present value of 0.13 to values on 0.2-0.3 in order to represent the experimental and CFD data better" [14].

CFD simulations for a hexagonal-geometry grid and subchannel layout were completed using the code CFX. Jaeger & Sanchez note the variation in results when the rod-spring contact location is included against when it is left out. Differences in the predicted Nusselt numbers ranged from approximately 10% to 20% depending on whether the simulated subchannel contained one of these rod-to-grid contact locations. This shows the azimuthal dependence of the spacer effects.

Jaeger & Sanchez also considered experimental data from Yang and Chung [19] for a 6x6 PWR test case. However, for these cases, TRACE offered good predictions with the nominal values set in the Yao-Hochreiter-Leech correlation.

Regarding the effects of vanes, Jaeger & Sanchez state "it was shown that the blockage ratio is the main contributor to the [heat transfer] enhancement while additional flow features like mixing vanes have only a small influence" [14]. Also, the authors note that the downstream range of the heat transfer enhancement effects is "not related to parameters like the Reynolds number,

the spacer type, the geometry or pin arrangement, the heat flux, or the fluid" [14]. They did, however, note a relationship between the enhancement factor (the Nusselt number ratio) and the grid's blockage ratio, which does fall in line with the Yao-Hochreiter-Leech correlation.

Miller, Cheung, and Bajorek updated the Yao-Hochreiter-Leech correlation to be dependent upon the blockage ratio and Reynolds number [17]. The authors note the original range of the blockage ratio for Equation (14) as $0.156 \leq \epsilon \leq 0.362$, which is based upon the experiments included in its development. Using data from the PSU/NRC Rod Bundle Heat Transfer (RBHT) experiments for single-phase steam heat transfer enhancement accounting for spacer grids, the authors arrived at Equation (18) for their Nusselt number enhancement ratio.

$$\frac{Nu_{RBHT}}{Nu_{\infty}} = 1 + 465.4\left(Re^{-0.50}\right)\epsilon^2 \exp\left(-b\frac{z}{D_h}\right) \tag{18}$$

In Equation (18), the $b = 7.31\text{E-}6\left(Re^{1.15}\right)$. The range of Reynolds number for the PSU/NRC RBHT experiments was 8000 to 30000.

Riley proposes a new model for both up- and downstream heat transfer enhancement based upon Equation (14) [16]. This takes into account the effects of multiple grids and their axial locations. This model is shown in Equation (19), and depends on the grid spacing, L_s, the enhancement due to the upstream grid, a, and the enhancement due to the downstream grid, c.

$$\frac{Nu}{Nu_{min}} = 1 + a\epsilon^2 \exp\left(-b\frac{z}{D_h}\right) + c\epsilon^2 \exp\left(-d\frac{L_s - z}{D_h}\right) \tag{19}$$

The parameters b and d of Equation (19) are the decay rate of the enhancement of the upstream grid and the rate of exponential increase of spacer grid enhancement as z approaches L_s, respectively. Riley notes that for large grid spacing, the combined effects become small.

Campbell et al. examined data from the PSU/NRC RBHT in both isothermal and heated flow conditions using the CFD code FLUENT 6.0 [9]. The authors found success in reducing the 7x7 experimental geometry down to 2x2 CFD geometry with appropriate boundary conditions

and symmetry. The RBHT grids contain dimples for their grid-to-rod contacts. The authors achieved good concurrence with experimental data for their detailed grid pressure drop predictions.

Campbell et al. mention that select previous (pre-2004) attempts to utilize CFD for accurate hydraulic predictions achieved limited success due to oversimplifications. Campbell et al. note the beneficial effects on the departure from nucleate boiling ratio (DNBR) caused by hydrodynamic features are a balance between pressure drop and enhanced heat transfer.

Numerical studies on spacer grid effects on flow patterns and cross-flow

Herr and Probstle showed that the axial velocity tends to increase near the rod surfaces in the presence of a spacer grid, and decrease near the center of the subchannel. This would have an impact on surface-to-fluid heat transfer as local conditions improve for extracting heat from the rods.

In investigated the mixing effects of four different spacer grid geometries using the CFD code CFX [21]. Designed as a study of the types of flow deflectors attached to grids, the geometries are listed as a split-vane, a side-supported vane, a swirl-vane, and a twisted-vane grid. Lateral velocities, turbulent kinetic energy, and a swirl factor are modelled in a single subchannel with each grid design and compared with measured data. The swirl factor is defined to compare the swirl magnitude, and compares lateral velocity magnitude along the subchannel centerline to the bulk velocity. This factor is shown in Equation (20) [21].

$$F_{SW} = \frac{1}{2P}\int \frac{|V_{lateral}|}{V_{bulk}} dl \tag{20}$$

In also provides information about the mesh applied to the CFD single-subchannel, single vane simulations. The hexahedral mesh is slightly altered for each grid design, and it extends for

500 mm to account for downstream effects. The y^+ value for the single-subchannel simulations was kept between 15 and 50 for the simulations.

In reports that the swirl vane produces very little cross-flow over the gaps, which is consistent with other literature. The magnitude of the lateral flow is given as 30% of the axial flow for the split-vane grid at the subchannel's axial centerline. Asymmetries within the subchannel lateral flow patterns are noted, as the split-vane grid causes a maximum lateral velocity of 27% of the axial velocity on one line (similar to a chord across a circle) through the subchannel, while another line shows a peak value of 43% of the axial flow magnitude. This shape can be somewhat described as a skewed ellipsis centered in the subchannel, with rotational lateral flow. Most of the decay in lateral velocities is stated to occur within 1.1 and 8.5 hydraulic diameters after the grid. The mixing effects are stated to propagate for 15 to 20 hydraulic diameters downstream of the grid location. Overall, the split-vane was found to produce higher levels of mixing than the swirl vane, largely due to the increased amount of subchannel-to-subchannel cross-flow produced.

In also performed a CFD study of the pressure drop across each of the four grid designs. A large pressure drop across the grid itself, and then a linear deviation as the flow moves away from the spacer grid. The swirl-vane grid is reported as having the smallest pressure drop due to its geometry pushing fluid into the center of the subchannel. The author notes that the CFD pressure drop predictions are not accurate, as the thickness of the grid's straps and vanes is not included in the simulation.

In et al. (2001) [33] studied the coolant mixing caused by spacer grid mixing vanes using the CFD code CFX. Five different types of spacer grid geometries were included, with their variations lying in their vane configurations. Lateral velocities downstream of the spacer grids were compared with experimental values, showing decent agreement just downstream of the spacer grid and improving predictions with downstream distance. CFD simulations of certain grid

geometries, however, such as the split-vane layout, produced large predictions of axial velocities downstream of the spacer grid than were measured. This shows that the CFD code is attenuating subchannel variations much more than the somewhat homogenized profile across the experiments downstream of the spacer grid location. The authors also varied their mesh depending on the geometry of the spacer grid, changing the structural configuration of the computational grids but preserving the number of mesh cells.

Navarro & Santos studied the effects of the spacer grid's vane arrangement on flow through a 5x5 PWR rod bundle simulated in the CFD code CFX 11.0 [18]. The authors discuss the balance of pressure drop over a grid against its downstream hydrodynamic benefits such as increased heat transfer. The spacer grid designs considered include a simple spacer without vanes, a spacer grid with the "standard" vane layout, in which split vane pairs are rotated 90 degrees at each strap intersection to produce a meandering flow pattern. For the standard grid design, two designs are considered with and without vanes on the peripheral straps. The "uniform" grid design utilizes the same split-vane pair layout at each grid strap intersection with no rotation, and peripheral vanes are not included. The "alternate" grid design is similar to the uniform layout, but split-vane pairs are mirrored at each grid strap intersection. Grid strap thickness and height were held constant, at 0.48 mm and 40 mm without vanes, respectively. The vane angle of 26 degrees with respect to the flow direction is a typical PWR vane angle. The authors did, however, neglect the grid springs and dimples from their CFD model as to avoid complexity in the simulation. An unstructured tetrahedral mesh was utilized with a base size of 0.5 mm and six prismatic layers near the simulation's walls.

Navarro & Santos [18] reported the secondary flow (SF) as a function of lateral and axial velocities at various axial locations in the simulation using Equation (21).

$$SF = \frac{\overline{U}_{cross}}{\overline{U}_{bulk}} = \frac{1}{A}\sum_{i}\frac{\left(\sqrt{U_{xi}^2 + U_{yi}^2}\right)A_i}{U_{z,bulk}} \quad (21)$$

In Equation (21), U_{xi} and U_{yi} are the lateral velocities of each subchannel i, and A_i is the corresponding flow area of subchannel i. $U_{z,bulk}$ is the bulk axial velocity. This method, which sums over all subchannels in the simulation, produces a single value for SF of the spacer grid at each axial location. The authors show the similarity between the profiles of the predicted Nusselt number and the predicted value of SF for the grids. The effects of the peripheral vanes are shown to cause more chaotic results in the secondary flow predictions, and when they are removed the flow patterns become more uniform. The authors even recommend removing peripheral vanes from simulations in order to provide better predictions of flow in the internal subchannels.

Anglart et al. modelled two-phase flow, including spacer grids, with the CFD code CFDS-FLOW3D [8]. They evaluated velocity fields and compared with FRIGG FT-6A data. The grid model is simplified and modelled as parallel plates, though it does preserve the blockage ratio of the original grid. Comparisons with experimental data showed that this assumption provided good agreement in pressure predictions. The authors then varied the thickness and lateral location of the spacer grids and noted the effect on the additional pressure drop over the grid.

Xu, Sung, and Tatil [53] utilized the CFD code STAR-CCM+ to model the PSBT [49] 5x5 PWR-like bundle. The bundle contains 17 grids of various geometries, and the authors examined the rotation of the mixing vane grids to see if they could fill in missing information, as the original PSBT grid rotation specifics have been neglected. The authors noted the typical behavior of rotating subsequent grids by 90 degrees and found good agreement with the measured outlet fluid temperatures with their single-phase simulation.

Karoutas et al validated the CFD code STAR-CCM+'s single- and two-phase flow predictions near spacer grids for temperature, velocity profiles, and CHF and departure from

nucleate boiling (DNB) predictions using experimental data [52]. Two 5x5 rod bundle spacer grid designs were utilized; one with mixing split-vanes and one without vanes. The single-phase predictions of subchannel temperatures and velocity profiles across the rod bundle matched experimental data very well. The CHF predictions did not show the same level of agreement with measured data, and this can be due to the CFD code's two-phase model configuration. The authors state that they utilized a hexahedral mesh and attempted to keep the y+ values near the rods greater than 30 in conjunction with STAR-CCM+'s k-epsilon turbulence model with high y+ wall treatment enabled.

Roelofs et al. [43] discuss the shortcomings of subchannel code models with respect to the effects which can be captured, and propose low resolution CFD simulations to capture the additional details. The authors discuss the need for models which can be applied to subchannel codes and are "as efficient as subchannel codes and … independent from experimental or empirical data". The reliance of subchannel codes upon empirical correlations provides an area of improvement when better modelling capabilities are involved, such as those offered by CFD simulations.

Simplifications in CFD modelling geometries are also discussed, with Roelofs et al. noting that merging a spiraling external wire-wrap into a fuel rod surface does improve meshing and CFD feasibility, but also introduces uncertainties and areas of mis-predictions. For instance, if the wire wrap is assumed to have square dimensions and be in complete contact with the rod's outer diameter, the original geometry's hotspots where the circular cross-section of wire and rod meet would not be included due to the simplification.

Roelofs et al. [43] demonstrated the application of high-resolution CFD data to a much coarser CFD simulation using the CFD code OpenFOAM. The volumetric forces from the high-resolution simulation were applied to the momentum equation of the coarse mesh's solver and the

results for the pressure drop over a simulated spacer grid were very similar. The authors note that the coarse mesh ran “three orders of magnitude faster” than the full-scale CFD simulation.

Baudry et al. [44] used the CFD code NEPTUNE_CFD to analyze the single-subchannel portion of the PSBT benchmark [49]. The predicted void fraction and bubble diameters were compared with available experimental data for a variety of CFD model variations, such as mesh size. The finest mesh model contained approximately ten times the number of cells as the coarsest mesh studied. The predicted void fractions did not change more than 0.01 absolute over each mesh in the report, indicating that void fraction predictions are not as reliant upon the CFD mesh as other parameters. The largest changes in the CFD predictions occurred when the bubble model was altered.

The MATRA (Multichannel Analyzer for steady states and Transients in Rod Arrays) subchannel code was developed by the Korea Atomic Energy Research Institute (KAERI) to include deflected cross-flow in a certain direction due to a grid’s mixing vanes [38]. The code is also capable of accounting for non-directional mixing caused by the presence of spacer grids. These two phenomena are stated to be experimentally derived based on geometric characteristics of items such as spacer grids. The authors also note the application of Rehme’s pressure drop models [22] for more accurate predictions in complex subchannel configurations.

Lo and Osman modelled boiling flow in the PSBT 5x5 bundle [49] using the CFD code STAR-CCM+ to compare predicted two-phase void fractions with experimental results [26]. The detailed effects of the rods and spacer grids on the flow were also examined. The authors used detailed CAD drawings of each of the three spacer grids present in the simulation and an unstructured polyhedral mesh over the flow domain. Sufficient polyhedral mesh is used in both axial directions from the grids, and in the regions between the spacer grid locations, an advancing layer extruded mesh is utilized to provide more efficiency. The mixing vanes are shown to provide slight relocations of the void regions in the flow patterns, as expected. The authors note

the analysis of the detailed 3-dimensional flow distribution around the spacer grids requires more detailed measured data to be more helpful.

Conner et al. [45] discussed the care in modelling the PSBT benchmark single-phase experiments which must be taken to ensure accurate results. The 5x5 rod bundle CFD simulations included multiple upstream spacer grids in order to properly condition the flow for results at the location of the spacer grid of interest. The authors desired y^+ values of the first mesh cells at the wall to be between 40 and 100. This meshing scheme, with a tetrahedral base mesh, was used in conjunction with the k-epsilon turbulence model which is stated to match the best with experimental results. The importance of capturing the azimuthal effects of heat transfer downstream of the PSBT's mixing vane spacer grid is discussed as well.

Ikeno [32] predicted flow characteristics downstream of a spacer grid, including the turbulent mixing, using turbulence modelling code. The k-epsilon model is utilized as its applicability to the Reynolds number and typical dimensions of LWR simulations is fitting. However, the author notes several deficiencies of this turbulence model such as the placement of a spacer grid in the simulation, which will produce eddies of magnitudes larger than the typical k-epsilon model is constructed to handle. Ikeno modifies the turbulence model to provide more applicable turbulent mixing predictions based on the geometry of subchannel flow including a spacer grid.

Jeong et al.

[34] utilized the CFD code CFX to predict turbulent mixing coefficients between adjacent subchannels. The CFD simulation comprised two subchannels with a 10°C difference and used the Reynolds stress model to calculate turbulence effects. The CFD-predicted turbulent mixing coefficient was less than the coefficient predicted by other sources and experiments. The authors attribute the discrepancy to how CFX treats the eddy diffusivity of enthalpy or momentum, with

the compared correlations improperly applying this calculation in their turbulence mixing coefficient results.

Sung et al. used the CFD code STAR-CCM+ to model portions of rod bundles with spacer grids and their resulting flows [35]. The STAR-CCM+ results were compared with results from another CFD code, HYDRA-TH, with parameters such as lateral velocities and temperature predictions analyzed. The realizable k-epsilon turbulence model with the two-layer approach and all y^+ wall treatment were applied in the STAR-CCM+ simulations. The authors studied the effects of different mesh densities and, at the finest mesh level applied to a 3x3 rod bundle with spacer grid, reported minimum values of 1.6 and 0.8 as y^+ values at the rod surfaces and spacer grid, respectively. Of the mesh sensitivity study results presented, the largest variation due to mesh base size was in the prediction of the turbulent kinetic energy.

Karoutas et al. [52] quantized the azimuthal velocity at the location of the grid vane tips as approximately 40% of the nominal axial velocity. The authors also stated that after 34 hydraulic diameters the lateral velocity effects from the spacer grid have decay to less than 5% of their maximum value. The axial velocity also returns to its initial value after 32 hydraulic diameters. The axial velocities are also not as strong in the gap regions as they are in the subchannel regions.

Li & Gao [25] examined the modelling techniques of a CFD simulation of a 17x17 PWR fuel assembly with spacer grids containing mixing vanes. In order to maintain accuracy with a fine enough mesh, the authors split the simulation domain into sub-regions for computational efficiency. The authors considered CFD meshing models, turbulence models, and outlet boundary conditions in their studies in addition to the effect of dividing the domain. There was not a large difference in the results compared from the polyhedral mesh to the tetrahedral mesh, and both provided decent agreement with experimental velocity results. The authors note that in a 17x17

fuel assembly, the vortices can grow larger than in a 5x5 rod bundle, and this results in higher predictions of parameters such as the Nusselt number at the rod surfaces.

Holman [30] assessed the ability of CFD code CFX to inform a subchannel code, COBRA-EN, and improve predictions of thermal-hydraulic properties in a rod bundle simulation. Turbulent mixing, cross-flow, and heat transfer coefficients were selected as key parameters affected by spacer grids and therefore offer potential for improvement with CFD results. While flow and thermal properties were generally well-predicted by the CFD code, the author notes that turbulent kinetic energy was often under-predicted by CFX. Varying the turbulence model in CFX did not aid the predictions of the turbulent kinetic energy. The mixing between subchannels due to turbulence is also noted to be a poorly-predicted parameter when compared with experimental studies.

Frank et al. presented a study of the PSBT void distribution benchmark [49] using the CFD code CFX [42]. Variation in the CFD simulation models such as the mesh configuration and the applied turbulence model provided good agreement with experimentally-measured void fractions. The shear stress transport (SST) turbulence model provided the best agreement of the single-subchannel void predictions. The authors do note obvious variations in the predicted secondary flow patterns when utilizing difference turbulence models in the CFD code's simulations.

Smith et al. [46] produced a summary of participants in the OECD/NEA-KAERI rod bundle CFD benchmark. The 5x5 rod bundle's spacer grids involve both a split-vane spacer grid and a swirl-type vane spacer grid for the participants to model. The turbulence models and near-wall treatment configurations used by the participants varied, as participants were tasked with capturing a range of fluid flow parameters. All participants for which results were submitted utilized y^+ values of the first near-wall cell of less than 10. An important note is that Smith et al.

report that the participants who utilized periodic boundary conditions rather than model the full 5x5 lateral geometry did not predict cross-flow velocities over the gaps as well.

Cho et al. [47] studied the effects that spacer grids have on the flow inside of a reactor during a loss-of coolant accident (LOCA) using an experimental set-up. Two geometries of spacer grids were examined; a swirl-inducing spacer grid and an egg-crate style spacer grid. The authors found a strong dependence on the spacer grid geometry to the amount of rewetting and the types of flows caused. The capability of the spacer grid with the swirl vanes attached to cool the cladding surface is greater than that of the spacer grid which is of the egg-crate style. This illustrates the dependence of heat transfer upon the spacer grid's geometry.

Agbodemegbe et al. (2015) [28] utilized the CFD code STAR-CCM+ to model cross-flow across subchannel gaps and compare the predicted results with experimental data. The rod bundle, a 5x5 rod layout, utilized spacer grids with mixing vanes. The authors applied STAR-CCM+'s meshing and turbulence models and checked for their effects on the predictions. A fairly coarse polyhedral mesh base size of 4.0 mm was utilized, with 5 prism layers of 2.0 mm total thickness. With these mesh settings and isothermal flow conditions in the 5x5 rod bundle and a single mixing-vane spacer grid, the authors found that STAR-CCM+'s two-layer realizable k-epsilon turbulence model did not perform as well in predicting fluctuations in turbulent viscosities as the standard k-epsilon and k-omega turbulence models. They do note insufficiencies in their computation mesh density, suggesting that a finer polyhedral mesh would improve predictions of the spacer grid-affected flow patterns.

Agbodemegbe et al. (2016) [29] studied the flow across the subchannel gaps downstream of spacer grids using the CFD code STAR-CCM+. The gap-wise flow conditions were examined downstream of an egg-crate style spacer grid and a spacer grid with mixing vanes. The cross-flow produced by the non-mixing vane grid is very small in comparison to the grid with mixing vanes. The predicted proportion of axial flow converted to lateral flow across the gap is about 7% for the

non-mixing vane grid, while it is close to 38% for the same flow conditions and the spacer grid with the split mixing vanes.

Spacer grid effects modelled in subchannel codes

Avramova [2] developed a grid-directed cross-flow model and a grid-enhanced turbulent mixing model for the subchannel code F-COBRA-TF. This document will further discuss these previously-developed spacer grid models.

Wang et al. examined the effects of crud formation on phenomena such as Crud-Induced Power Shift (CIPS) and Crud-Induced Localized Corrosion (CILC) [52]. The authors noted the dependence of crud growth on the surface location within the rod bundle, and applied CFD simulations for better predictions. Partial-length and quarter-symmetry PWR fuel assemblies with spacer grids were analyzed at suspected locations of crud growth. The CFD code determined heat transfer data and passed the information to the Westinghouse Electric Company (WEC) subchannel code VIPRE-W and chemistry code BOA. The heat transfer coefficients calculated by the CFD code are grouped by surface location around the rod, azimuthally, and then provided as a multiplier to the Equation (106), the Dittus-Boelter equation used within the subchannel code. The subchannel code then shares information with the chemistry code to determine possible areas of concern related to crud formation. The authors state that single-phase liquid CFD simulations are performed. No values for the peak heat transfer multiplier or length scale for the decay are provided, nor make any comparison with experimentally-measured data, however.

Chapter 3

Methodology, Computer Codes, and Benchmark Experimental Data

Selected Low-Fidelity Subchannel Code, CTF

CTF, based upon the COolant Boiling in Rod Arrays, Two Fluid code (COBRA-TF) is a thermal-hydraulic subchannel code designed for LWR analysis. CTF is currently developed and maintained by the Reactor Dynamics and Fuel Modeling Group (RDFMG) at North Carolina State University (NCSU) and is in use with many research institutions and laboratories, such as Oak Ridge National Laboratory (ORNL). COBRA-TF was originally developed at the Pacific Northwest National Laboratories (PNL) in the early 1980s. CTF utilizes a two-fluid, three-field approach with vapor, continuous liquid, and entrained liquid droplets as its fields. CTF solves four mass conservation equations (vapor, continuous liquid, entrained liquid, and non-condensable gases), two energy conservation equations (one for vapor/gases, one for the continuous and entrained liquid combined), and three momentum equations in each direction.

The four main spacer grid-related phenomena in the focus of this work are the grid-enhanced turbulent mixing, the vane-directed cross-flow, the downstream grid-enhanced heat transfer, and the pressure losses of spacer grids. CTF is not equipped with models for capturing all spacer grid effects on the flow. Many variations in spacer grid geometries and heterogeneous effects across a rod bundle create issues with flow modelling, especially when specific vane patterns are considered.

CTF conservation equations

CTF's conservation equations provide the bounds for mass, momentum, and energy calculations throughout its simulations. Each fluid cell's iterations are not complete until the provided convergence criteria are met for each of these three terms. These equations contain terms that are time-dependent and include appropriate source terms that apply to each phase as needed.

The general phasic momentum conservation equation is shown in Equation (22).

$$\frac{\partial}{\partial t}\left(\alpha_k \rho_k \vec{V}_k\right) + \frac{\partial}{\partial x}\left(\alpha_k \rho_k u_k \vec{V}_k\right) + \frac{\partial}{\partial y}\left(\alpha_k \rho_k v_k \vec{V}_k\right) + \frac{\partial}{\partial z}\left(\alpha_k \rho_k w_k \right. \\ = \alpha_k \rho_k \vec{g} - \alpha_k \nabla P + \nabla \cdot \left(\alpha_k \tau_k^{ij}\right) + \vec{M}_k^L + \vec{M}_k^d + \vec{M}_k^T \quad (22)$$

On the LHS of Equation (22):

- The first term is the change in volume momentum over time
- The next three terms account for advection of momentum in each of three directions

On the RHS of Equation (22):

- The first term is the gravitational force
- Second is the pressure force
- Third is the viscous shear stress, which captures wall drag and form losses
- Fourth is the momentum source term due to phase change and entrainment/de-entrainment
- Fifth is the interfacial drag source term
- Sixth is the momentum source term due to turbulent mixing and void drift

The general phasic energy conservation equation is shown in Equation (23).

$$\frac{\partial}{\partial t}(\alpha_k \rho_k h_k) + \nabla \cdot (\alpha_k \rho_k h_k \vec{V}_k) = -\nabla \cdot (\alpha_k \vec{q}_k^{T}) + \Gamma_k h_k^i + q_{wk}''' \quad (23)$$

On the LHS of Equation (23):

- The first term is the change of energy over time
- Second is the advection of energy

On the RHS of Equation (23):

- The first term is the inter-cell energy exchange due to void drift and turbulent mixing
- Second is the energy transfer due to phase change
- Third is the volumetric wall heat transfer
- Fourth is the work done on the fluid cell due to pressure

The general phasic mass conservation equation is shown in Equation (24).

$$\frac{\partial}{\partial t}(\alpha_k \rho_k) + \nabla \cdot (\alpha_k \rho_k \vec{V}_k) = L_k + M_k^T \quad (24)$$

On the LHS of Equation (24):

- The first term is the change in mass over time
- The second is the advection of mass

On the RHS of Equation (24):

- The first term is the mass transfer into or out of phase *k* (e.g. evaporation/condensation)
- The second is the mass transfer due to turbulent mixing and void drift

The CTF theory manual [1] covers the conversion of these general phasic conservation equations to a discretized form that can be solved numerically for the independent variables of the current iteration: phase enthalpy, phase mass, mixture pressure, and phase velocity.

CTF Spacer Grid Modelling

CTF's current spacer grid modeling capability for enhanced heat transfer includes the Yao-Hochreiter-Leech model [1]. This model allows for CTF to capture the basic geometry of the spacer grid and calculate a pressure drop coefficient associated with each grid. This correlation may be applied to vapor phase or both the liquid and vapor phases. The details for the Yao-Hochreiter-Leech implementation within CTF are provided starting with Equation (109).

For pressure losses due to blockages, there is the option for the user to specify the loss coefficients manually. Equation (70) shows how this can be performed as well as provides other details to how CTF calculates pressure losses due to spacer grids.

The pressure drop model is further discussed in Chapter 5, and the heat transfer augmentation is discussed further in Chapter 6.

Other effects due to spacer grids are included in CTF, such as de-entrainment models, radiation models, rewet/reflood effects, and droplet breakup models, though these models are not applied during steady-state single-phase liquid simulations.

Avramova inspected the use of spacer grid models within CTF and noted that they are based on the spacer grid models from a specific version of COBRA-TF, the FLECHT SEASET version [2]. Various portions of the Reynolds-averaged Navier-Stokes equations that are modeled within CTF are affected by the inclusion of spacer grids within a simulation. These models were intended to suit both steady-state and transient calculations and could work in some accident scenarios. The pressure drop is affected by the spacer grids and this drop is modeled with a

change in the momentum equations which is affected by local flow conditions and grid geometry. There is also a simple de-entrainment model to account for the small droplets that come in contact with the leading edge of the grid and start to establish a liquid film on its surfaces. Grid rewet models are also in place in CTF. This occurs during a reflood scenario when the flow past the grids is mostly vapor and therefore they have an effect on cooling due to their temperature difference. The location of the quench front along the grid's length can be calculated as well. This shows where the temperature difference should occur due to the presence of the liquid film on the grid surface. When the grid is exposed directly to vapor, its radiation effects are considered. The radiosity of the grid and surrounding rods are taken into account for the calculation of the amount of radiative heat within the system. CTF also has a droplet breakup model which can account for the formation of microdroplets after a larger droplet strikes the grid. This model depends on the grid's exposed area and again is only used when there is enough vapor in the subchannel. Though not all of the Reynolds-averaged Navier-Stokes terms that can be affected by spacer grids are accounted for in CTF, it does a fair job of modeling the effects the grids generally cause. Some of the missing effects, such as the change in the lift forces acting on the direction in which bubbles will migrate after forming on the rod surfaces, are not investigated or modeled. Avramova chose to model the directed cross-flow and turbulent mixing effects as they were two large features that were missing from CTF at the time.

CTF Heat Transfer

CTF considers the following heat transfer regimes:

- Single phase liquid convection
- Single phase vapor convection
- Subcooled nucleate boiling

- Saturated nucleate boiling
- Transition boiling
- Inverted annular film boiling
- Dispersed droplet film boiling
- Dispersed droplet deposition heat transfer

Table 1 outlines the equations considered for the HTC calculation by CTF for either single-phase liquid or vapor simulations.

Table 1: CTF heat transfer coefficient calculations by regime

Heat Transfer Regime	Heat Transfer Coefficient
Single-phase vapor	$h_{wv} = \max(h_{DB}, h_{WH}, h_{lam})$, where: $h_{DB} = 0.023\frac{k_v}{D_h}Re^{0.8}\mathrm{Pr}^{0.4}$ $h_{WH} = 0.07907\frac{k_v}{D_h}Re^{0.6774}\mathrm{Pr}^{0.333}$ $h_{lam} = 10.0\frac{k_v}{D_h}$ Grid impact (if present): $h_{wv} = F_{grid}h_{wv}$
Single-phase liquid	$h_{wl} = \max(h_{DB}, h_{lam})$, where: $h_{DB} = 0.023\frac{k_l}{D_h}Re^{0.8}\mathrm{Pr}^{0.4}$ $h_{wl,\,lam} = 7.86\frac{k_l}{D_h}$

General description of how CTF calculates the HTC parameters

For single-phase liquids, CTF calculates the heat transfer coefficient from the liquid to the rod surfaces through an iterative manner. For single-phase liquid calculations, this process starts by using the Dittus-Boetler correlation to set the Nusselt number based upon the Reynolds and Prandtl numbers. Then, the HTC is extracted from the Nusselt number using Equation (104). This HTC value is then passed to surfaces connected to the subchannel for which these dimensionless parameters have been calculated. Each of the rod surfaces connected to a subchannel at a given axial level has the same value for its HTC in single-phase liquid conditions. To set the wall temperature, CTF first solves a system of equations to determine the fluid temperature depending on local heat flux and other conditions, and then utilizes the HTC value for each surface to determine that rod's wall temperature.

Detailed description of how CTF performs its HTC parameter calculations

This section details the method CTF currently employs to calculate the heat transfer coefficient for the liquid to rod surface interface with single phase liquid flow conditions. Within CTF there are multiple object types which help group parameters and attributes of certain objects, such as rods and fluid cells. Attached to these object types are attributes, such as temperatures, densities, and heat capacities for the fluidcell type, which allow for clearer calls and designations. A list of the parameters and objects relevant to the HTC calculation is provided here.

Surface type parameters:

- `htcl(:)` is the liquid heat transfer coefficient at axial node j

- `Tl(:)` is the liquid temperature of the fluid adjacent to the surface at axial node j
- `Tw(:)` is the wall temperature at axial node j

fluidcell type parameters:

- `hspl` is the heat transfer coefficient for single phase liquid to the adjacent surface
- `Tl` is the liquid temperature of the fluid mesh cell

CTF notation:

i is the subchannel index

j is the axial node index

k is the gap index (fluidcell type) or azimuthal surface index (surface type)

n is the rod index

The CTF simulation is initiated with a call to subroutine *Init_TF* from *cobra_tf*. This call occurs only once per simulation. *Init_TF* is used to set variables after the CTF input deck is read. Calls to initialize the surface type parameters are made and the surface object value for $htcl(:)$ is set to 0.0, while the values for $Tl(:)$ and $Tw(:)$ are set to the value of the temperature provided by the user as the inlet temperature.

Next, CTF enters the transient solve portion of the simulation and calls subroutines to solve the heat transfer calculations. The fluidcell object initialization process occurs each iteration and first sets the fluidcell liquid temperature, $Tl(:)$, based on fluid properties of the mesh cell. The Prandtl number and Reynolds number values for the fluidcell are calculated based off of local velocities and cell geometry using Equations (25) and (26).

$$Pr_l = \frac{cp_l \mu_l}{k_l} \tag{25}$$

$$Re_l = \frac{g_l D_h}{\mu_l} \tag{26}$$

The parameter g_l is the mass flux in kg/m^2-s and it is calculated using the lateral mass flux, g_x, as well as the axial mass flux, g_z. Equations (27) through (30) show these equations for the liquid phase, which is denoted with the subscript l.

$$g_l = \frac{g_{l,1} + g_{l,2}}{2} \tag{27}$$

$$g_{l,1} = \sqrt{(g_{z,l}(j-1))^2 + (g_{x,l}(j))^2} \tag{28}$$

$$g_{l,2} = \sqrt{(g_{z,l}(j))^2 + (g_{x,l}(j))^2} \tag{29}$$

$$g_{x,l} = \frac{suml(i,j)}{area\_sum(i,j)} \tag{30}$$

The lateral mass flux term requires two more parameters, $suml(i,j)$ and $area\_sum(i,j)$. These parameters represent the sum of the liquid flow over the gaps attached to the current subchannel and the flow area of each of these gaps, respectively. The summation of the lateral mass flow over gap k, $wlm(k,j)$, is shown in Equation (31). Please note that this refers to the gaps connected to subchannel i, which is typically 4 gaps for a subchannel-centered analysis. The absolute value of the liquid mass flow is used as there is a convention for positive gap flow specifying flow from a lower-numbered subchannel to a higher-numbered subchannel, and the opposite for a negative gap flow.

$$suml(i,j) = \sum_{k=1}^{gaps} |wlm(k,j)| \tag{31}$$

The flow area of each gap is simply the width of the gap multiplied by the height of the current axial section. This area is summed to determine $area\_sum(i,j)$ for each subchannel i, as shown in Equation (33).

$$A\_gap(k,j) = x_{gap} z_{gap} \tag{32}$$

$$area\_sum(i,j) = \sum_{k=1}^{gaps} A\_gap(k,j) \tag{33}$$

In both Equation (32) and Equation (33), the parameter $gaps$ refers to the total number of gaps connected to subchannel i.

After the fluidcell values for the Reynolds and Prandtl number are determined, CTF utilizes the Dittus-Boelter correlation which relates the Nusselt number to the Reynolds number as well as the Prandtl number. For single-phase liquid flow, the Nusselt number is defined as the maximum of a constant value of 7.86 and the Dittus-Boelter correlation's value, as shown in Equation (34).

$$Nu_{SPV} = \max\left(7.86, 0.023(Re_l)^{0.8}(\mathrm{Pr_l})^{0.4}\right) \tag{34}$$

Once the Nusselt number for the fluidcell type is defined, the single-phase liquid heat transfer coefficient can be set using Equation (35).

$$h_{SPL} = \frac{Nu_{SPV} k_l}{D_h} \tag{35}$$

Now that the fluidcell object type has a value stored for its heat transfer coefficient, a call is made to set the value for the surface type HTC. On the first iteration, the surface object's HTC for each of the surfaces connected to the current subchannel is set equal to that subchannel's fluidcell type HTC. On subsequent iterations, the surface type HTC is weighted to 80% of the previous iteration's value and 20% to the new iteration's value. This is to limit the amount that

the HTC can change over a given iteration and aids in stability of the solve process. Equation (36) shows this, with the superscript $t-1$ referring to the previous iteration for the HTC value of the fluidcell.

$$HTC_{suface} = \left(HTC_{cell}^{t-1}\right)^{0.8}\left(HTC_{cell}^{\ t}\right)^{0.2} \tag{36}$$

The surface type HTC value is used to set the liquid temperature, which is another surface type parameter. The liquid temperature, $Tl(jh)$, is stored for each subchannel on a per axial node, jh, basis. It is set in CTF using Equation (37), which, for SPL flow, sets the surface type liquid temperature equal to the fluidcell type's liquid temperature.

$$Tl_{surface}(jh) = Tl_{cell}(jh) \tag{37}$$

CTF then steps into the solve_conduction subroutine (of the heat module) and sets up a matrix used to solve for the wall temperatures. A call to the open-source third-party library LAPACK gives CTF the values which are then set as the surface type's wall temperatures. After this value is set, CTF starts the process at the next iteration by calculating new fluidcell velocities for the Reynolds number.

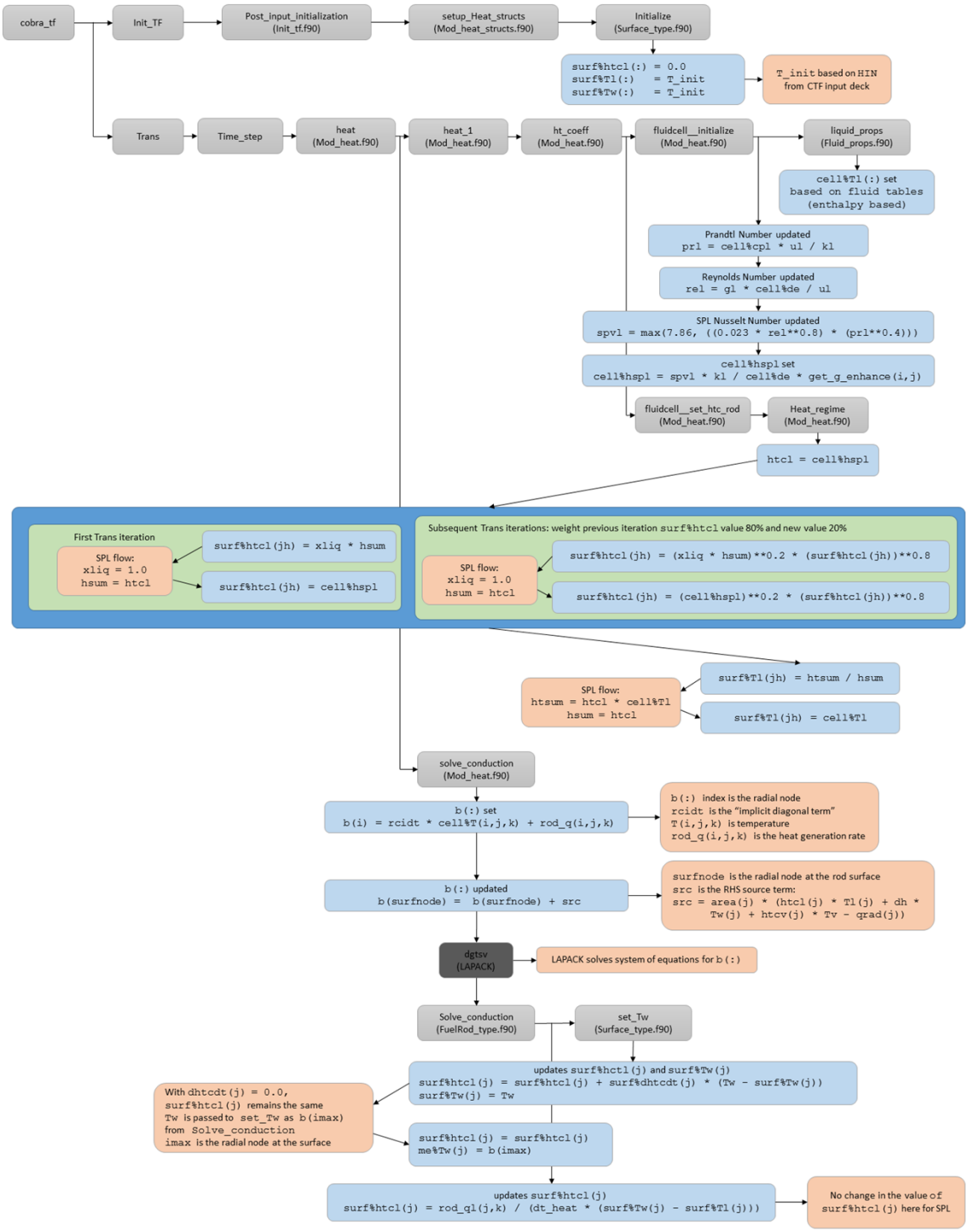

Figure 1: CTF flowchart for the HTC-related parameters

Selected High-Fidelity CFD Code, STAR-CCM+

STAR-CCM+ background

A computational fluid dynamics (CFD) code, such as STAR-CCM+ [50], is designed to provide approximate solutions to the governing equations of a fluid [55]. The fluid dynamics conservation of mass equation defines the rate of change of mass of a control volume of fluid, and that it must be equal to the net flow of fluid into or out of the control volume. Equation (38) shows the differential form of the mass continuity equation.

$$\frac{\delta \rho}{\delta t} + \nabla \cdot \left(\rho \vec{V}\right) = 0 \tag{38}$$

Similarly, the conservation of momentum, shown in Equation (39), specifies that a change in momentum of the fluid volume must be caused by external forces or fluid entering/leaving the control volume. Frictional and gravitational forces may act on the fluid volume and are capable of altering momentum.

$$\rho \frac{\delta \vec{V}}{\delta t} + \rho(\vec{V} \cdot \nabla)V = -\nabla p + \rho \vec{g} + \nabla \cdot \tau_{ij} \tag{39}$$

The energy conservation over the fluid volume states that total energy in the closed system must not change. The viscous dissipation term in Equation (40), Φ, defines the rate at which heat is generated from mechanical energy in the fluid.

$$\rho \frac{\delta h}{\delta t} = \frac{\delta p}{\delta t} + \nabla \cdot (k \nabla T) + \Phi \tag{40}$$

When considering the case of three-dimensional compressible and viscous flow, the Navier-Stokes equation set may be derived from the momentum conservation equation to provide solutions for fluid velocities.

Due to complexity of the equations and the relatively small size of the considered fluid volumes, analytical solutions of these equations are not possible for the majority of simulations involving fluid dynamics. CFD codes are designed to provide these approximate solutions to the aforementioned fluid continuity equations. Their application to calculating flow solutions covers a wide set of conditions varying based on fluid, flow regime, and state of matter. STAR-CCM+ allows users to specify fluid properties and control solution mechanisms through an intuitive graphical user interface.

CFD codes rely on discretization of the flow domain and solving for fluid parameters at each node. Differential equations defining the flow characteristics can be converted to algebraic expressions on the discretized domain. The solution, which may entail a large number of properties to solve at each node, is optimized and accelerated using matrix properties in order to greatly reduce runtime and memory consumption. Nonlinearities, such as those introduced with turbulent flow, require additional attention and defining equations.

There are several methods for treating and capturing turbulence in CFD simulations. A direct numerical simulation (DNS) actually solves the Navier-Stokes equations numerically at a computational cost proportional to the Reynolds number of the simulation. Though it provides some advantages in resolving turbulence, the small time steps and memory costs are often prohibitive for applying DNS to the complex geometry of nuclear reactor flow simulations. Large eddy simulations (LES) reduce the computational costs by filtering smaller-scale turbulent effects from the simulations and applying a scheme across these small length scale calculations.

STAR-CCM+ v.11.04 offers a variety of turbulence models for its users. The Reynolds-Averaged Navier-Stokes (RANS) models include the K-Epsilon and K-Omega models, and there are also options for Reynolds Stress Transport and LES.

Within the K-Epsilon turbulence models, there are nine selections for specific modelling techniques. The application within the simulations of this research all utilize the Realizable K-

Epsilon Two-Layer model. The realizable method differs from the standard method in STAR-CCM+ by how it treats the turbulent dissipation rate [50]. The 'K' term refers to the turbulent kinetic energy, and the epsilon term, ε, is the turbulent dissipation rate. The two-layer approach treats the viscous sublayer parameters of turbulent viscosity and turbulent dissipation rate as functions of wall distance. The parameters in the region far from the wall are blended with the near-wall parameters using smoothing functions. STAR-CCM+ states that its two-layer approach works well with fine near-wall meshing ($y^+ \approx 1$) as well as for sparser mesh ($y^+ > 30$) [50].

STAR-CCM+ Heat Transfer

STAR-CCM+ performs its convective heat transfer calculations based upon Equation (41). This method depends on modelling options set by the user as well as boundary conditions and mesh parameters.

$$q_s'' = \frac{\rho_f(y_c) c_{p,f}(y_c) u_\tau}{t^+\left(y^+(y_c)\right)}(T_s - T_c) \tag{41}$$

In Equation (41), q_s'' is the surface heat flux in W/m^2, and it is based upon the value for the heat flux specified by the user at the surface of interest. Other parameters in Equation (41) are the fluid density, ρ_f, in kg/m^3, the isobaric specific heat of the fluid, $c_{p,f}$, in J/K, and the normal distance to the wall from the near-wall cell centroid, y_c, in meters. The reference velocity, u_τ, is often related as a function of the wall shear stress and the fluid density as shown in Equation (42).

$$u_\tau = \sqrt{\frac{\tau_w}{\rho}} \tag{42}$$

Though in practice, the reference velocity is derived from a turbulence quantity specific to the selected turbulence model within STAR-CCM+. This calculation utilizes STAR-CCM+'s "Standard Wall Functions", which depend upon parameters such as the laminar and turbulent

Prandtl numbers, the turbulent kinetic energy, and the non-dimensional velocity, u^+. Other terms of Equation (42) are the non-dimensional temperature, t^+, as well as the non-dimensional wall distance, y^+. Equation (43) shows the relation for calculating the y^+ values within STAR-CCM+.

$$y^+ = y\frac{u_\tau}{\nu} \tag{43}$$

In Equation (43), ν is the kinematic viscosity of the fluid in m^2/s and y is the cell centroid distance from the wall. The last portion Equation (43) contains the temperature difference between the surface and the near-wall cell, with both values in units of Kelvin.

STAR-CCM+'s Standard Wall Functions are used to calculate parameters of Equation (43) such as the reference velocity and the non-dimensional temperature. With a two-layer turbulence model, STAR-CCM+ treats two portions of the near-wall flow as the viscous sublayer and the logarithmic layer. Depending on the models chosen, the buffer region at the interface of these two regions is treated to either smooth the slope discontinuities or leave the discontinuity. STAR-CCM+ considers flow to be within the viscous sublayer if its y^+ value falls under a certain value, as shown in Equation (44).

$$y^+ < y_m^+ \tag{44}$$

Typically, this border value of y^+ is around 10 for dividing flow into the viscous and the log-law regions, though the buffer region can extend in both directions from this value, generally applied between 5 and 30 units.

Within STAR-CCM+, the user can select several options for determining an HTC across the solution domain. The choice of this post-processing HTC method does not affect calculations. The choice in HTC extraction method can allow the user to specify a reference temperature or allow STAR-CCM+ to calculate the reference temperature. This is to account for differences in the bulk fluid temperatures. STAR calculates the reference temperature at each surface mesh cell

location, so setting a single reference temperature for the entire simulation would have an impact on the extracted HTC values.

Introduction to the PSBT Benchmark

The Pressurized Water Reactor (PWR) subchannel and bundle tests (PSBT) Benchmark specification [49] provides information and results for various 5x5 heated bundle experiments performed by the Nuclear Power Engineering Corporation (NUPEC) in Japan. PSBT specification includes spacer grid details, boundary conditions, and power profiles for the PWR-like experiments.

The exercises of the PSBT Benchmark are separated by effects and measured quantities of interest. These experiments are grouped as:

Phase I – Void Distribution Benchmark

- Exercise 1 – Steady-state single subchannel benchmark
- Exercise 2 – Steady-state bundle benchmark
- Exercise 3 – Transient bundle benchmark
- Exercise 4 – Pressure drop benchmark

Phase II – Departure from Nucleate Boiling (DNB) Benchmark

- Exercise 1 – Steady- state fluid temperature benchmark
- Exercise 2 – Steady-state DNB benchmark
- Exercise 3 – Transient DNB benchmark

The data from the PSBT Benchmark used for comparison in this research falls under the steady-state fluid temperature exercise of the DNB Measurement Phase. This corresponds to PSBT Test Series Number 1, which contains the fluid exit temperature results from single-phase experiments.

PSBT Test Series 1

Details for the bundle utilized for Test Series 1 are provided in Table 2. The axial locations of the grids refers to the distance to the leading edge of the grid. The normalized radial power profile of the 5x5 rod bundle is shown in Figure 2. Details to the spacer grid locations and spacing are provided in Table 3.

Table 2: PSBT Test Series 1 bundle geometry data [49]

Bundle Assembly ID	A1
Number of electrically-heated rods	25
Rod OD	9.5 mm
Rod pitch	12.6 mm
Heated length	3658 mm
Number of MVG spacer grids	7
MVG axial locations	457, 914, 1372, 1829, 2286, 2743, 3200 mm
Number of NMV spacer grids	2
NMV axial locations	0, 3658 mm
Number of SSG spacer grid	8
SSG axial locations	229, 686, 1143, 1600, 2057, 2515, 2972, 3429 mm
Axial power profile	Uniform
Radial power profile	See Figure 2

Table 3: Details of the spacer grid placement in the PSBT Test Series 1 experiment

Grid number	Grid type	Axial location [mm]	Δz [mm]
1	NMV	0	229
2	SSG	229	228
3	MVG	457	229
4	SSG	686	228
5	MVG	914	229
6	SSG	1143	229
7	MVG	1372	228
8	SSG	1600	229
9	MVG	1829	228
10	SSG	2057	229
11	MVG	2286	229

12	SSG	2515	228
13	MVG	2743	229
14	SSG	2972	228
15	MVG	3200	229
16	SSG	3429	229
17	NMV	3658	-

The fluid temperature is measured using thermocouples located in each subchannel 457 mm past the end of the heated length, which is 4115 mm from the beginning of the heated length. The flow outlet occurs at 4500 mm, and the inlet is at -25 mm where 0 mm corresponds to the beginning of the heated length. Estimated values of accuracy for the PSBT experimental test conditions are provided in Table 4.

Table 4: Estimated accuracy in PSBT experimental conditions [49]

Pressure	1%
Flow rate	1.5%
Power	1%
Fluid temperature	1 degree Celsius

Each of the 69 experiments for PSBT Test Series 1 has its flow conditions detailed in Table 5. The linear power is provided instead of total bundle power because CTF accepts linear power in its input file. CTF simulations of these 69 test cases with no spacer grid modelling options reveals that 41 have subchannel results entire within CTF's single-phase liquid heat transfer regime. The remaining 18 experimental runs produce subchannel results partially in CTF's subcooled nucleate boiling heat transfer regime. These CTF heat transfer regimes are discussed in more detail in Chapter 3. The variation in the Test Series 1 flow conditions covers a large range of inlet and thermal conditions.

- Pressure varies from 49 to 165.9 bar
- Flow rate varies from 0.298 to 11.576 kg/s

- Inlet temperature varies from 84.5 to 89.2 C
- Linear power varies from 1.2 to 37.62 kW/m

Table 5: PSBT DNB Test Series 1 experimental flow conditions [49]

Test case ID	Pressure [bar]	Flow rate [kg/s]	Inlet temperature [°C]	Linear power [kW/m]
01-3233	98.1	3.131	166.1	10.72
01-3232	98.2	1.315	164.4	4.48
01-3239	98.2	0.840	165.3	2.73
01-3231	98.2	0.298	166.2	1.20
01-5343	147.4	3.409	165.3	13.67
01-5342	147.1	1.301	164.5	5.69
01-5242	147.0	1.301	185.1	4.48
01-5243	147.4	3.314	184.7	10.72
01-5143	147.3	3.158	202.9	7.65
01-5333	147.6	3.118	211.6	13.56
01-5233	147.5	3.328	230.9	10.61
01-5235	147.1	7.435	230.3	23.07
01-5325	147.4	7.449	255.7	29.31
01-5225	147.3	7.435	272.6	22.85
01-5215	147.4	7.422	282.9	22.85
01-5125	147.4	7.415	289.2	16.40
01-5123	147.9	3.328	288.5	7.65
01-5213	147.1	3.375	282.3	10.61
01-5223	147.2	3.382	272.2	10.61
01-5222	147.2	1.349	273.0	4.37
01-5212	147.2	1.335	282.2	4.37
01-5322	147.2	1.328	255.7	5.58
01-5133	147.1	3.375	247.1	7.65
01-5323	147.2	3.368	254.7	13.45
01-5135	147.1	7.476	247.0	16.40
01-5237	147.2	11.488	229.4	35.32
01-5335	147.2	7.462	211.7	29.63
01-5145	147.2	7.476	203.3	16.73
01-5245	147.2	7.496	184.4	23.18
01-5345	147.1	7.510	165.1	29.74
01-3225	98.4	7.503	224.5	23.18
01-3215	98.3	7.523	238.6	23.07
01-5231	147.1	0.468	230.9	1.20

01-6231	165.8	0.366	252.9	1.20
01-6239	165.7	0.800	254.5	2.84
01-5239	148.8	0.834	231.6	2.84
01-5332	147.1	1.356	211.5	5.80
01-5232	147.2	1.383	231.0	4.59
01-6232	165.8	1.423	251.5	4.59
01-6233	165.8	3.321	254.0	11.15
01-6235	165.9	7.455	253.0	24.06
01-6237	165.8	11.576	253.0	37.07
01-3235	99.1	7.489	164.8	24.49
01-3237	99.1	11.563	164.9	37.40
01-1231	49.8	0.495	98.6	1.20
01-1239	49.8	0.779	84.5	2.73
01-1232	49.9	1.356	87.2	4.48
01-1233	49.1	3.409	85.0	11.04
01-1235	49.0	7.489	86.0	24.49
01-1237	49.2	11.522	86.0	37.62
01-3245	98.2	7.449	103.6	24.28
01-5255	147.2	7.469	113.8	24.28
01-5355	147.1	7.476	94.3	31.16
01-5155	147.2	7.469	133.2	17.39
01-5153	147.2	3.423	132.9	7.87
01-5253	147.2	3.402	113.3	11.04
01-5353	147.1	3.409	93.4	14.32
01-5352	147.1	1.349	93.3	5.69
01-5252	147.1	1.322	113.9	4.48

1.6393	1.6393	0.4098	0.4098	0.4098
1.6393	1.6393	1.6393	0.4098	0.4098
1.6393	1.6393	0.4098	0.4098	0.4098
1.6393	1.6393	1.6393	0.4098	0.4098
1.6393	1.6393	0.4098	0.4098	0.4098

Figure 2: Normalized radial power profile for the PSBT Test Series 1 experimental cases

PSBT spacer grid details

This section provides details for the three types of spacer grids located within the PSBT A1 bundle used in Test Series 1. These three PSBT spacer grids are:

- Non-Mixing Vane spacer grid (NMV)
- Mixing Vane spacer Grid (MVG)
- Simple Spacer Grid (SSG)

The SSG contains only horizontally-oriented dimples, as detailed in Figure 3, to maintain the positions of the rods. The MVG and NMV both contain springs as well as vertically-oriented springs for constraining the rods. The SSG is detailed in Figure 7, Figure 8, and Figure 9. The SSG has the smallest strap height of the three grids, and, as previously mentioned, constrains each rod from all four sides using the lateral dimples, which exist at two different elevations along the strap height. The PSBT NMV details are provided in Figure 10, Figure 11, and Figure 12. The PSBT MVG geometry is shown in Figure 13, Figure 14, Figure 15, and Figure 17. The details of the mixing vanes, which are angled at 28 degrees from the flow direction, are provided in Figure 16. The springs and dimples are the same on both the NMV and the MVG. The main differences between the grids are the strap heights and the inclusion of mixing vanes.

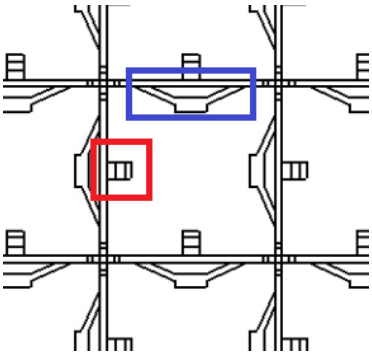

Figure 3: Top view of a spacer grid spring (left box) and a spacer grid dimple (upper box)

The flow area blockages for each grid component were measured using the CAD program SolidWorks [5] by projecting each feature individually on to the cross-sectional view perpendicular to the flow direction in order to determine the flow blockage area of each component.

The dimples of each spacer grid have a calculated blockage area of 3.66 mm^2 each. The MVG/NMV springs calculated blockage area is 1.65 mm^2 each. There are two springs and two dimples per internal subchannel of the NMV and MVG. There are four dimples in the internal subchannels of the SSG. The projected area of the vanes is calculated as 8.17 mm^2 per vane (two per internal subchannel). The grid straps for each of the PSBT grids have a blockage area of 12.60 mm^2 per internal subchannel. The flow area of the internal subchannel is calculated using the rod pitch of 12.6 mm and rod outer diameter of 9.5 mm to obtain 87.88 mm^2. Table 6 summarizes the flow blockage areas of the internal subchannel for each PSBT spacer grid.

Table 6: Details of the flow blockages for an internal subchannel in each PSBT spacer grid

PSBT spacer grid	MVG	NMV	SSG
Grid straps area [mm^2]	12.60	12.60	12.60
Springs area [mm^2]	3.30	3.30	-
Dimples area [mm^2]	7.32	7.32	14.64
Vanes area [mm^2]	16.34	-	-
Bare flow area [mm^2]	87.88	87.88	87.88

The blockage ratios can then be calculated for each PSBT spacer grid by dividing the blockages by the bare flow area of the internal subchannel. Geometric details as well as the results for the flow blockage ratio of each PSBT spacer grid broken down by grid component is shown in Table 7.

Table 7: Summary of geometry details for the internal subchannels with spacer grids in the PSBT A1 rod bundle

PSBT spacer grid	MVG	NMV	SSG
Overall height	63.646 mm	41.148 mm	12.800 mm
Strap height	58.928 mm	41.148 mm	12.800 mm
Vane height	4.718 mm	-	-
Strap thickness	0.508 mm	0.508 mm	0.508 mm
Blockage ratio (no vanes)	0.26	0.26	0.31
Vane angle	28 degrees	-	-
Vane blockage ratio	0.19	-	-
Total blockage ratio	0.45	0.26	0.31
Spacer grid material	Inconel 600	Inconel 600	Inconel 600

The naming scheme for the subchannels based on their geometry within the rod bundle is shown in Figure 4. Subchannels are identified as either internal, side, or corner subchannels in this work.

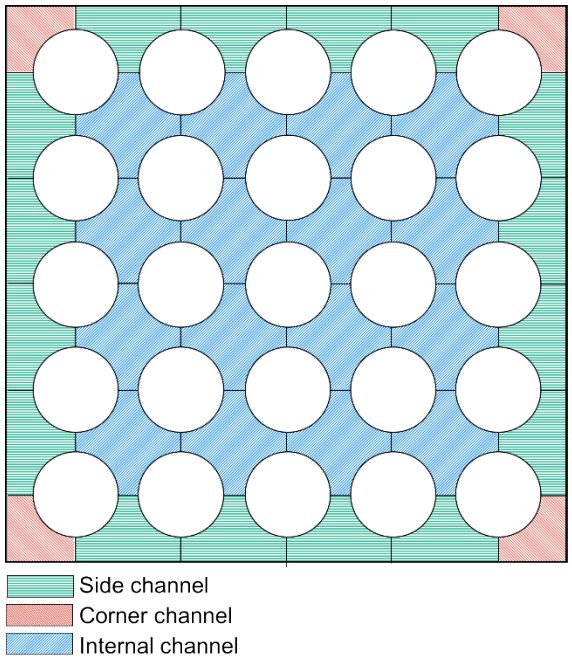

Figure 4: Location of subchannel types within the PSBT A1 5x5 rod bundle

Modelling simplifications for the PSBT spacer grid in CFD simulations

The grid strap thickness of all three PSBT grids was slightly altered from the PSBT Benchmark value of 0.508 mm to 0.500 mm to aid in the geometric layout of the CFD simulation. In order to remove some small-angle cells from the simulations, the region where the springs/dimples contact the rods has been expanded laterally in order to merge with the rod along a continuous surface. This is shown in Figure 5, highlighted by the red boxes. This has an impact on flow just up/downstream of these locations, but as the focus is on a larger-scale subchannel approach, the deviations in this small region are acceptable. Neykov presented another method for simplifying the springs and dimples of a spacer grid by replacing them with rectangular prisms while keeping the flow blockage ratio constant [7]. This method greatly reduces the complexity of the mesh near the grids at the cost of detailed modelling potential. While the method of merging the grid's contact region into the rod does slightly alter the blockage ratio, it also preserves the other intricate geometry details of each spacer grid better than the method of Neykov and allows for detailed simulations in CFD.

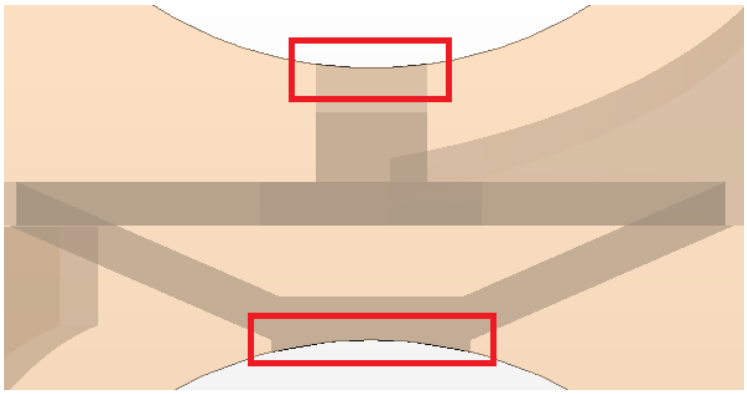

Figure 5: PSBT spacer grid and rod completely merged intersection

CFD simulations were performed with a narrower merged area as shown in the blue box of Figure 6. Note the incomplete contact between the grid and the rod, which only contacts the grid's dimple near its center. This partial merge potentially allows for better fluid flow around the rod at the grid locations but it also contains a region of small-angle mesh cells. The full merging method illustrated in Figure 5 is used for all PSBT CFD simulations in this research.

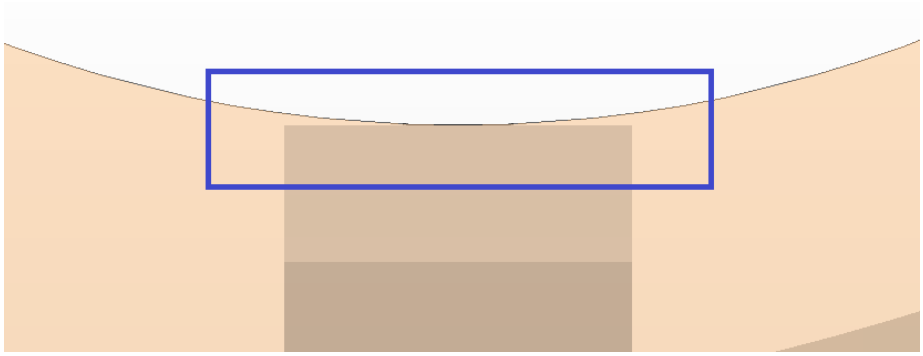

Figure 6: PSBT spacer grid and rod partially merged

CFD simulations were also performed with the spacer grid dimples and springs removed in order to greatly simplify the flow domain mesh. These types of simplifications provide good agreement with downstream temperatures but do not allow for the details of grid asymmetry effects to be captured.

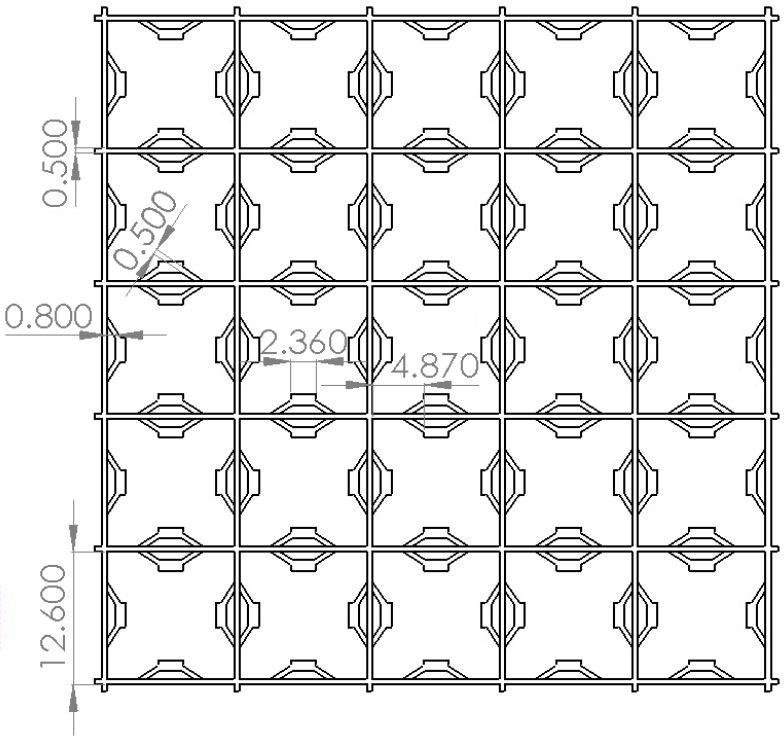

Figure 7: PSBT SSG geometry details, top view

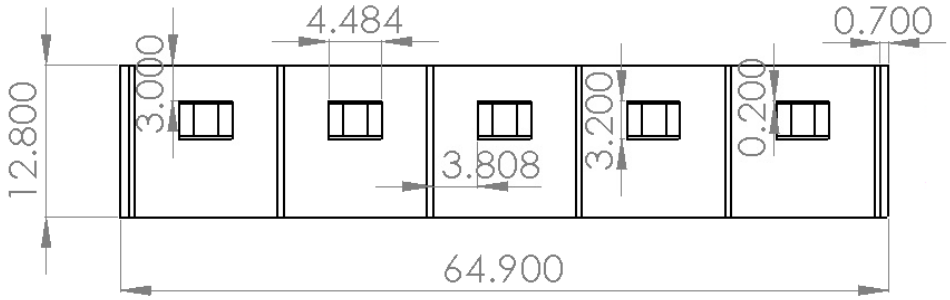

Figure 8: PSBT SSG geometry details, side view

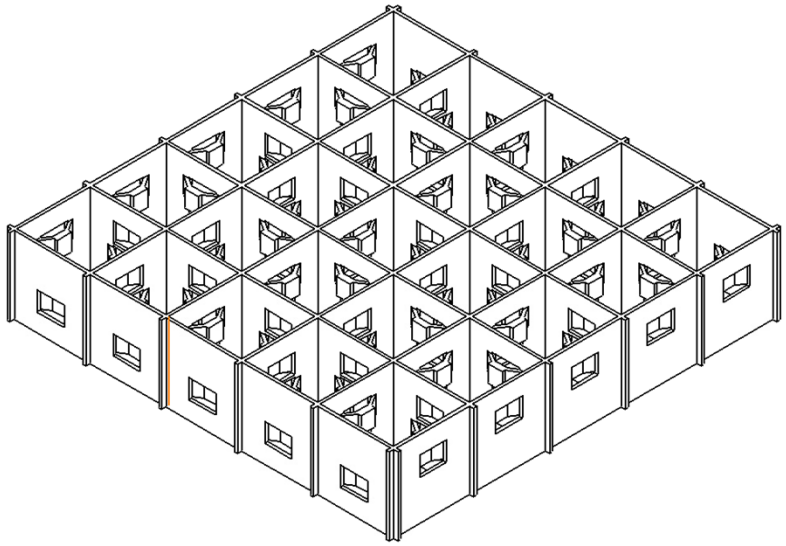

Figure 9: PSBT SSG geometry details, isometric view

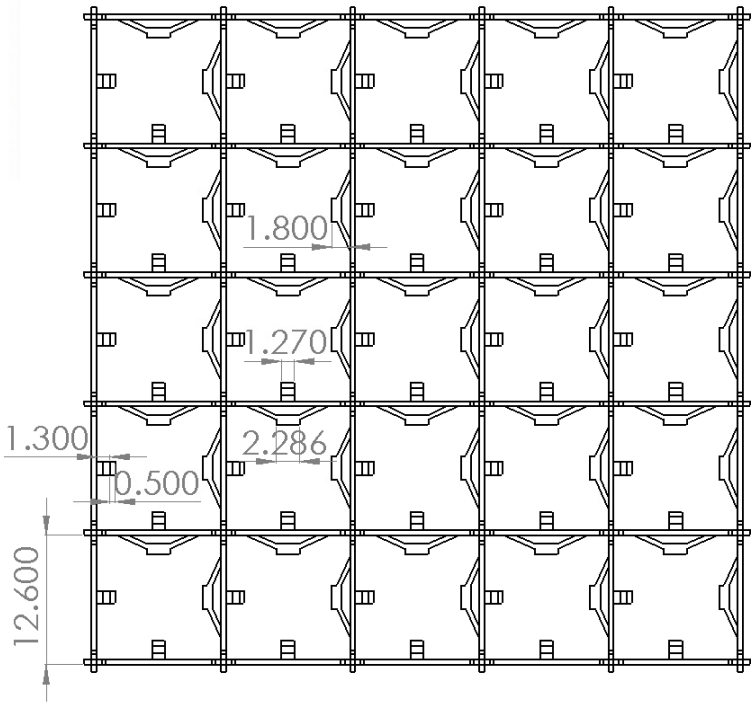

Figure 10: PSBT NMV geometry details, top view

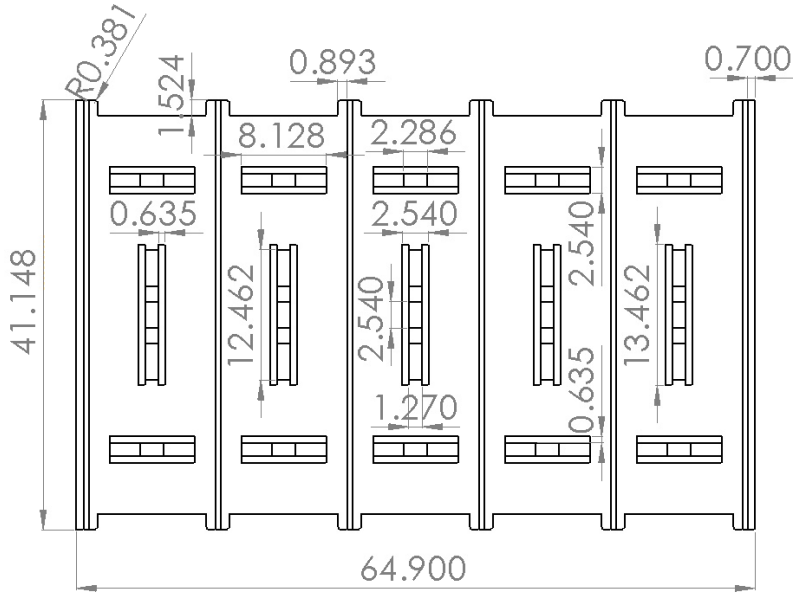

Figure 11: PSBT NMV geometry details, side view

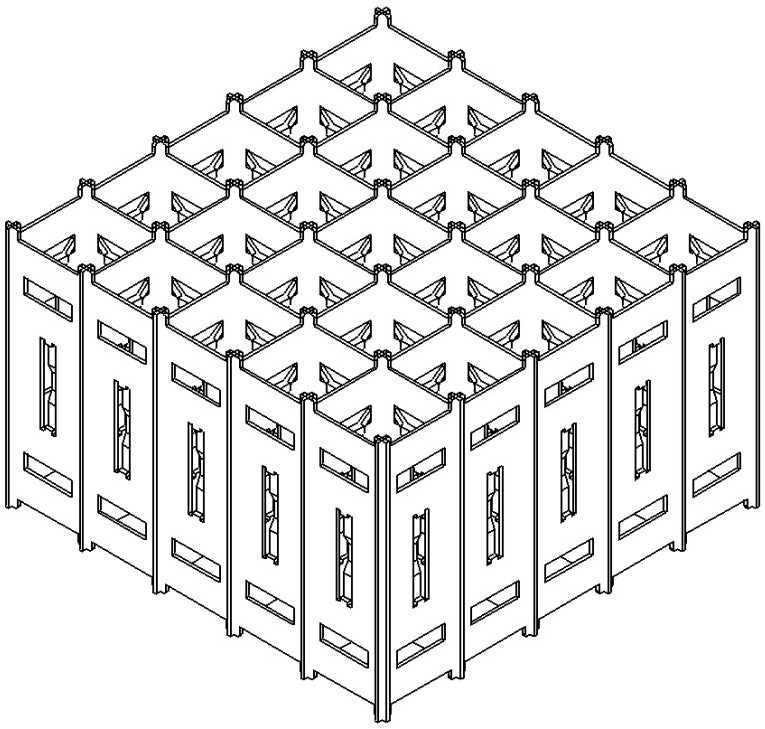

Figure 12: PSBT NMV geometry details, isometric view

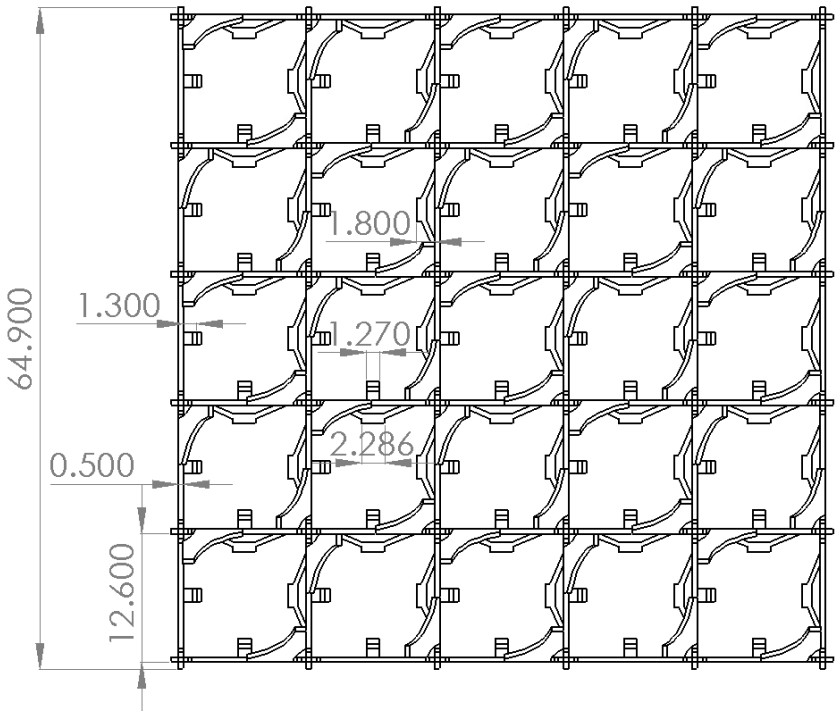

Figure 13: PSBT MVG geometry details, top view

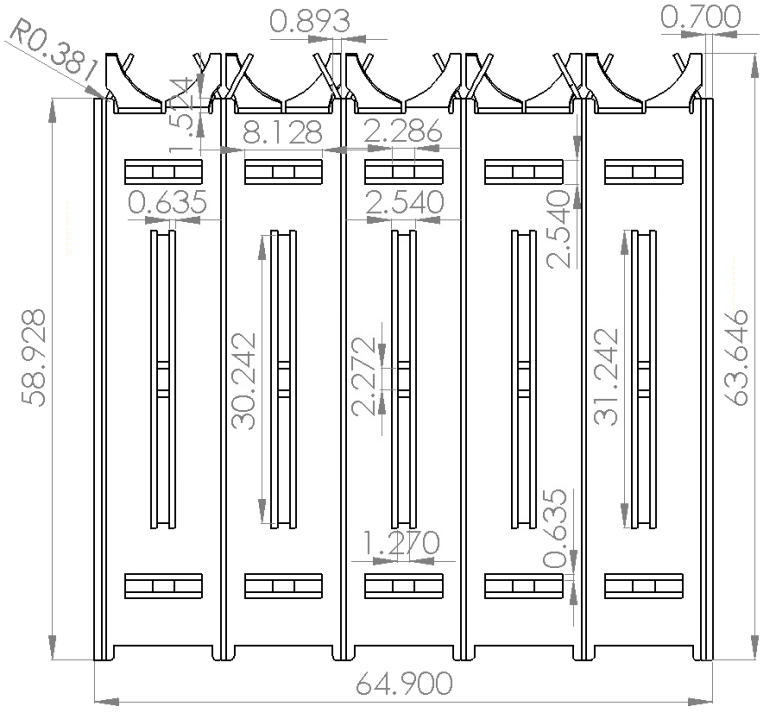

Figure 14: PSBT MVG geometry details, side view

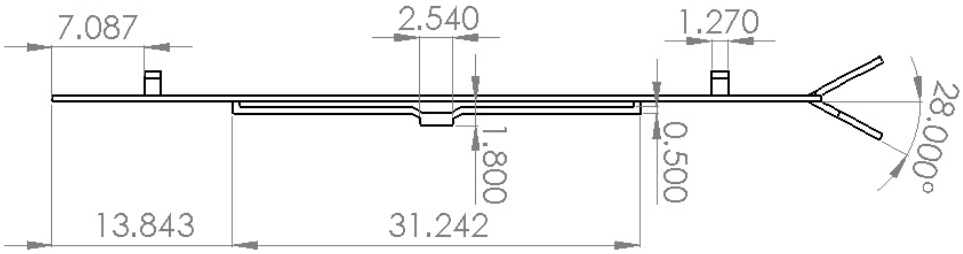

Figure 15: PSBT MVG geometry, grid strap side view

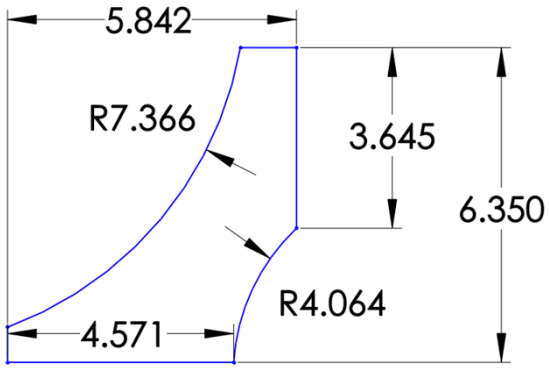

Figure 16: PSBT MVG mixing vane geometry details

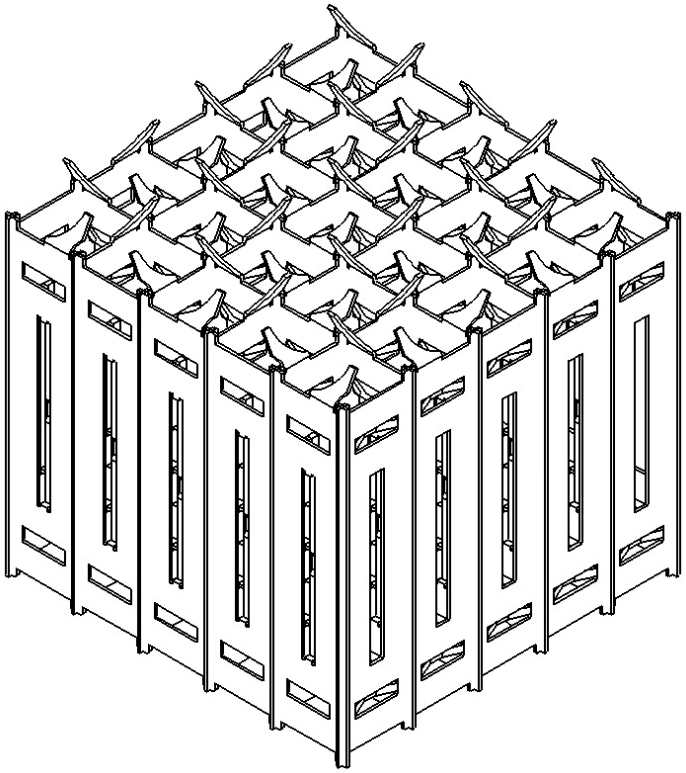

Figure 17: PSBT MVG geometry details, isometric view

Chapter 4

CFD-Informed Models for Spacer Grid-Enhanced Cross-flow in CTF

The cross-flow over subchannel gaps in a rod bundle can be caused by a spacer grid placed in the flow path. Its non-zero strap thickness and structural features increase turbulence downstream, and if the spacer grid has mixing vanes attached, these vanes may direct flow across subchannel gaps. Accounting for these spacer grid-caused effects in the subchannel code CTF can improve predictions near and downstream of spacer grids. This research implemented and tested models of previously-developed CFD-informed subchannel models into the current code CTF. Details for how the spacer grid-enhanced turbulent mixing model and the mixing vane-directed cross-flow model were developed and implemented into CTF are in this chapter.

CFD-Informed Model for Spacer Grid-Enhanced Turbulent Mixing

The method for calculating the turbulent mixing multiplier is based on the method previously presented by Avramova [2]. While Avramova produced a single turbulent mixing multiplier for each axial location in the simulation, it is possible to refine this by determining a multiplier which is dependent on the type of connection between the subchannels. These different gap connections considered for each spacer grid in the PSBT Benchmark [49] are as follows:

1. Internal subchannel to internal subchannel
2. Internal subchannel to side subchannel
3. Side subchannel to side subchannel
4. Corner subchannel to side subchannel

These gap connections types are illustrated in Figure 18 to show their respective locations within the PSBT A1 bundle [49].

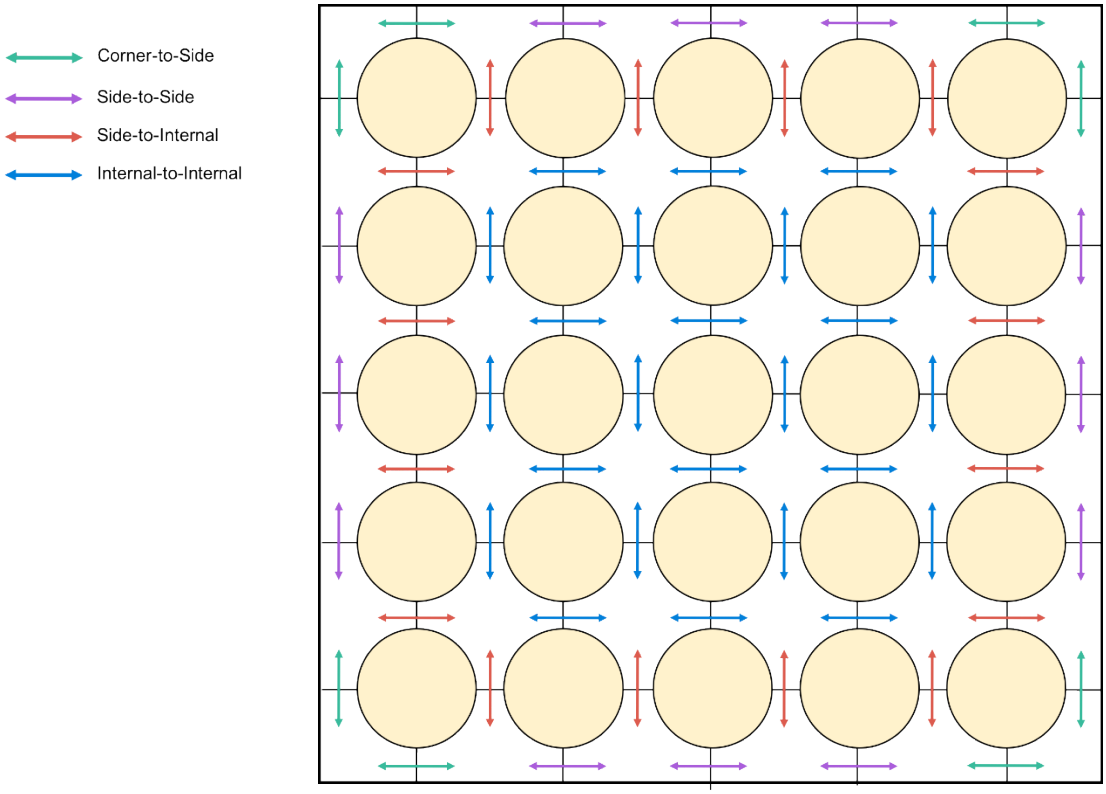

Figure 18: Gap connection types for the PSBT A1 bundle

The CFD models developed by Avramova are limited to internal-internal subchannel geometry, and accounting for the other types of connections requires using the same methods with new CFD models. For the PSBT grids, the gaps differ in their geometric subchannel connections as well as the physical width of the gap itself. Table 8 details the PSBT A1 bundle gap geometry details. The peripheral gaps are in contact with the PSBT's outer walls, which act as a shroud around the bundle. These peripheral gaps are also narrower than their internal counterparts and are only in contact with one heated surface, instead of two.

Table 8: PSBT A1 bundle gap details

Total number of gaps	60
Internal-internal gaps	24
Internal-side gaps	16
Side-side gaps	12
Corner-side gaps	8
Internal gap width (lateral)	3.1 mm
Peripheral gap width (lateral)	2.5 mm

For grids with two mirrored and rotated mixing vanes—such as the PSBT A1 bundle's MVG—this approach for the calculation of the turbulent mixing effects will not separate the effects of the directed cross-flow caused by the vanes. Instead of a balance of flow along the gap divided by the thermal gradient set by the initial conditions, the MVG causes the interface between the thermal effects to move too much for Avramova's methods to effectively capture its mixing along the gap. For this research, the MVG's turbulent mixing coefficient is assumed to be the same as the NMV's as their blockage ratios are the same for the strap portion of the grid. In this way the vane effects on turbulent mixing will not be quantized.

If more detailed turbulent mixing results are desired, a full bundle can be modelled and results extracted at each axial level on a per-gap basis. This level of detail, however, is counter-intuitive to the method's relative simplicity and time-efficient setup, though the option is available and modifications for CTF to use these data can be made.

The calculation of the turbulent mixing multiplier begins with the CFD model setup. Details of the CFD simulation are provided in Table 9. The 2x1 subchannel layout geometry for the PSBT MVG case is shown in Figure 19. As the calculations for the turbulent mixing multiplier rely on temperature differences, one subchannel is set to 300 C while the other is set to 310 C in order to create a gradient across the gap connecting the two subchannels. A mass flux inlet condition was eschewed in favor of a velocity inlet condition, which aids in preserving a balanced inlet condition along the gap due to differences in densities at each of the two

conditions. Another method for preserving gap flow would be to eliminate the temperature dependence of the density calculation.

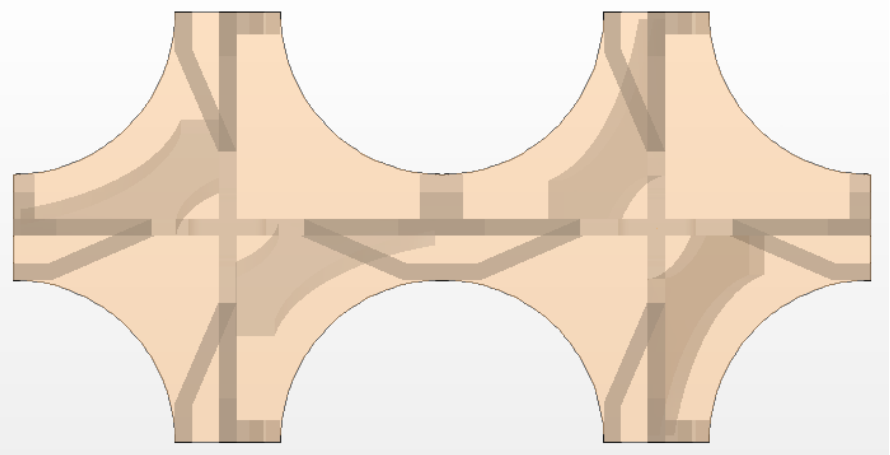

Figure 19: PSBT 2x1 MVG geometry layout for turbulent mixing simulations

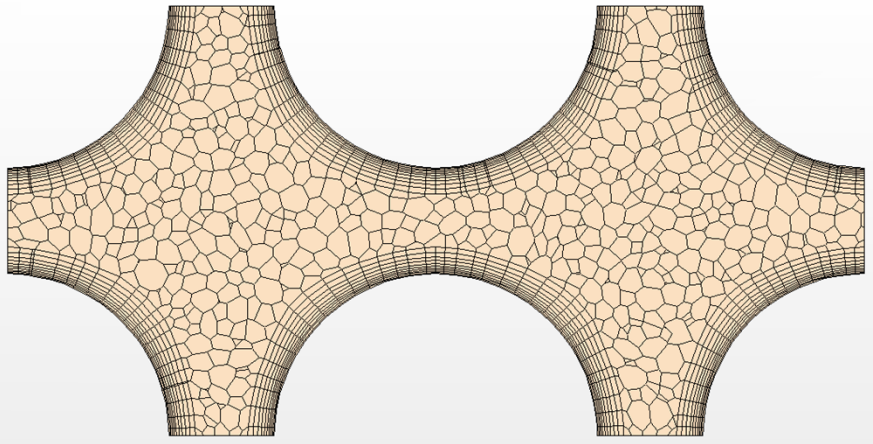

Figure 20: PSBT 2x1 subchannel layout mesh overview

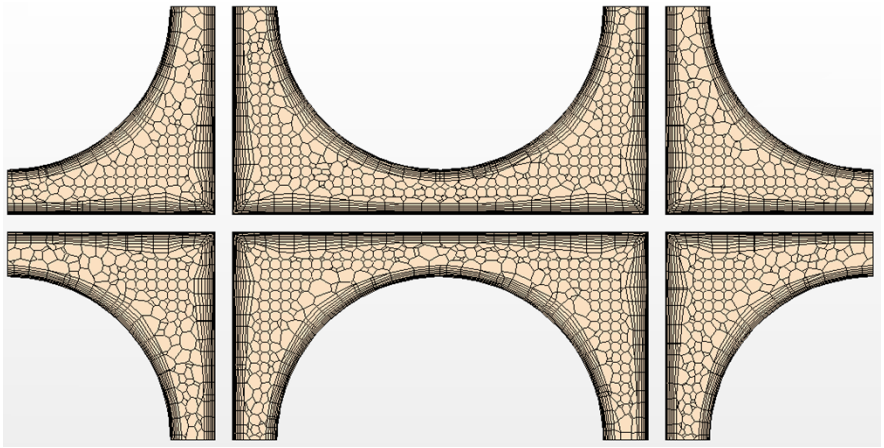

Figure 21: PSBT 2x1 SSG mesh overview in the region at the spacer grid straps

Table 9: Turbulent mixing CFD modelling details for the PSBT spacer grids

Geometry details	
Subchannel layout	2 subchannels, connected via interface along their gaps
Domain length	400 mm (including extruded inlet region)
Grid leading edge axial location	120 mm
Mesh details	
Models	Polyhedral mesher Prism layer mesher Extruder Surface remesher
Base size	0.3 mm
Prism layer details	10 layers at 1.2 spacing, 1.0 mm thickness
Extruder details	100 mm extrusion from inlet, 100 layers at 1.0 spacing
Flow conditions	
Inlet temperature	300 C / 310 C (separated by subchannel)
Inlet velocity	5.0 m/s
Pressure	15.5 MPa
Boundary conditions	
Walls	Wall-type except at gap connection (in-place interface)
Inlet	Velocity inlet
Outlet	Pressure outlet
Physics details	
Models	Liquid Steady Three dimensional Reynolds-averaged Navier-Stokes Turbulent Realizable K-epsilon turbulence Two-layer all y+ wall treatment Exact wall distance Segregated flow Segregated fluid enthalpy User-defined equations of state (Defined in Equation (45) - (47))

The user-defined equations of state for the liquid water are defined in Equation (45) for density, Equation (46) for thermal conductivity, and Equation (47) for dynamic viscosity. T is the temperature, in Kelvin.

$$T < 618\ K:$$
$$\rho = -0.0000116905(T^3) + 0.01225(T^2) - 4.84697(T) + 1670.325859 \text{ kg/m}^3$$
$$T \geq 618\ K:$$
$$\rho = 594.17 \text{ kg/m}^3 \tag{45}$$

$$T < 618\ K:$$
$$\text{k} = -0.3111\text{E} + 01 + 0.3026\text{E} - 01(T) - 0.8131\text{E} - 04(T^2) + 0.4635\text{E} - 07(T^3) + 0.1677\text{E} - 09(T^4) - .3094\text{E} - 12(T^5) + 0.1510\text{E} - 15(T^6) \frac{\text{W}}{\text{m} - \text{K}} \tag{46}$$

$$T \geq 618\ K:$$
$$\text{k} = 0.458331015 \frac{\text{W}}{\text{m} - \text{K}}$$

$$T < 618\ K:$$
$$\mu = \frac{0.1183\text{E} + 12 + 0.2419\text{E} + 09(T)}{1 - 0.4177\text{E} + 13(T) + 0.1638\text{E} + 11(T^2)} \text{ Pa - s} \tag{47}$$

$$T \geq 618\ K:$$
$$\mu = 7.2876\text{E} - 05 \text{ Pa - s}$$

The intent of the grid-enhanced turbulent mixing model is to account for the specific grid geometry effects on the two-phase mixing multiplier in CTF. This modification is employed within CTF in the form of a multiplicative factor which is applied to the two-phase phase component of turbulent mixing. This corresponds to term $\overrightarrow{M_k^T}$ of Equation (22), term $\nabla \cdot \left(\alpha_k \overrightarrow{q_k^T}\right)$ of Equation (23), and term M_k^T of Equation (24). This factor, f_θ, is applied to the two-phase portion of the mixing source terms only. The transverse mass flow caused by turbulent mixing in CTF is defined in Equation (48).

$$W_{ij}^M = \frac{\beta_{\text{tp}} \overline{G}}{\overline{\rho}_{mix}} (G_{iz} - G_{jz}) A_{gap} \tag{48}$$

In Equation (48):

- W_{ij}^{M} is the lateral mixing of mass due to turbulence
- β_{tp} is the two-phase mixing coefficient
- $\overline{G}$ is the average axial mass flux between subchannels i and j
- ρ_{mix} is the average mixture density between subchannels i and j
- G_{iz} and G_{jz} are the axial mass fluxes of subchannels i and j, respectively
- A_{gap} is the cross-sectional area of the gap

Mixing of energy and momentum are similarly defined, and their implementation in CTF can be referenced from the CTF Theory Manual [1]. The grid-enhanced turbulent-mixing model is applied by modifying the mixing coefficient, β_{tp}, using a factor, f_{θ}, as shown in Equation (49).

$$\beta_{tp} = \beta_{tp} f_{\theta} \tag{49}$$

The turbulent mixing factor, f_{θ} is calculated from a CFD simulation of the geometry of interest and must be supplied by an external data-file to CTF. The f_{θ} factor is defined in Equation (50).

$$f_{\theta}(y,\varphi) = \frac{\beta_{SP}^{spacers}}{\beta_{SP}^{no\ spacers}} \tag{50}$$

In this PhD research the CFD-informed model for spacer grid-enhanced turbulent mixing has been implemented in CTF, and the validation database for the model has been extended by including the OECD/NRC PSBT experimental benchmark data. The implementation of the spacer grid-enhanced turbulent mixing model in CTF is shown in Figure 22.

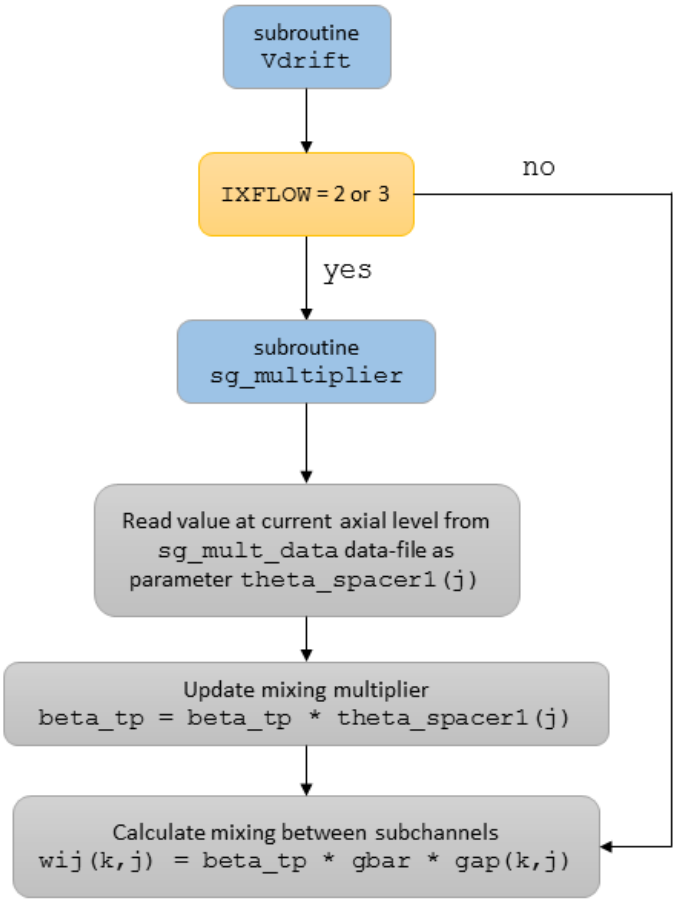

Figure 22: Flowchart of the spacer grid-enhanced turbulent mixing model in CTF

Results required for the turbulent mixing multiplier are split into gap results and subchannel results. The gap results are defined along the interface between the two subchannels and the subchannel results are averaged over each subchannel individually. Figure 23 shows the two subchannels with the flow direction and gap width, S_{ij}, and gap height, Δx, illustrated. The gap results are extracted by creating constrained planes parallel to the gap between the two subchannels within the CFD model, with spacing consistent with the desired axial resolution of the results. A small lateral offset distance from the gap is utilized in order to assure some difference in the results from each subchannel and to provide a distance for the gradient calculations. For this work with the CFD turbulent mixing determination, an offset of 0.1 mm in

either direction is used. Though CFD results are almost as fine as the base mesh size, a spacing of 2 mm was utilized for this research, as it gives detailed insight near the spacer grids but also considers the coarser resolution of the subchannel code, CTF. Details for the geometric parameters used in the result extraction from the CFD simulation are shown in Table 10.

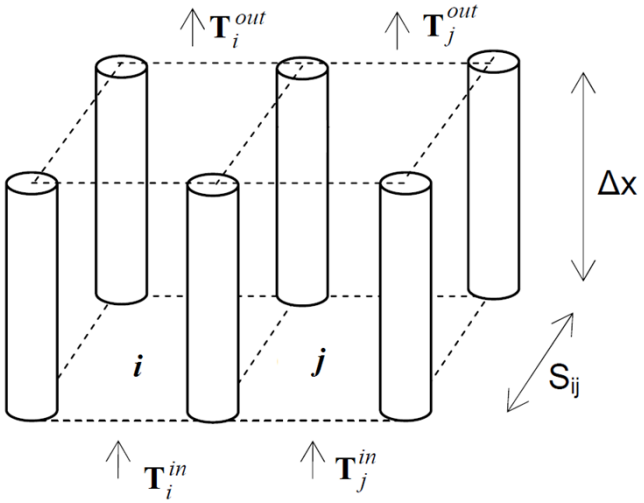

Figure 23: 2x1 subchannel layout used for the CFD determination of the mixing coefficient factor [2]

The fluid temperature conditions applied to subchannels *i* and *j* for a side-internal gap connection are shown in Figure 24. Subchannel *i* is set to 300 C (573.15 K) and subchannel *j* is set to 310 C (583.15 K).

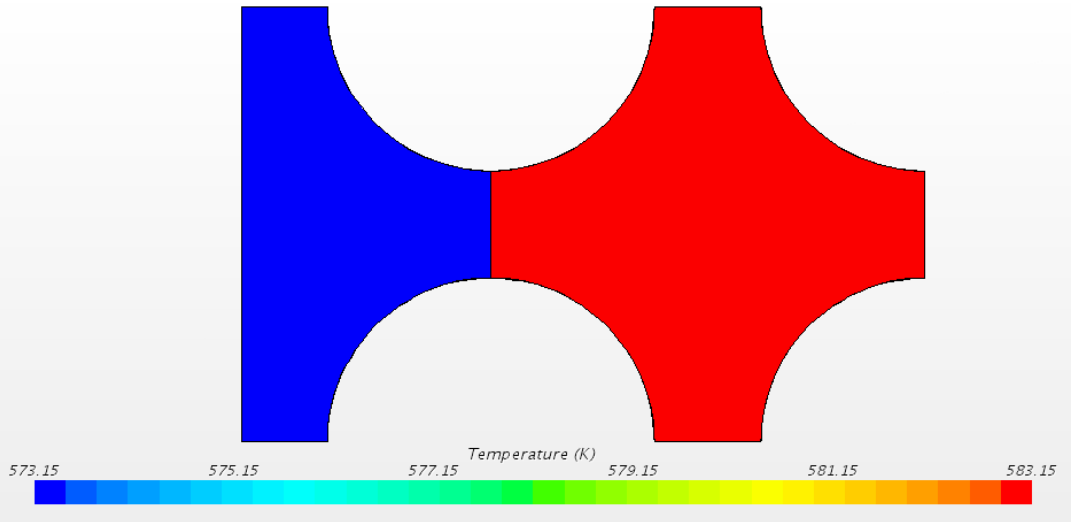

Figure 24: 2x1 subchannel geometry for the turbulent mixing CFD simulations

Table 10: CFD turbulent mixing model data extraction details

Axial spacing	2 mm
Lateral offset from gap	0.1 mm

The results extracted from the CFD simulations are as follows:

- The volume-averaged fluid density of subchannel i
- The volume-averaged axial velocity of subchannel i
- The volume-averaged specific heat of subchannel i
- The surface-averaged fluid temperature at the inlet and outlet of subchannel i
- The average volume-averaged specific heat over subchannels i and j
- The average volume-averaged fluid densities over subchannels i and j
- The average volume-averaged axial velocity over subchannels i and j
- The volume-averaged fluid temperature of subchannels i and j

Constant water properties are also assumed, with the fluid density and specific heat remaining the same over the entire axial length. Table 11 provides the volume-averaged values from subchannel i for the bare subchannel CFD simulation.

Table 11: Turbulent mixing CFD-determined parameters for the cold (300 C) bare subchannel

Volume-averaged specific heat	5509.7 J/kg-K
Volume-averaged fluid density	715.2 kg/m^3
Volume-averaged axial velocity	5.078 m/s

The first step in the turbulent mixing multiplier calculation is determining the thermal gradient across the gap. Equation (51) utilizes the lateral offset (0.1 mm in these calculations) as well as the surface-averaged temperature from either side of the gap.

$$T_{grad,gap}(z) = \frac{T_{gap,j}(z) - T_{gap,i}(z)}{2\Delta x_{gap}} \tag{51}$$

The surface-averaged turbulent viscosity values taken at the gap are averaged using Equation (52).

$$\mu_{turb,gap}(z) = \frac{\mu_{turb,i}(z) + \mu_{turb,j}(z)}{2} \tag{52}$$

The effective heat flux acting at the gap is then calculated utilizing the volume-averaged values for specific heat of subchannel i and the turbulent Prandtl number, which is assumed to be equal to 0.9 for these calculations. Equation (53) gives the procedure for determining the gap heat flux based on the thermal gradient.

$$q''_{gap}(z) = \frac{c_{p,i}}{Pr_{turb}}\left[T_{grad,gap}(z)\right]\left[\mu_{turb,gap}(z)\right] \tag{53}$$

The value for the single-phase mixing coefficient between the two subchannels, β_{sp}, is then calculated using Equation (54). $U_{z,i}$ is the average axial velocity in subchannel i.

$$\beta_{sp}(z) = \frac{q''_{gap}(z)}{[T_{sub,j}(z) - T_{sub,j}(z)]c_{p,i}\rho_i U_{z,i}} \quad (54)$$

The turbulent mixing multiplier is a ratio of the single-phase mixing coefficient for the gridded geometries to the bare subchannel geometries, as defined in Equation (50). This axial distance-based ratio is specific to each gap connection geometry, such as whether the simulation considers the internal-internal type or the side-side type.

With the leading edge of the spacer grids located at 20 mm along the simulation's axial domain, Figure 25 shows the results for the internal-internal subchannel connections. The single-phase mixing coefficient, β_{sp}, increases sharply at the location of the grid, whether it's the PSBT NMV or SSG.

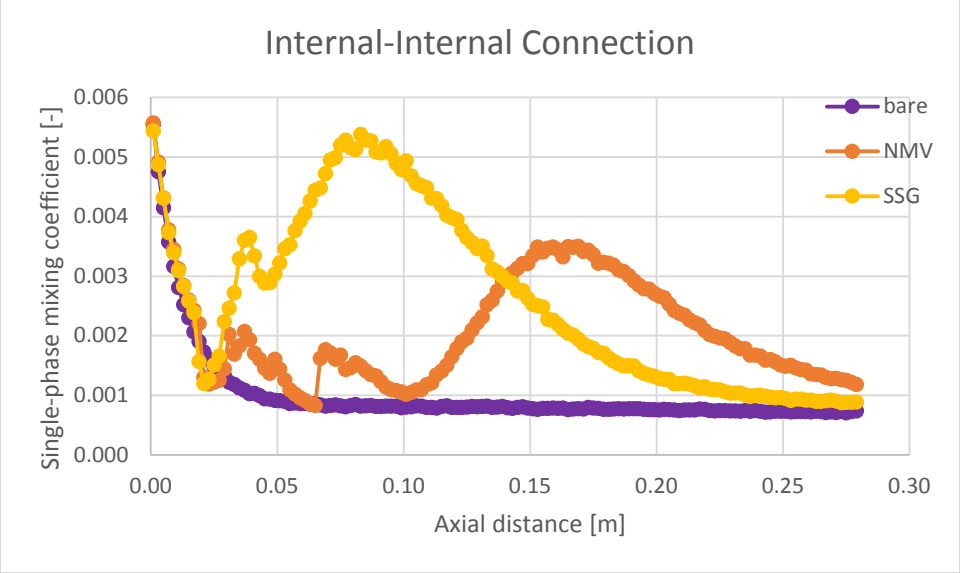

Figure 25: Single-phase mixing coefficient of the internal-internal gaps calculated from CFD simulation for the PSBT grids

Following the technique of Equation (50) and dividing by the results from the bare case allows for the calculation of the multiplier. The results for the internal-internal subchannel

connection turbulent mixing multipliers are shown in Figure 26. The multiplier reaches its maximum value of approximately 6.5 in the SSG simulation. This means that, at its maximum, a factor of 6.5 will be applied to CTF's mixing coefficient during its calculation of the lateral mixing due to turbulence across an internal-internal subchannel gap.

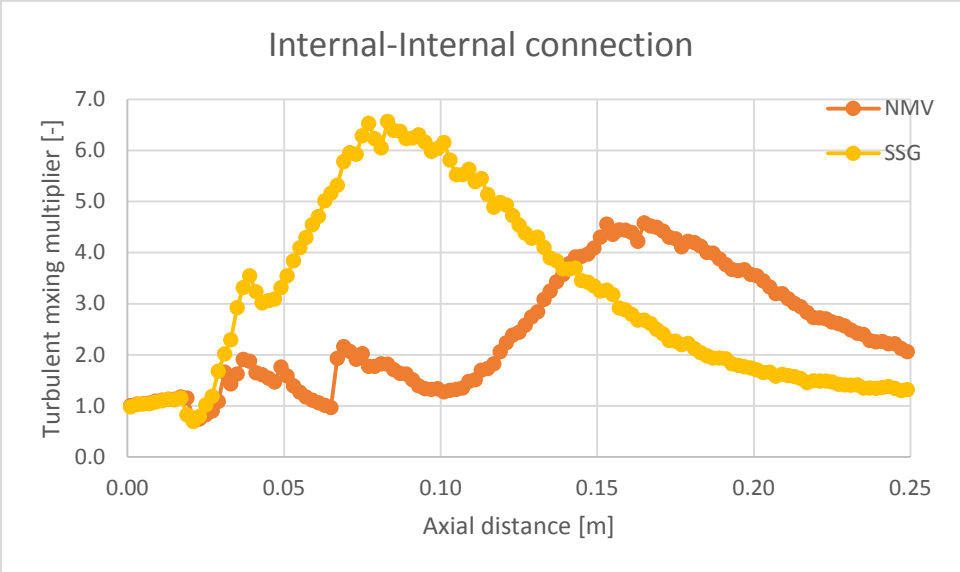

Figure 26: Turbulent mixing multiplier of the internal-internal gaps calculated from CFD simulation for the PSBT grids

The results for the internal-side subchannel gap connection are shown in Figure 27. The maximum value, again for the SSG, is less than for the case of the internal-internal connection. Its peak near 3.5 indicates that there is not as much mixing driven by turbulence along the periphery of the bundle as there is in the central region.

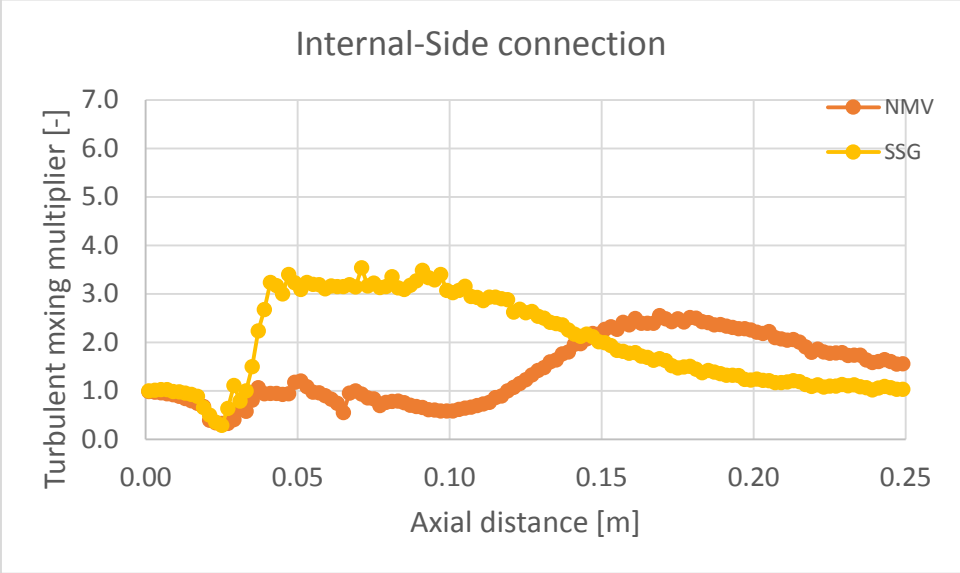

Figure 27: Turbulent mixing multiplier of the internal-side gaps calculated from CFD simulation for the PSBT grids

The turbulent mixing multiplier results for the side-side connections are very similar to those of the internal-side connection, with a similar peak magnitude near 3.5 for the SSG and 2.5 for the NMV. These results are plotted in Figure 28. The results for the corner-side connections are shown in Figure 29.

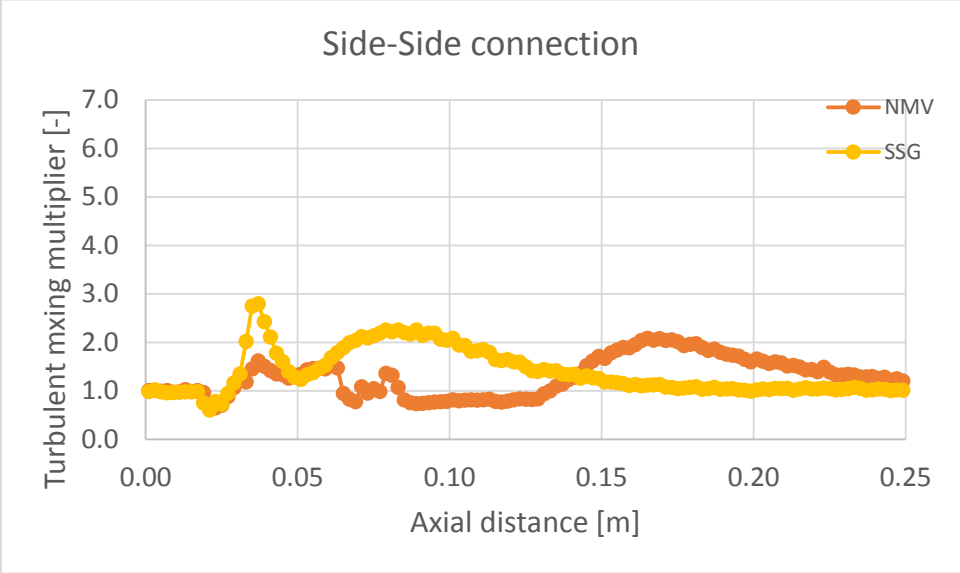

Figure 28: Turbulent mixing multiplier of the side-side gaps calculated from CFD simulation for the PSBT grids

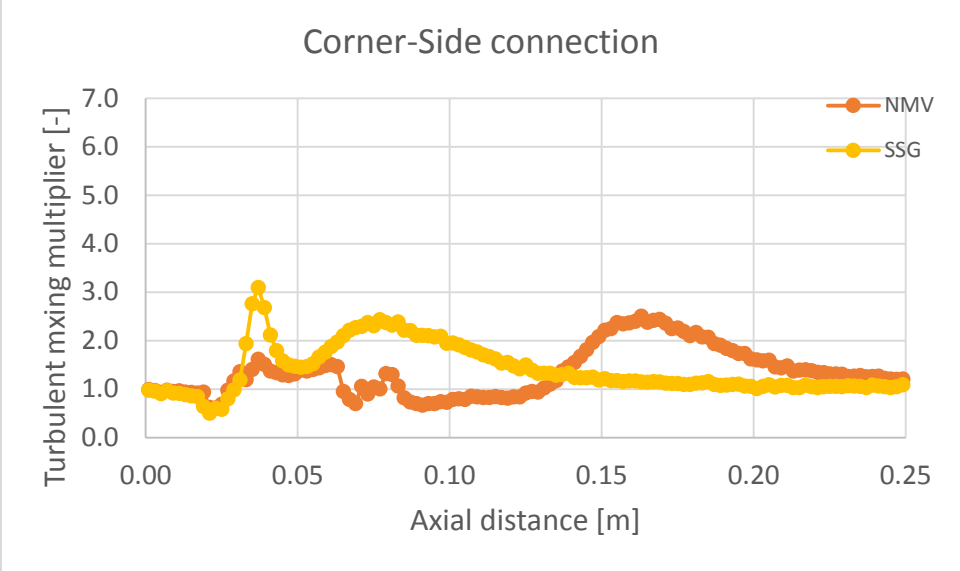

Figure 29: Turbulent mixing multiplier of the corner-side gaps calculated from CFD simulation for the PSBT grids

For the gridded 2x1 simulations, there is a steep increase in the turbulent mixing multiplier at the location of the grid as well as in the region immediately downstream of the grid.

Further downstream, the multiplier decays towards its nominal value of unity. With PSBT bundle A1 axial spacing of 229 mm between grid leading edges, it is surmised from these results that the turbulent mixing has not dropped back to its value of unity by the time the next downstream grid is encountered in the flow. Figure 30 and Figure 31 show the results for the mixing multiplier grouped by grid in order to show the difference in magnitudes among the connection types. It is worth noting the difference in overall grid lengths in the NMV against the SSG, which leads to the difference in the axial location of the peak magnitudes. Both grids have their leading edges located at 20 mm in the simulation.

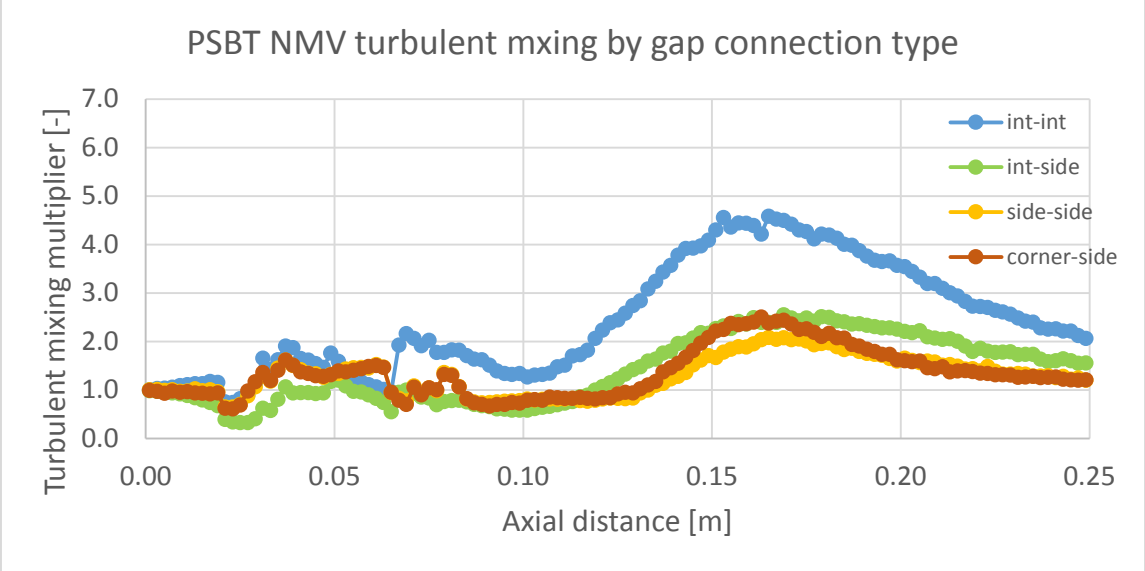

Figure 30: Turbulent mixing multiplier results for each gap geometry in the PSBT NMV grid

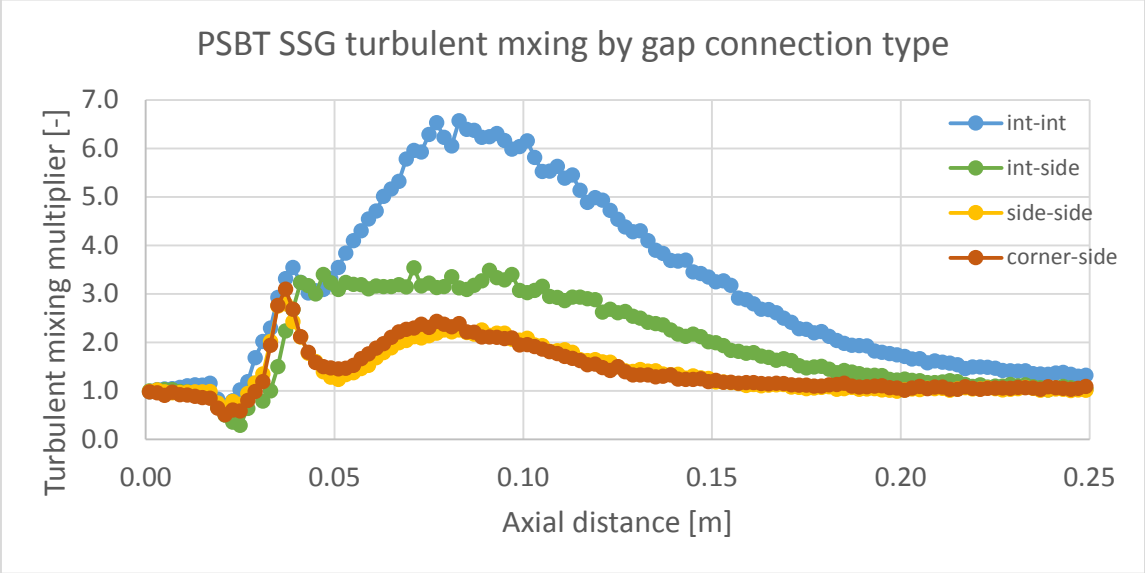

Figure 31: Turbulent mixing multiplier results for each gap geometry in the PSBT SSG grid

Cross-sectional views taken from the NMV turbulent mixing CFD simulation are shown in Figure 32 and Figure 33 of axial distances of 45 and 250 mm, respectively. The increase in turbulent mixing is apparent as the visualized thermal gradient at the gap's location decreases.

The results of the turbulent mixing multiplier are placed into a data-file for use by CTF, and are tabulated by axial distance. An example of this file is shown in Appendix A. The results may be indexed by vane angle (if applicable) as CTF has a linear interpolation scheme to handle a user-defined vane angle in the CTF input deck.

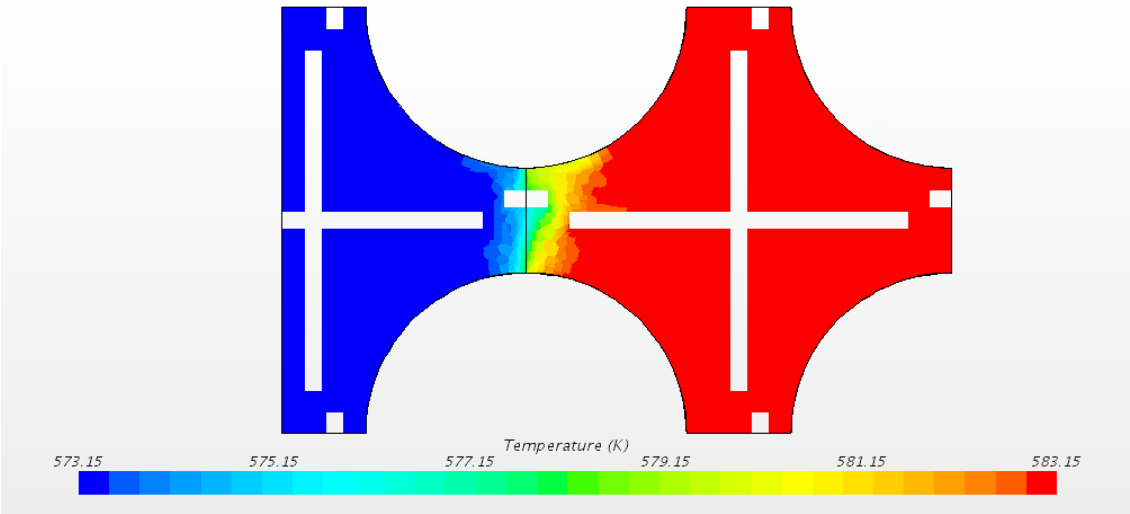

Figure 32: CFD results of the NMV 2x1 CFD simulation at 45 mm axially (5 mm downstream from leading edge of spacer grid)

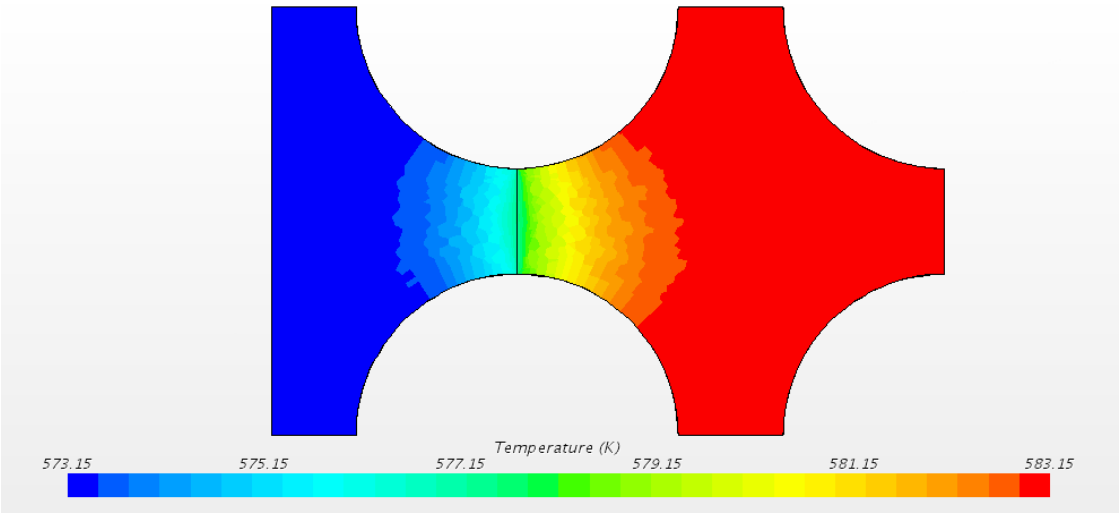

Figure 33: CFD results of the NMV 2x1 CFD simulation at 250 mm axially (210 mm downstream from leading edge of spacer grid)

CFD-Informed Spacer Grid-Directed Cross-flow Model

Avramova proposed a source term to account for the spacer grid-directed cross-flow effect within the subchannel code F-COBRA-TF [2]. This model is intended to capture the flow diverted by grid features such as vanes into adjacent subchannels.

This model adds an additional source term to the liquid lateral momentum equation that captures the grid-directed cross-flow effects. The modified subchannel form of the liquid transverse momentum as implemented within CTF is shown in Equation (55).

$$\begin{aligned}&\frac{\partial}{\partial t}\left(\alpha_l\rho_l\vec{V}_l\right)+\frac{\partial}{\partial x}\left(\alpha_l\rho_l u_l v_l\right)+\frac{\partial}{\partial y}\left(\alpha_l\rho_l v_l v_l\right)\\&=\alpha_l\rho_l\vec{g}-\alpha_l\nabla P+\nabla\cdot\left(\alpha_l\tau_l^{ij}\right)+\vec{M}_l^L+\vec{M}_l^d+\vec{M}_l^T+\vec{M}_l^{GDCF}\end{aligned} \tag{55}$$

The final term in Equation (55), $\vec{M}_l^{GDCF}$, is the source term added to the code to represent grid-directed cross-flow effects. The derivation of this factor is based on the results from the CFD simulation of a similar geometry model. The definition of this source term is shown in Equation (56).

$$\vec{M}_l^{GDCF}=f_{lat,SG}{}^2\left(u_l^2\right)\left(\rho_l\right)A_{gap}\mathrm{S} \tag{56}$$

In Equation (56):

- $f_{lat,SG}$ is the lateral convection factor
- u_l is the axial liquid velocity
- ρ_l is the liquid density
- A_{gap} is the cross-sectional area of the gap
- S is a factor to account for the direction of the force across the gap, and takes the value of either -1, 0, or 1

Most of the terms in Equation (56) are supplied by CTF, although the lateral convection factor, $f_{\text{lat,SG}}$, and the direction factor, S, must be supplied by external input. The lateral convection factor is derived by means of processing results from CFD simulations. This factor is defined as the ratio between lateral and inlet axial velocity at a given location downstream of the grid [65], as shown in Equation (57).

$$f_{lat,SG}(z - z_g) = \frac{V_{z-z_g}^{CFD}}{U_{inlet}^{CFD}} \tag{57}$$

In Equation (57), z is the downstream distance from the spacer grid's leading edge at z_g, and this is used to provide dimensional dependence of the lateral convection factor, which is expected to decrease with increasing distance. Avramova analyzed spacer grids with mixing vanes—AREVA FOCUS™ grids—and determined a factor for cross-flow from CFD simulations by extracting results at each gap in the simulation.

In this PhD research the CFD-informed model for spacer grid-directed cross-flow has been implemented in CTF, and the validation database of the model has been extended to include the OECD/NRC PSBT experimental benchmark data. A flowchart detailing the implementation of the spacer grid-directed cross-flow within the current structure of CTF is shown in Figure 34.

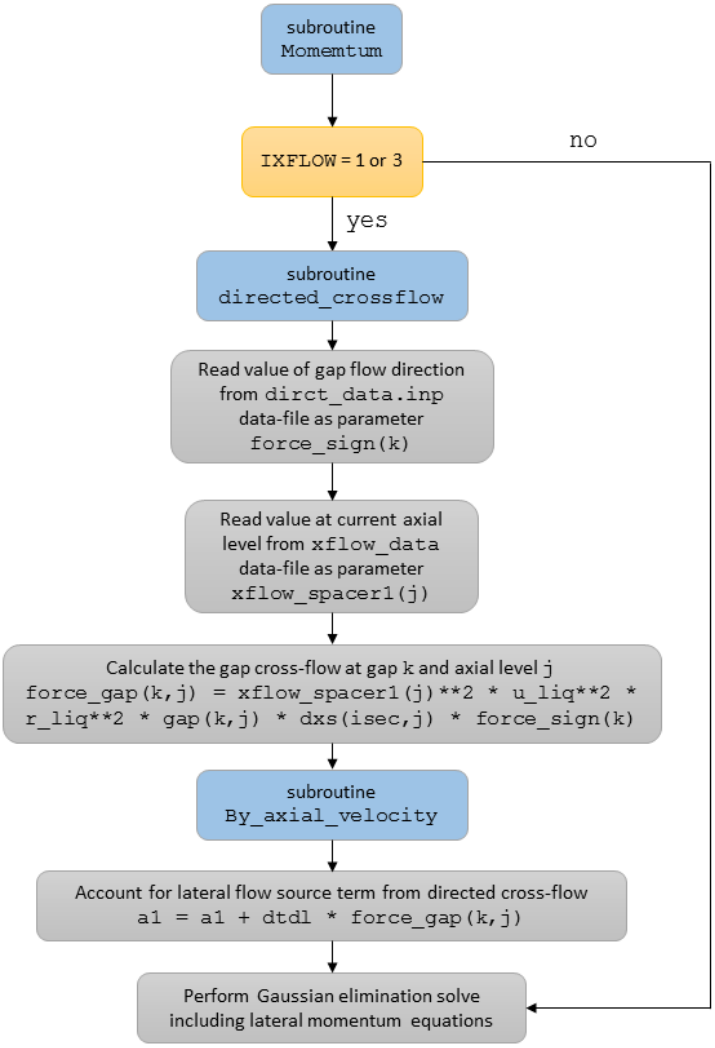

Figure 34: Flowchart for the spacer grid-directed cross-flow scheme in CTF

In this work, a 2x2 CFD simulation with periodic boundaries is utilized in order to determine the lateral convection factor. Details of the CFD simulation are provided in

Table 12. The 2x2 subchannel layout with boundary conditions for the PSBT MVG is illustrated in Figure 35. The overall geometry of the CFD model is shown in Figure 36. The simulation is adiabatic, with PWR boundary conditions of 15.5 MPa and 300 C single-phase liquid water. A mass flux inlet and pressure outlet were applied to each subchannel.

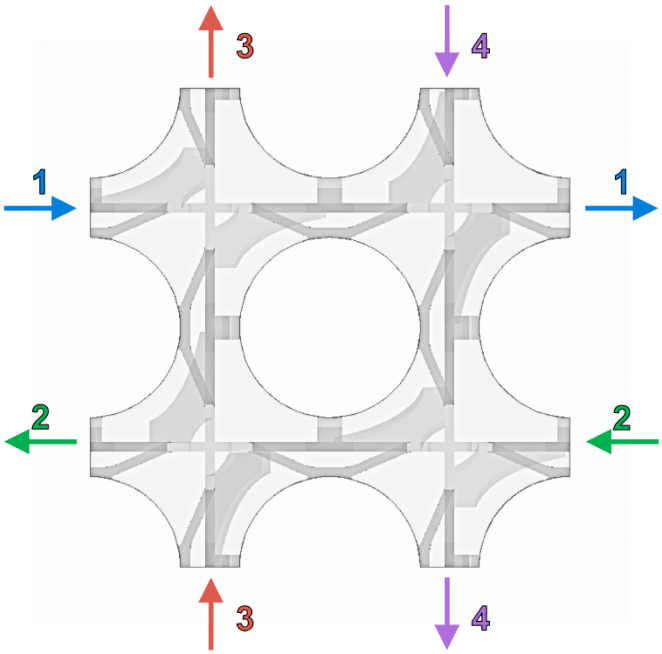

Figure 35: PSBT MVG 2x2 CFD simulation interface connection geometry

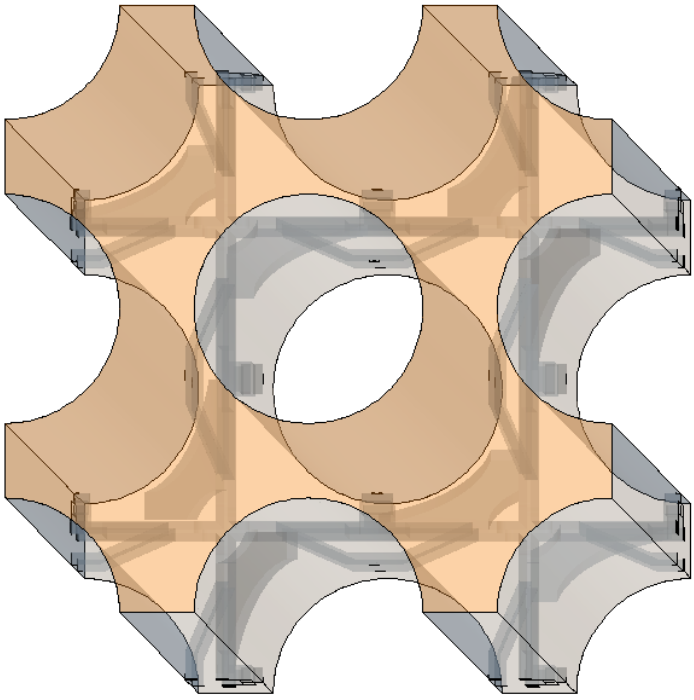

Figure 36: Overall geometry of the PSBT MVG 2x2 CFD simulation

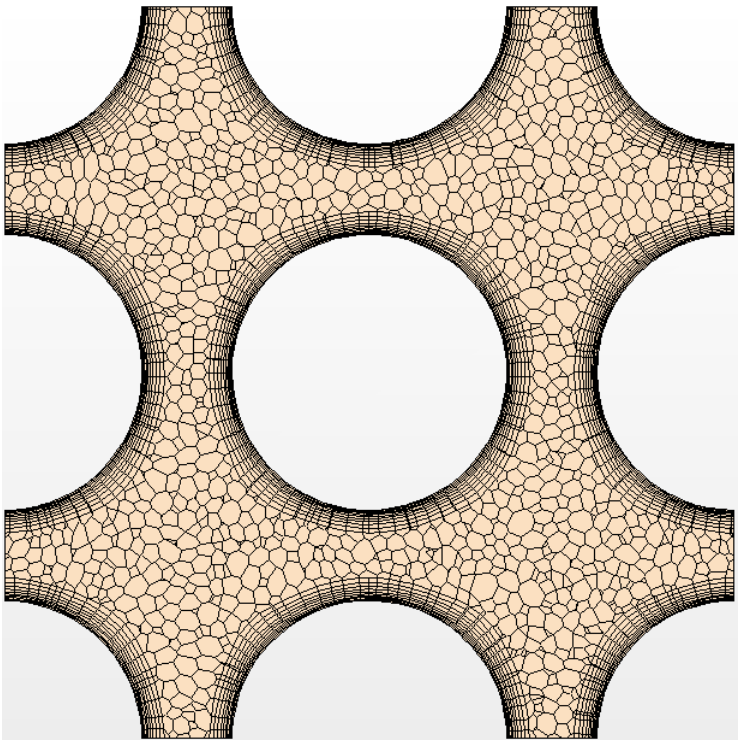

Figure 37: PSBT 2x2 subchannel layout mesh overview for directed crossflow simulations

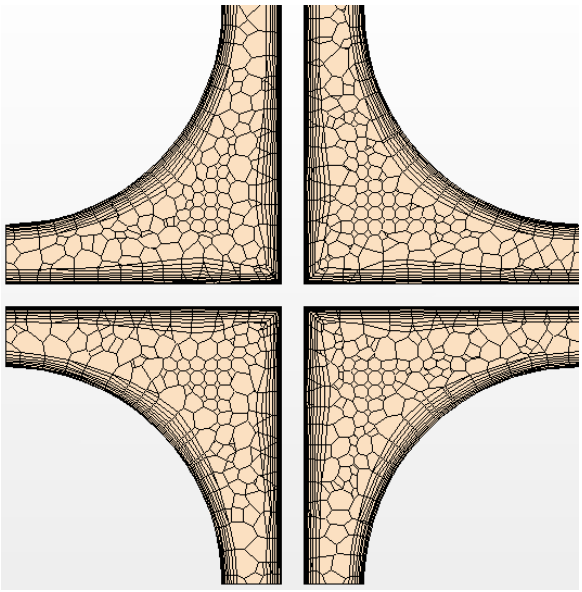

Figure 38: PSBT detailed subchannel mesh view for directed crossflow simulations

Table 12: Directed Cross-flow CFD modelling details for the PSBT spacer grids

Geometry details	
Subchannel layout	4 subchannels, connected via interface along their gaps
Domain length	400 mm (including extruded inlet region)
Grid leading edge axial location	80 mm
Mesh details	
Models	Polyhedral mesher Prism layer mesher Extruder Surface remesher
Base size	0.3 mm
Prism layer details	10 layers at 1.2 spacing, 1.0 mm thickness
Extruder details	60 mm extrusion from inlet, 60 layers at 1.0 spacing
Flow conditions	
Inlet temperature	300 C
Inlet mass flux	3630 kg/m^2-s
Pressure	15.5 MPa
Boundary conditions	
Rods	Wall-type, adiabatic
Gaps	Connected via periodic interfaces (Figure 35)
Inlet	Mass flow inlet
Outlet	Pressure outlet
Physics details	
Models	Liquid Steady Three dimensional Reynolds-averaged Navier-Stokes Turbulent Realizable K-epsilon turbulence Two-layer all y+ wall treatment Exact wall distance Segregated flow Segregated fluid enthalpy User-defined equations of state (Defined in Equation (45) - (47))

The method for extracting the lateral convection factor from CFD results begins with setting up constrained planes along each of the four gaps, not including the gaps created by the interfaces. A lateral offset of 0.1 mm is used in each direction from the gap in order to provide data specific to each subchannel. The axial spacing used in this research is 2 mm to provide

enough resolution around the spacer grid, although coarser spacing would work well due to CTF's larger axial nodes.

From each vertical plane offset from the gap, the lateral velocity components are extracted. These values are then averaged from subchannel i and subchannel j connected to gap k, as shown in Equation (58), which assumes flow is in the positive z direction.

$$U_{lat,k}(z) = \sqrt{\left(\frac{u_{x,i}(z) + u_{x,j}(z)}{2}\right)^2 + \left(\frac{u_{y,i}(z) + u_{y,j}(z)}{2}\right)^2} \tag{58}$$

Using appropriate data from the CFD results, Equation (58) creates a lateral velocity with downstream dependence for each of the four physical gaps in the CFD simulation. To determine the lateral velocity for the entire simulation, average the gap-specific value over each of the K gaps, as shown in Equation (59). Then, Equation (57) may be applied to determine the spacer grid's lateral convection factor, $f_{lat,SG}$.

$$U_{lat}(z) = \frac{1}{K}\sum_{k=1}^{K} U_{lat,k}(z) \tag{59}$$

Avramova's CFD simulations encompassed a 2x2 subchannel layout with four internal-type subchannels [2]. As previously noted in the spacer grid enhanced turbulent mixing derivation, this model does not account for different geometries of subchannel gaps. This simulation setup also ignores any wall effects such as those which are encountered in rod bundles surrounded by a shroud, as in the case of the PSBT's 5x5 A1 bundle. Effects of cross-flow along the sides and corners of fuel assemblies are harder to predict as the bundle-driven cross-flow typically follows a meandering pattern across the internal subchannels. The subchannels which are located on the edges of multiple fuel assemblies may contain grid straps from two or more spacer grids and inherently have more complex flow patterns.

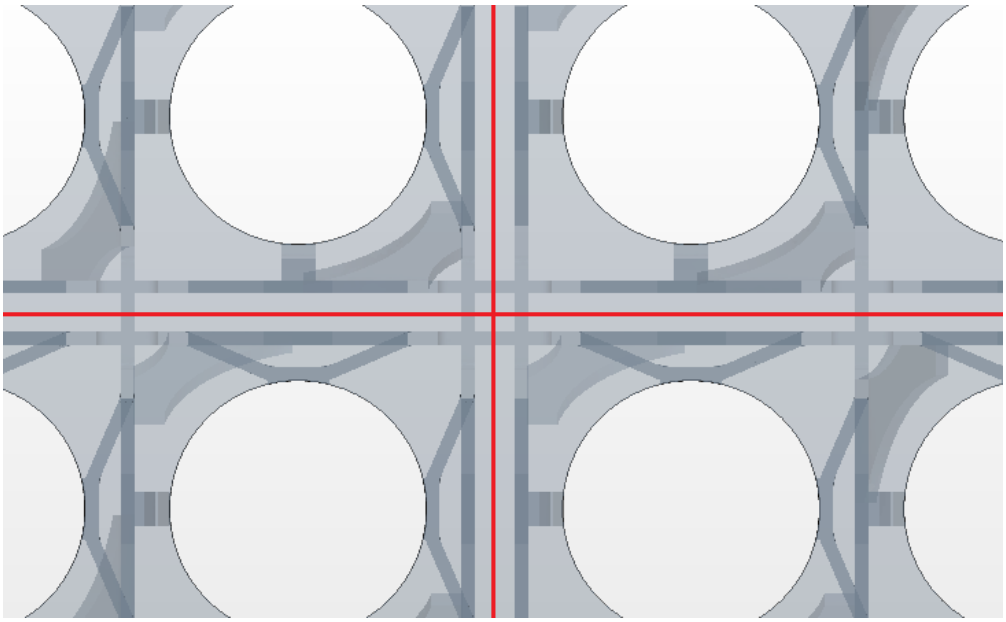

Figure 39: Geometry of hypothetical PSBT MVG inter-assembly subchannels at the intersection of four rod bundles

As experimental multi-assembly tests with PSBT grids do not exist, accounting for these details are not within the scope of this research. It requires assumptions as to the assembly pitch as well as the geometry of the grid straps outside of the bundle's internal subchannels. Figure 39 shows what a combination of four MVG spacer grids would look like at the convergence location of the four PSBT bundles. The red lines distinguish between each of the four rod bundles in the image. Note that in Figure 39 there is no spacing between the edges of the grid straps and they come in contact, which is not realistic in an LWR. However, Figure 39 does illustrate the deviation from typical gap configurations caused in the subchannels between adjacent grids with mixing vanes attached. Further CFD simulations are required in order to determine the effects of cross-flow along bundle side and corner subchannels and in inter-assembly subchannels.

The PSBT MVG grid is the only of the three grids found within the PSBT A1 bundle to contain mixing vanes. Therefore, it is the only grid expected to have a true directional impact on cross-flow over the gaps. The cross-flow effect caused by the MVG vanes are shown in Figure

40. The other, non-mixing vane grids will cause some cross-flow caused by divergence when the flow encounters the leading edge as well as the springs/dimples, but it will not be as strong or directional as that caused by vanes.

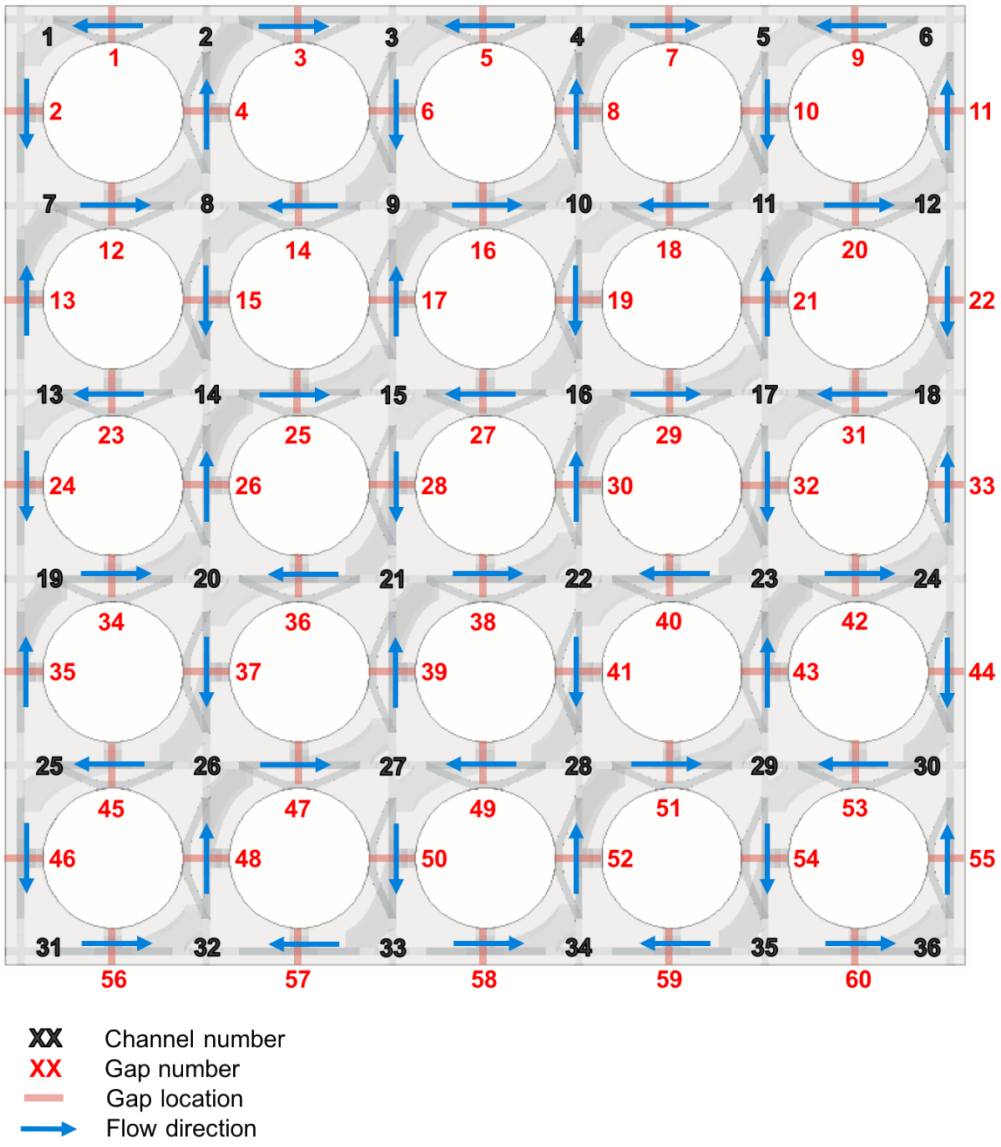

Figure 40: PSBT MVG cross-flow directions, and gap/subchannel indices

The values determined for the lateral convection factor of the PSBT MVG as a function of axial distance are shown in Figure 41. The MVG has its leading edge placed at 80 mm, axially. The peak value of approximately 0.27 for the MVG means that the lateral cross-flow across the gap is close to 27% of the magnitude of the inlet velocity.

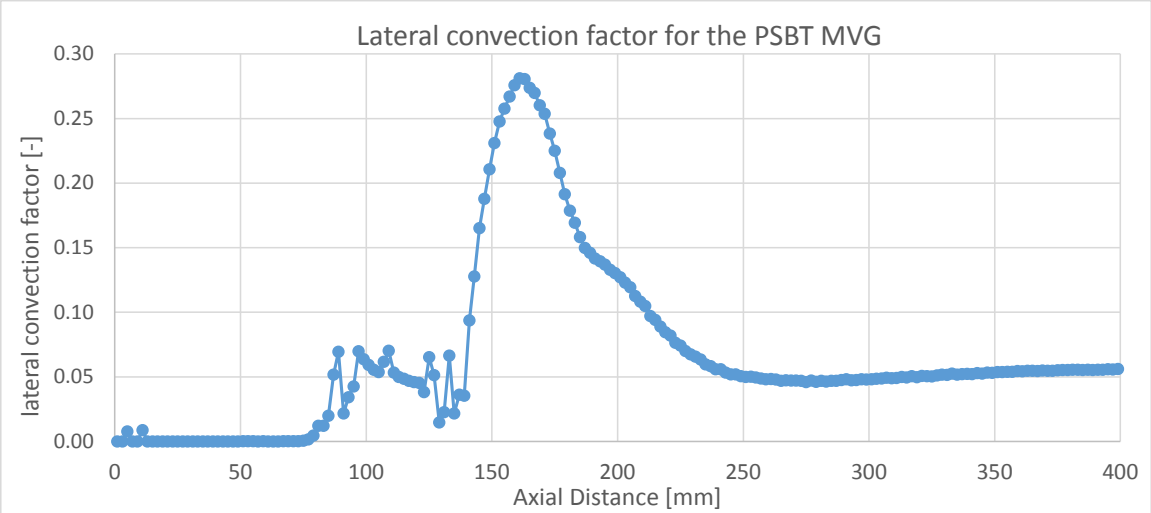

Figure 41: Lateral convection factor calculated for the PSBT MVG spacer grid

There is some variation in the lateral velocity calculated at each of the four gaps within the MVG CFD simulation. Figure 42 holds the results at the gap level, and there are two distinct patterns in the results. The west and north gaps as shown in Figure 35 have a slightly higher downstream lateral velocity field, which is not consistent with the symmetric geometry of the simulation. Each of the four gaps should have the same magnitude of flow across its threshold due to the fact that a vane is located in the same position relative to each gap. These differences may be attributed to the asymmetry in the grid's spring/dimple configuration. Figure 44 shows the lateral velocity magnitude at 148 mm, which is just downstream of the MVG vane tips. The horizontal protrusion of the grid's spring has an impact on the axial flow reaching the vane, causing a lower overall lateral velocity to be diverted by the vane. Figure 43 shows the lateral

velocity magnitude at 200 mm (120 mm downstream of the grid's leading edge) for the PSBT MVG and highlights the difference in magnitude at several locations. The two upper red boxes hold regions with higher magnitude of lateral velocity than the two lower boxes on Figure 43, and the boxes corresponding to the lower magnitude have the horizontal spacer in their flow paths.

As indicated by the slight difference in lateral velocity magnitudes caused by specific spacer grid geometry, more accurate and realistic results for the cross-flow model may be obtained by specifying a lateral convection factor for each gap instead of just for each axial level over the whole grid.

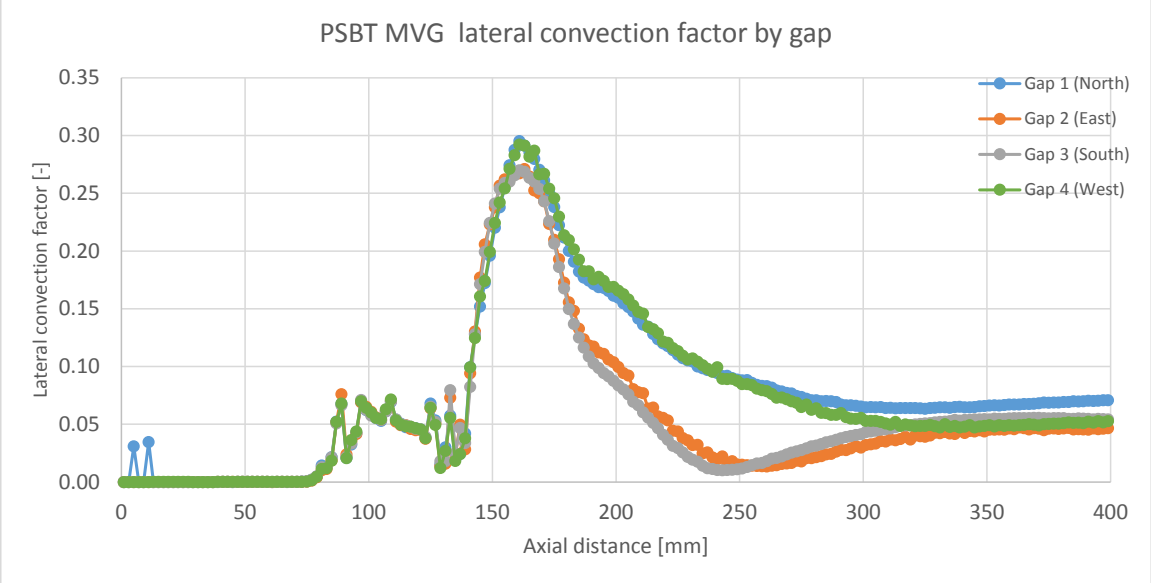

Figure 42: Lateral convection factor for the PSBT MVG broken down by gap (gap geometry in Figure 35)

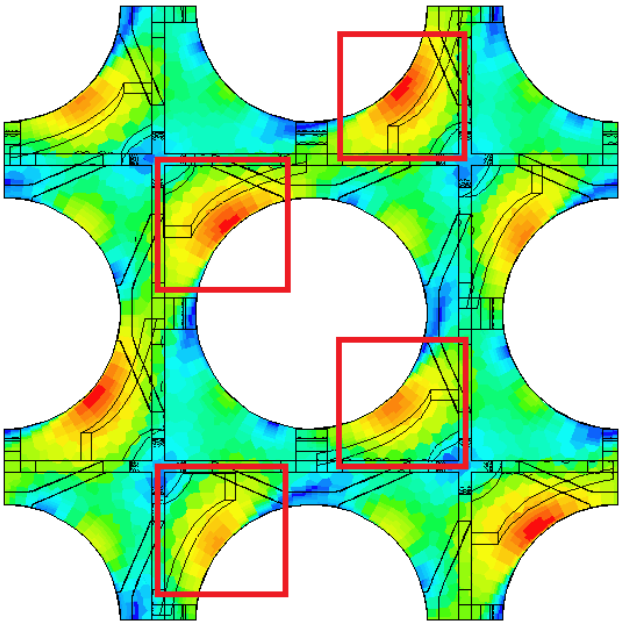

Figure 43: PSBT MVG lateral velocity magnitude visual at 200 mm from the flow inlet

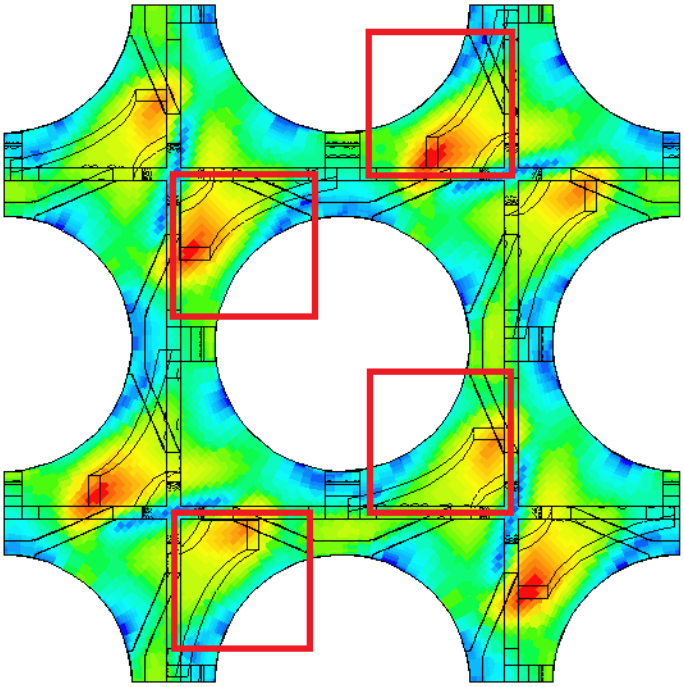

Figure 44: PSBT MVG lateral velocity magnitude visual at 148 mm from the flow inlet

The lateral convection induced by the MVG does not drop back down to zero by the time the next grid is encountered by the flow in the PSBT, as it has 229 mm between grids. Subsequent investigation into whether the initial lateral flows will have an influence on downstream grid showed that the flow is shown in Figure 45, where a PSBT MVG was placed at 40 mm and a PSBT SSG was placed 229 mm downstream of this, at 269 mm. As the results in Figure 45 indicate, the downstream SSG acts to remove almost all lateral velocity from the gap regions as calculated with the method presented by Avramova and used in this research [2].

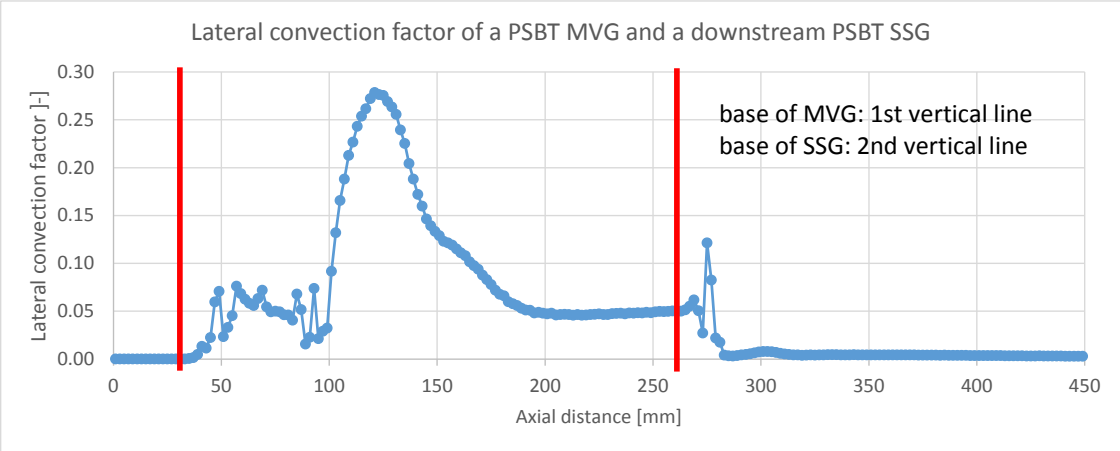

Figure 45: Calculated lateral convection factor for the PSBT MVG with a PSBT SSG located 229 mm

Data for the vane-less PSBT NMV and SSG spacer grids were also produced, and show very little cross-flow effects as calculated with this method. Lateral convection factors for each of the three PSBT grids as well as for bare subchannels are shown in Figure 46, where the base of each grid is set at 80 mm of axial distance. Immediately after the location of the spacer grid itself, the cross-flow effects drop back to zero for both the NMV and the SSG.

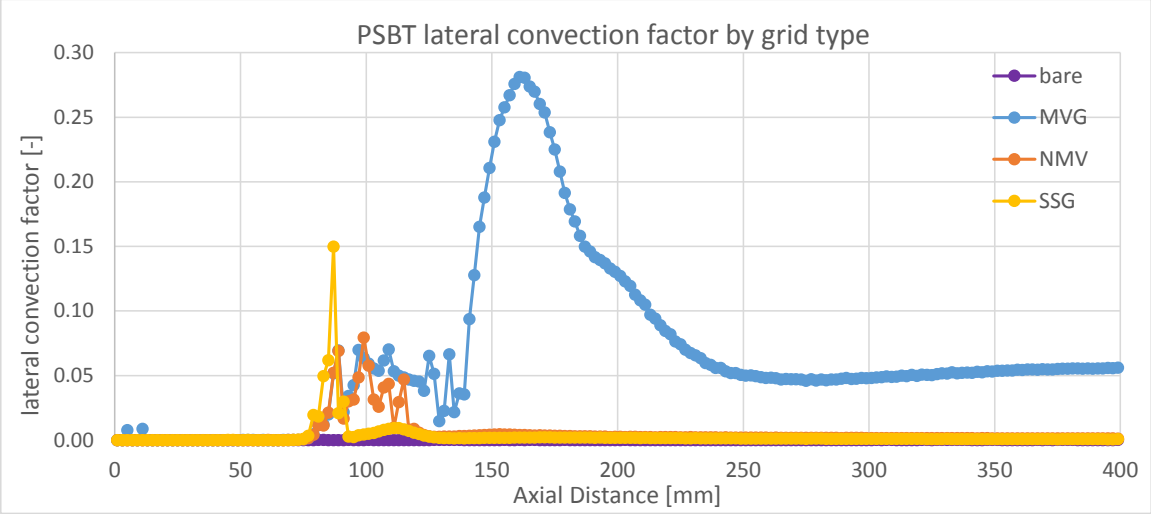

Figure 46: Lateral convection factor calculated for each type of PSBT spacer grid

The calculated lateral convection factors are tabulated for each spacer grid into a data-file to be read into CTF during its simulation. An example of this data-file is presented in Appendix A. The values are grouped by axial distance and may be provided for various vane angles as well. This structure allows users to provide information for a generic mixing-vane grid with multiple vane angles using CFD-derived lateral convection factors for each vane angle. CTF will then interpolate to use data for the vane angle specified in the CTF input file.

For certain grid applications in CTF, it may be desirable to only apply cross-flow across certain gaps. An example where cross-flow is only applied across internal-internal subchannel connections is shown in Figure 47. Such an implementation may be used if insufficient information about peripheral gaps is known. In this situation, CTF will only apply the lateral convection factor to the specified gaps. The information specifying which gaps will have cross-flow is specified in an additional data-file read by CTF. An example of this gap direction data-file is provided in Appendix A. The values for each gap are either -1, 1, or 0, and are designated by the user with consideration for the direction of each gap's flow as caused by the mixing vanes. A zero means that the directed cross-flow factor will not be applied at that gap, for any axial

location. The positive/negative signs indicate whether it is flow from a lower-to-higher numbered subchannel or vice versa, respectively. CTF's subchannel numbering is set by the user in the input deck, and follows a left-to-right numbering scheme in these simulations as shown in Figure 40.

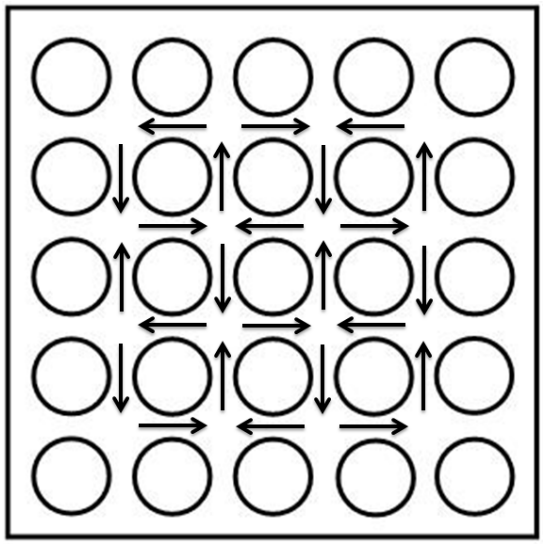

Figure 47: Directed cross-flow for a 5x5 bundle across only internal subchannel connections

These previously-developed models are implemented in CTF and are used to compare the calculated subchannel exit temperatures to experimental data from the PSBT Series 01 experiments. Details for the geometry of the PSBT experimental setup are provided in Chapter 3. CTF was run in six different modelling configurations:

1. CTF with no spacer grid models enabled
2. CTF with the turbulent mixing model enabled
3. CTF with the directed cross-flow model enabled, all gaps
4. CTF with the directed cross-flow model enabled, internal gaps only

5. CTF with both the turbulent mixing model and directed cross-flow enabled, all gaps
6. CTF with both the turbulent mixing model and directed cross-flow enabled, internal gaps only

To enable the spacer grid models in CTF, the `IXFLOW` parameter is set in card group 7 of the input deck. Depending on the specified options, data-files may be required as well to provide the CFD-derived information to CTF.

- IXFLOW = 0: No spacer grid model enabled
- IXFLOW = 1: Grid-directed cross-flow model enabled
- IXFLOW = 2: Grid-enhanced turbulent mixing model enabled
- IXFLOW = 3: Both grid-directed cross-flow and grid-enhanced turbulent mixing models enabled

For the cases utilizing the directed cross-flow over all gaps, the cross-flow directional information is shown in Figure 40. For the cases where cross-flow is only specified across internal-internal gap connections, Figure 48 shows the direction of the lateral flows.

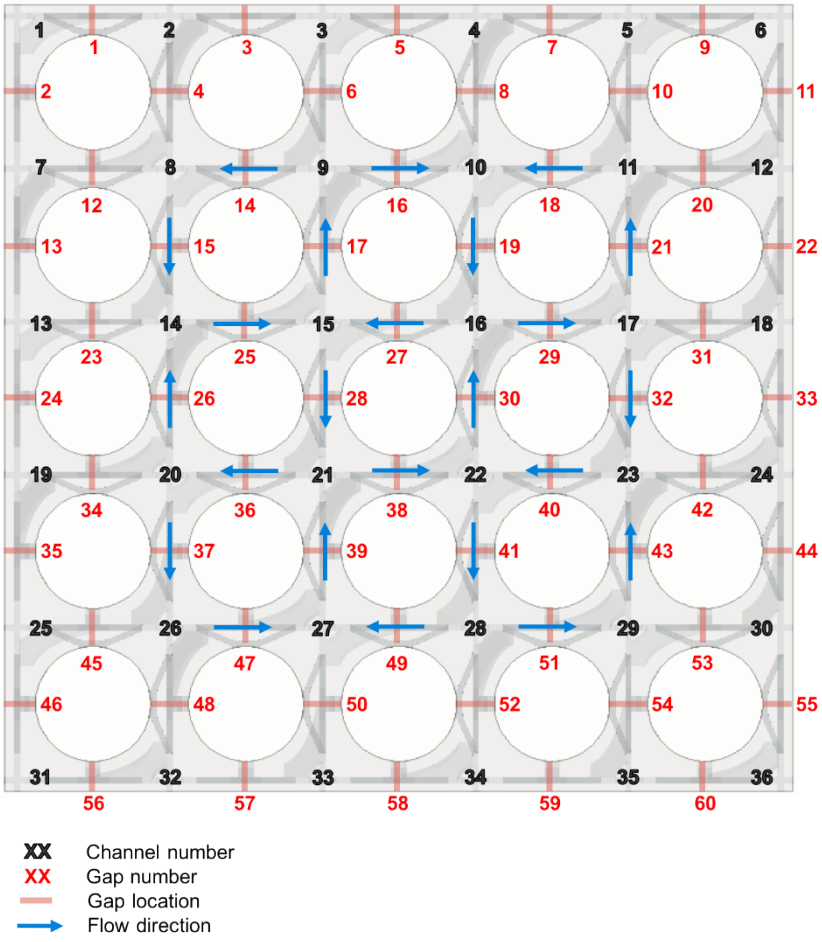

Figure 48: PSBT MVG cross-flow directions over only internal subchannel gaps

For the CTF cases with no spacer grid models enabled aside from the standard pressure loss coefficient specification, the exit temperature of each of the 36 subchannels is compared with the experimental results. The PSBT measurement error for the subchannels temperatures is provided as 1 degree Celsius [49]. The measured results are subtracted from the CTF-predicted exit temperatures. For a reference point of the Series 01 experimental results, the measured values from Test 01-5343 are illustrated in Figure 49. These results clearly show the power bias and resulting homogenization effects caused by the meandering flow driven by the mixing vane spacer grids.

261.3	259.9	251.9	249.7	243.5	239.1
263.5	261.9	253.2	248.6	242.1	238.5
259.6	257.2	253.0	243.5	239.4	236.9
257.1	252.7	246.4	238.6	237.8	235.6
256.6	254.2	246.7	236.4	234.3	232.5
256.7	254.8	251.3	240.2	233.7	230.0

Figure 49: Experimentally measured subchannel exit temperatures [°C] for PSBT Test 01-5343

The results of this difference are averaged over each of the 69 PSTB Series 01 test cases and summarized in Figure 50. Recall the left-skewed radial power profile of the PSBT Test Series 01, as shown in Figure 2. For the predicted results in this section, the grid-enhanced turbulent mixing model is applied as the same factor to each subchannel in the current axial region (i.e., there is no dependence on the type of the subchannel connection).

0.0	-2.1	-4.8	-8.5	-8.8	-7.2
-0.8	-2.1	-3.3	-7.4	-9.2	-8.5
1.4	0.8	-3.3	-5.9	-7.9	-7.9
2.6	3.3	1.8	-0.4	-6.4	-6.8
2.0	1.8	0.5	0.5	-3.2	-4.1
1.7	0.6	0.6	-1.6	-2.4	-1.9

Figure 50: Predicted – Experimental results averaged for PSBT Test Series 01, no CTF spacer grid models enabled, in Celsius

With the directed cross-flow model enabled over all subchannel gaps in CTF, the prediction results are summarized in Figure 51. The most over-predicted subchannel is now the bottom right corner, subchannel 36. The region of over-prediction has shifted from the bottom-left to the bottom-right.

-4.2	-5.1	-6.0	-6.5	-4.7	-2.1
-5.4	-6.1	-4.8	-5.6	-5.1	-2.9
-3.3	-3.2	-5.1	-4.4	-3.5	-2.6
-2.1	-1.0	0.2	1.3	-2.1	-1.2
-2.4	-1.8	-1.0	2.3	1.3	1.3
-2.0	-2.6	0.1	0.7	2.0	3.6

Figure 51: Predicted – Experimental results averaged for PSBT Test Series 01, CTF directed cross-flow model enabled on all gaps, in Celsius

Applying the directed cross-flow model over just the bundle's internal subchannel gaps still shifts the region of over-prediction to the bottom-right, but with less extreme predictions in the side and corner subchannels overall. Figure 52 contains the comparison for this CTF spacer grid model configuration.

-3.4	-5.0	-6.2	-7.2	-5.5	-3.3
-4.7	-6.0	-4.8	-6.1	-5.8	-4.4
-2.7	-2.9	-5.0	-4.6	-3.7	-3.5
-1.3	-0.6	0.5	1.2	-2.3	-1.9
-1.4	-1.1	-0.4	2.4	1.2	0.5
-1.4	-2.0	0.4	0.4	1.3	2.4

Figure 52: Predicted – Experimental results averaged for PSBT Test Series 01, CTF directed cross-flow model enabled on internal gaps only, in Celsius

The grid-enhanced turbulent mixing in CTF does not have any directional dependence, and merely increases the mixing between adjacent subchannels. The shift in regions of over- and under-predictions shown in Figure 53 is almost as strong as with the directed cross-flow model turned on.

-2.5	-4.1	-5.3	-7.1	-6.0	-3.8
-3.6	-4.4	-4.2	-6.3	-6.5	-5.1
-1.4	-1.7	-4.3	-4.9	-5.2	-4.6
-0.3	0.8	0.7	0.6	-3.7	-3.4
-0.7	-0.5	-0.4	1.6	-0.5	-0.7
-0.8	-1.4	0.1	-0.2	0.4	1.5

Figure 53: Predicted – Experimental results averaged for PSBT Test Series 01, CTF turbulent mixing enabled, in Celsius

Figure 54 shows the results when both the grid-enhanced turbulent mixing model and the directed cross-flow model over all subchannel gaps are enabled. The temperature predictions are more extreme in their variation than with any other combination of models.

-5.3	-6.1	-6.2	-5.9	-3.4	-0.5
-6.6	-7.1	-5.2	-5.1	-3.9	-1.5
-4.6	-4.3	-5.6	-3.9	-2.4	-1.1
-3.4	-2.0	-0.3	1.7	-0.9	0.2
-3.6	-2.9	-1.4	2.8	2.4	2.8
-3.3	-3.6	-0.3	1.2	3.2	5.0

Figure 54: Predicted – Experimental results averaged for PSBT Test Series 01, both CTF directed cross-flow and turbulent mixing models enabled on all gaps, in Celsius

When both the grid-enhanced turbulent mixing model and the directed cross-flow model over just the internal subchannel gaps are applied, the predictions are slightly worse in the corner and side subchannels than when directed cross-flow is applied across all subchannel gaps. The difference in the predicted and measured subchannel exit temperatures for this configuration of CTF spacer grid models is shown in the results of Figure 55.

-4.8	-6.0	-6.3	-6.3	-3.9	-1.3
-6.2	-7.0	-5.2	-5.5	-4.3	-2.4
-4.1	-4.1	-5.5	-4.1	-2.5	-1.7
-2.9	-1.8	-0.1	1.6	-1.1	-0.3
-3.0	-2.4	-1.0	2.8	2.4	2.3
-2.9	-3.1	-0.1	1.1	2.8	4.3

Figure 55: Predicted – Experimental results averaged for PSBT Test Series 01, both CTF directed cross-flow and turbulent mixing models enabled on internal gaps only, in Celsius

A summary of the six CTF spacer grid model configurations is provided in Table 13. In general, CTF under-predicts the subchannel exit temperatures. The main shift in differences between the CTF modelling options is apparent in the side and corner subchannel predictions. The average predicted temperature of the corner subchannels changes greatly when examining results of Figure 50 through Figure 55 on a subchannel-by-subchannel basis. This indicates a strong redistribution of flow across the predicted PSBT bundle. Applying directed cross-flow to just all gaps in the grid instead of just the internal gaps provides better predictions. The root mean square error terms are also provided, grouped by subchannel geometry, for each of the mixing model configurations employed.

Table 13: Summary of CTF spacer grid modelling predictions for the PSBT Series 01 test cases

CTF configuration	1	2	3	4	5	6
IXFLOW option in CTF	0	1	1	2	3	3
Gaps for cross-flow	-	All	Internal	-	All	Internal
Subchannel exit temperature differences (Predicted – Experimental), in Celsius						
Corner subchannels	-1.8	-1.2	-1.4	-1.4	-1.0	-1.2
Side subchannels	-3.1	-2.5	-2.7	-2.7	-2.4	-2.5
Internal subchannels	-2.5	-2.4	-2.4	-2.4	-2.4	-2.4
All subchannels	-2.8	-2.3	-2.4	-2.4	-2.3	-2.3
Root Mean Square Error, subchannel exit temperature differences, in Celsius						
Corner subchannels	4.7	5.0	4.6	4.3	5.7	5.3
Side subchannels	5.6	4.9	4.9	4.8	5.2	5.1
Internal subchannels	5.1	4.7	4.7	4.6	4.8	4.8
All subchannels	5.3	4.8	4.8	4.7	5.1	5.0

An additional comparison using the directed cross-flow model in CTF is conducted using data from a Siemens experiment, detailed in [2]. The vane angle for the experiment is 22 degrees and the exit temperature at most of the subchannels is measured. These data allow the users to see an improvement in CTF's predictive abilities when the model is turned on and these specific cases are run. The spacer grid data used for the directed cross-flow portion come from the AREVA FOCUS™ spacers [2]. There are experimental data for comparison which include the outlet temperatures at each of 36 subchannels in a 5x5 rod grid. There are 21 experimental cases for which these grids were used. Measurements were taken for 21 different cases utilizing the 5x5 bundle and the mixing vane grids. The inlet flow rate and pressure were held constant but the inlet temperature and bundle power (electrically heated rods) were varied for each case. There are five mixing vane spacers along the 5x5 bundle, which has a total length of 3.0 meters. More details about the bundle geometry can be found in [2]. The cross-flow effects are only applied to the internal subchannels, as illustrated in Figure 47. With this implementation, the effects are expected to improve the prediction in the central subchannels but not the peripheral subchannels.

The subchannel exit fluid temperature was measured for each case. Many of the experimental cases are missing certain measurements. The total number of measurements grouped by subchannel location is shown in Figure 56. It is not specified why certain subchannels have as few as 2 measurements out of the 21 total experimental tests conducted. The maximum number of data points is 21, which is the number of cases that were run. Three of the corner subchannels have less than half of these data points. The lack of measurements for certain subchannels can possibly be attributed to failed sensors or inconsistent readings. The actual reason does not seem to be specified in the literature. Figure 56 uses a color scale to show where the subchannels with the fewest measurements are located by highlighted them in a darker shade of red. The experimental data are claimed to have an uncertainty between ± 0.61 K and ± 1.0 K on the temperature range of 205°C to 343°C.

2	14	11	21	20	7
21	21	21	21	21	21
21	21	21	21	21	21
21	20	21	21	21	20
21	21	21	14	21	13
8	21	21	21	21	21

Figure 56: Number of experimental measurements for subchannel in the model

Each of the 21 cases was simulated in the current version of CTF with the directed cross-flow model off and on. The subchannel exit fluid temperatures were extracted from the results and compared with the experimental data.

0.971	0.985	0.993	0.992	0.984	0.969
0.985	1.008	1.019	1.019	1.007	0.984
0.992	1.019	1.032	1.032	1.018	0.992
0.992	1.018	1.032	1.032	1.018	0.992
0.984	1.007	1.019	1.019	1.007	0.985
0.970	0.985	0.992	0.992	0.985	0.970

Figure 57: Normalized subchannel temperatures averaged over 21 cases with directed cross-flow modeling off

0.990	0.994	0.996	1.003	0.998	0.988
1.001	1.008	1.009	1.008	1.004	0.992
1.006	1.010	1.013	1.012	1.004	0.996
1.010	1.014	1.015	1.012	1.008	1.004
1.005	1.012	1.012	1.008	1.001	0.998
0.997	1.002	1.000	1.001	0.997	0.982

Figure 58: Normalized subchannel temperatures averaged over 21 cases with directed cross-flow modeling on

The normalized, averaged subchannel maps with the cross-flow option off and on are shown in Figure 57 and Figure 58, respectively. Note the flattening of the overall temperature distribution when the cross-flow option is turned on due to the transfer of mass/momentum/energy from the hot, central channels to the outer ones. The internal

subchannels in Figure 58, on average, are cooler than the subchannels in Figure 57 (where directed cross-flow due to spacer grids is not modeled). The darker shades of color (either red or blue) show greater variation from a homogenized temperature bundle. An entirely homogenized bundle would have subchannels all at normalized values of unity. The variation with the model turned off is about 6.0% from the corner to the central subchannels, and when the model is invoked this is reduced to about 3.5%.

Figure 59 and Figure 60 show the temperature differences on a subchannel by subchannel basis. Although the average discrepancy for the subchannels over all 21 cases increases when the turbulent mixing model is activated, the effect is seen to improve prediction for the internal subchannels substantially. This is partially because the model is only designed for and applied to the central subchannels, due to the CFD data that were recorded. By causing more mixing in the central subchannels, the flow becomes more homogenized and the standard deviation, which is shown by the length of the lines at each subchannel location, decreases. This indicates that the predictions become more consistent as the cross-flow model is utilized, mostly due to the homogenization of flow.

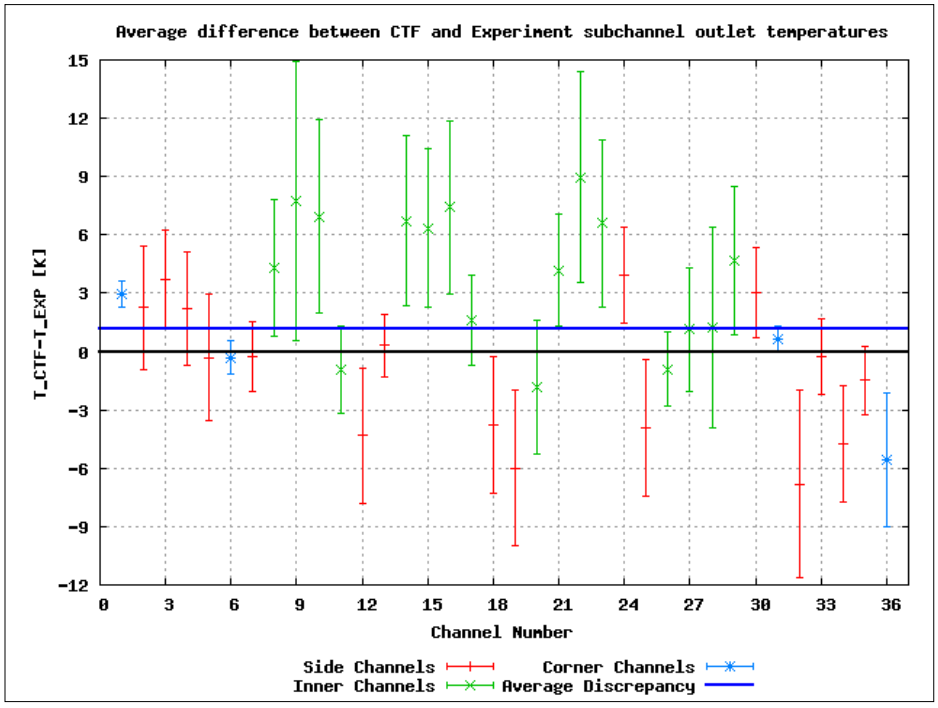

Figure 59: Comparison of the average temperature difference by subchannel with the cross-flow model turned off

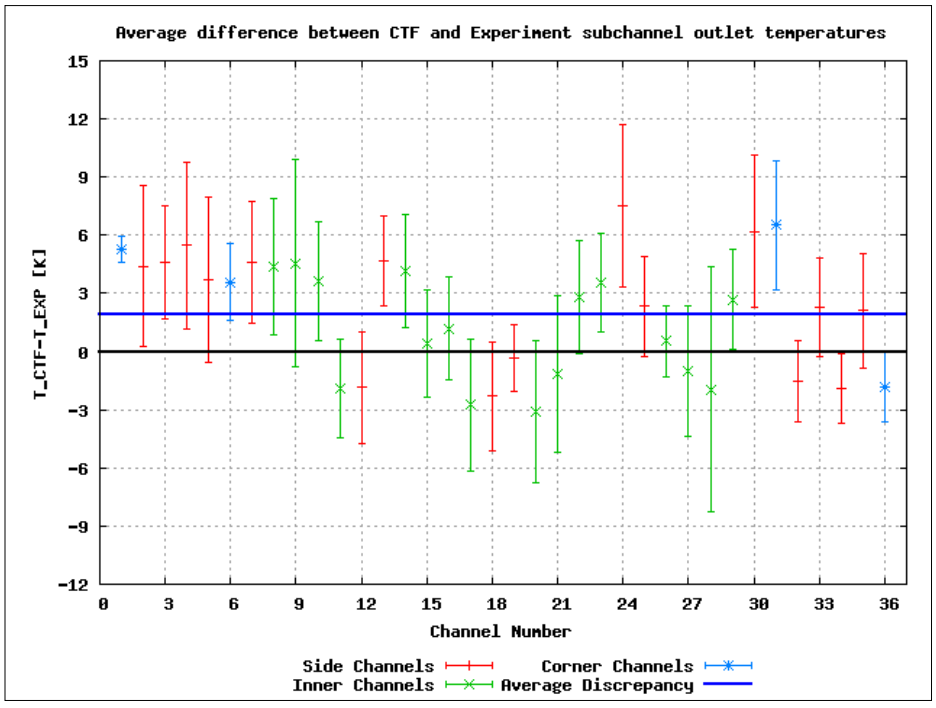

Figure 60: Comparison of the average temperature difference by subchannel with the cross-flow model turned on

Chapter 5

CFD-Informed Model for Spacer Grid Loss Coefficient Calculations

Introduction

In this chapter, a CFD-informed model for spacer grid loss coefficient evaluation to be used in CTF is developed and tested. Methods for predicting the spacer grid loss coefficients of the PSBT spacer grid designs are examined and applied using CFD simulations. 2x2 CFD simulations examine the pressure drop within internal subchannels for each of the three PSBT spacer grids and are used to calculate loss coefficients. A meshing study of the 2x2 subchannel layout is used to decide on a base mesh size for larger-scale simulations. More geometrically-comprehensive 5x5 PSBT bundles are simulated to determine a bundle-averaged spacer grid loss coefficient. The inlet flow parameters are altered to determine the effect on the CFD-predicted loss coefficients with results discussed in this chapter. The results of the CFD-predicted spacer grid loss coefficients are placed into CTF and the pressure drop profiles are compared from CTF to STAR-CCM+ to ensure CTF's predictions are in line with the CFD code's results. A full-length PSBT test case is modelled in CFD containing 17 spacer grid spans and the results are reported. A discussion of the effects of multiple spacer grid straps in a single subchannels, such as what occurs at the intersection of fuel assemblies in a reactor, is presented.

Background

Inside of an LWR, pressure drops are characterized by their cause. The typical losses in a reactor are 1) entrance and exit losses as the flow travels to/from the reactor core, 2) friction

caused by skin drag as the flow moves along the rods, 3) form losses due to objects in the flow's path such as spacer grids, and 4) gravity [62]. If spacer grids are present, such as those found within an LWR fuel assembly, they represent a significant portion of the overall pressure drop with their form losses. Therefore, detailed modelling of spacer grid pressure losses is important in providing realistic LWR predictions using subchannel codes.

Accounting for exact grid geometry instead of relying on the current pressure drop models in CTF gives users an advantage if the sometimes-proprietary spacer grid designs are available. Using CFD measurements of the fluid pressures at axial locations will give data specific to a grid design that can be used within CTF. The idea is to develop a more grid-specific form loss coefficient that can be used in the momentum equation. The loss coefficient of a grid is generally the sum of the form and friction loss coefficients acting on the grid and its mixing vanes.

A main component of the spacer grid's effect on the pressure drop is the presence of mixing vanes. While the vanes promote flow homogenization and provide thermal benefits, these effects must be balanced against the negative effect of pressure drop. Their impact on the pressure drop can be related to the amount of area a cross-sectional projection on to a plane perpendicular to the flow's direction. Vanes which extend far from the grid straps and/or have a large angular deviation from the direction of flow will have a larger blockage ratio. Fuel assembly spacer grid designs must be designed such that their placement within an existing reactor is compatible with existing structures and turbomachinery, such as the main reactor coolant pumps. The pumps are carefully sized to provide sufficient cooling and moderation for the reactor design of the LWR they serve.

Lateral pressure differences across subchannels drive the motion of fluid from one subchannel to an adjacent subchannel following the direction of the lateral pressure gradient. If a spacer grid has a large effective blockage ratio in one subchannel and the adjacent subchannel

does not have the large blockage, the pressures in the subchannels will balance at some distance downstream of the spacer grid location. This scenario may arise when one subchannel contains a mixing vane while adjacent subchannels do not. Excessive axial and lateral pressure gradients can also cause vibration in the rods, which increases contact at the grid-to-rod interface and may accelerate fretting at the rod surface.

The equation for the pressure drop in a fluid flow due to a spacer grid's form loss is provided in Equation (2). This contains a loss coefficient, ζ_{grid}, to be specified for the spacer grid causing the form loss.

$$\Delta P_{form} = \frac{1}{2}\zeta_{grid}\rho u^2 \tag{60}$$

The spacer grid loss coefficients for the CFD simulations can be calculated by rearranging Equation (2) and solving for the spacer grid loss coefficient, ζ_{grid}, as shown in Equation (61).

$$\zeta_{grid} = 2\frac{\Delta P_{form}}{\rho u^2} \tag{61}$$

It is important to note that due to the thermal boundaries presented by the rods in a reactor, the temperature of the fluid will change as it flows through the reactor. The temperature change is also reflected in the density and velocity, which must maintain mass flux boundaries at steady-state conditions. If a single-phase liquid is considered flowing vertically through a subchannel with heated rods, its temperature will increase as it reaches the upper subchannel exit. The density will decrease and, therefore, the axial velocity of the liquid will increase as it approaches the exit. In this research, the volume-average density and the inlet axial velocity are used in pressure loss coefficient calculations.

Spacer grid loss coefficient calculations

Rehme related the pressure drop to the grid loss coefficient of a bundle with a square pitch to be related to the Reynolds number of the surrounding flow as well as the geometric features of the spacer grid [22].

$$\Delta P_{grid} = C_B \frac{\rho}{2} U_{ax}^2 \tag{62}$$

Equation (62) presents Rehme's relation, and it contains C_B, which is a loss coefficient of the spacer grid calculated from experimental results. Rehme found a suitable method for relating a spacer grid's loss coefficient to its blockage ratio as a manner for calculating pressure drops, and proposed that the loss coefficient is correlated with the square of the blockage ratio as shown in Equation (63). The value of C_V is set between 6 and 7 depending on the Reynolds number of the flow.

$$C_B = C_V \varepsilon^2 \tag{63}$$

Assuming a value of 7.0 for Reynolds numbers above 500000, the effective loss coefficient of the spacer grid as correlated by Rehme is shown in Equation (64). The blockage ratio, ε, is defined as the projected area of the spacer grid divided by the unobstructed flow area perpendicular to the main direction of flow.

$$C_B = 7\varepsilon^2 \tag{64}$$

The blockage ratio does not include mixing vanes such as those found on the PSBT MVG spacer grid, so this correlation is best suited for general egg-crate style spacer grids.

Yao et. al expanded upon the work of Rehme and suggested a value of 10.5 instead of 7.0 to counteract the observed under-prediction [20]. Holloway et al. grouped the loss coefficient of the spacer grid into two components; the portion caused by the spacer grid straps and the portion caused by the grid's flow-enhancing features (such as mixing vanes). Holloway et al's

experiments with spacer grids found loss coefficients for spacer grids ranged from 0.64 for a simple spacer grid to 1.60 for a spacer grid with geometric blockages at its grid strap intersections. Additionally, the flow-enhancing features are found to be responsible for close to 50% of the overall pressure loss coefficient.

Shiralkar and Radcliffe provided an approach to take more detailed grid parameters into account to calculate a loss coefficient based upon form and friction losses [59]. Equation (65) shows the sum of the form loss, K_L, and the friction loss, K_f over a spacer grid span.

$$K_{shiralkar} = K_L + K_f \tag{65}$$

The form loss for Shiralkar and Radcliffe's method is dependent upon the flow ratio of the spacer grid, σ, as well as an orifice loss factor, k'. The orifice loss coefficient is assumed to be 0.5, which is consistent with flow entering a sharp orifice. The flow ratio, σ, is defined in Equation (66).

$$\sigma = \frac{A_U - A_R}{A_U} = 1 - \varepsilon \tag{66}$$

Equation (67) provides the loss coefficient portion of Shiralkar and Radcliffe's correlation.

$$K_L = \left[\frac{\sqrt{k'(1-\sigma))} + (1-\sigma)}{\sigma}\right] \tag{67}$$

In Equation (66), A_U is the upstream area of the ungridded region and A_R is the flow area in the location of the grid. The friction losses caused by the spacer grid are calculated using Equation (68), which depends upon wetted perimeters of the gridded region (P_R) and the upstream portion (P_U). The grid's axial length is also considered, which is a parameter other correlations do not consider even as it is an important factor in skin friction calculations. A friction factor, f, is assumed to be equal to 0.015.

$$K_f = \frac{fLP_U}{4A_U}\left[\frac{P_R}{P_U}\left(\frac{1}{\sigma}\right)^3 - 1\right] \tag{68}$$

The total loss coefficient as calculated by the Shiralkar and Radcliffe correlation then becomes Equation (69).

$$K_{shiralkar} = \left[\frac{\sqrt{k'(1-\sigma))} + (1-\sigma)}{\sigma}\right] + \frac{fLP_U}{4A_U}\left[\frac{P_R}{P_U}\left(\frac{1}{\sigma}\right)^3 - 1\right] \tag{69}$$

The spacer grid loss coefficients are calculated for each spacer grid in the PSBT A1 5x5 rod bundle and the results are segregated by subchannel geometry type. The results are shown in Table 14. The spacer grid features, such as dimples and springs, are averaged over each side and corner subchannel geometry to obtain an average for the 5x5 bundle. For example, two of the MVG corner subchannels contain mixing vanes while the other two do not, so this is averaged to place 0.5 mixing vanes in each corner subchannel.

Table 14: Spacer grid pressure loss coefficients calculated with Shiralkar and Radcliffe's method [59]

PSBT spacer grid		MVG	NMV	SSG
L		58.928 mm	41.148 mm	12.800 mm
f		0.015	0.015	0.015
k'		0.5	0.5	0.5
A_U	Internal	87.88 mm^2	87.88 mm^2	87.88 mm^2
	Side	55.91 mm^2	55.91 mm^2	55.91 mm^2
	Corner	34.84 mm^2	34.84 mm^2	34.84 mm^2
ε	Internal	0.45	0.26	0.31
	Side	0.41	0.27	0.24
	Corner	0.45	0.33	0.29
σ	Internal	0.55	0.74	0.69
	Side	0.59	0.73	0.76
	Corner	0.55	0.67	0.31
P_R	Internal	80.25 mm	80.25 mm	80.25 mm
	Side	65.32 mm	65.32 mm	65.32 mm
	Corner	47.16 mm	47.16 mm	47.16 mm
P_U	Internal	29.85 mm	29.85 mm	29.85 mm
	Side	27.52 mm	27.52 mm	27.52 mm
	Corner	21.96 mm	21.96 mm	21.96 mm
K_L	Internal	2.82	0.70	1.04
	Side	2.14	0.76	0.60
	Corner	2.82	1.21	0.89
K_f	Internal	1.14	0.30	0.12
	Side	1.15	0.39	0.10
	Corner	1.66	0.60	0.15
$K_{shiralkar}$	Internal	3.96	1.00	1.16
	Side	3.29	1.15	0.70
	Corner	4.48	1.80	1.04

The values for the PSBT MVG appear very large in comparison with the other two PSBT grids. This is because the projected area of the mixing vanes is considered in the calculation of the blockage ratio used in the Shiralkar and Radcliffe calculations. If the PSBT MVG vanes are removed from the calculations of Equation (67) and Equation (68), then the resulting loss coefficients are shown in Table 15.

Table 15: PSBT MVG spacer grid loss coefficients calculated with Shiralkar and Radcliffe's method while ignoring the projected area of the mixing vanes

PSBT spacer grid		MVG – vanes not considered
$K_{shiralkar}$	Internal	1.13
	Side	1.32
	Corner	2.06

The loss coefficient values which ignore the vanes in the blockage ratio appear more consistent with the loss coefficients calculated by other means. Therefore, it is recommended to calculate the blockage ratio without considering the projected area of the mixing vanes when using Shiralkar and Radcliffe's method, but only because it appears the method over-predicts the spacer grid loss coefficient when the vanes areas are included.

Current form loss model in CTF

CTF utilizes Equation (2) to calculate pressure drops due to flow obstructions. Currently, the user can either specify a per-subchannel grid loss coefficient to CTF or else allow CTF to calculate the local grid-loss coefficient based on general grid geometric parameters (e.g. blockage ratio and vane angle). The grid loss coefficient is then used to calculate a loss term of the momentum continuity equation solved within CTF. For this work, it is proposed that this local grid-loss coefficient be supplied to CTF via an external input file that was generated based on a CFD simulation of that specific grid's geometry. This would leverage the existing CTF ability to take local grid-loss coefficients via input and would not require any modification of the CTF governing equations or source code.

In the current version of CTF, the local pressure losses in the vertical direction caused by the grids are modeled as velocity head losses using Equation (2). This form loss is applied to each

of the phases and includes ζ_{grid}, the form loss coefficient, u_z, the fluid velocity in the axial direction, and ρ, the fluid density. The value for ζ_{grid} in Equation (2) can either be supplied by the user at each grid's axial location, or can be calculated by the code using Equation (70). The user may specify a different value of the loss coefficient for each subchannel at a given axial node, offering the opportunity to account for differences in subchannel geometries.

$$\zeta_{grid} = \min\left\{20, 196\mathrm{Re}_{mix}^{-0.333}\right\} f_{loss}\left(A_{blockage}^{spacer} + A_{blockage}^{springs}\right)^2 \tag{70}$$

If Equation (70) is utilized, the user must supply values for f_{loss}, the pressure loss coefficient multiplier, as well as for the flow blockage ratios for both the spacer and its springs. As these parameters are user-supplied values, there is room for improvement using CFD and computer drafting data specific to the grid.

Current friction loss models in CTF

In CTF's calculations, the pressure drop model is a two-phase (liquid and vapor) model based on the work of Wallis [56]. Equation (71) shows the implementation within CTF.

$$\frac{dP_{fric}}{dz} = f\frac{G_z^2}{2\rho D_h}\Phi^2 \tag{71}$$

In Equation (71), z is the direction of flow, G_z is the mass flux of the fluid in the z-direction, ρ is the fluid density, f is the friction factor of the surfaces, and Φ is a two-phase multiplier. The two-phase multiplier accounts for differences between the liquid and vapor phases, and depends on the void fraction, α, as displayed in Equation (72).

$$\Phi = \begin{cases} \dfrac{1}{1-\alpha} & \text{for normal wall conditions} \\ \dfrac{1}{\alpha} & \text{for hot wall conditions} \end{cases} \tag{72}$$

The friction factor used in CTF is split into a laminar friction factor, f_L, and a turbulent friction factor, f_T. In CTF calculations, the maximum value of the laminar and turbulent friction factors is applied within Equation (71).

$$f = \max\left(f_L, f_T\right) \tag{73}$$

The laminar friction factor, f_L, is calculated using the Darcy-Weisbach laminar regime correlation shown in Equation (74).

$$f_L = \frac{64}{Re} \tag{74}$$

CTF calculates the Reynolds number of the flow of phase k in the subchannel using Equation (75).

$$Re = \frac{G_z D_h}{\mu_k} \tag{75}$$

In Equation (75), μ_k is the dynamic viscosity of phase k of the fluid. There are five user-selected options for CTF to calculate the friction factor, f, of Equation (71). The user specifies which of the five friction models to use in the CTF input deck. These options are:

- Original (CTF) correlation
- McAdam's correlation
- Zigrang-Sylvester correlation
- Churchill correlation (overrides Equation (73))
- User-defined parameters

The original CTF friction factor correlation is shown in Equation (76).

$$f_T = \max\left(1.691Re^{-0.43}, 0.117Re^{-0.74}\right) \tag{76}$$

McAdam's correlation follows a similar approach as the original CTF equation, and is shown in Equation (77). Both the original and McAdam's correlations are intended for smooth wall predictions.

$$f_T = 0.204Re^{-0.20} \tag{77}$$

The Zigrang-Sylvester correlation allows for the user to specify the surface roughness, ε. Its implementation is specified in Equation (78) [58]. The logarithms functions are base-10 in this correlation.

$$\frac{1}{\sqrt{f_T}} = -2\log\left(\frac{\varepsilon}{3.7D} + \frac{2.51}{Re}\left[1.14 - 2\log\left(\frac{\varepsilon}{D} + \frac{21.25}{Re^{0.9}}\right)\right]\right) \tag{78}$$

The Churchill correlation takes the place of Equation (73) and is shown in Equation (79) [57]. This correlation also allows for surface roughness to be specified.

$$f = \left[\left(\frac{8}{Re}\right)^{12} + \frac{1}{(a+b)^{\frac{3}{2}}}\right]^{\frac{1}{12}} \tag{79}$$

In Equation (79), the parameters a and b are described in Equation (80) and Equation (81), respectively.

$$a = \left(2.475\ln\left[\frac{1}{\left(\frac{7}{Re}\right)^{0.9} + 0.27\left(\frac{\varepsilon}{D}\right)}\right]\right)^{16} \tag{80}$$

$$b = \left(\frac{37530}{Re}\right)^{16} \tag{81}$$

Lastly, CTF allows for users to set their own friction factor correlation, with the parameters A, B, and C in Equation (82) available for custom values. This correlation is set to be Reynolds number dependent, as is typical with the other friction factor correlations.

$$f_T = A + BRe^{-C} \tag{82}$$

Form and friction losses in STAR-CCM+

STAR-CCM+ contains a roughness factor, f, which is used in calculations of near-wall parameters and is incorporated into the logarithmic layer velocity distribution calculations. It is used as a direct multiplier to STAR-CCM+'s wall function coefficient, E, which is utilized in wall law correlations. If domain walls in the simulation are designated as rough instead of smooth, the roughness factor is calculated based on the provided roughness information. If the walls are smooth, then the roughness factor is equal to unity. This roughness factor depends on user-defined values of coefficients B and C, as well as the roughness height in equivalent sand-grain units. Equation (83) is used to calculate the roughness parameter, R^+, based on the user-supplied parameters.

$$R^+ = \frac{ru^*}{\nu} \tag{83}$$

In Equation (83), r is the roughness height, u^* is the wall function velocity, and ν is the kinematic viscosity of the fluid. The limits for the roughness parameter in regards to the rough and smooth distinction are recommended to be $R_{smooth}^{+} = 2.25$ and $R_{rough}^{+} = 90$. If the calculated value of R^+ is less than the specified smooth limit, then the roughness function is set equal to 1. If the calculated roughness parameter is in between the smooth and rough limits, the roughness parameter is used to determine the roughness function, f, as shown in Equation (84).

$$f = \left[B\left(\frac{R^+ - R_{smooth}^{+}}{R_{rough}^{+} - R_{smooth}^{+}} \right) + CR^+ \right]^a \tag{84}$$

The default values of user-defined coefficients B and C are 0 and 0.253, respectively. The exponent a is determined from Equation (85).

$$a = \sin\left[\frac{\pi \ \log\left(R^{+}/R_{smooth}^{+}\right)}{2\log\left(R_{rough}^{+}/R_{smooth}^{+}\right)}\right] \tag{85}$$

If the roughness factor is found to be greater than the rough limit,R_{rough}^{+}, the roughness factor is calculated using Equation (86).

$$f = B + CR^{+} \tag{86}$$

The skin friction coefficient defined within STAR-CCM+ is shown in Equation (87). This is calculated based on the CFD-determined wall shear, τ_w, and fluid properties of the flow.

$$C_f = \frac{|\tau_w|}{0.5\rho_{ref}U_{ref}^{2}} \tag{87}$$

The pressure solution in STAR-CCM+ occurs during the solve of the governing Navier-Stokes equations.

CFD modelling details

A 2x2 subchannel layout of internal-type subchannels is employed for a study of the base mesh size on pressure predictions. The relevant CFD modelling parameters of this study are outlined in Table 16. The overall length is 740 mm, of which 160 mm is an extruded inlet. The remainder is a polyhedral mesh with a base size varying for each simulation, from 0.3 to 0.7 mm. Non-heated rods and smooth walls are used as well.

The function of the prism mesher in STAR-CCM+ is to generate mesh cell layers from surfaces where boundary layer effects and calculations are important. In these CFD simulations, the solution of flow around the rod and spacer grid surfaces is of interest. The prism mesh settings allow for users to specify the number of prismatic layers, the absolute distance from the surface which the layers extend, and the relative spacing between cell centroids of adjacent layers. The

spacing of the mesh cells near the wall determines the non-dimensional y^+ value of the prismatic mesh cells and can have a large impact on the simulation's solution. Equation (88) shows the calculation of y^+, which depends on the distance to the cell centroid from the wall, y, the kinematic viscosity of the fluid, ν, and a reference velocity, u_τ, which is a function of the wall shear stress.

$$y^+ = \frac{yu_\tau}{\nu} \tag{88}$$

These STAR-CCM+ simulations all utilize the Realizable K-Epsilon Two-Layer turbulence model in conjunction with the built-in two-layer all y^+ wall treatment option.

The relative spacing of the prism cells defines the spacing between consecutive centroids from the wall. This research typically uses spacing of 1.2, which allows for cells relatively close to the wall with a 1.0 mm thickness and 10 layers. With typical LWR flow conditions, the y^+ value of the first mesh cell is less than 30 with this spacing and prism thickness.

The value of y^+ is used in two-layer calculations to separate the viscous/laminar sublayer from the logarithmic-law region. A buffer region exists between the laminar and turbulent regions. STAR-CCM+ either applies its standard wall laws, which are slope-discontinuous, or its blended wall laws, which smooth the slope discontinuities over the buffer region. In the laminar sublayer, the reference laminar velocity, u^+, is simply set equal to the non-dimensional distance y^+, as shown in Equation (89).

$$u_{lam}^+ = y^+ \tag{89}$$

The solution of the reference velocity in the logarithmic layer also depends on y^+, but also includes a constant, κ, known as the Von Karman constant and typically set near 0.42. Equation (90) shows the general form of the velocity in the turbulent profile, as constant are added and factored in to provide better agreement with data.

$$u_{trb}^{+} = \frac{1}{\kappa}\ln\left(y^{+}\right) + \beta \tag{90}$$

If a friction factor is included in STAR-CCM+'s simulations assuming rough rod or grid surfaces, its effects would show in the calculation of the turbulent region's velocities.

Table 16: PSBT MVG 2x2 subchannel meshing study CFD modelling parameters

Geometry details	
Subchannel layout	4 subchannels, connected via interface along their gaps
Domain length	740 mm (including extruded inlet region)
Grid leading edge axial location	80 mm
Mesh details	
Models	Polyhedral mesher Prism layer mesher Extruder Surface remesher
Base size	0.5 mm
Prism layer details	10 layers at 1.2 spacing, 1.0 mm thickness
Extruder details	200 mm extrusion from inlet, 100 layers at 1.02 spacing
Flow conditions	
Inlet temperature	300 C
Inlet velocity	5.0 m/s
Pressure	15.5 MPa
Boundary conditions	
Rods	Wall-type, smooth, adiabatic
Outer flow boundaries (walls)	Wall-type, smooth, adiabatic
Gaps	Connected via periodic interfaces
Inlet	Velocity inlet
Outlet	Pressure outlet
Physics details	
Models	Liquid Steady Three dimensional Reynolds-averaged Navier-Stokes Turbulent Realizable K-epsilon turbulence Two-layer all y+ wall treatment Exact wall distance Segregated flow Segregated fluid enthalpy User-defined equations of state (Defined in Equation (45) - (47))

There are two different types of internal subchannels which vary slightly depending on their specific orientation of the mixing vanes with respect to the placement of the grid's springs and dimples. Each of the four corner subchannels is different with the PSBT MVG spacer grid, as shown in Figure 13. Two of the corner subchannels contain mixing vanes, while the other two are distinct based on whether they contain springs or dimples.

The simulations for the full-size 5x5 rod bundles are similar to those of the 2x2 bundles with a few exceptions. The prism layer mesh settings were decreased from 10 layers to 5 layers at 1.5 spacing and 0.8 mm thickness in order to decrease computational requirements of the larger domain. The spacer grid has its base located at 0.0 mm, and the mesh is extruded from both the inlet and the outlet planes.

Table 17 details the parameters used within the CFD simulations for the PSBT A1 5x5 rod bundle spacer grids. The grids were modelled individually with one PSBT spacer grid per 5x5 rod bundle simulation.

Additional wall friction occurs in the full PSBT A1 5x5 CFD simulation, as the flow's outer boundaries are included in the domain. The 2x2 internal subchannel layout only contains walls from the rod surfaces.

Table 17: PSBT A1 bundle 5x5 CFD modelling parameters for the pressure study

Geometry details	
Subchannel layout	36 subchannels (full PSBT A1 5x5 bundle geometry)
Domain length	800 mm (including extruded inlet and outlet regions)
Grid leading edge axial location	0 mm
Mesh details	
Models	Polyhedral mesher Prism layer mesher Extruder Surface remesher
Base size	0.5 mm
Polyhedral mesh region	From -40 to 125 mm
Prism layer details	5 layers at 1.5 spacing, 0.8 mm thickness
Extruder details	260 mm extrusion from inlet, 260 layers at 1.0 spacing 375 mm extrusion from outlet, 375 layers at 1.0 spacing
Flow conditions	
Inlet temperature	300 C
Inlet velocity	5.0 m/s
Pressure	15.5 MPa
Boundary conditions	
Rods	Wall-type, smooth, adiabatic
Outer flow boundaries (walls)	Wall-type, smooth, adiabatic
Gaps	Connected via periodic interfaces
Inlet	Velocity inlet
Outlet	Pressure outlet
Physics details	
Models	Liquid Steady Three dimensional Reynolds-averaged Navier-Stokes Turbulent Realizable K-epsilon turbulence Two-layer all y+ wall treatment Exact wall distance Segregated flow Segregated fluid enthalpy User-defined equations of state (Defined in Equation (45) - (47))

Figure 61 shows the geometry of the flow volume used in the 5x5 PSBT A1 bundle simulations. The spacer grid's base is placed at 0.0 mm axially, and the polyhedral mesh is applied from -40 to 125 mm. The remaining volume is extruded. Figure 61 shows two PSBT

MVG 5x5 bundles; the bottom portion of the figure shows the region of the polyhedral mesh and the top portion shows the overall domain with the extruded inlet and outlet regions.

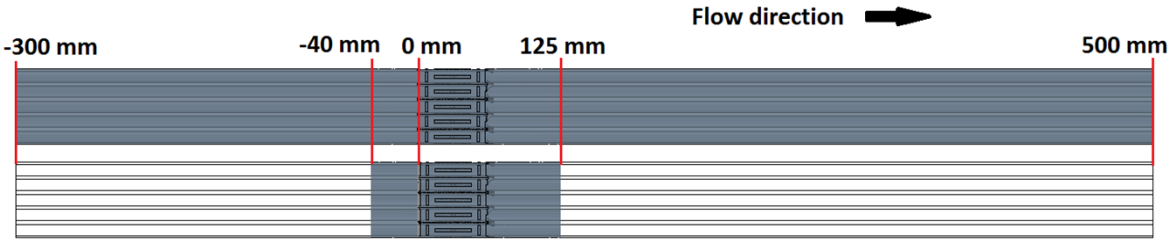

Figure 61: CFD simulation geometry for the PSBT 5x5 spacer grid cases

In order to improve convergence of the CFD simulation, the volumes of flow outside of the PSBT grid straps were not included in the CFD simulations. These volumes are thin (0.7 mm) and stretch the length of each spacer grid, and when including in simulations often proved difficult to solve at the considered mesh sizes. These volumes were removed by confining the lateral domain to the midpoint of the grid strap's thickness at each boundary strap. Figure 62 illustrates their locations with respect the spacer grids, with the red outer regions being the removed volumes, the purple being the volume of the spacer grid straps/features retained, and the blue the remaining flow volumes for the PSBT 5x5 SSG CFD model.

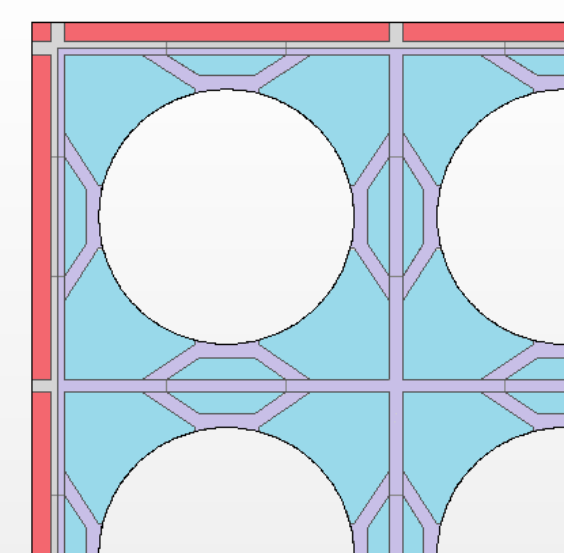

Figure 62: Flow volumes removed (red regions) from the PSBT 5x5 models

The flow volumes outside of the subchannels exist due to the fact that the PSBT spacer grid straps do not truncate at the outer edges of the subchannels, and there is some overlap and excess material outside of the subchannels. The PSBT bundle flow width is provided as 64.9 mm, and the rod pitch is 12.6 mm. With uniform grid spacing and a strap thickness of 0.5 mm, this equates to a distance of $5(12.6\text{ mm}) + 2(0.25\text{ mm}) = 63.5\text{ mm}$ expected from grid strap outer edge to grid strap outer edge. Therefore, an additional 1.4 mm may exist in each lateral direction outside of the standard subchannels for fluid flow to meet the PSBT-defined width of 64.9 mm. This distance is assumed to be split evenly, with 0.7 mm of extra grid strap stretched on either side of the boundary straps. Figure 63 highlights these regions using a top view of the PSBT MVG.

Alternatively, the PSBT grids could be drawn without this additional grid strap extension and the flow outside of the spacer grids could be ignored in similar fashion, with the same effect as the truncated models.

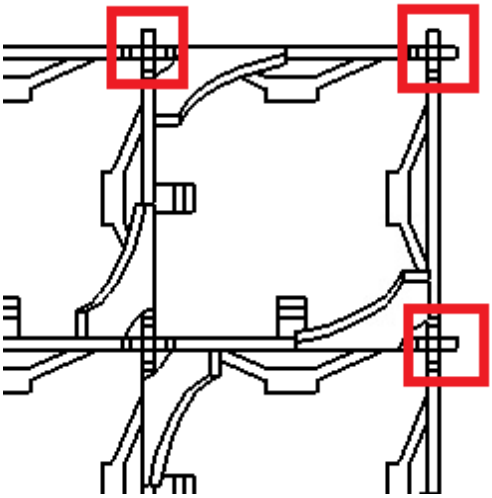

Figure 63: Detailed view of the PSBT grid's 0.7 mm protrusions from the nominal grid boundaries

CFD polyhedral mesh base size study

A mesh study was carried out to assess the effect of mesh base size on STAR-CCM+'s pressure predictions of flow across a spacer grid. The CFD modelling parameters for the meshing study are provided in Table 16, with the notable change being the mesh base size for the polyhedral mesher model. This base size was altered among values of 0.3, 0.4, 0.5, and 0.7 mm. It is important to note that the number of layers in the prism mesh—as well as its thickness—were not changed during this study of mesh size. The total flow domain of the 2x2 CFD simulation spans from -160 to 580 mm. The inlet region is extruded 200 mm to create a volume to allow for flow development without adding much computational cost. There is no extrusion at the outlet, and the polyhedral mesh is on the axial range of 40 to 580 mm. The leading edge of the PSBT MVG spacer grid is located at 80 mm axially along the domain. Therefore, there are 40 mm of polyhedral mesh and then an additional 160 mm of extruded mesh before the flow encounters the grid's leading edge.

Only internal subchannels for the PSBT MVG spacer grid are considered in the 2x2 subchannel layout. There are interfaces at the gaps in the CFD simulation to preserve the meandering flow pattern caused by the mixing vane orientation. The MVG was selected for the meshing study due to its geometric complexity in comparison to the other two PSBT spacer grids.

A bare 2x2 subchannel CFD simulation with the same rod outer diameter and rod pitch was also performed in order to provide a comparison for the frictional losses along the axial domain. The presence of a spacer grid is then the only difference between the two geometries, bare and gridded. The polyhedral base mesh size for the bare 2x2 simulation is set to 0.3 mm, and the other modelling parameters are defined in Table 16.

The spacer grid loss coefficients are calculated using surface-average pressure results extracted every 2 mm along the flow domain. The pressure drops from the gridded simulations

are compared with those from the bare simulation to obtain the pressure drop due to the grid. This method allows for the frictional pressure loss to be removed, leaving only the form pressure losses as gravity terms are not included in these simulations. Figure 64 shows the results from each CFD simulation with a pressure that has been zeroed (from the reference value of 15.5 MPa) against the axial distance. The leading edge of the spacer grid is located at 80 mm. The profile of the pressure results as the flow passes through the spacer grid is very similar for each base mesh size. The main difference is in the upstream pressure prediction, which varies by approximately 1.0 kPa from the 0.3 mm mesh size to the 0.7 mm mesh size.

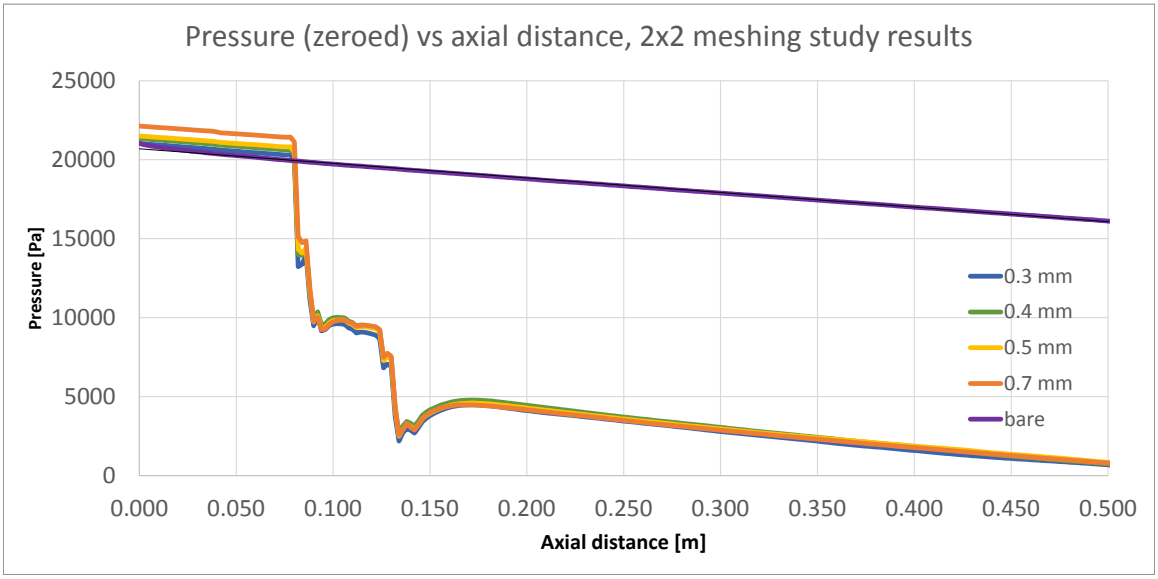

Figure 64: CFD Pressure predictions from the 2x2 meshing study with the PSBT MVG

The averaged pressure losses caused by the MVG in the 2x2 subchannel layout are shown in Table 18. The loss coefficient for the MVG acting on the internal subchannels is calculated using Equation (61) and the results are also included in Table 18.

Table 18: Results of the meshing study using the PSBT MVG in a 2x2 internal subchannel layout

Base mesh size (mm)	0.3	0.4	0.5	0.7
Pressure drop over spacer grid	15.8 kPa	16.1 kPa	16.3 kPa	16.9 kPa
Spacer grid loss coefficient	1.75	1.79	1.81	1.88
Loss coefficient deviation (% difference from 0.3 mm case)	---	1.9%	3.0%	7.0%

The results were compared and the predicted pressures at the inlets were compared to see the effect of changing the polyhedral mesh base size on the pressure calculations. The results in Table 18 show the difference in STAR-CCM+'s prediction of the loss coefficient for the MVG spacer grid in the CFD simulation in relative percent error, with a mesh size of 0.3 mm as the theoretical value. These results indicate that a mesh size of 0.5 mm predicts pressures within 3% of the case with a mesh size of 0.3 mm, and it uses approximately one-third of the amount of memory.

A comparison of the meshes is shown in Table 19, which contains information on the mesh and simulation file sizes. The computational costs are also considered when choosing a mesh size, as scalability to the full PSBT 5x5 simulation becomes very memory-intensive, and smaller mesh sizes compound memory usage. For instance, the simulation for the PSBT 01-5343 case contains 17 spacer grids on a full-length 5x5 rod bundle. While the prediction of the mesh size of 0.4 mm are better than the case of 0.5 mm, the RAM required for a mesh of 0.4 mm base size exceeded the available memory on a compute node, at over 300 GB required. The mesh size of 0.5 mm provides acceptable performance and keeps the simulation file's RAM usage under 256 GB. This information helped lead to the eventual selection of 0.5 mm as the base size for the polyhedral mesh.

Table 19: Details for the mesh sizes used in the 2x2 PSBT spacer grid mesh study

Base mesh size (mm)	0.3	0.4	0.5	0.7

Number of mesh cells	19.5E6	11.0E6	6.47E6	3.29E6
Mesh cells ratio (based on 0.7 mm)	5.93	3.34	1.97	1.00
File size ratio (based on 0.7 mm)	6.78	3.61	2.12	1.00

PSBT spacer grid loss coefficient calculations from 5x5 CFD simulations

Each of the three PSBT spacer grid designs from Chapter 3 was modelled and simulated in STAR-CCM+ following the CFD modelling parameters listed in Table 17. An additional simulation of a bare 5x5 rod bundle with the same geometry and mesh scheme, but with no spacer grid was performed as well. The pressure loss coefficients of each grid can be calculated using Equation (2). This requires the calculation of ΔP_{form}, ρ, and u from the CFD results. The fluid density does not change much along the axial length of the domain as the simulations are isothermal and gravity effects are neglected. A domain-averaged density is obtained from the simulation as $\rho = 715.32\ \mathrm{kg/m^3}$. The axial velocity used in the calculations is defined as the inlet velocity of the simulation. The inlet boundary condition in the CFD simulation is a velocity inlet of 5.0 m/s.

The definition of the pressure drop caused by the spacer grid is important to these calculations. Pressure results were taken every 2 mm in axial planes and averaged over the surface of each plane. The form loss is determined for the PSBT 5x5 simulations by averaging the difference in these planar pressure measurements from the bare bundle simulations. The average is taken over an axial span of 100 mm, which includes 51 of these surfaces spaced every 2 mm. The axial span of the pressure difference average is from -250 mm to -150 mm in the CFD simulation. The entire simulation domain is on the axial range of -300 to 500 mm. The bottom-most 50 mm were not considered to allow for the flow to properly develop in the CFD model.

The frictional drop can be determined from the bare 5x5 rod bundle. The effects of the rod surfaces and walls are included in this simulation and cause a linear decline in pressure as the

flow travels upward through the domain. The slope of the CFD-calculated pressure over the axial distance represents the amount of pressure drop per unit distance along the domain. Table 20 shows the CFD-calculated pressure drops over axial distance for the bare 5x5 rod bundle, grouped by subchannel type.

Subchannel-specific results for pressure drop predictions are taken from the CFD simulation using line probes aligned with the direction of flow placed in each subchannel. Four of these probes exists within each internal subchannel, two probes are in each side subchannel, and one probe is in each corner subchannel. Figure 65 shows the related locations of these line probes inside of an internal subchannel. Figure 66 shows the overall locations of each linear probe used for data extraction. The line probes are set with a resolution of 1 point per mm in their axial direction.

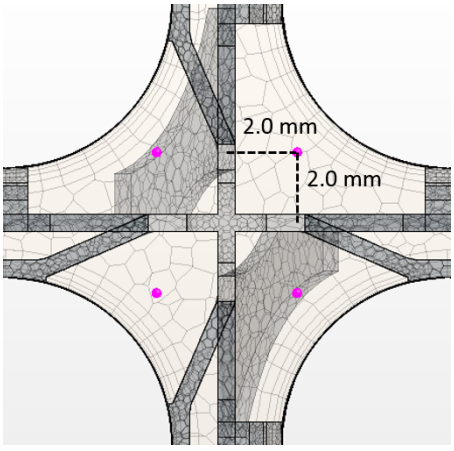

Figure 65: Detailed view of the line probe locations within an internal subchannel

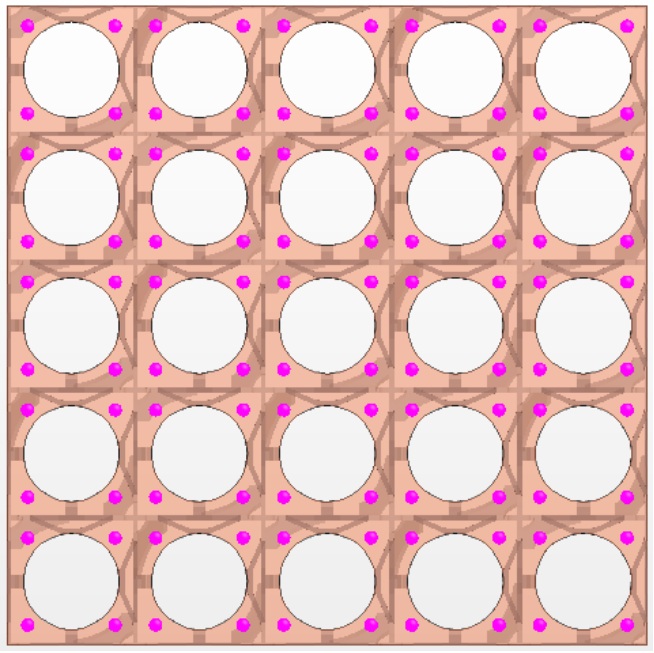

Figure 66: Locations of the line probes used to extract subchannel-specific results from CFD simulations

These pressure drop results are calculated for each of the three types of subchannel geometries in the PSBT bare bundle. The wetted perimeter area encountered by each subchannel geometry in the bare bundle is also displayed in Table 20. The result of the pressure drop over distance is the same for each subchannel geometry, even though the wetted perimeters differ. This is due to the fact that these CFD simulations are not isolated subchannels and therefore each subchannel's results are affected by lateral pressure gradient-driven equalization over the axial length. Figure 67 shows the pressure over the axial distance for each of the four corner subchannels in the MVG spacer grid. There are two corner subchannels which contain mixing vanes, subchannels #1 and #36, and their pressure profiles featuring matching drops at the axial locations of these vanes. As all side subchannels contain one mixing vane and all internal subchannels contain two mixing vanes, the differences in these subchannel geometries are not as pronounced as the results for the corner subchannels are.

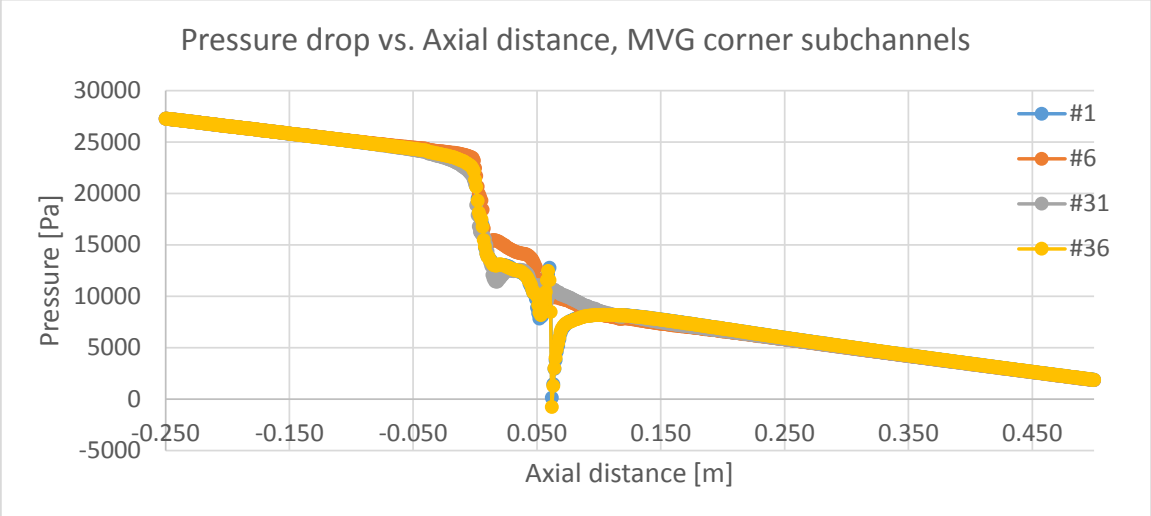

Figure 67: Pressure vs. axial distance for the corner subchannels in the 5x5 PSBT MVG CFD simulation

This 5x5 bundle CFD simulation method does provide a proper method for determining the pressure losses due to friction as no geometric simplifications are made in the CFD model which would affect the frictional pressure drop.

Table 20: PSBT A1 5x5 rod bundle pressure drop over axial distance with no spacer grid present

Bare PSBT A1 5x5 rod bundle	Wetted Perimeter [mm]	ΔP_{fric} over the [-0.250, -0.150] m axial range [kPa/m]
Corner subchannels	20.06	-14.6
Side subchannels	27.52	-14.6
Internal subchannels	29.85	-14.6
Overall bundle	998.1	-14.6

The CFD simulations for the three PSBT spacer grids can be expected to have the same rod surface and wall effects, as the geometry is the same aside from the introduction of the spacer grid. The pressure drop calculated in STAR-CCM+ is a sum of the form and the frictional pressure losses. The introduction of spacer grids to the CFD simulations does create additional frictional losses due to the non-negligible surface area of the spacer grids. The form loss coefficient for the spacer grid as calculated with these CFD methods is then assumed to be a combination of the spacer grid's form and friction losses. The pressure drop caused by the spacer grid can be determined by subtracting the frictional pressure drop from the overall pressure drop observed in the gridded CFD simulations.

The overall pressure drops from the 5x5 CFD simulations are calculated by assessing the total pressure drop over the entire axial domain. Surface-averaged pressure results are extracted every 2 mm. The inlet and outlet pressures are extracted in order to determine the overall pressure drop, and then the frictional effects are subtracted, as shown in Equation (91).

$$\Delta P_{grid,CFD} = \Delta P_{total,CFD} - \Delta P_{fric,CFD} \tag{91}$$

Once again, pressure probes are employed to extract pressure results from the CFD simulations for each subchannel geometry for the PSBT MVG, NMV, and SSG. The results for each subchannel type within the bundle are nearly identical, so the bundle results are shown only for the overall 5x5 spacer grid configuration. The results for the total pressure drops are shown in Table 21. The frictional pressure drop represents the pressure drop due to friction along the entire domain length in the CFD simulation.

Table 21: Form pressure drop across PSBT spacer grids, from CFD

PSBT spacer grid	MVG	NMV	SSG
Total pressure drop	27.3 kPa	22.0 kPa	20.4 kPa
Frictional pressure drop	11.7 kPa	11.7 kPa	11.7 kPa
Form pressure drop	15.6 kPa	10.3 kPa	8.7 kPa

The calculation for the PSBT MVG is derived from Equation (61) and shown in Equation (92).

$$\zeta_{grid,MVG} = 2\frac{15600\ \text{Pa}}{\left(715.3\ \text{kg/m}^3\right)\left(5.00\ \text{m/s}\right)^2} = 1.74 \tag{92}$$

Results for the PSBT spacer grids after applying Equation (61) are tabulated in Table 22, which shows that the PSBT MVG has the highest loss coefficient and the simple-space grid (SSG) has the lowest value.

Table 22: PSBT spacer grid loss coefficients as calculated for the 5x5 rod bundle, from CFD

PSBT Grid	CFD-calculated loss coefficient
MVG	1.74
NMV	1.15
SSG	0.97

As mentioned, these loss coefficients for the PSBT spacer grids include the effects of friction acting along the length of the grid's straps, but not the friction along the rod surfaces as this friction drop was subtracted out. These values are also intended to be applied equally at each subchannel within the 5x5 rod bundle, as they are developed from surface-averaged pressure results. The PSBT MVG produces the largest value, as expected, at 1.74. This is largely a result of its mixing vanes, which are aligned at 28 degrees from parallel with the flow. The NMV's loss coefficient of 1.15 is partially caused by its intrusive springs and dimples as well as its relatively large length; 41.1 mm compared to the 12.8 mm strap height of the SSG.

Study on the effects of flow conditions on pressure loss coefficients

A study into the effect of axial velocity on the CFD-calculated spacer grid pressure loss coefficient was completed by altering the inlet velocity of the CFD simulations. The nominal inlet velocity value, 5.0 m/s, was changed by ±10% and ±20%, for inlet velocity values of 4.0 m/s, 4.5 m/s, 5.0 m/s, 5.5 m/s, and 6.0 m/s. The 2x2 subchannel layout was utilized and the CFD modelling parameters are provided in Figure 4. The mesh base size used for this comparison is 0.5 mm. The bare simulations were also rerun at the same array of inlet velocities in order to provide data for the frictional losses caused by the rod surfaces.

The pressure drop due to frictional losses, which is extracted from the slope of the bare 2x2 subchannel simulations, increases as the flow's axial velocity increases. The spacer grid loss coefficient is a sum of the spacer grid's form loss coefficient and its frictional loss coefficient. Form loss coefficients are functions of geometry, not flow conditions, and therefore the form portion of the spacer grid loss coefficient is expected to remain the same for the PSBT spacer grids no matter the surround flow field conditions. The pressure drop due to form losses, shown in Equation (2), is proportional to the axial velocity squared. Similarly, the pressure drop due to

surface friction, Equation (71), is proportional to the axial mass flux squared, which is directly related to the axial velocity. Based on these correlations, if the inlet velocity were increased by a factor of 3.0, the magnitudes of both the pressure drop due to form losses and the frictional pressure losses along the spacer grid surfaces are expected to increase by a factor of 9.0. The fluid temperature and density are unchanged for each simulation.

Using the results of the 2x2 PSBT MVG simulation with an inlet axial velocity of 5.0 m/s as the standard velocity, the expected pressure drop over the spacer grid span in each flow condition can be predicted. The drop over the 5.0 m/s inlet velocity case was calculated as 16.3 kPa, and this value is used in the predictions of the other CFD pressure drops by applying a factor shown in Equation (93), which sets 5.0 m/s as U_{ref}.

$$f_{vel} = \left(\frac{U_z}{U_{ref}}\right)^2 \tag{93}$$

The velocity factor of Equation (93) is calculated for each case studied in this flow study and tabulated in Table 23. The expected pressure drop over the spacer grid span can be determined from this velocity factor assuming the value of 16.3 kPa as the pressure drop for the 5.0 m/s case. The estimation is performed by multiplying the velocity factor, f_{vel}, by the pressure drop for the 5.0 m/s case.

Table 23: Pressure drop parameters for the 2x2 MVG varied flow CFD simulations

Axial velocity at CFD model inlet	4.0 m/s	4.5 m/s	5.0 m/s	5.5 m/s	6.0 m/s
f_{vel}	0.64	0.81	1.00	1.21	1.44
Expected pressure drop over spacer grid	10.4 kPa	13.2 kPa	16.3 kPa	19.7 kPa	23.4 kPa

Table 24 details the pressure loss for each inlet velocity, grouped by the source of the loss. The magnitude of the frictional pressure drop caused by the rod surfaces also follows a

quadratic pattern with relation to the axial velocity, as expected. The CFD-predicted pressure loss coefficients for the MVG 2x2 internal subchannel simulations are very similar, ranging from 1.80 to 1.82.

Table 24: Pressure drop results for the 2x2 MVG varied flow CFD simulations

Axial velocity at CFD model inlet	4.0 m/s	4.5 m/s	5.0 m/s	5.5 m/s	6.0 m/s
Frictional pressure loss per distance	6.1 kPa/m	7.5 kPa/m	9.2 kPa/m	11.1 kPa/m	13.2 kPa/m
Pressure drop over the spacer grid	10.4 kPa	13.1 kPa	16.3 kPa	19.7 kPa	23.3 kPa
CFD-calculated spacer grid loss coefficient	1.82	1.80	1.81	1.82	1.81

CTF and STAR-CCM+ pressure prediction comparison

CTF simulations were carried out with the PSBT A1 bundle geometry to compare the results of CTF to the results of STAR-CCM+. The results of interest are the pressure drops over the axial length of the simulation. The pressure drops are split into the frictional and the form losses, with the form losses assumed to be attributed to the placement of the spacer grids.

The CTF axial length was set to 0.740 m, which is based off of the axial length of the CFD simulations. The full PSBT 5x5 bundle geometry as well as 2x2 internal subchannels were modelled in CTF. The spacer grids were located at 0.24 m axially, which corresponds to a pressure loss coefficient specified at node 24 (out of the 74 axial nodes with 0.01 m spacing set in CTF). The CFD simulation boundary conditions were applied in CTF as well. The inlet temperature is 300 °C, the pressure is set as 15.5 MPa, and the inlet velocity is 5.0 m/s. The rod surfaces are modelled as wetted perimeters in the corresponding subchannels in CTF.

The frictional pressure drop is determined by analyzing the amount of pressure drop over the portions of the CTF model where no grids exist. The frictional pressure drops as calculated by CTF are compared with the results from STAR-CCM+ and shown in Table 25. As expected, the frictional pressure drop increases in the 5x5 model geometry due to the presence of additional boundaries around the bundle. The 2x2 simulations do not contain any walls or surfaces aside from the rods. It is also important to note that CFD simulations model the spacer grid straps as surfaces, and the friction pressure drop along the spacer grid surfaces is considered in the overall pressure drop over the spacer grid span. CTF does not model the surface effects of spacer grids individually and relies only on a single loss coefficient to be specified.

A main difference in the two simulation methods is that the CFD model ignores the effects of gravity while CTF counts gravity in its pressure drop simulations. Therefore, the effects of the pressure drop due to elevation changes must be subtracted from the CTF results to obtain only the pressure drop caused by friction. Equation (94) shows the calculation of the pressure drop in a single-phase fluid due to gravity. This result can be converted to a per-unit length amount by dividing by the axial domain length of the simulation. The CTF-predicted fluid density is 724.3 kg/m^3, and the gravitational acceleration constant, g, is equal to 9.81 m/s^2.

$$\Delta P_{grav} = \rho g L \tag{94}$$

The CTF pressure drop per unit length due to gravity—called the geodetical pressure loss in CTF—is calculated as 7.1 kPa/m. This value is then subtracted from the pressure losses in the CTF simulations to obtain the pressure losses due to friction along the surfaces, as shown in Table 25.

Table 25: Frictional pressure losses calculated by CTF and STAR-CCM+

Model geometry	2x2	5x5
CTF	-11.5 kPa/m	-14.5 kPa/m
STAR-CCM+	-9.2 kPa/m	-14.6 kPa/m

The form pressure losses caused by the spacer grid are calculated from CTF results by examining the bundle-averaged pressures at axial nodes 24 and 25 and subtracting the frictional and elevation losses over that 0.01 m axial span. The results for the pressure drops caused by the spacer grids are shown in Table 26.

Table 26: Form pressure losses for the 5x5 spacer grid geometry calculated by CTF and STAR-CCM+

PSBT spacer grid	MVG	NMV	SSG
CTF (PSBT-recommended loss coefficient)	9.1 kPa	6.4 kPa	3.6 kPa
CTF (CFD-determined loss coefficient)	15.8 kPa	10.4 kPa	8.8 kPa
STAR-CCM+	15.6 kPa	10.3 kPa	8.7 kPa

When CTF is provided with the pressure loss coefficients for the spacer grids, its pressure drops over the grid spans match well with the CTF results. Based on the results in Table 26, it appears that CTF slightly over-predicts the pressure drop over the grid span by about 0.1 kPa.

A small difference in the results between CTF and STAR-CCM+ is the prediction of the frictional pressure drop caused by the walls and rod surfaces. The friction option for CTF is set to 2, which indicates that McAdam's correlation, Equation (77), is used. If this friction calculation option is changed to 1, the original CTF model, Equation (76), is used for determining the friction factor. The original CTF model provides a larger predicted value of the frictional pressure drop, at 17.7 kPa/m, than McAdam's correlation, which calculates a frictional drop of 14.5 kPa/m. Both of these values are similar to the 14.6 kPa/m predicted by STAR-CCM+ in the 5x5 PSBT A1 bundle geometry simulation, but it appears that McAdam's correlation provides much more consistent agreement. Both of these CTF friction models are viable options in the case of smooth wall surfaces.

Study on subchannels containing multiple spacer grid straps

A study is performed to see the effect of multiple spacer grid straps located within a single flow subchannel. These types of subchannels occur where the fuel assemblies converge in an LWR, as the fuel assemblies are also arranged on a square lattice throughout the reactor core.

The rod bundles in this simulation, which are shown generally in Figure 71, are all assumed to have the same fluid properties. In an LWR, this may not be the case as adjacent fuel assemblies vary in power and therefore heat levels, causing gradients from bundle to bundle. Lateral pressure effects can be strong from one assembly to another causing additional flow mixing near and around the boundaries of the adjacent bundles. The PSBT MVG spacer grids were spaced consistent with LWR fuel assembly spacing, such that the gap between the rods at the bundle intersection is the same as is found in a typical PWR.

As geometric asymmetry prevents modelling a single subchannel for the PSBT MVG due to the vane placement and orientation, results for a single subchannel cannot be accurately produced with CFD simulations. Even though the CFD model contains subchannels which hold multiple spacer grid straps, the downstream pressure effects will equalize due to the lateral pressure gradient effects. Therefore, obtaining results for the effects of spacer grid straps on PSBT MVG pressure predictions is an issue. Figure 68 shows the CFD-predicted pressure at the axial plane located 80 mm from the MVG's leading edge. This is approximately 10 mm past the vane tips, and it shows the central subchannel as having the largest pressure deviations. The effect of multiple spacer grid straps increases the subchannel blockage and causes a larger pressure drop, but the drop is not as significant as the losses caused by the mixing vanes themselves.

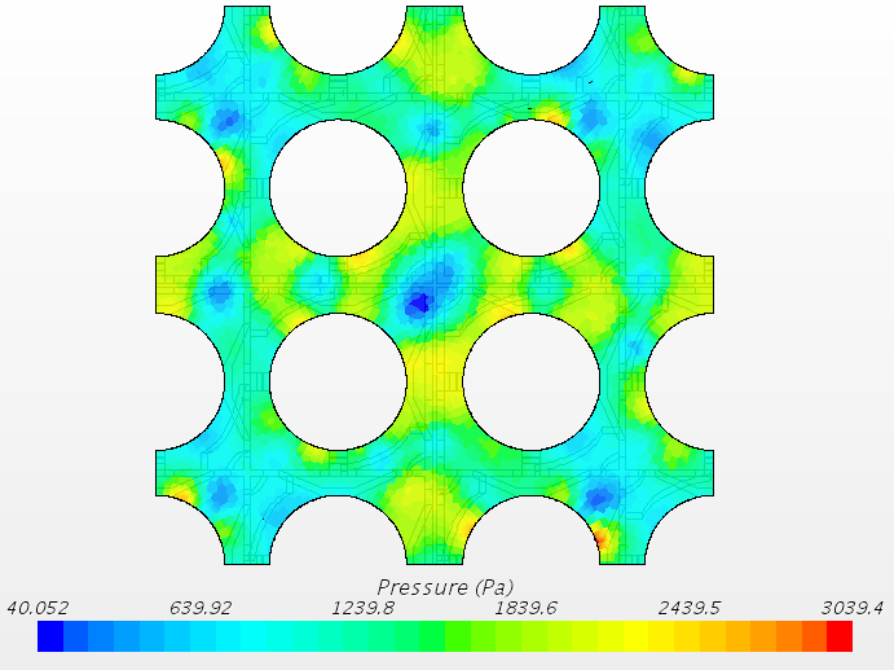

Figure 68: CFD results for the pressure profile 80 mm from the 4 MVG spacer grids' leading edges (~10 mm downstream from the vane tips)

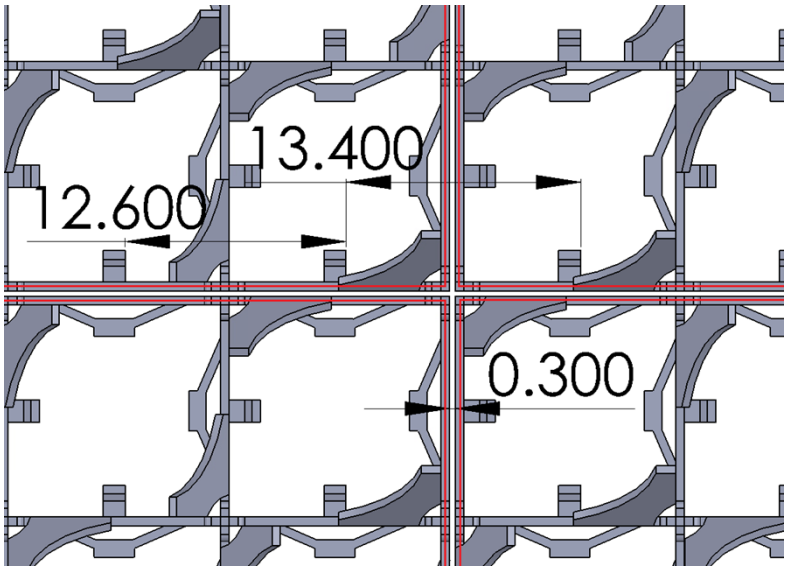

Figure 69: Geometric details at the intersection of four PSBT MVG spacer grids

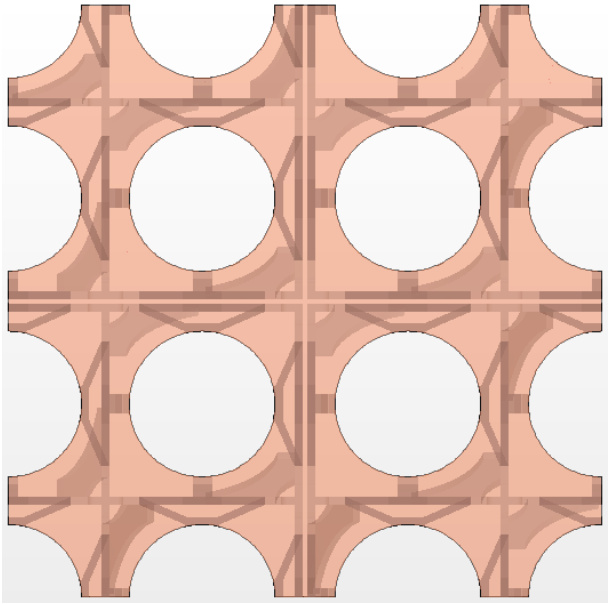

Figure 70: Overall geometry at the intersection of four PSBT MVG spacer grids used in STAR-CCM+

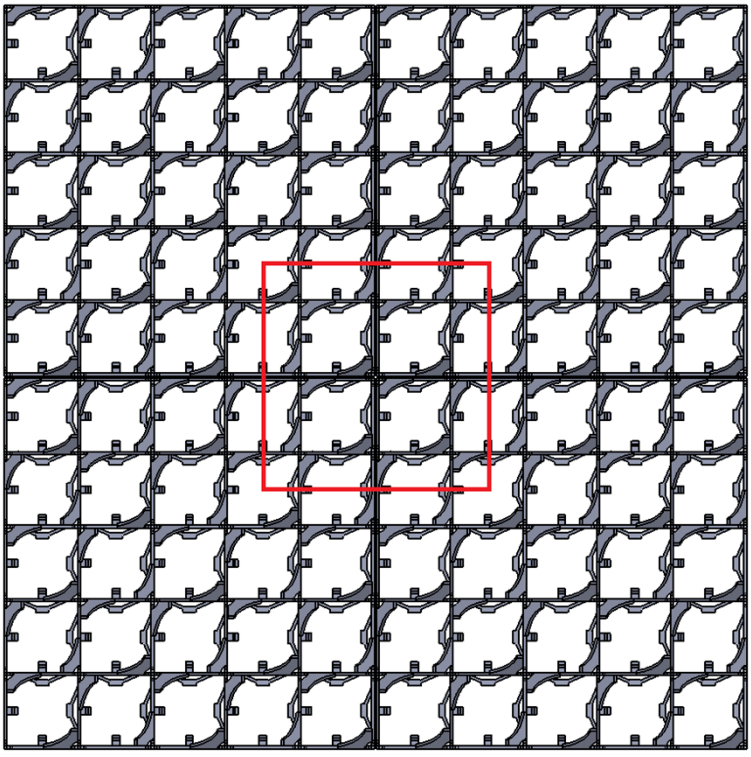

Figure 71: Full view of four PSBT MVG grids located with typical PWR fuel assembly spacing

PSBT Experiment 01-5343 CFD simulation

The full PSBT 5x5 model for Test Case 01-5343 was modelled and simulated in STAR-CCM+. The grid segments were split apart into volumes of either 228 or 229 mm in length, depending on the spacing in the PSBT details for bundle A1 as shown in Table 3. An extruded inlet region allowed for flow to develop by the time the first NMV is reached, and the outlet is extruded to the 4115 mm axial location at which the PSBT subchannel temperature measurements were taken during the original experiments. As was done for the 5x5 PSBT CFD models, the flow outside of the grid spans was ignored in this simulation, as shown in Figure 62. The results for the pressure drop over each spacer grid span from the full PSBT 01-5343 test case are documented in Table 27.

Table 27: Results from the PSBT 01-5343 CFD simulation with full A1 bundle geometry

Grid number	ΔP_{form} over the grid span [Pa]	Grid type	CFD-calculated loss coefficient
1	2150	NMV	1.20
2	1834	SSG	0.97
3	2763	MVG	1.58
4	2007	SSG	1.09
5	2851	MVG	1.62
6	2021	SSG	1.09
7	2870	MVG	1.61
8	2044	SSG	1.09
9	2895	MVG	1.61
10	2060	SSG	1.09
11	2922	MVG	1.61
12	2092	SSG	1.10
13	2958	MVG	1.61
14	2114	SSG	1.09
15	2994	MVG	1.60
16	2133	SSG	1.09
17	2320	NMV	1.22

Average spacer grid loss coefficients by PSBT grid type are calculated from the PSBT 01-5343 CFD simulation. The averaged results for the 7 MVG spacer grids, 2 NMV spacer grids, and 8 SSG spacer grids are:

- MVG: 1.61
- NMV: 1.21
- SSG: 1.08

These values are similar to those determined from the 5x5 CFD models, which were 1.74, 1.15, and 0.97 for the MVG, NMV, and SSG, respectively. Percent differences from the CFD predictions of single-spacer grid spans are -7.5%, 5.2%, and 11.3% for the MVG, NMV, and SSG respectively. The differences may arise from compounded modelling simplifications which were required to keep the file size manageable. This full-length simulation also featured heated rods, which means that the temperature and density of the water changes much more than for the isothermal simulations. The spacer grid loss coefficients were calculated using the volume-averaged density and the axial velocity at the inlet. The axial velocity enters the simulation at 1.71 m/s and the CFD results show this axial velocity magnitude increasing to 1.89 m/s by the time the fluid exits the bundle at the top of the simulation. This is a change of over 10% in axial velocity. Similarly, the density of the fluid entering the simulation is 913 kg/m^3, while the density at the exit is 817 kg/m^3, which is a decrease of over 10% from the value at the inlet. The velocity and density parameters must be directly related to maintain mass flux similarity at the inlet and outlet.

BFBT Single-Phase Pressure-Drop Experiment CFD simulations

A comparison is made with the BFBT Benchmark [67] single-phase pressure drop measurements. This comparison is performed to show the ability of STAR-CCM+ to predict pressures of flow around a complex spacer grid with respect to experimentally measured results. This corresponds to Phase II, Experiment 0 within the benchmark. Test cases from the P7 single-phase pressure drop studies are examined in this section. The experiments involve spacer grids consisting of conjoined ferrules used within an 8x8 electrically-heated rod bundle with a central, large diameter water rod. Heat is not applied to this simulation, and only the inlet conditions are considered from the BFBT benchmark. Please see the BFBT reference for detailed drawings and dimensions of the spacer grid.

A base polyhedral mesh size of 0.5 mm is utilized, with 10 prism layers at 1.40 spacing and 1.00 mm total thickness. The rod pitch is 16.2 mm, the rod outer diameter is 12.3 mm, and the heated length is 3708 mm. There are 7 spacer grids along the axial length, spaced 512 mm apart. The geometry is reduced to 1/8 using symmetry as shown in Figure 72. The general and detailed mesh cross-sectional view are shown in Figure 73 and Figure 74.

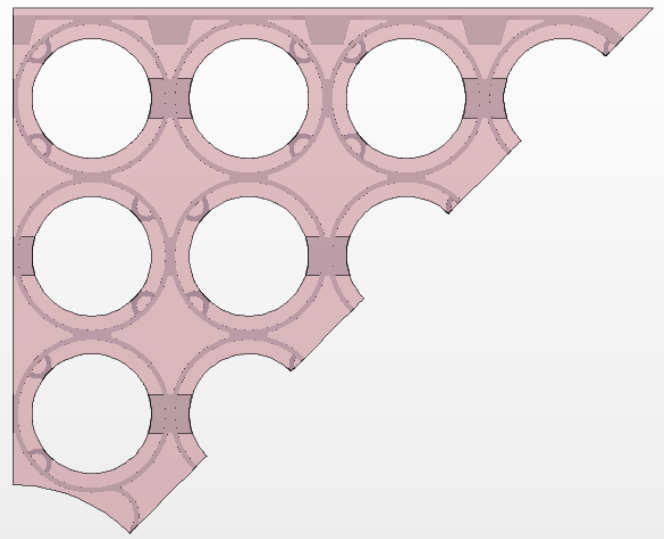

Figure 72: BFBT CFD simulation geometry reduced with symmetry

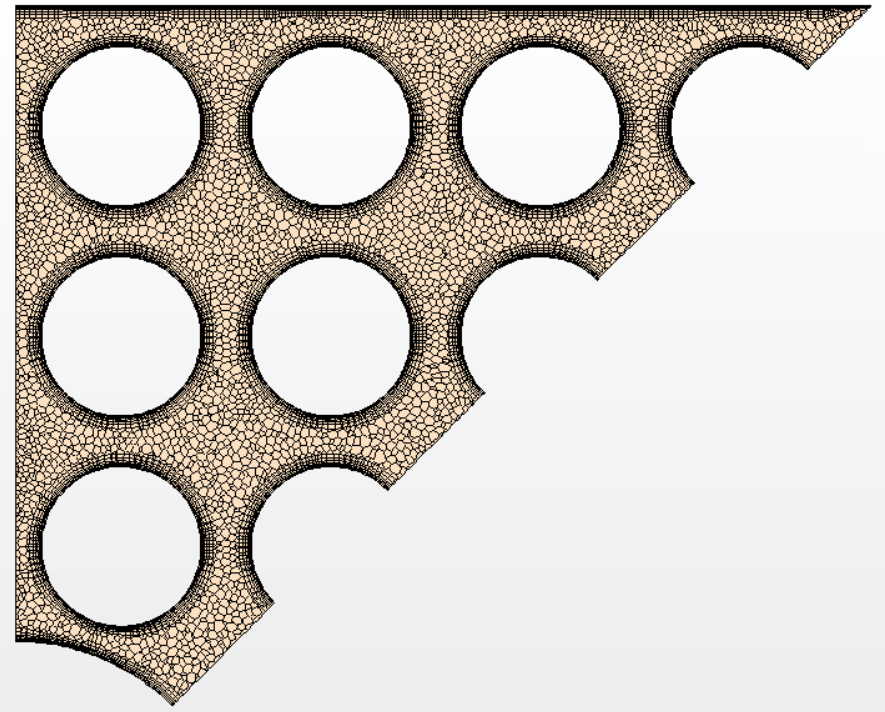

Figure 73: BFBT general mesh overview

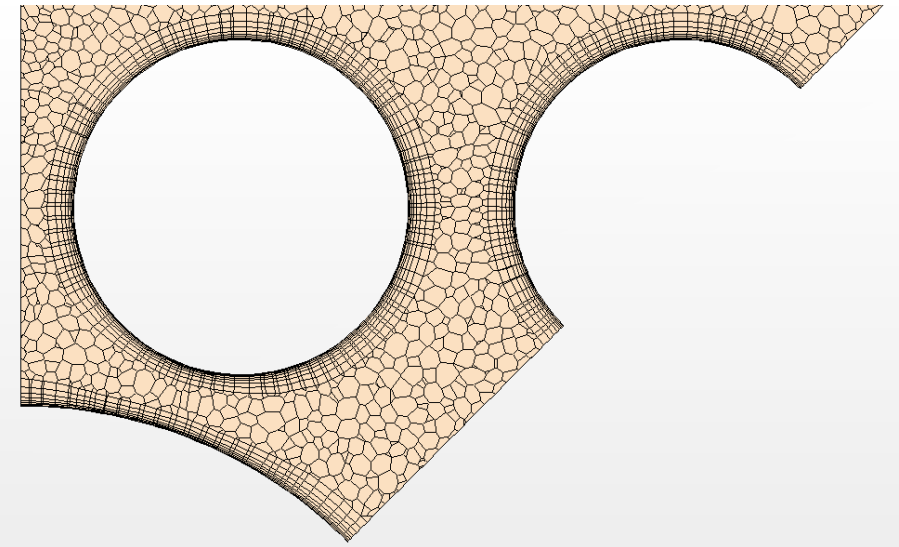

Figure 74: BFBT detailed mesh overview

The overall geometry of the BFBT simulation is shown in Figure 75, which is scaled to 10% in the axial direction to aid in viewability. An inlet region for flow development is included prior to the first spacer grid's leading edge.

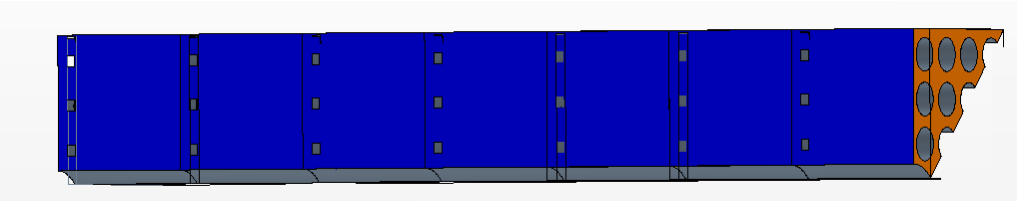

Figure 75: BFBT CFD simulation geometry, scaled to 10% axially

There are measured results from the BFBT experiment of pressure drops across several axial ranges within this full-length model. These pressure tap locations are detailed in Table 28, where the axial location of 0.0 refers to the beginning of the heated length, which is at the bottom of the geometry.

The boundary conditions for this case are:

- Pressure of 7.15 MPa
- Inlet temperature of 284.9 C
- Inlet velocity of 0.796 m/s

Table 28: BFBT Phase II Experiment 0 pressure tap location details

Pressure tap ID	Lower elevation [mm]	Upper elevation [mm]	Span [mm]
dp1	3498.0	3708.0	210.0
dp2	2986.0	3242.0	256.0
dp3	3242.0	3708.0	466.0
dp4	2730.0	3242.0	512.0
dp5	2218.0	2730.0	512.0
dp6	1706.0	2218.0	512.0
dp7	682.0	2218.0	1536.0

The steady-state CFD simulation is carried out to assess the CFD predictions of the pressures at these axial locations. The frictional pressure drop of the 1/8 bundle model is measured as -0.34 kPa/m. This frictional pressure loss can be subtracted from the total simulated pressure drops to obtain the CFD-predicted form losses over each pressure tap span. The experimentally-measured pressure drops for a single experimental case, #70027 (of the ten BFBT single-phase pressure drop cases) are compared with the CFD results and tabulated in Table 29. Comparisons with experimental data are fair, with values over the smaller spans typically higher than those of the larger spans. The experimental errors in measurement for this case, which is a low inlet velocity case, are a large factor due to the relative effect of frictional pressure drop.

Table 29: BFBT Test 70027 comparison of CFD results for pressure drop

Span ID	CFD-predicted drop [Pa]	# of spacer grids in span	Frictional drop [Pa]	Form drop [Pa]	Grid loss coeff.	Experimental measured drop [Pa]	Error [%]
dp1	371.2	1	72.4	298.8	1.260	300	23.7
dp2	387.9	1	88.2	299.7	1.264	350	10.8
dp3	462.5	1	160.6	302.0	1.274	390	18.6
dp4	478.6	1	176.4	302.2	1.275	450	6.4
dp5	477.6	1	176.4	301.2	1.270	470	1.6
dp6	478.3	1	176.4	301.9	1.273	460	4.0
dp7	1436.2	3	529.3	906.9	1.275	1330	8.0
dp8	555.8	1	226.4	329.4	1.389	520	6.9
dp9	3410.7	7	1277.7	2133.0	1.285	3120	9.3

The CFD-calculated spacer grid loss coefficients, as performed with Equation (60), are very consistent for each span except for dp8, which may require a better flow development region. The results from each of the ten BFBT single-phase pressure drop cases are presented in Table 30. The calculated spacer grid loss coefficients for each experimental case over each pressure tap span are shown in Table 31.

Table 30: BFBT single-phase pressure drop CFD percent error by case

BFBT case ID p700##	**27**	**28**	**29**	**30**	**31**	**32**	**33**	**34**	**35**	**36**
dp1	23.7	19.3	20.2	29.2	18.8	20.5	21.0	21.3	22.4	22.1
dp2	10.8	11.7	10.8	11.9	9.8	12.1	13.1	13.6	13.4	14.1
dp3	18.6	17.3	17.3	20.0	15.1	17.1	19.0	18.8	20.6	20.5
dp4	6.4	8.0	7.6	9.5	6.0	8.9	9.7	10.1	10.1	11.0
dp5	1.6	9.3	5.3	2.9	4.7	7.2	7.7	8.3	9.2	9.3
dp6	4.0	3.6	4.2	4.1	2.4	5.2	6.3	6.5	6.8	6.7
dp7	8.0	6.6	5.5	4.7	3.4	5.5	6.8	6.8	7.5	7.8
dp8	6.9	8.7	10.3	10.9	9.5	12.4	12.3	13.4	13.0	13.4
dp9	9.3	9.1	8.2	8.2	6.4	8.6	9.6	9.9	10.4	10.7

Table 31: CFD-calculated BFBT single-phase pressure drop spacer grid loss coefficients

BFBT case ID p700##	**27**	**28**	**29**	**30**	**31**	**32**	**33**	**34**	**35**	**36**
dp1	1.260	1.243	1.223	1.196	1.193	1.188	1.179	1.172	1.174	1.165
dp2	1.264	1.238	1.217	1.196	1.196	1.197	1.186	1.182	1.169	1.173
dp3	1.274	1.253	1.233	1.204	1.211	1.204	1.182	1.170	1.171	1.164
dp4	1.275	1.250	1.228	1.205	1.211	1.214	1.192	1.182	1.167	1.176
dp5	1.270	1.243	1.229	1.197	1.211	1.205	1.184	1.174	1.175	1.169
dp6	1.273	1.256	1.229	1.203	1.205	1.207	1.192	1.180	1.171	1.166
dp7	1.275	1.253	1.232	1.204	1.215	1.209	1.194	1.182	1.176	1.175
dp8	1.389	1.363	1.342	1.310	1.322	1.332	1.286	1.288	1.261	1.262
dp9	1.285	1.262	1.242	1.214	1.224	1.222	1.199	1.190	1.182	1.181
velocity [m/s]	0.796	0.976	1.168	1.360	1.556	1.748	2.156	2.340	2.540	2.740

There is a slight overall trend of decreasing spacer grid loss coefficient with increasing flow rate, which is not expected due to the flow-independence of the loss coefficient term. Other improvements to better the match between the CFD and experimental data could be to fine-tune the roughness model parameters within STAR-CCM+.

The relative root mean square error results from CTF are derived from comparison with experimental data, and the same is done for results from CFD, and these are shown in Table 32. This comparison shows the differences in how well the codes are able to predict the experimental pressures.

Table 32: Relative root mean square error comparison of CTF and CFD results for BFBT single-phase pressure predictions

Pressure tap span	CTF rRMSE (%)	CFD rRMSE (%)
dp1	6.8	22.0
dp2	3.3	12.2
dp3	7.5	18.5
dp4	10.0	8.9
dp5	8.1	7.1
dp6	6.6	5.2
dp7	5.2	6.4
dp8	1.6	11.3
dp9	3.9	9.1

Grid Convergence Index (GCI) Study

A grid convergence study is performed to analyze the effect of the mesh cell distribution and construction on the quantities of interest from the CFD simulations. Following the method proposed by Roache (1994) [69], a Grid Convergence Index (GCI) is calculated. This index is used to assess whether the volumetric meshes utilized in this research allow for results in the asymptotic region of convergence.

This method employs a form of Richardson Extrapolation [70] to obtain an approximation for the exact solution. Richardson Extrapolation involves the calculation of discrete solutions, f_i, calculated at a certain grid spacing, h_i, to extrapolate to find the exact solution. With solutions from a fine grid, denoted by $i = 1$, and a coarse grid, $i = 2$, the exact solution, f_{exact}, is calculated using Equation (93).

$$f_{exact} \approx f_1 + \left[\frac{f_1 - f_2}{r^p - 1}\right] \tag{95}$$

The grid refinement ratio, r, is defined as the ratio between the fine and coarse grid spacing as shown in Equation (96). This ratio is greater than 1.0 as the spacing of the coarse grid is larger than the spacing between fine mesh cells.

$$r = \frac{h_2}{h_1} \tag{96}$$

The calculated order of convergence, p, is obtained using Equation (97).

$$p = \frac{\ln\left(\varepsilon_{32}/\varepsilon_{21}\right)}{\ln\left(2\right)} \tag{97}$$

The error estimate terms, ε_{32} and ε_{21}, refer to the absolute differences in solution at each grid refinement, as given in Equation (98).

$$\begin{aligned} \varepsilon_{32} &= f_3 - f_2 \\ \varepsilon_{21} &= f_2 - f_1 \end{aligned} \tag{98}$$

The convergence ratio, R, is defined by the errors of consecutive grid spacing, as given in Equation (99).

$$R = \frac{\varepsilon_{21}}{\varepsilon_{32}} \tag{99}$$

Roache [69] proposes Equation (100) to account for an effective grid refinement ratio, r_{eff}, when multi-dimensional unstructured meshes are utilized.

$$r \approx r_{eff} = \left(N_1/N_2\right)^{1/D} \tag{100}$$

In Equation (100), N_1 is the number of mesh cells in the fine mesh model and N_2 is the number of mesh cells in the coarse mesh model, and D is the number of dimensions, which is three in this research. This approach is used for unstructured meshes which cannot have their refinement ratios quantified more conveniently due to their irregular mesh distribution in place of a structured and more linearly-based mesh spacing.

A factor of safety is introduced by Roache [69] to produce a measure of the grid convergence result in the same manner as a range given by a standard deviation. For studies which contain fewer than three different grid refinement levels, a more conservative factor of 3.0 is recommended, while for studies with three or more grid levels, a factor of 1.25 can be used. Using this factor of safety, F_s, the GCI value can be calculated as shown in Equation (101).

$$GCI_{12} = F_s \frac{f_1 - f_2}{f_1(r^p - 1)} \tag{101}$$

This calculated value of the GCI is used to provide a reference for the effect of grid refinement on resulting parameters, and can be applied over various modelling methods, such as the number of spatial dimensions. For the calculations in this research, three-dimensional unstructured meshes are utilized. A different value of the GCI can be calculated for any two grid refinement levels. For example, it would be typical to report GCI_{12} and GCI_{23} in terms of percentage to show the difference in stepping from the coarse mesh to the medium mesh (GCI_{23}), compared with the change from the medium mesh spacing to the fine mesh (GCI_{12}).

The result of the GCI calculation provides an approximation to the exact solution, f_{exact}, with an error band equal to the GCI (in percentage) for the considered grid meshes. The solutions are considered to be within the asymptotic range of convergence when compared with the results of Equation (102).

$$GCI_{23} \approx r^p GCI_{13} \tag{102}$$

The effect of changing the polyhedral mesh base size is examined on the effects of the CFD-calculated pressure drop and heat transfer coefficient. The prism layer mesh is held constant while the polyhedral base size is altered between three values; 0.4, 0.5, and 0.6 mm. The details for the prism layer are:

- 1.00 mm total thickness

- 18 prism layers
- 1.4 grid spacing ratio

With these prism layer parameters and the typical LWR single-phase conditions utilized in this work, the first cell y^+ value comes out to be $y^+ \approx 1.0$. This is due to the fact that the first prism layer will have its centerpoint a distance of 5.0E-7 m from the walls, while the required distance for $y^+ = 1.0$ under LWR conditions is approximately 5.3E-7 m. This calculated value takes the fluid parameters and local velocity into account. 18 layers were calculated to be sufficient to hold this spacing to the first cell with a grid stretching ratio of 1.40 in the radial direction. Keeping the prism mesh constant ensures that the same wall treatment functions are used within STAR-CCM+ to resolve parameters in this region.

The pressures were extracted from a PSBT MVG 2x2 subchannel layout CFD simulation performed at each of the three base mesh sizes. The simulations were run at the nominal conditions for the pressure loss coefficient calculations; namely at 15.5 MPa, 5.0 m/s inlet velocity, and 300 C inlet temperature, with 800 kW/m^2 heat flux at the rod surfaces. The number of mesh cells for each case are shown in Table 33.

Table 33: GCI calculation mesh cell counts by base mesh size

ID	Base mesh	Number of mesh cells
N1	0.40 mm	10080313
N2	0.50 mm	7269530
N3	0.60 mm	5188800

With these mesh cell counts, the effective grid refinement ratio can be calculated using Equation (100) with $D = 3$:

$$r_{eff} = \left(\frac{10080313}{7269530}\right)^{\frac{1}{3}} = 1.12$$

As was performed with the spacer grid loss coefficient calculations earlier in this chapter, the pressure drops are taken on either side of the spacer grid in order to calculate the form pressure loss. Table 34 shows the results from each of the three base mesh sizes, with the quantity of interest, f_n, as the pressure drop due to the form loss over the PSBT MVG spacer grid. The difference from the extrapolated value of the exact solution for the pressure drop gives the error terms of the last two columns, indicating that the 0.40 mm solution is within 9.1% of the exact solution with a factor of safety of 1.25 applied.

Table 34: GCI calculation results from the pressure drop study with varied base mesh size

f_1 dP [Pa]	f_2 dP [Pa]	f_3 dP [Pa]	r	F_s	p	f_{exact} [Pa]	GCI_{12} [%]	GCI_{23} [%]
15694.7	15973.5	16320.1	1.12	1.25	1.9970	14548.0	9.1	11.2

As the rods had a surface heat flux condition, it was also possible to extract the local heat transfer coefficient from the CFD simulations for each of the base mesh sizes. The values for the local HTC do not, however, show any meaningful change in magnitude, indicating that this parameter is dependent nearly entirely upon the prism mesh, which was unchanged for this study.

Summary and Conclusions

A CFD-informed model for spacer grid loss coefficient evaluation to be used in CTF is developed and tested. CFD simulations of the PSBT A1 bundle spacer grids in 5x5 rod (6x6 subchannel) geometry were utilized to produce pressure loss coefficients which combine the effects of the spacer grid's geometric drag and its surface drag.

A base mesh size of 0.5 mm was selected based on computational costs and favorable comparison with results of finer mesh sizes. Results from the full-scale PSBT 01-5343 test case show spacer grid loss coefficients consistent with those calculated from the single-grid span CFD simulations.

Supplying CTF with the CFD-derived loss coefficients produces pressure results which are close to the pressure drops predicted by STAR-CCM+. There are small differences in both the pressure loss predictions due to form losses and due to frictional losses between the CFD and CTF simulations. Ideally, a study into these effects could expose why there is a small disparity in the predicted frictional and form losses between the two codes.

While separating the effects of the spacer grid into individual loss coefficients for subchannels based on geometry is beneficial plan, it poses challenges for modelling. Performing CFD simulations of singular subchannels such as those present in the MVG geometry is a difficult task due to the issue of the mixing vane-driven cross-flow boundary conditions. The other PSBT grids, the NMV and the SSG, could have their loss coefficients modelled individually but the applicability of this approach wanes as the PSBT simulations employ all three spacer grids in the experiments.

Another difference between CFD predictions and CTF predictions is the downstream behavior of the pressure drop. In CTF, the pressure drop is applied at a single axial node, and a difference between the node containing the spacer grid and the next node capture all of the pressure effects caused by the grid. CFD simulations show that in reality, the pressure profile does not instantly return to only frictional losses. There is an axial decay length of the spacer grid's effects on the pressure drop profile, and this decay length is affected by flow conditions as well as the spacer grid geometry.

Future work on the pressure loss coefficient includes examining the effects of surface roughness models on the spacer grid's form and frictional losses. Comparisons with other

relevant single-phase, LWR-geometry experiments with spacer grids would also enhance the validation of these CFD-driven predictions. These experiments must have clearly-defined spacer grid geometries and preferably use water as their working fluid.

Chapter 6

CFD-Informed Spacer Grid-Enhanced Heat Transfer Model in CTF

Introduction

In this chapter, a CFD-informed model for spacer grid-enhanced heat transfer to be used in CTF is developed and tested. In order to develop such a model, the effects of spacer grids on convective heat transfer in a rod bundle are examined. All spacer grids, especially those with flow-enhancing features such as mixing vanes, have an impact on downstream heat transfer from the bulk fluid to the rod surfaces. This extraction of heat from the rod surfaces is an important parameter in the nuclear reactor as it allows the coolant water to remain in its designed quality and state. PWR operating conditions set water near its boiling point at the top of the fuel assemblies through which it flows. As the surface temperatures of the nuclear fuel rods increase past the saturation temperature of the coolant, subcooled boiling may occur at certain locations. Insufficient heat transfer may lead to dry spots on the cladding surface and a further decrease in heat removal from the surface as the fluid's local void fraction increases. Spacer grids help homogenize flow and mix the bulk fluid with the fluid near the surfaces in order to lower the thermal gradient across the subchannel. Whether they are designed with mixing vanes or not, the axial acceleration as the flow passes through the constrained area caused by the grid straps benefits heat transfer. Mixing vanes aid further by moving cooler flow from the central region of the subchannels to the rod surfaces.

Background

A general calculation of the heat transfer coefficient (HTC) for convective heat transfer between a surface and a fluid is shown in Equation (103).

$$h = \frac{q''}{\Delta T} = \frac{q''}{T_{wall} - T_{bulk}} \tag{103}$$

In Equation (103), q'' is the heat flux from the surface to the fluid, T_{wall} is the temperature of the fluid at the wall, and T_{bulk} is the temperature of the fluid at a distance away from the wall. The definition of the heat flux and wall temperature values are not ambiguous, which means that the calculation of the HTC depends strongly on the choice of the bulk fluid temperature. For example, the bulk temperature in a subchannel code may be considered as the volume-averaged temperature of the fluid between axial nodes.

Dimensionless Parameters

Dimensionless or similarity parameters are used within fluid mechanics to quantify flow characteristics in a method which can be compared through scaling. Even with differing fluid properties and flow geometries, similar Reynolds numbers of the flows indicate similar flow patterns which could cause the flows to fall under the same applicability ranges of Reynolds number-based correlations. Examples of these dimensionless quantities often encountered in heat transfer calculations are the Nusselt, the Reynolds, and the Prandtl number.

Nusselt number

The Nusselt number, used for relating the conductive and convective heat transfer, can be expressed by Equation (104).

$$Nu = \frac{hD_h}{k} \tag{104}$$

The Nusselt number is a defining characteristic of the thermal boundary layer

[61]. There are methods of relating the Nusselt number to other flow similarity parameters such as the Reynolds number and the Prandtl number.

$$Nu = f(Re,Pr) \tag{105}$$

A relationship for convective heat transfer is the Dittus-Boelter correlation [6]. This correlation, applicable to turbulent flow regimes with Reynolds numbers greater than 10,000 [63], relates the Nusselt number to the Reynolds and Prandtl numbers. This correlation is intended for smooth surfaces as does not account for a friction factor due to surface roughness.

$$Nu = 0.023(Re)^{0.8}(Pr)^{0.4} \tag{106}$$

In this work, the exponent for the Prandtl number term is equal to 0.4 as this research considers heated rods which have higher surface temperature values than the bulk fluid temperatures. If the fluid were at a higher temperature than the surfaces, then an exponent of 0.3 is recommended to account for the fluid cooling effect [54].

Reynolds number

The Reynolds number is a ratio of inertial to viscous forces and is typically used as a main parameter for determining whether a flow is laminar or turbulent. Viscosity, density, and velocity have effects on the calculated value of the Reynolds number, as is shown in Equation (107).

$$Re = \frac{\rho V D_h}{\mu} \tag{107}$$

Above a certain Reynolds number, flow is generally considered to be in the turbulent regime. Flows through the fuel assemblies of an LWR have a Reynolds number on the order of

5e6, which is well in the turbulent region based on the Reynolds number alone. As there can be cases where flow conditions reach the laminar-turbulent interface, codes need to be able to properly resolve flow parameters at that junction.

Prandtl number

The Prandtl number, which has no length scale, is a measure of the fluid's momentum diffusion rate compared to its energy diffusion rate as shown in Equation (108).

$$Pr = \frac{c_p \mu}{k} \tag{108}$$

A fluid with a high thermal conductivity, such as a liquid metal, will have a low Prandtl number indicating its energy diffusion is strong and its thermal boundary layer is large in comparison to its momentum boundary layer. As the simulations in this research are single-phase water at PWR conditions, the variation in its properties are not large. Therefore, the ratio between the thermal and momentum boundary layer thicknesses is not largely altered, but it is changed enough to have an effect on the heat transfer coefficient.

CTF solves for the heat transfer coefficient, h, by using the user-defined heat flux at the rod surface and the Dittus-Boelter correlation, Equation (17) as well as the definition of the Nusselt number, Equation (104). As previously shown, the Nusselt number is calculated from the CTF fluidcell velocity and fluid parameters and is updated each iteration. The heat transfer coefficient is used during a system of equations solve to determine the wall temperature of the fluid. CTF's process of solving for HTC parameters is detailed in Chapter 3.

In CTF simulations, the calculated bulk fluid temperature of the subchannel remains the same with constant boundary conditions, as neither the heat flux from the rods nor the bulk flow rate of the fluid is affected by elevated heat transfer coefficients in single-phase calculations. The

effects of increased convective heat transfer result in a smaller difference in the bulk and surface temperatures of the fluid.

Consider how the Yao-Hochreiter-Leech (YHL) model is currently used within CTF to predict the change in heat transfer caused by a spacer grid. The YHL formula is used to calculate an enhanced heat transfer due to the effect of a grid, which is applied to the CTF energy equation. The YHL correlation is a function of the projected area of the grid, the vane angle, and the distance downstream of the grid. The correlation was developed from experimental data involving a collection of different grid types used in varying operating conditions. The correlation augments the dimensionless Nusselt number, which can be calculated by CTF. This allows for the application of the heat transfer enhancement model in a variety of different conditions. The original correlation, as it appears as a multiplier in CTF [1], is shown in Equation (109).

$$\frac{Nu}{Nu_0} = \left[1 + 5.55\epsilon^2 \exp\left[-0.13\frac{z}{D}\right]\right]\left[1 + A^2 \tan^2(\Phi) \exp\left[-0.034\frac{z}{D}\right]\right] \quad (109)$$

In Equation (109), the subscript 0 on the Nusselt number refers to the bare subchannel geometry (no grid present) and the ratio is presented as a product of two terms. The first term contains the blockage ratio, ϵ, as well as a dimensionless downstream distance, $\frac{z}{D}$. The second term accounts for the projected area of the grid onto the subchannel, A, the mixing vane angle, Φ, and the downstream non-dimensionalized distance, z/D, as well. CTF stops applying this YHL-calculated multiplicative factor after the effects are less than 1% of the nominal HTC.

Shortcomings of the YHL implementation within CTF are that all subchannels in the simulation must receive the same treatment, i.e. there can be no blockage ratios or vane angles specified on a subchannel-by-subchannel basis. Axial levels, however, may be calculated separately to allow for multiple geometries of spacer grids located axially along the domain. It would be preferable to give the users the ability to independently control each subchannel's

enhanced heat transfer model using information from spacer grid simulations. CTF input does allow users to tune the parameters of Equation (109) by specifying coefficients as well as the blockage ratio and the vane angle.

Another area of potential improvement is that within CTF, the YHL model is applied at the node corresponding to the specification of the grid. Therefore, there is no accounting for the height of the grid or the behavior of the HTC within the grid span. The current model only provides a decay profile for downstream HTC enhancement. Some improvement to this model can be added with careful selection of axial nodes around the grid area in order to achieve better HTC prediction in the vicinity. This also requires knowledge of the height of the spacer grids used as well, if axial nodes are used to move the beginning of the YHL effect within the subchannel.

The YHL correlation recommended coefficients are shown in Equation (109) and are 5.55, 0.13, 0.34, and 0.4. Experimental and numerical studies have been performed to optimize the values of these coefficients, with Jaeger and Sanchez recommending the value of 0.13 be changed to a higher value, more on the order of 0.2 to 0.3. This decay coefficient change is recommended to allow for a better fit of the downstream distance over which the effects are noticed, which Jaeger and Sanchez state curtail the original YHL model by approximately 10-20 hydraulic diameters to better match their experimental and CFD results [14].

Another model for the Nusselt number multiplier caused by spacer grids is presented by Holloway et al as a function of the spacer grid's blockage ratio [13]. This can capture the effect of the mixing vanes, as the vanes themselves generally account for a large portion of the grid's flow blockage. Equation (110) shows the model of Holloway et al.

$$\frac{Nu_{avg}}{Nu_{fd}} = 1 + (0.8K_g - 0.4)e^{\frac{-0.25z}{D_h}} \tag{110}$$

In Equation (110), K_g is the blockage ratio of the spacer grid measured perpendicular to the bulk fluid flow direction. In similar fashion to the YHL correlation, this model provides a downstream decay from an initial peak value which is determined from spacer grid geometry. The main difference from the YHL correlation is that there is no separate portion for the treatment of mixing vanes; all effects are based upon the blockage ratio.

As shown by the dependence of the Yao-Hochreiter-Leech correlation and the Holloway et al heat transfer enhancement correlation, the magnitude of heat transfer depends strongly on the spacer grid's blockage ratio. Therefore, heat transfer enhancement often comes at the sacrifice of pressure drop through the reactor.

In order to improve the subchannel code CTF's predictions of heat transfer coefficients, CFD simulations can be utilized to analyze the behavior of heat transfer near the spacer grid locations. The simulations are able to show the variations in the heat transfer coefficient caused by the grids. From the results, a multiplier can be derived which compares the gridded bundle HTC value to the HTC value of an equivalent but ungridded (bare) bundle. This multiplier will be applied to the HTC value in the same manner as another CTF model, the Yao-Hochreiter-Leech model [20]. The bare bundle case is used as a reference for the HTC deviations when grids are in place. The ratio of the gridded simulation to the bare bundle simulation is used as a multiplier. The definition of this ratio is shown in Equation (111).

$$f_{HTC} = \frac{HTC_{gridded}}{HTC_{bare}} \tag{111}$$

For application in CTF, the HTC enhancements will be broken down on a surface-by-surface basis, which is the best resolution for heat transfer available in CTF. Currently, the YHL correlation is applied evenly to all surfaces at the current axial level, so this geometric sharpening would allow for more realistic representation of spacer grid effects laterally across the rod bundle.

The Nusselt number multiplier is calculated and plotted in Figure 76 and Figure 77 for both the YHL correlation and the Hollow et al correlation. The spacer grid in Figure 76 is assumed to have a blockage ratio of 0.45 with mixing vanes contributing 0.21 of that total, and a pressure loss coefficient of 1.7. Its mixing vanes are angled at 28 degrees from the flow direction, the same as the PSBT MVG spacer grid's vane angle. The spacer grid in Figure 77 is assumed to be the same spacer grid as in Figure 76, but without the mixing vanes, and its blockage ratio and pressure loss coefficient are therefore lower at 0.24 and 1.10, respectively. This blockage ratio is calculated by using the other spacer grid's total blockage less the blockage caused by its vanes.

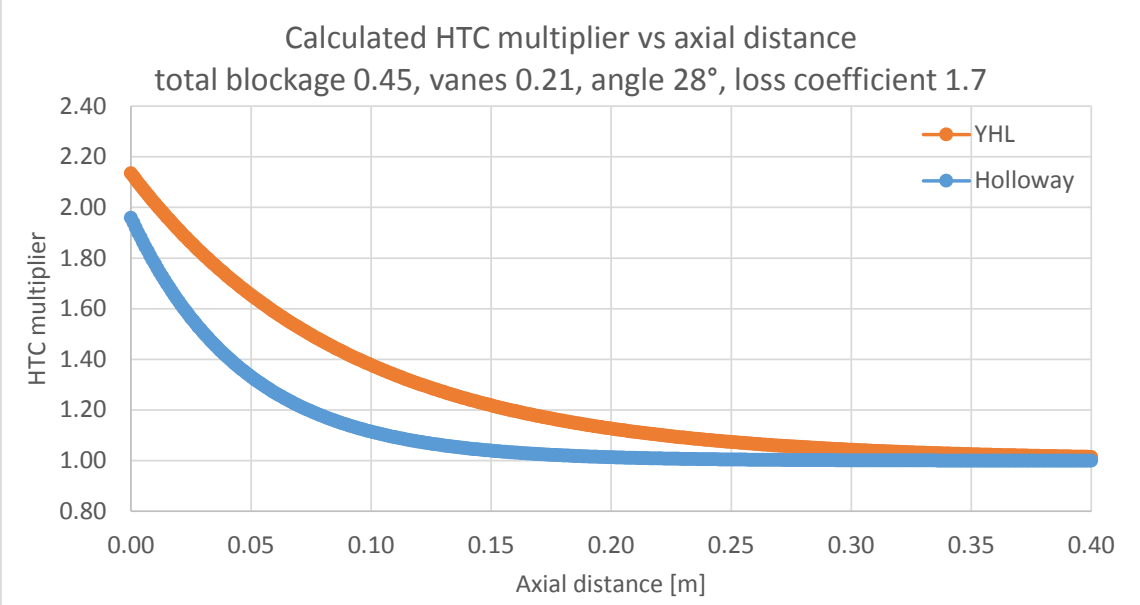

Figure 76: Nusselt number (HTC) multipliers calculated by the Yao-Hochreiter-Leech correlation and the Holloway et al correlation for a spacer grid with mixing vanes

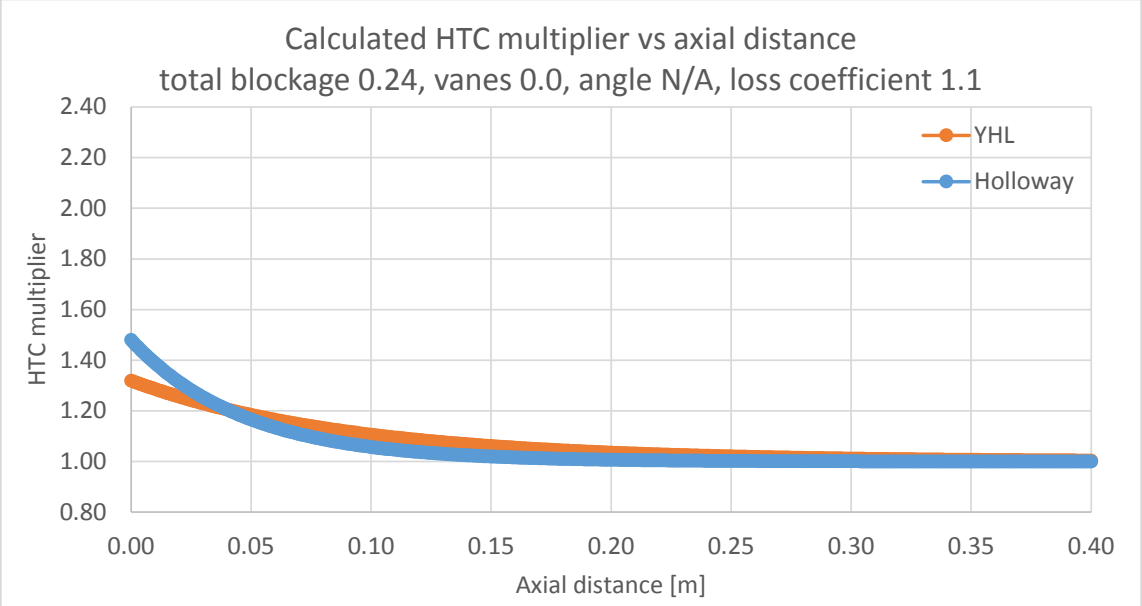

Figure 77: Nusselt number (HTC) multipliers calculated by the Yao-Hochreiter-Leech correlation and the Holloway et al correlation for a spacer grid with no mixing vanes

Figure 76 shows that the Holloway et al model predicts a steeper decline in the Nusselt number multiplier after the spacer grid's location. The YHL correlation's effects last farther downstream and are also predicted to be of a higher magnitude for the spacer grid with vanes, 2.15 to 1.95 as the Nusselt number multipliers. Figure 77, which predicts the Nusselt number multiplier for a spacer grid with no mixing vanes, shows that the Holloway et al model actually predicts a higher initial peak magnitude of the HTC ratio, but once again decays more quickly than the YHL model. The magnitudes of the HTC multiplier's initial value are again closer together for the case with no spacer grid, 1.50 for the Holloway et al prediction to 1.32 for the YHL correlation.

Accounting for the effects of spacer grid mixing vanes causes disparity in the results. These correlations also do not take the geometry type of the vanes into consideration. For example, a typical BWR spacer grid with vanes may create intra-channel swirling patterns which affect the surfaces of the rods within a subchannel almost evenly. A PWR meandering flow

pattern caused by rotated orientations of mixing vanes causes much more crossflow than the BWR's swirling vanes, and its effects on surface heat transfer will also change much more within the subchannel as the effects are not azimuthally symmetric.

Heat transfer coefficient factor calculations

For this chapter, the relevant results from the CFD simulations are the local heat transfer coefficient predictions. The local HTC is a post-processing option for STAR-CCM+ which calculates a reference temperature for each surface location at which the HTC is desired. A similar option for HTC values is the standard STAR-CCM+ heat transfer coefficient, which utilizes a constant user-supplied reference temperature in its determination of the convective HTC at all locations.

The results from the bare (un-gridded) 2x2 subchannel simulations are split into four surfaces azimuthally per full rod circumference, at 90° sections apiece corresponding to the subchannel in which they lie. These surfaces are labelled in Figure 78 for a 2x2 subchannel geometry, which shows four rod surfaces attached to each of the four subchannels. This numbering scheme is consistent with the one used within CTF to identify surfaces.

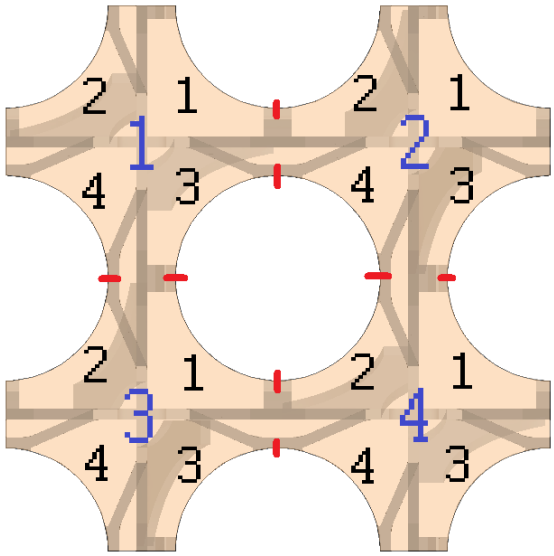

Figure 78: Numbering for the rod surfaces by subchannel, following CTF's numbering scheme on a 2x2 subchannel layout

These surfaces then have their CFD-calculated local HTC results averaged every 2.0 mm axially, so that the results are a function of surface location as well as axial location within the CFD simulation. 2 mm spacing was selected as it is finer than most CTF simulations and can effectively capture the effects of the HTC variation within the spacer grid's strap length. The PSBT spacer grids range in height from 12.8 mm for the SSG to 63.6 mm for the MVG.

A control case is simulated with the same flow conditions, meshing configuration, and geometry, albeit without the spacer grid in place. This bare simulation provides the knowledge of STAR-CCM+'s calculation of the local HTC in the event that no spacer grid is encountered by the flow.

CFD model description

The CFD models used for the heat transfer enhancement study are detailed in Table 35. The 2x2 subchannel layout is utilized with periodic boundary conditions. The spacer grid's

leading edge is placed at 80 mm from the flow inlet plane, and the outlet is 500 mm more downstream from that location. Each of the three PSBT spacer grid geometries was modelled in addition to the bare (un-gridded) subchannel layout. Each of the rod surfaces in the CFD simulation is set with heat flux thermal wall conditions. The heat flux starts axially 55 mm before the spacer grid leading edge location, which provides a short adiabatic region to allow the flow to develop and provide a buffer for the temperature boundary condition at the flow inlet.

Table 35: Details of the CFD 2x2 HTC simulations

Geometry details	
Subchannel layout	4 subchannels, connected via interface along their gaps
Domain length	580 mm (including extruded inlet region)
Grid leading edge axial location	80 mm
Mesh details	
Models	Polyhedral mesher Prism layer mesher Extruder Surface remesher
Base size	0.5 mm
Prism layer details	10 layers at 1.2 spacing, 1.0 mm thickness
Extruder details	120 mm extrusion from inlet, 120 layers at 1.00 spacing
Volumetric control	100 mm axially of finer polyhedral base size, 0.3 mm
Volumetric control axial range	70 mm to 170 mm (starts 10 mm upstream of grid)
Flow conditions	
Inlet temperature	300 C
Inlet mass flux	1.276 kg/s
Pressure	15.5 MPa
Boundary conditions	
Rods	Wall-type, smooth, heat flux
Heat flux	800 kW/m^2
Outer flow boundaries (walls)	Wall-type, smooth, adiabatic
Gaps	Connected via periodic interfaces
Inlet	Mass flux inlet
Outlet	Pressure outlet
Physics details	
Models	Liquid Steady Three dimensional Reynolds-averaged Navier-Stokes Turbulent Realizable K-epsilon turbulence Two-layer all y+ wall treatment Exact wall distance Segregated flow Segregated fluid enthalpy User-defined equations of state (Defined in Equation (45) - (47))

The prism mesh spacing of 1.20 was selected to allow for smaller values of y^+ at the areas near the wall, where the heat transfer surface is considered. The overall prism layer thickness is set to 1.0 mm with 10 layers. Figure 79 shows the 10 prism layers with a spacing

factor of 1.05, starting from the rod surface at the left and moving towards the polyhedral volume mesh at the right. This small spacing factor creates layers which do not grow much in thickness as the distance from the wall increases. The very near-wall effects are captured on a coarser scale than those when the prism spacing is 1.20 or 1.50, as shown in Figure 80 and Figure 81, respectively. Placing more mesh layers inside of the viscous sublayer theoretically improves accuracy of the predictions, though in practice the treatment of the near-wall calculations in the CFD code has a larger impact. The grid convergence study performed earlier in this research indicated that 18 layers are required within the 1.00 mm prism layer thickness to place y^+ equal to 1.0, but the spacing suggested here will place this value close to 5.0. As the all y^+ wall treatment in STAR-CCM+ is enabled, each of these meshing densities is within the capability of the CFD code, but the results in near-surface parameters will vary.

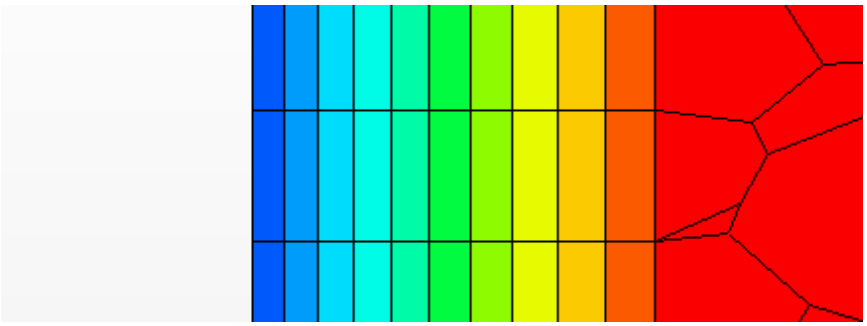

Figure 79: Near-wall prism mesh layers with a spacing ratio of 1.05

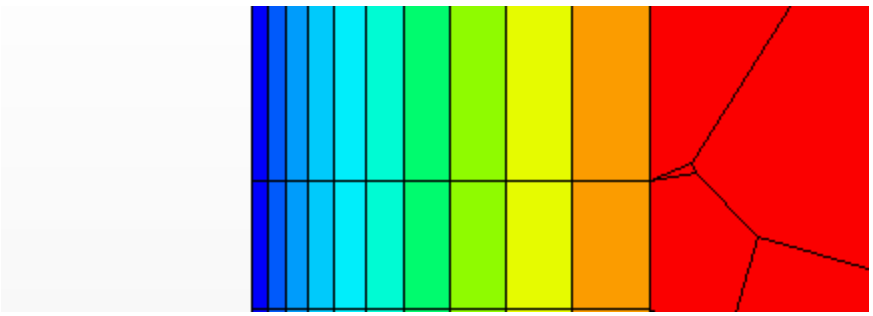

Figure 80: Near-wall prism mesh layers with a spacing ratio of 1.20

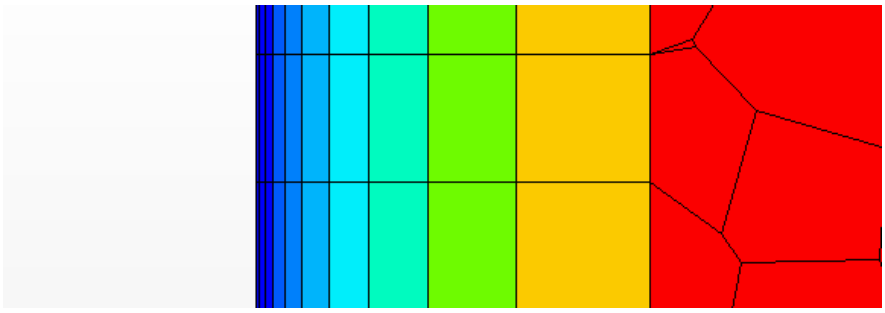

Figure 81: Near-wall prism mesh layers with a spacing ratio of 1.50

HTC multiplier results for the 2x2 CFD simulations

The CFD simulations, performed using the modelling parameters listed in Table 35, provided results for each of the three PSBT spacer grid geometries. The results were averaged every 2.0 mm axially for each of the 16 rod surface divisions in the geometry, as detailed in Figure 78. The bare 2x2 subchannel simulation results were used as the reference values for the local HTC calculated at each surface in order to generate HTC multipliers. These multipliers are then able to portray the amount of heat transfer at each surface in the 2x2 subchannel layout relative to the results from the un-gridded simulation.

Figure 82 shows the results for the PSBT MVG spacer grid 2x2 simulation's central rod. The surfaces of this rod correspond to surface 3 of subchannel 1, surface 4 of subchannel 2, surface 1 of subchannel 3, and surface 2 of subchannel 4 as shown in Figure 78. The variation in the downstream behavior is apparent at distances increase past the height of the spacer grid. Surfaces 3 and 2 are both adjacent to mixing vanes, and their local HTC profiles in the axial locations near the top of the spacer grid (near 0.15 m) are very similar. The same is true for

surfaces 4 and 1, which show similar behavior as the flow leaves the presence of the spacer grid's axial length.

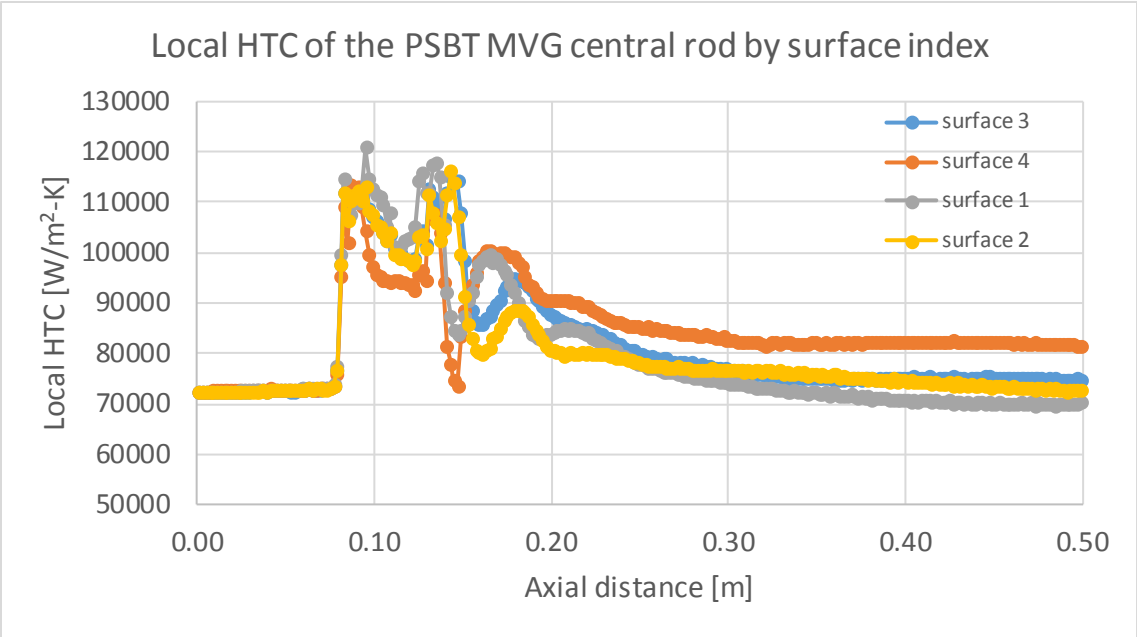

Figure 82: STAR-CCM+ predicted local HTC values of the central rod surfaces in the PSBT MVG 2x2 simulation

Within the spacer grid, the lowest local HTC value is that of surface 4, which contains two horizontal spacer grid dimples near its location. These act to cause wide local stagnation points near the surfaces due to the CFD model simplification of merging the springs and dimples into the rod surfaces. Though the flow is accelerated more near this surface due to the decreased flow area, the stagnation points have more of an effect on the predicted heat transfer.

The downstream profile shows that the heat transfer effects propagate at least 400 mm downstream of the spacer grid's leading edge. The decay from the peak magnitudes, however, occurs rather quickly in comparison to the spacing between the grids. The PSBT spacer grid spacing for Test Series 1 is close to 230 mm.

Figure 83 shows a closer look at the axial region in which the spacer grid lies, with a profile of the grid placed in the upper portion of the figure for help with visualization. The base of the grid, which lies at 0.08 m, shows the location where the flow area is initially compressed leading to a quick spike in velocity and, thereby, heat transfer. The top of the mixing vanes occurs about 65 mm later, near 0.15 m axially. At this location, the effects from the mixing vanes can be seen immediately on two surfaces, and then slightly further downstream at the other two surfaces as the directed flow makes its way across the subchannel.

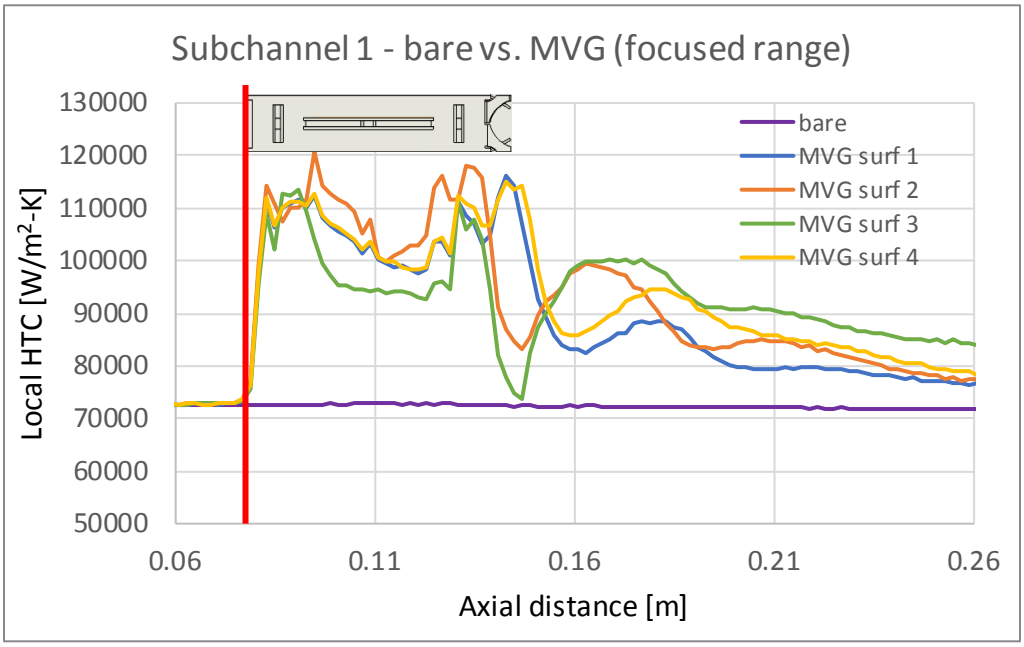

Figure 83: Zoomed axial region of the STAR-CCM+ local HTC predictions in subchannel 1 of the 2x2 simulations

The results for the local HTC for the PSBT NMV spacer grid are shown in Figure 84. These results are similar in peak magnitude to those of the MVG, which is consistent as the spacer grids are nearly identical until the mixing vanes. The STAR-CCM+ predictions for surface 1 of subchannel 3 shows a variation from the other three surfaces downstream of the spacer grid. Its decay is much more pronounced over a longer distance. Even with different mesh schemes,

this surface still showed this deviation in its HTC predictions. This is attributed to the lack of horizontally-aligned spacer grid dimples at this azimuthal location, which cause stagnation points and lower heat transfer at the other surfaces.

Figure 85 contains the HTC predictions for the PSBT SSG spacer grid. The profile is very similar for each of the four surfaces around the central rod in the 2x2 subchannel simulation. The peak magnitude is similar to that of the other PSBT spacer grids, but the effects last for a much shorter duration axially. The SSG is only 12.8 mm tall, which is less than half the height of the NMV or the MVG.

The STAR-CCM+ predicted local HTC values for the un-gridded, bare 2x2 subchannel simulation are shown in Figure 86. These values are utilized as the reference point for the simulation, and the HTC multiplier values are derived by using these as the comparison values. There is no apparent deviation from the linear trend in the results for the bare simulation. The fluid is heated, so the reference temperatures are slightly altered along the axial domain as heat is absorbed.

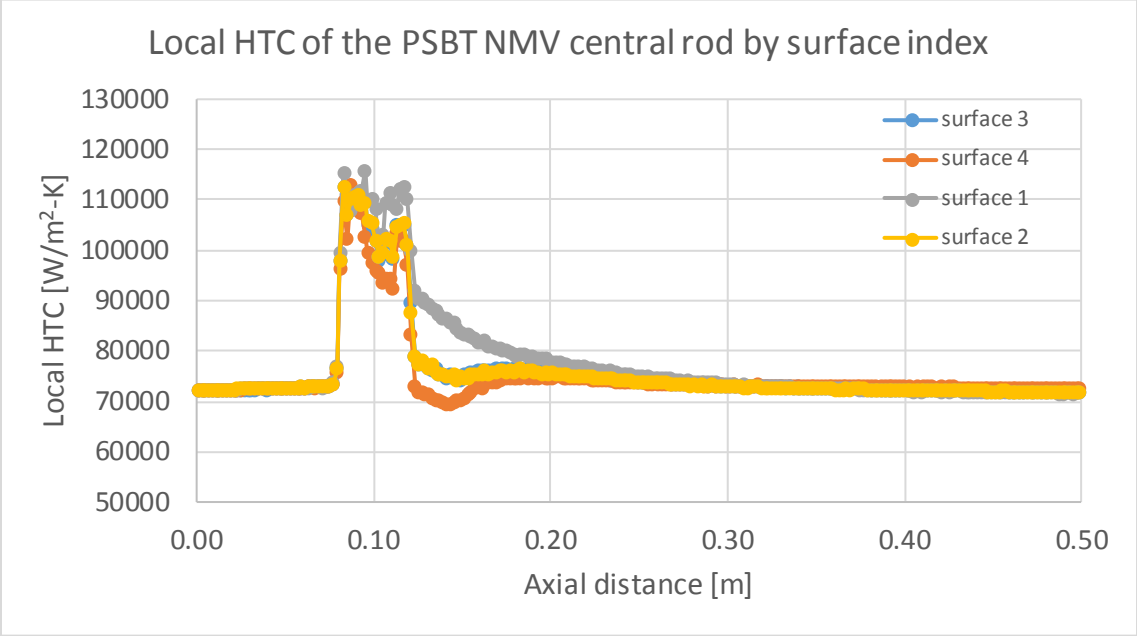

Figure 84: STAR-CCM+ predicted local HTC values of the central rod surfaces in the PSBT NMV 2x2 simulation

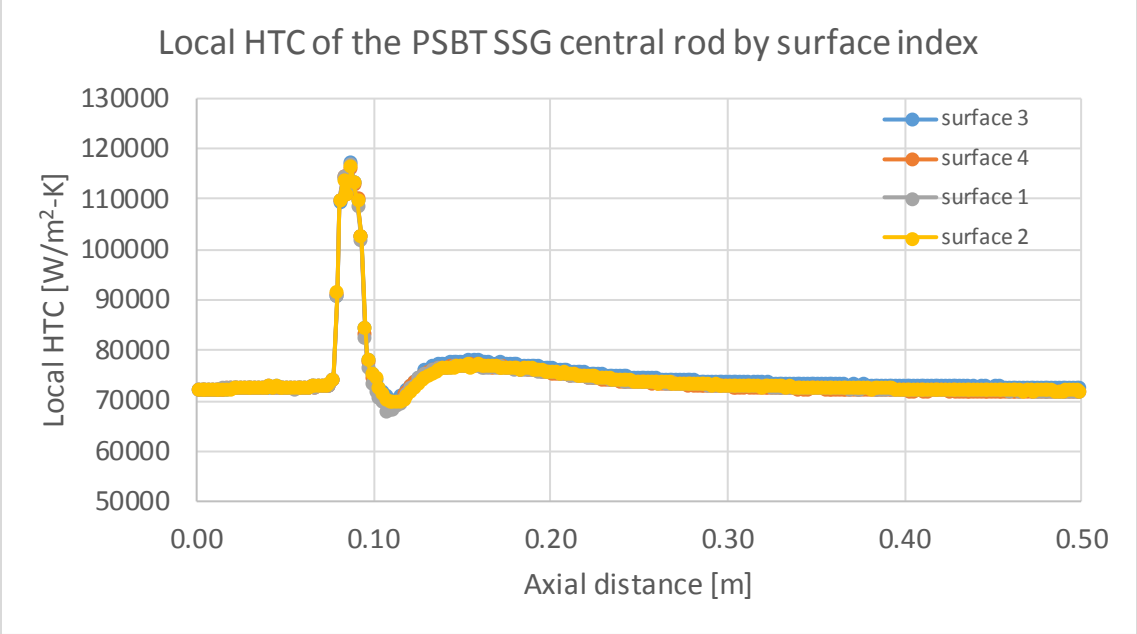

Figure 85: STAR-CCM+ predicted local HTC values of the central rod surfaces in the PSBT SSG 2x2 simulation

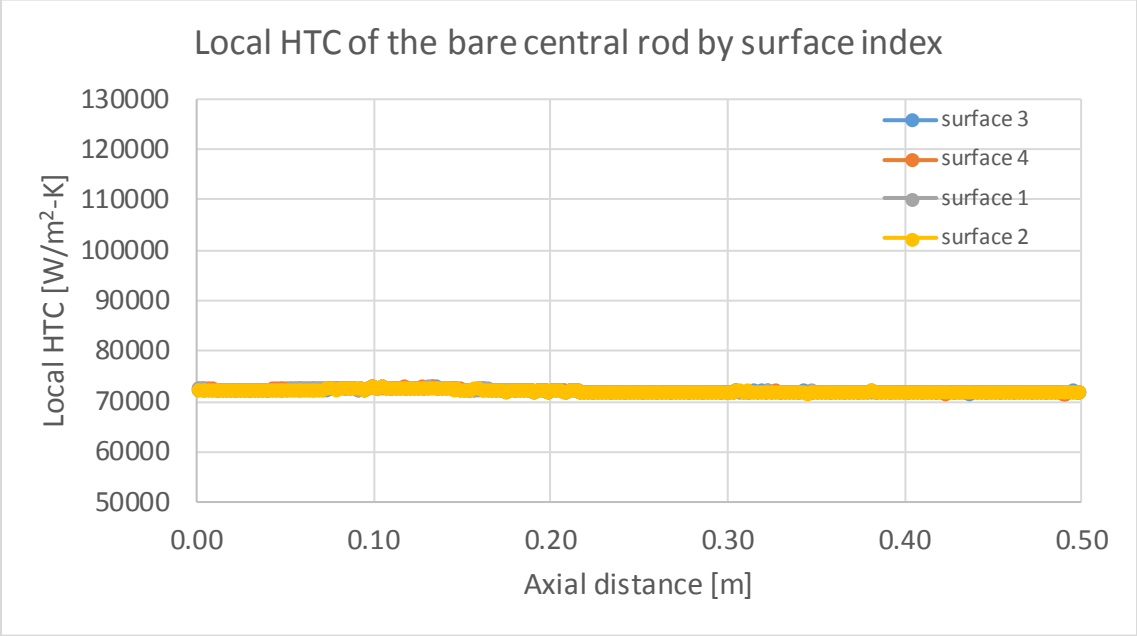

Figure 86: STAR-CCM+ predicted local HTC values of the central rod surfaces in the bare 2x2 simulation

The results of the HTC multiplier calculations, averaged over the entire domain at each axial location, are shown in Figure 87. The differences in the downstream decays are observable, with the MVG spacer grid causes the most enhancement after the spacer grid location. Both the NMV and the SSG reach a similar initial peak ratio as the MVG, close to 1.6, as this location is observed to occur at the spacer grid's leading edge in each case. This is the point where the flow undergoes the most abrupt change in axial motion due to the initial confinement.

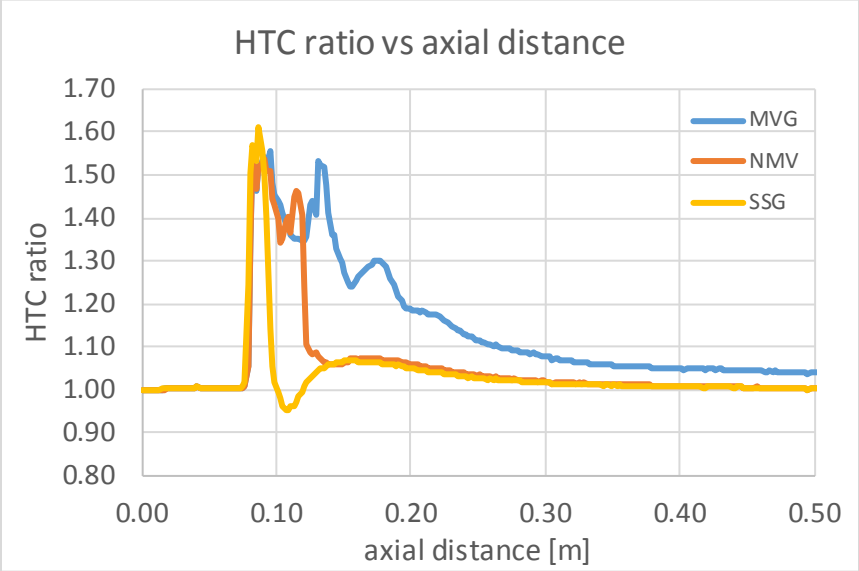

Figure 87: STAR-CCM+ predicted HTC multipliers for each of the PSBT spacer grid types

These HTC multipliers can be sorted by surface location, axial location, and grid type and be applied to a data-file for use in CTF simulations. The ability to enhance heat transfer from CFD simulation results affords a method for improving calculations without affecting runtimes.

The STAR-CCM+ predicted local HTC results are shown in Figure 88 for the MVG, corresponding to surface 3 and surface 1 on the central rod as numbered in Figure 78. The same parameter for surfaces 4 and 2 are presented in Figure 89. Both Figure 88 and Figure 89 are scaled to 15% of their axial lengths to improve readability, and the displayed local HTC results begin 40 mm before the spacer grid's leading edge. Overall, the PSBT MVG HTC predictions show an immediate increase as soon as the flow enters the axial region of the spacer grid, consistent with the constrained flow acceleration. The mixing-vane driven effects are clearly visible just downstream of the top of the MVG spacer grid. The pattern of counter-clockwise driven flows, as viewed from the top, around the central rod in the 2x2 subchannel simulation are apparent and are the main source in the differences between the four surfaces of the central rod. The regions far downstream of the spacer grid show some residual effects of the mixing vanes on

surface 1, with slightly lower predictions for this surface, and surface 1, with slightly higher than average downstream HTC predictions. On all of these local HTC figures, the color-scale for the STAR-CCM+ results is set from 50000 to 150000 W/m^2-K. The flow direction is from the left to the right in these figures.

Figure 90 shows an un-scaled region of the downstream mixing vane effects on the surface HTC values predicted by STAR-CCM+. These are surfaces 3 and 1 on the central rod as shown in Figure 78.

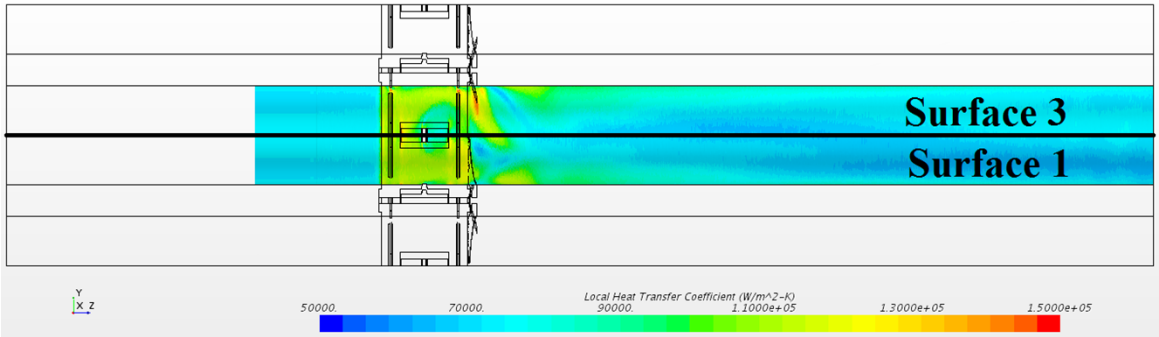

Figure 88: STAR-CCM+ local HTC predictions for the PSBT MVG central rod, surfaces 3 and 1 (15% scaled axially)

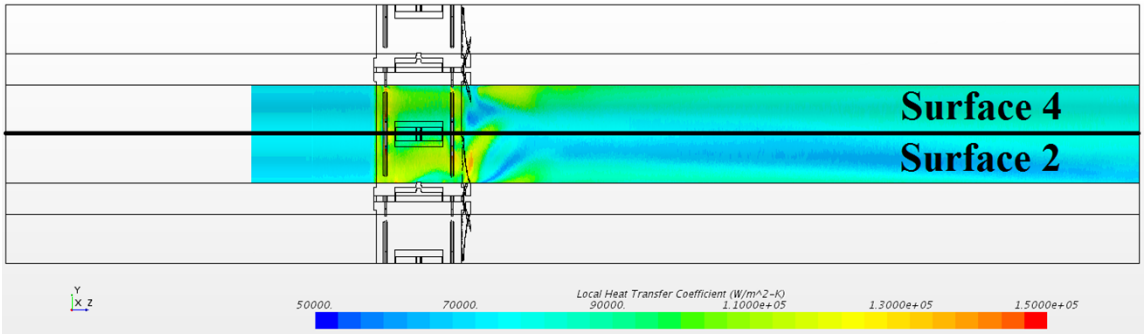

Figure 89: STAR-CCM+ local HTC predictions for the PSBT MVG central rod, surfaces 4 and 2 (15% scaled axially)

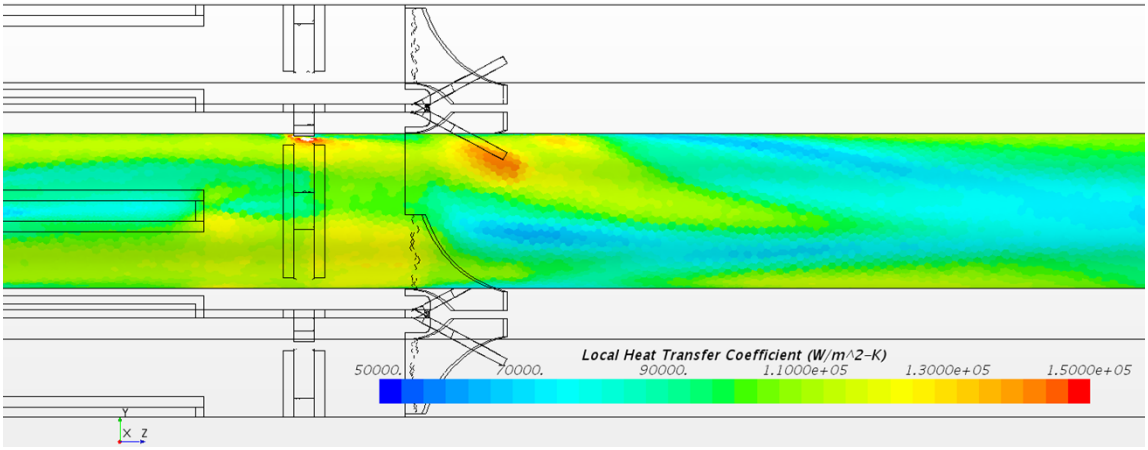

Figure 90: STAR-CCM+ local HTC predictions of the PSBT MVG central rod surfaces showing the mixing vane downstream pattern

Even within the surfaces, which each comprise 90° azimuthally of the central rod, there is large variation in the predicted HTC values near the mixing vane locations. However, without further division of the subchannels into smaller regions, the subchannel code CTF is unable to process data for the surfaces at any level smaller than these 90° surfaces. Therefore, the appropriate method is to supply averaged HTC multipliers at each axial level for the spacer grid of the simulation.

Figure 91 and Figure 92 show the local HTC predictions for the PSBT NMV spacer grid, scaled to 15% in the axial direction. From these images, it is apparent that the lack of mixing vanes results in a much more symmetric downstream heat transfer region. There are somewhat pronounced areas just downstream of the top of the spacer grid which show a decreased level of heat transfer. These spots are due to the upstream spacer grid features, which block some of the flow at the spring and dimple intersections with the central rod. The majority of the heat transfer enhancement due to the presence of the NMV is inside of the spacer grid region where the flow is accelerated in the axial direction.

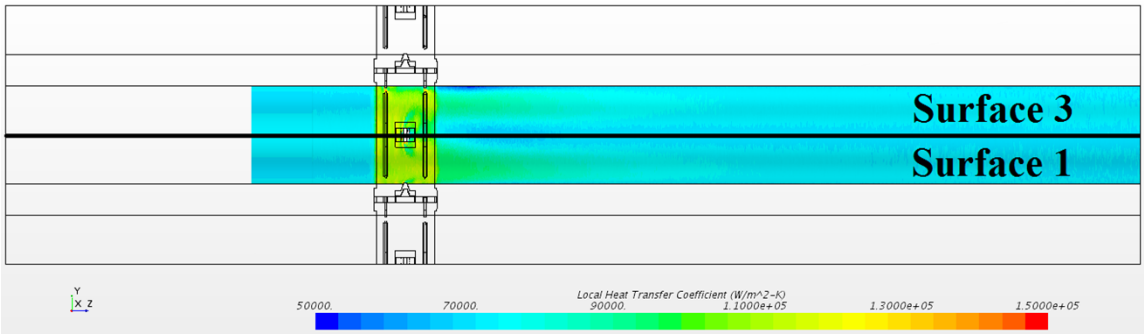

Figure 91: STAR-CCM+ local HTC predictions for the PSBT NMV central rod, surfaces 3 and 1 (15% scaled axially)

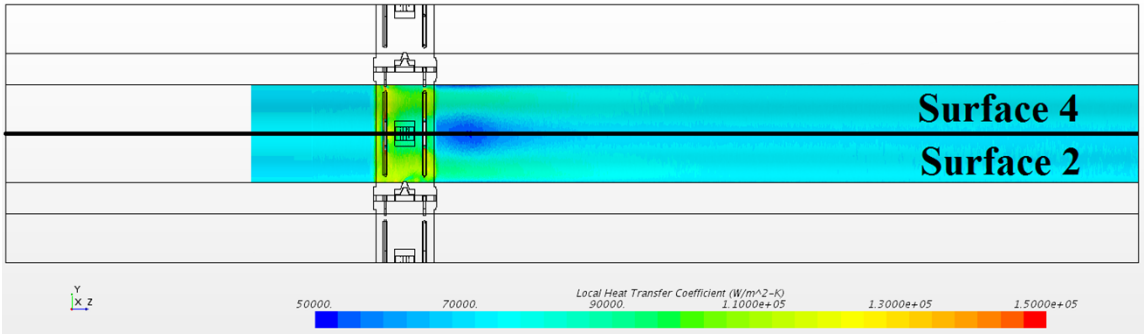

Figure 92: STAR-CCM+ local HTC predictions for the PSBT NMV central rod, surfaces 4 and 2 (15% scaled axially)

The STAR-CCM+ predicted local HTC values for the PSBT SSG spacer grid are shown in Figure 93 and Figure 94. Similar to the results of the NMV, the downstream effects of the spacer grid on the heat transfer coefficient are very small in comparison to those of the MVG. The absence of mixing vanes and a smaller spacer grid strap length for the SSG (12.8 mm) lead to a small axial region inside of the spacer grid where the flow velocity is elevated due to the physical constriction. Again, there are some regions downstream of the grid with lower-than-average HTC predictions due to the presence of the spacer grid dimple connections, which

partially block the flow upstream. The intensity of these decreased HTC regions fades with increased distance downstream of the spacer grid.

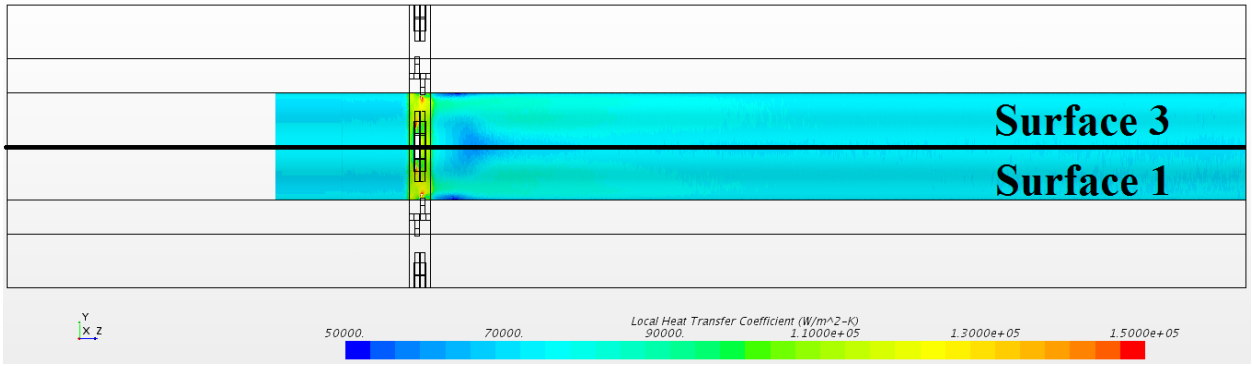

Figure 93: STAR-CCM+ local HTC predictions for the PSBT SSG central rod, surfaces 3 and 1 (15% scaled axially)

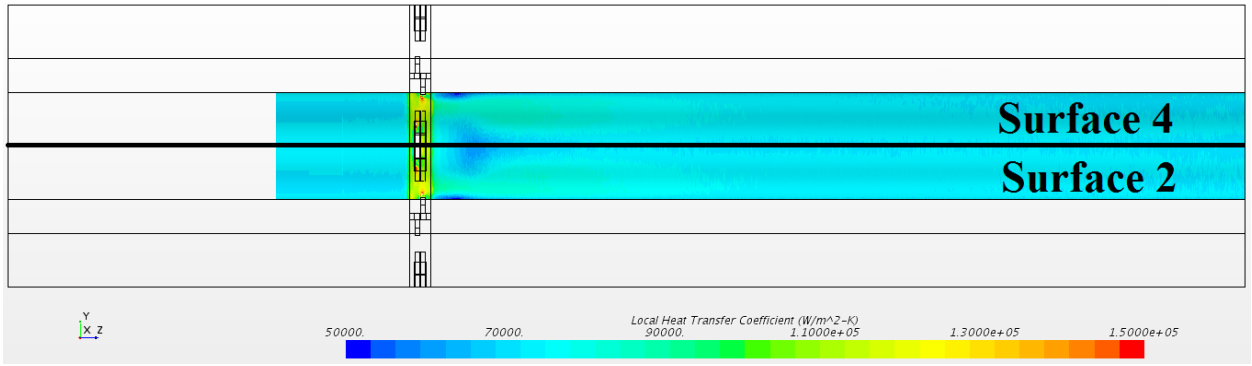

Figure 94: STAR-CCM+ local HTC predictions for the PSBT SSG central rod, surfaces 4 and 2 (15% scaled axially)

Comparing the results of the STAR-CCM+ 2x2 subchannel simulations for the HTC multiplier with those predicted by the Yao-Hochreiter-Leech correlation and by Hollow et al. (2008) reveals similarities in their downstream profiles. Figure 95 shows the comparison for the PSBT MVG results and the STAR-CCM+ predictions are smaller in magnitude but overall match

fairly well with those of the YHL correlation. The downstream distance of the decay is similar, and the magnitudes of both predictions past the top of the spacer grid are comparable.

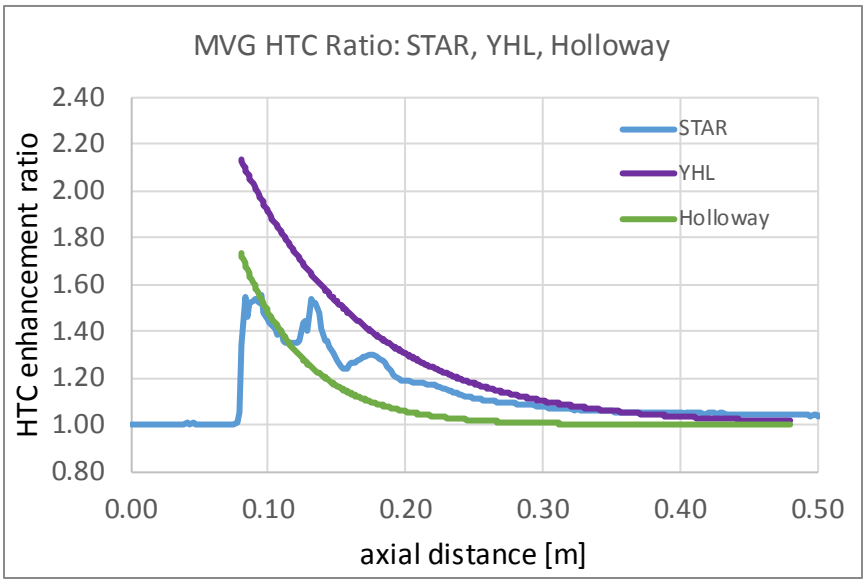

Figure 95: Comparison of HTC correlation predictions for the PSBT MVG spacer grid

Figure 96 shows the predicted HTC multipliers for the PSBT NMV, which has the same blockage ratio as the MVG without its mixing vanes. Therefore, the YHL correlation's vane component is removed and the magnitude of the YHL prediction is much more in line with those of the Holloway et al. prediction as well as STAR-CCM+ results. A main difference in these correlations and the STAR-CCM+ results is the downstream effects, where STAR-CCM+ predicts a very rapid return to the nominal heat transfer effects after the flow leaves the grid. A decay curve is observable from near 0.18 m to 0.40 m in the STAR-CCM+ predictions.

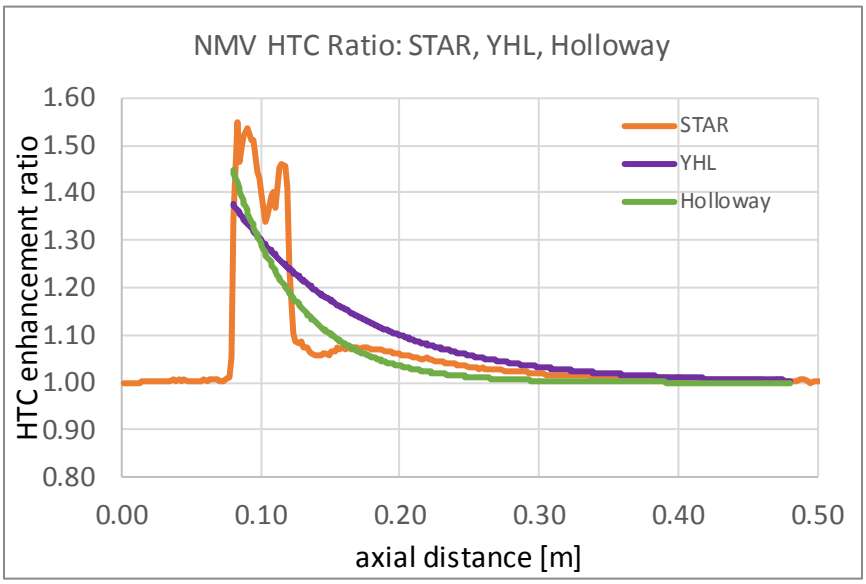

Figure 96: Comparison of HTC correlation predictions for the PSBT NMV spacer grid

HTC multiplier notes for full rod bundle geometry CFD simulations

The full 5x5 rod bundle CFD simulations allow for examination of the HTC predictions at surface locations within the PSBT bundle geometry. The previous 2x2 subchannel layout simulations contain four internal subchannels with symmetric rod surfaces and geometry. The full 5x5 rod bundle contains 36 subchannels of three main subchannel type geometries; internal, side, and corner. Figure 97 shows the types of these subchannels as well as the rod surfaces contained within each. Of the 100 rod surfaces considered in the simulation geometry, 4 are grouped as corner surfaces, 32 are side surfaces, and 64 are internal surfaces. The differences in heat transfer coefficients at the rod surfaces will be dictated by the flow conditions in each of these subchannels. As the internal subchannels are larger in area and also have a smaller proportion of wetted perimeter to flow area, the flow is able to reach higher peak axial velocities. The peripheral subchannels have the bundle wall in addition to smaller flow areas, and therefore experience less overall axial flow due to friction effects and geometric constraints.

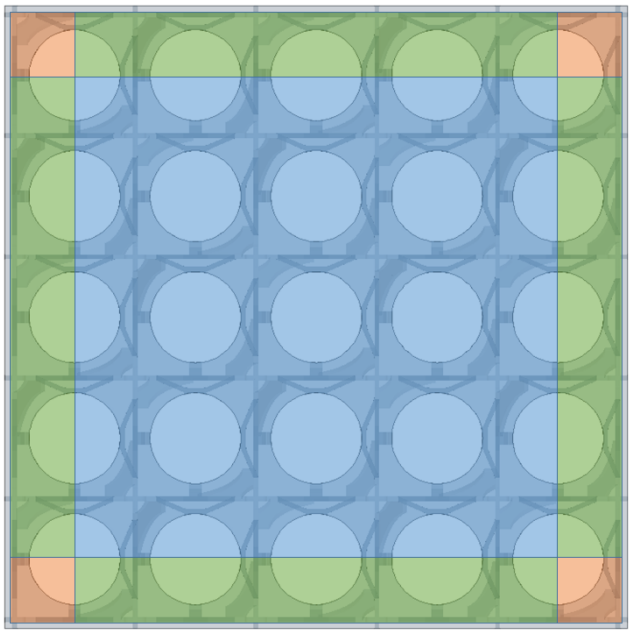

Figure 97: PSBT 5x5 rod bundle surfaces grouped by subchannel type

The same heat flux and boundary conditions are applied as defined in Table 35, the geometry is expanded to the full PSBT rod bundle for a single spacer grid span. The results of the bare (un-gridded) 5x5 STAR-CCM+ simulation provide the reference for the average magnitude differences between the types of rod surfaces grouped by geometry.

Table 36 contains the averaged values of the STAR-CCM+ predicted local HTC at each rod surface, grouped by surface location. The reference for these values is the internal subchannel values. This reference is selected due to the previous 2x2 subchannel layout simulations utilizing only internal subchannels. The results for the MVG spacer grid show that the difference between the HTC predictions at the corner and side surfaces are not as far from the internal surface predictions as for the bare rod bundle. The corner and side surfaces have average HTC ratios of 0.83 and 0.95, respectively, meaning that the corner surface experienced 83% of the heat transfer at the internal rod surfaces in the MVG simulation, on average. Therefore, if the heat transfer at

an internal surface is 10.0 W/m^2-K, the corner surface in the 5x5 MVG rod bundle is expected to be at 8.3 W/m^2-K at the same axial location. The corner surfaces in the bare simulation only experienced 75% of the heat transfer experienced at the internal surfaces. This can be attributed to stronger lateral flow patterns produced by the PSBT MVG, leading to more uniform heat transfer at all surfaces in the simulation.

Table 36: STAR-CCM+ predicted HTC ratios for rod surfaces relative to internal surfaces

Rod surface location	un-gridded 5x5 rod bundle HTC ratio to internal surfaces	PSBT MVG 5x5 rod bundle HTC ratio to internal surfaces
Corner subchannel	0.75	0.83
Side subchannel	0.85	0.95
Internal subchannel	1.00	1.00

These ratios, acting as a sort of “geometry factor”, allow for users to run a CTF simulation with heat transfer enhancement information from a simplified CFD simulation, such as a smaller scale geometry with only internal subchannels. The application of these ratios to CTF allows for more detailed surface multiplier values in CTF from CFD simulations which only involve internal subchannels.

It should be mentioned that within the subsets of surface types, there can still be variations from surface to surface. For example, in the MVG 5x5 rod bundle simulation, 2 of the corner surfaces are adjacent to mixing vanes while the other 2 corner surfaces are not. The downstream patterns experienced by these corner surfaces varies greatly with subchannel location within the simulation. Figure 98 shows the rod surfaces grouped by downstream effect due to the PSBT MVG spacer grid’s mixing vanes. The repeating pattern shows that some surface, which lie in regions adjacent to mixing vanes, experience similar flow patterns as other surfaces with the same relative mixing vane positions. In Figure 98, the box denotes the region of the 2x2 subchannel simulations with the surface flow patterns categorized by surface location.

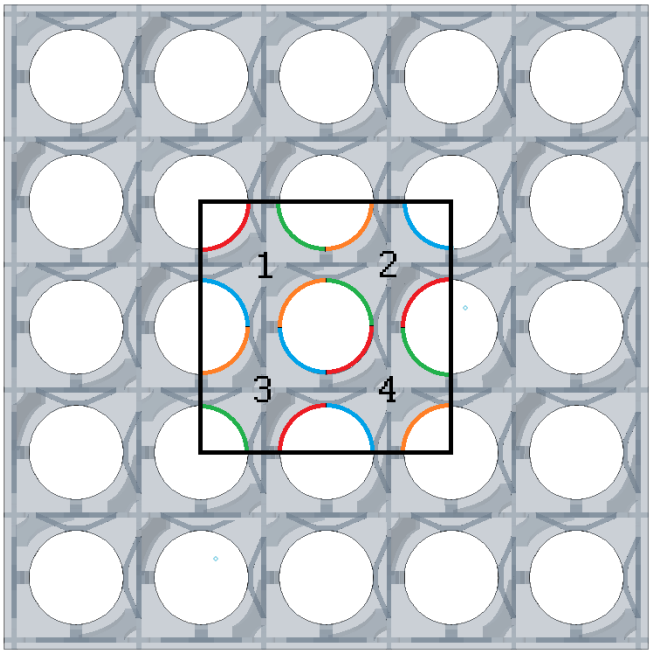

Figure 98: PSBT MVG spacer grid surface similarity generated by meandering flow patterns

Effects of varied flow inlet conditions on the CFD-predicted HTC

A study of the effects of the flow conditions involved changing the inlet mass flux by 10% to produce approximate axial velocities of 4.5 m/s and 5.5 m/s. The nominal value for typical simulations is 5.0 m/s, which corresponds to 1.276 kg/s with four PSBT subchannels at 300°C and 15.5 MPa. The impact of the inlet flow velocity on the STAR-CCM+ predicted local heat transfer coefficient is studied for the PSBT MVG spacer grid in a 2x2 subchannel layout. The remainder of the CFD simulation parameters were left unchanged from the values defined in Table 35. The details of the varied inlet mass flow rates are shown in Table 37.

Table 37: Inlet flow conditions used in the CFD 2x2 subchannel study of axial velocity effects

Flow variation case	Mass flow rate	Axial velocity
-10% flow rate	1.148 kg/s	4.5 m/s
Nominal flow rate	1.276 kg/s	5.0 m/s
+10% flow rate	1.404 kg/s	5.5 m/s

The results of the inlet flow variations in the PSBT MVG 2x2 subchannel simulations, shown in Figure 99, illustrate that the predicted local HTC profiles are similar in shape, but are shifted to higher and lower HTC values. The average HTC values before the spacer grid, at 0.80 m, were examined to determine the effect of flow velocity on the CFD-predicted heat transfer. Please note that these results are averaged over each of the four rod surfaces found within subchannel 1, and are identified in Figure 78.

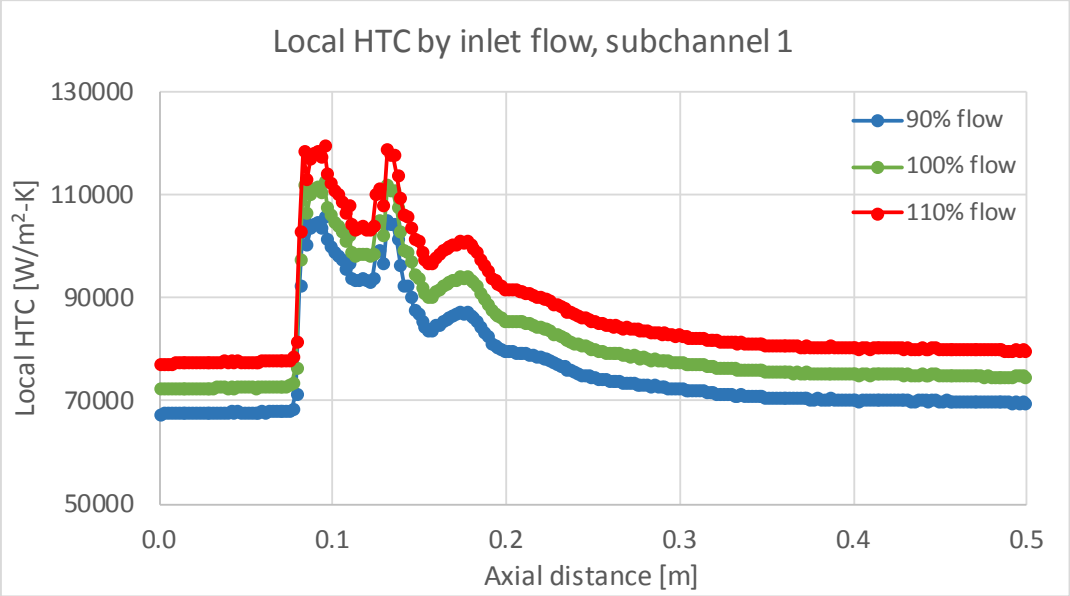

Figure 99: STAR-CCM+ predicted local HTC results for the PSBT MVG 2x2 simulation with varying inlet flow

The results, in Table 38, show that the difference in the CFD predictions for the HTC in which the inlet flow is changed by 10% in the second column. If the flow velocity is assumed to

be the only component of the calculation of the HTC which is changed, then the prediction of the Dittus-Boelter correlation, Equation (17), shows a dependence on the Reynolds number to the 0.8 power when calculating the Nusselt number. The Reynolds number, Equation (26), is directly proportional to the flow velocity. Therefore, if using the Dittus-Boelter to obtain a Nusselt number and the heat transfer coefficient, the result is expected to vary by the factor of change to the 0.8 power. The Prandtl number, which is a measure of fluid thermal properties, is not dependent upon flow velocity. This expected change, assuming that only changes in the liquid velocity affect the heat transfer coefficient, are also shown in Table 38, in the third column. The actual CFD predictions of the local HTC are under-predicted in magnitude when compared with their expected changes.

Table 38: STAR-CCM+ HTC predictions with flow variations for the PSBT MVG 2x2 simulation

Flow variation case	STAR-CCM+ predicted pre-grid HTC [kW/m^2-K]	STAR-CCM+ HTC difference from nominal case	Expected HTC difference, if only a function of velocity
-10% flow rate	67.7	-7.7%	-9.2%
Nominal flow rate	72.5	---	---
+10% flow rate	77.5	6.9%	7.9%

The effect of the flow rate on the length of the downstream decay of the HTC enhancement is not determined from this study. A larger variation in flow rates may be required to relate the axial distance at which the HTC enhancement drops back to nominal values to the axial velocity of the flow. As the results for the STAR-CCM+ HTC values are highly dependent upon the meshing scheme near the walls, the actual magnitudes of the CFD and CTF heat transfer coefficients will vary.

Changing the inlet flow rate in the 2x2 subchannel CTF simulations provides insight to how CTF's calculation of the HTC at the rod surfaces is affected by flow inlet conditions. Table 39 shows the differences in the CTF-predicted HTC values at the central rod for the cases of 4.5 m/s, 5.0 m/s, and 5.5 m/s inlet flow velocities. The differences are very similar to those expected if the HTC calculation is purely a function of the axial velocity-driven Dittus-Boelter correlation deviation.

Table 39: CTF HTC predictions with flow variations for the PSBT MVG 2x2 simulation

Flow variation case	CTF-predicted pre-grid HTC [kW/m^2-K]	CTF HTC difference from nominal case	Expected HTC difference, if only a function of velocity
-10% flow rate	34.1	-8.1%	-9.2%
Nominal flow rate	37.1	---	---
+10% flow rate	40.0	7.9%	7.9%

Application of CFD simulation results to CTF

A data-file containing the results of the CFD-predicted HTC ratios can be supplied to CTF to improve the downstream heat transfer enhancement predictions near spacer grids. The data-file contains data which are a function of spacer grid type, axial location, and rod surface location. The ratios corresponding to the surface index and axial node are read in to CTF and used to modify the single-phase liquid heat transfer coefficient used in calculations of the surface temperatures.

This allow users to run their own CFD simulations and extract the relevant HTC information and then apply these results to CTF without having to modify CTF itself. An example

of this data-file is provided in Appendix A, and sample details for the structure of the file are shown in Table 40, assuming 3 axial locations and 4 rod surfaces in the geometry.

Table 40: Sample HTC ratio data-file content for CTF simulations

*Axial location	*Surface 1	*Surface 2	*Surface 3	*Surface 4
0.00 m	1.00	1.00	1.00	1.00
0.05 m	1.20	1.15	1.15	1.00
0.10 m	1.25	1.20	1.20	0.95

The modification to CTF to enable the use of data-files to inform of HTC multiplier data is shown in the flowchart of Figure 100.

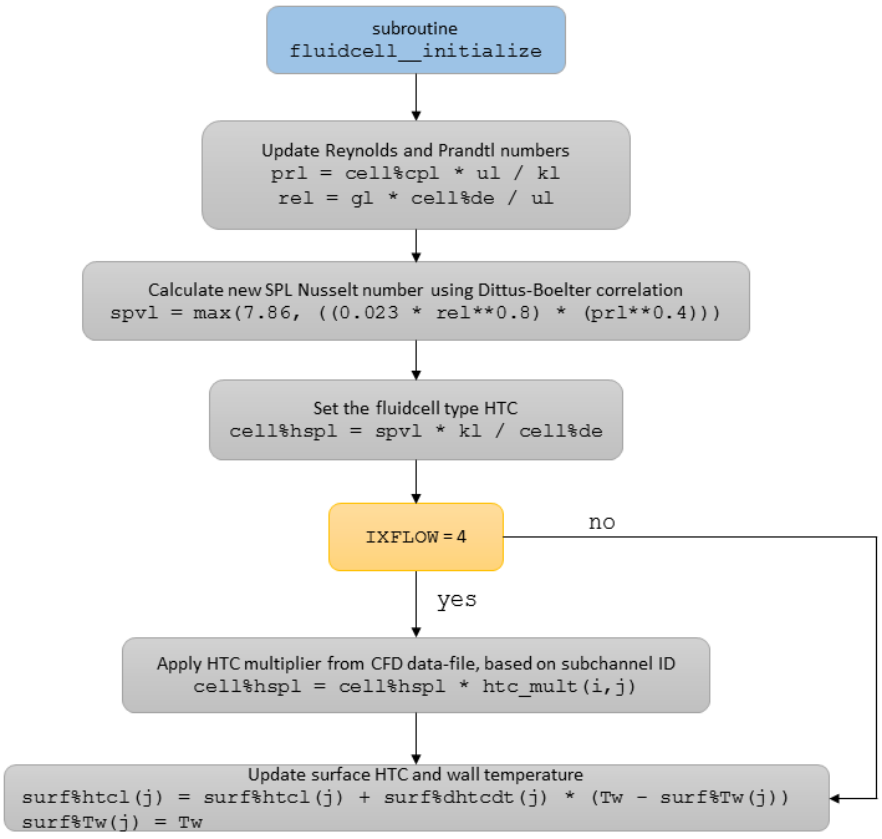

Figure 100: Flowchart for the spacer grid-enhanced HTC in CTF

As the developed models were only simulated in single-phase liquid conditions in STAR-CCM+, the applied HTC multiplier is only valid for CTF models in the single-phase heat transfer regime.

CTF simulations with CFD-informed HTC data

The CFD-produced HTC multiplier data for the PSBT MVG was applied within a 2x2 subchannel layout CTF simulation to observe the effects on the predicted surface temperatures. The flow conditions were kept the same as those provided in Table 35 in order to compare codes at similar conditions. Observations of the surface temperatures around the central rod in the 2x2 subchannel layouts, as depicted in Figure 78, were performed first with a bare (un-gridded) CTF simulation. The bare results were compared with CFD simulations of a bare 2x2 subchannel layout to determine the differences in predictions between the codes. Figure 101 shows that the CFD predictions of the surface temperatures are higher for the bare simulation, though the slopes of the lines are similar. The heat flux values are the same, with both CTF and STAR-CCM+ utilizing wall flux values of 800 kW/m^2. The results for the STAR-CCM+ simulations were first measured at 120 mm from the flow inlet after allowing for a flow development region, and, if present, the spacer grid's leading edge is 200 mm from the flow inlet.

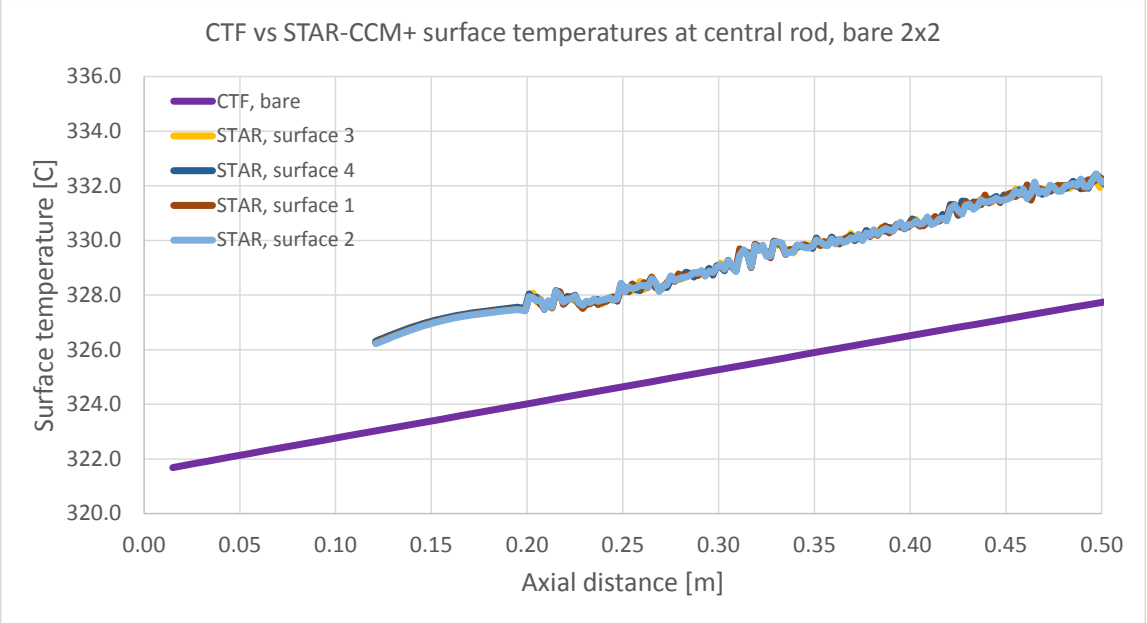

Figure 101: STAR-CCM+ vs CTF prediction of surface temperatures at the central rod in a 2x2 bare simulation

In order to ascertain that the bulk fluid temperatures are in agreement between CTF and STAR-CCM+, the results are plotted in Figure 102. This shows good comparison between the two codes of predicting the subchannel temperatures given an inlet temperature and a heat flux. Again, the CFD results are measured from 120 mm axially to allow for the flow development region. Also, please note the smaller axial temperature scale.

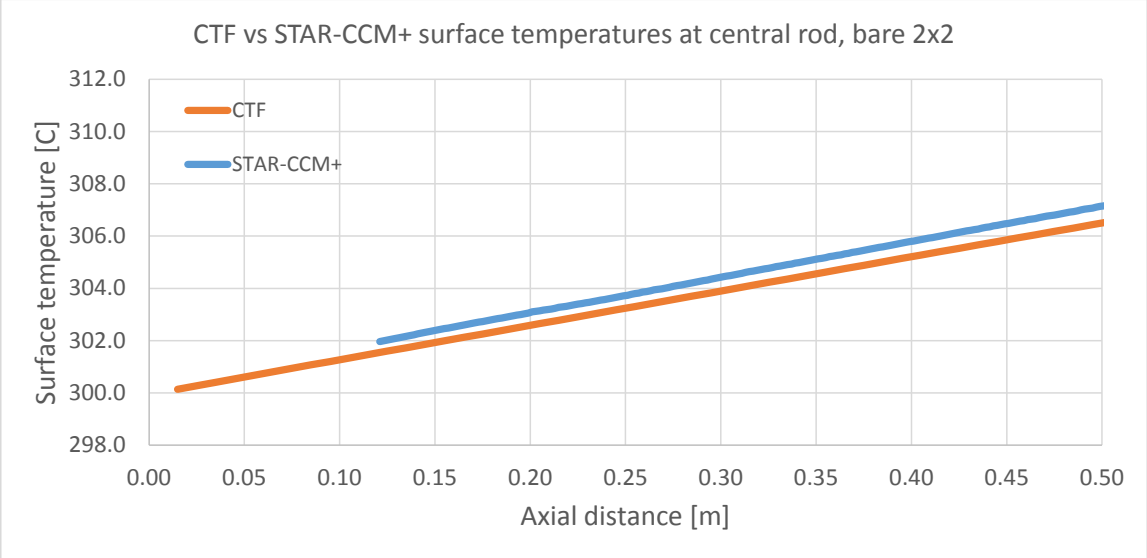

Figure 102: STAR-CCM+ vs CTF prediction of the bulk fluid temperature in a 2x2 bare simulation

CTF's Yao-Hochreiter-Leech correlation, which is built in to account for the heat transfer effects of spacer grids, requires users to supply information about the spacer grid to CTF in order to provide an updated heat transfer coefficient. The results, shown in Figure 103, align well with the CFD-informed HTC multipliers for the prediction of surface temperatures in the PSBT MVG 2x2 simulations. The input parameters required to apply the YHL correlation to the CTF simulation require precise knowledge of the spacer grid's vanes, grid straps, and spring/dimples, however.

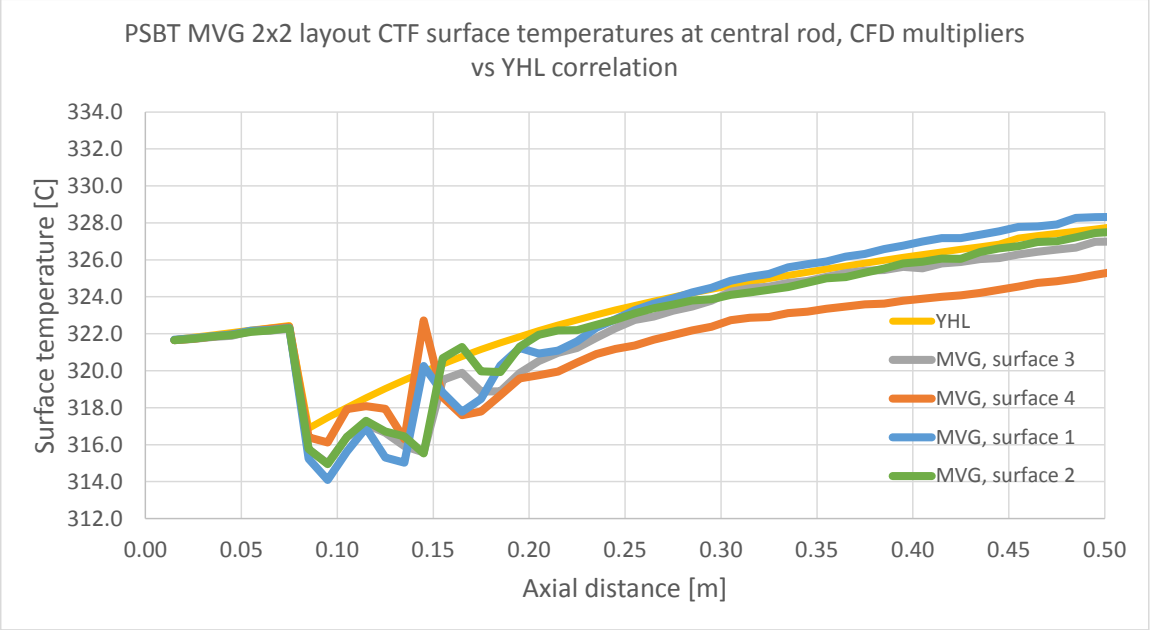

Figure 103: Comparison of surface temperature predictions with the CFD-informed HTC multipliers vs the CTF YHL correlation

The CFD-derived HTC multipliers from the 2x2 subchannel layout PSBT MVG simulation in STAR-CCM+ were applied to CTF with the method noted in Figure 100. The effect on the surface temperature predictions of the central rod was examined, with Figure 104 showing the results. Each of the four rod surfaces was provided with a different HTC multiplier for each of the azimuthal portions of the central rod. The results show a strong decrease at the location of the spacer grid's leading edge, which how STAR-CCM+ predicted. The surface temperatures slowly move back towards their pre-grid trends as distance from the spacer grid increases.

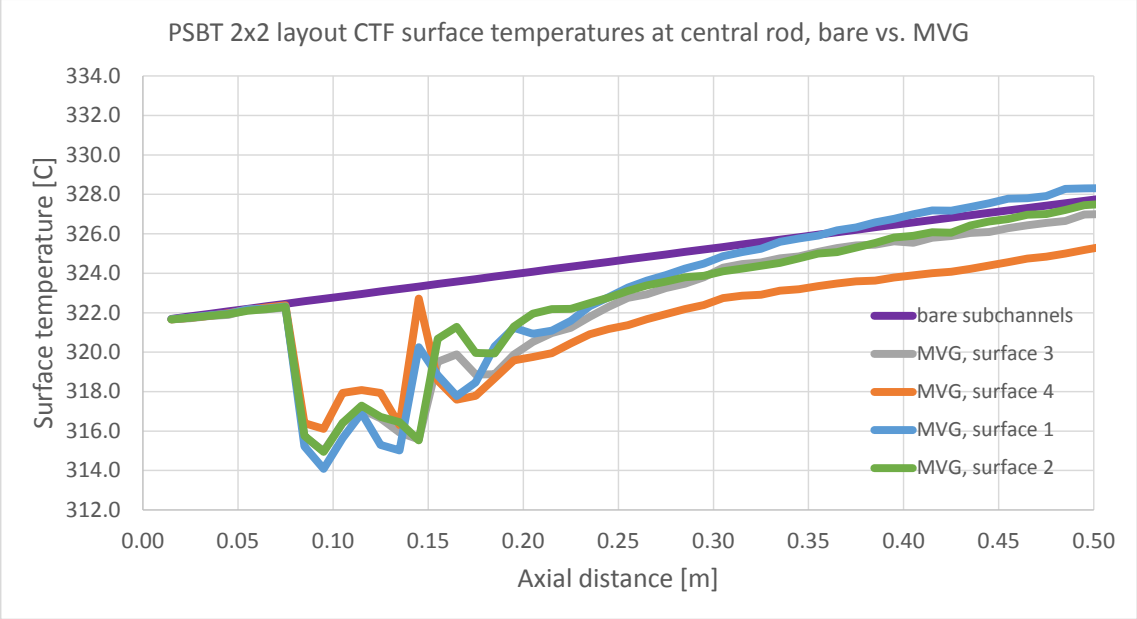

Figure 104: Comparison of surface temperature predictions from CTF for the bare simulation and the PSBT MVG HTC multiplier simulation at the central rod

Finally, a comparison of the CTF surface temperature predictions and the STAR-CCM+ predictions is shown in Figure 105. The flow inlet location was adjusted for these results in order to provide the same relative locations of the spacer grid and the flow inlet in both the CTF and STAR-CCM+ simulations. Aside from the initial prediction differences in the region before the spacer grid, the results line up well for the downstream regions. The prediction of the CFD surface temperatures is also highly dependent upon the meshing scheme near the walls.

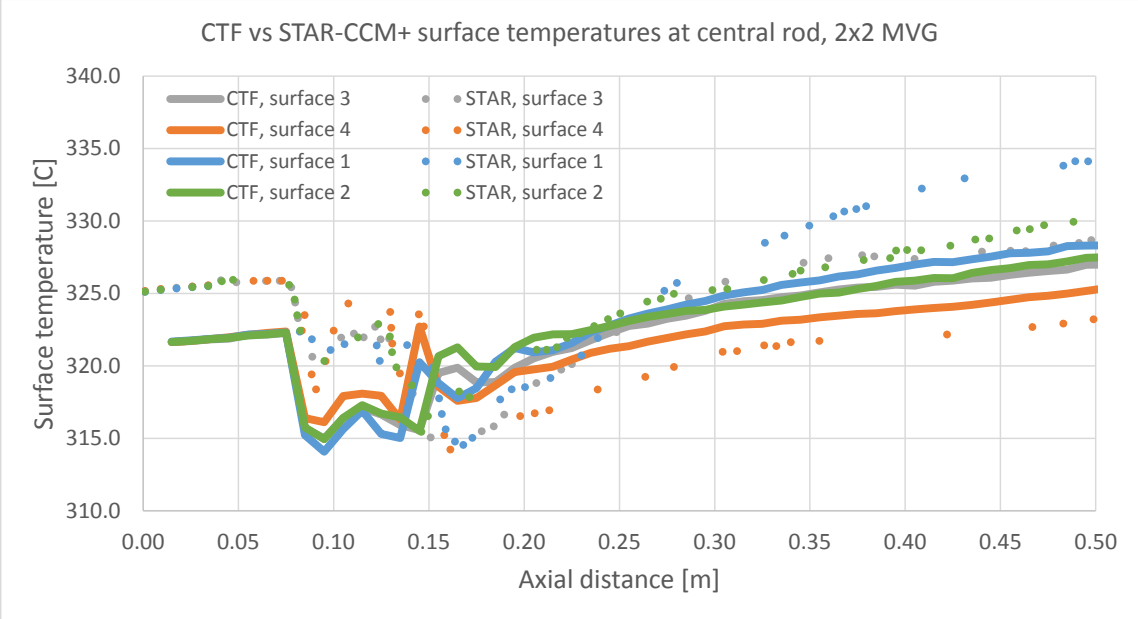

Figure 105: Surface temperature predictions of CTF and STAR-CCM+ with the PSBT MVG HTC multiplier applied in CTF at the central rod

Summary and Conclusions

In this chapter, a CFD-informed model for spacer grid-enhanced heat transfer to be used in CTF is developed and tested. These activities involved CFD simulations, which have been performed to develop a set of multipliers for the surface to liquid HTC values in CTF. These simulations provided ratios of the gridded geometries to the bare geometries to study the effect of the spacer grid on the surrounding HTC predictions. The ratios are then transferred to CTF in the form of a data-file which holds multipliers split azimuthally for each of these four surfaces connected to a rod.

Application of the CFD-predicted HTC ratios to CTF produces a downstream decrease in surface temperatures due to the increased heat transfer occurring. The bulk fluid temperature remains the same as the amount of heat flux and the flow velocity are unchanged. The surface

temperature is related to the DNB phenomenon as well as safety margins designed to protect the integrity of the cladding itself. An existing heat transfer enhancement method in CTF, the Yao-Hochreiter-Leech correlation, produces results of similar magnitude, though its implementation requires precise knowledge of the spacer grid geometry.

Comparison with the STAR-CCM+ predictions of the surface temperatures show that CTF correctly predicts the profile of the downstream temperatures. The study of the subchannel/surface location within the rod bundle and its overall HTC value also allows users to generate HTC multipliers from smaller scaled CFD simulations. If only internal subchannels are modelled, a good approximation for the average HTC difference between the internal and side subchannels can be applied to the results and then used within CTF for a full-scale bundle simulation.

Improvements for the CFD-developed HTC multipliers could be made by studying more parameters which affect the STAR-CCM+ prediction of the local HTC values. These parameters include meshing, grid geometry parameters such as grid strap thickness and vane angle, as well as simplifications made to the CFD simulation domain in order to improve modelling such as the spring and dimple details. Finally, expansion into more than single-phase simulations would provide details for modifying a larger range of CTF simulations containing spacer grids with spacer-grid enhancement multipliers.

Chapter 7

Conclusions and Future Work

The research described in this PhD thesis contributes to the development of efficient methods for the utilization of high-fidelity models and codes to inform low-fidelity models and codes in the area of nuclear reactor core thermal-hydraulics. The objective is to increase the accuracy of predictions of quantities of interests using high-fidelity CFD models (based on STAR-CCM+) while preserving the efficiency of low-fidelity sub-channel (based on CTF) core calculations. An original methodology called the Physics-based Approach for High-to-Low Model Information has been further developed and tested. The overall physical phenomena and corresponding localized effects (which are introduced by spacer grids in LWR cores, and which low-fidelity models such as sub-channel codes are not able to capture) are divided into four basic spacer-grid related processes, and corresponding models are informed using high-fidelity CFD codes. These models are a spacer grid-directed cross-flow model, a spacer grid-enhanced turbulent mixing model, a heat transfer enhancement model, and a pressure losses model. The localized CFD-models are developed and tested with STAR-CCM+, and the corresponding global model development and testing in sub-channel formulation is performed in CTF. The improved CTF simulations utilize data-files derived from CFD STAR-CCM+ simulation results covering the spacer grid design desired for inclusion in the CTF calculation. The implemented and validated CFD-informed spacer grid models allow for the spacer-driven effects of turbulent mixing, and vane-driven directed cross-flow across subchannels to be included in the CTF simulations. The current implementation of these models is examined and possibilities for improvement and further development are suggested. The validation experimental database is extended by including PSBT benchmark data. Further this PhD research provides a method for

developing heat transfer coefficient factors to improve predictions at the rod surfaces within the subchannel code CTF as well as a method for calculation for improved spacer grid loss coefficient evaluation to be used in CTF. These heat transfer factors can be applied at the surface level and offer better versatility and adaptability than the currently implement method of grid-enhanced heat transfer. The development of overall methodology (Physics-based Approach for High-to-Low Model Information) and individual four models, their implementation and associated verification and validation activities constitute the original PhD contributions of this thesis. The outcome is an enhanced accuracy of CTF predictions while preserving the computational efficiency. Another contribution is the utilization of the OECD/NRC PSBT benchmark data to validate the developed methodology and models.

Future Work

General

Ideally, a large study on flow conditions and effects on the phenomena studied in this research could provide correlations to relate varying inlet conditions to properly describe the appropriate behavior. For example, doubling the inlet velocity would cause the heat transfer enhancement to be prevalent a certain amount farther downstream than at the nominal velocity. Being able to quantize the length scale and magnitude of effects based on flow conditions would greatly reduce the number of CFD simulations required by users as more general models could be utilized.

The data-files required for CTF simulations with CFD-derived information could be more flexible. The length scale of the effects should be calculated within CTF and not be hard-coded into the data-file. This decreases the appropriateness of applying a CFD data-file from one

simulation to another using the same spacer grid configuration but at different flow conditions. If the user provided the spacer grid as well as more general, non-distance based properties to CTF then the predictions would become more flexible, and the issue of generating the data-file structure is greatly simplified.

A parameter study on the fine details of the spacer grid geometry could provide useful insight on which portions of the design affect CTF and CFD simulations. Varying details such as the grid strap thickness, grid height, and vane angle could be used to develop a complex correlation possibly suited for more general spacer grid effect characterization.

Spacer grid enhanced turbulent mixing

Applying turbulent mixing values on a per-gap basis is described in this work, but not yet implemented. It would require knowledge of CTF's subchannel gap scheme, which is user-set, to become truly viable over a range of rod bundle geometries.

Spacer grid mixing vane-directed cross-flow

Similar to the turbulent mixing, the directed cross-flow effects caused by the spacer grids are specific to subchannel and gap geometries. Applying a geometric factor to account for the differences in side-side gap velocity magnitudes in comparison to internal-internal gap velocities would be one method, but this would still require the user to set up the directions of the flow across each gap.

Spacer grid pressure loss coefficients

The BWR Full-size Fine-mesh Bundle Tests (BFBT) contain single-phase pressure drop experiments with ferrule-type spacer grids [67]. Additional comparisons between the measured pressure drops, the CFD-predicted pressure drops, and CTF's pressure loss modelling would provide a more validated method for developing spacer grid loss coefficients.

Varying the surface treatment and friction models in CFD would produce more general results which could become more advanced. A method for isolating subchannels to determine specific pressure loss coefficients per subchannel geometry could provide data for a more modular approach to pressure loss modelling. Lateral pressure losses could also be examined for bundle-to-bundle flow effects. The areas where multiple rod bundles connect at a subchannel needs more investigation as well, especially if the rod bundle flow conditions vary.

Spacer grid-enhanced heat transfer

Comparisons with azimuthally-dependent surface temperature measurements would be beneficial to this model. The Combustion Engineering 5x5 experiment contains single-phase measurements at several locations downstream of grids [68]. The spacer grids are not very well detailed, so it may be difficult to develop accurate and representative models for the CFD simulations.

BIBLIOGRAPHY

[1] Salko, R. K., & Avramova, M. N. (2016). *CTF Theory Manual*, North Carolina State University.

[2] Avramova, M. N. (2007). *Development of an innovative spacer grid model utilizing computational fluid dynamics within a subchannel analysis tool* (Doctoral dissertation). The Pennsylvania State University.

[3] Colameco, D., Ivanvov, B., Beacon, D., & Ivanov, K. (2013). *Iterative transport-diffusion methodology for LWR core analysis*. Paper presented at the Joint International Conference on Supercomputing in Nuclear Appications and Monte Carlo (SNA + MC), Paris, France.

[4] Clifford, I., Ivanov, K., & Avramova, M. (2013). A multi-scale homogenization and reconstruction approach for solid material temperature calculations in prismatic high temperature reactor cores. *Journal of Nuclear Engineering and Design*, 256, 1-13.

[5] SolidWorks 2015 [Computer software] (2015). Dassault Systèmes, Vélizy-Villacoublay, France.

[6] Dittus, F. W., & Boelter, L, M. K. (1930). Heat transfer in automobile radiators of the tubular type. *Publications in Engineering 2*, University of California, Berkeley, 443-461.

[7] Neykov, B. (2010). *Development and validation of advanced CFD models for detailed predictions of void distribution in a BWR bundle* (Doctoral dissertation). The Pennsylvania State University.

[8] Anglart, H., Nylund, O., Kurul, N., & Podowski, M. Z. (1997). CFD prediction of flow and phase distribution in fuel assemblies with spacers. *Nuclear Engineering and Design*, 177, 215-228.

[9] Campbell, R. L., Cimbala, J. M., & Hochreiter, L. E. (2005). Computational fluid dynamics prediction of grid spacer thermal-hydraulic performance with comparison to experimental results. *Nuclear Technology*, 149, 49-61.

[10] Cui, X., & Kim, K., (2003). Three-dimensional analysis of turbulent heat transfer and flow through mixing vane in a subchannel of nuclear reactor. *Journal of Nuclear Science and Technology*, 40, 719-724.

[11] Miller, D. J. (2012). *Single-phase and two-phase grid-enhancement heat transfer in the reflood stage of a loss of coolant accident* (Doctoral dissertation). The Pennsylvania State University.

[12] Holloway, M. V., McClusky, H. L., Beasley, D. E., & Conner, M. E. (2004). The effect of support grid features on local, single-phase heat transfer measurements in rod bundles. *Journal of Heat Transfer*, 126, 43-53.

[13] Holloway, M. V., Beasley, D. E., & Conner, M. E. (2008). Single-phase convective heat transfer in rod bundles. *Nuclear Engineering and Design*, 238, 848-858.

[14] Jaeger, W., & Sánchez, V. (2013). Validation of the heat transfer enhancement models for spacer grids in the system code TRACE. *Nuclear Engineering and Design*, 265, 272-287.

[15] Kim, K., & Seo, J., (2005). Numerical optimization for the design of a spacer grid with mixing vanes in a pressurized water reactor fuel assembly. *Nuclear Technology*, 149, 62-70.

[16] Riley, M. P. (2015). *Spacer grid induced heat transfer enhancement in a rod bundle under reflood conditions* (Doctoral dissertation). The Pennsylvania State University.

[17] Miller, D. J., Cheung, F. B., & Bajorek, S. M. (2013). On the development of a grid-enhanced single-phase convective heat transfer correlation. *Nuclear Engineering and Design*, 264, 56-60.

[18] Navarro, M. A., & Santos, A. C. (2009). *Numerical evaluation of flow through a 5x5 PWR rod bundle: effect of the vane arrangement in a spacer grid*. Paper presented at the International Nuclear Atlantic Conference, Rio de Janeiro, RJ, Brazil.

[19] Yang, S., & Chung, M. K. (1996). Measurements of turbulent flow in a 6x6 rod bundle with spacer grids. *Journal of the Korean Nuclear Society*, 28, 162-174.

[20] Yao, S. C., Hochreiter, L. E., & Leech, W. J. (1982). Heat-transfer augmentation in rod bundles near grid spacers. *Journal of Heat Transfer*, 104, 76-81.

[21] In, W. K., Oh, D. S., & Chun, T. H. (2001). *Pressure drop correlation for a PWR fuel assembly with mixing vane*. Paper presented at the Korean Nuclear Society Spring Meeting, Cheju, Korea.

[22] Rehme, K. (1973). Pressure drop correlations for fuel element spacers. *Nuclear Technology*, 17, 15-23.

[23] Chun, T. H., & Oh, D. S. (1998). A pressure drop model for spacer grids with and without mixing vanes. Journal of Nuclear Science and Technology, 35, 508-510.

[24] Endo, M., Takaki, W., Nishioka, D., Hirakata, Y., Kawahara, A., & Sadatomi, M. (2016). Effects of mixing-vane attached to grid spacer on pressure drop and deposition rate in BWR simulated channel. *Universal Journal of Mechanical Engineering*, 4, 57-62.

[25] Li, X, & Gao, Y. (2014). Methods of simulating large-scale rod bundle and application to a 17x17 fuel assembly with mixing vane spacer grid. *Nuclear Engineering and Design*, 267, 10-22.

[26] Lo, S. & Osman, J. (2012). CFD modeling of boiling flow in PSBT 5x5 bundle. *Science and Technology of Nuclear Installations*, 2012, 1-8.

[27] In, W. K., Sin, C. H., & Chun, T. H. (2010). *CFD simulation of PWR subchannel void distribution benchmark*. Paper presented at the ASME International Mechanical Engineering Congress & Exposition, Vancouver, BC, Canada.

[28] Agbodemegbe, V. Y., Cheng, X., Akaho, E. H. K., & Allotey, F. K. A. (2015). Correlation for cross-flow resistance coefficient using STAR-CCM+ simulation data for flow of water through rod bundle supported by spacer grid with split-type mixing vane. *Nuclear Engineering and Design*, 285, 134-149.

[29] Agbodemegbe, V. Y., Cheng, X., Akaho, E. H. K., & Allotey, F. K. A. (2016). An investigation of the effect of split-type mixing vane on extent of crossflow between subchannels through the fuel rod gaps. *Annals of Nuclear Energy*, 88, 174-185.

[30] Holman, B. (2012). A study on the merits of using computational fluid dynamics to predict thermal-hydraulic properties in rod bundles (Master's thesis). North Carolina State University.

[31] Holloway, M. V., Beasley, D. E., & Conner, M. E. (2006). *Investigation of swirling flow in rod bundle subchannels using computational fluid dynamics*. Paper presented at the International Conference on Nuclear Engineering, Miami, FL, USA.

[32] Ikeno, T. (2001). *An application of the model of flow pulsation to the rod gap in the nuclear fuel assembly*. Paper presented at the International Symposium on Flow Modeling and Turbulence Measurements, Tokyo, Japan.

[33] In, W. K. (2001). Numerical study of coolant mixing caused by the flow deflectors in a nuclear fuel bundle. *Nuclear Technology*, 134, 187-195.

[34] Jeong, H., Ha, K., Lee, Y., Hahn, D., Dunn, F. E., & Cahalan, J. E. (2004). *Evaluation of turbulent mixing between subchannels with a CFD code*. Paper presented at the International Conference on Nuclear Thermal Hydraulics, Operations, and Safety, Nara, Japan.

[35] Sung, Y., Kucukboyaci, V. N., Tatli, E., Xu, Y., Karoutas, Z. E., Christon, M. A., … Popov, E. (2014). *Application of multi-scale thermal-hydraulic models to DNB analysis* (Report No. L1:CASL.P9.02). Consortium for Advanced Simulation of LWRs.

[36] Lewis, A., Smith, R., & Williams, B. (2014). *An information theoretic approach to use high-fidelity codes to calibrate low-fidelity codes* (Report No. L3:VUQ:V&V:P9:02). Consortium for Advanced Simulation of LWRs.

[37] Hyvärinen, J. P. (2014). *Two-phase flow measurements with spacer grid in a rod bundle geometry* (Master's thesis). Lappeenranta University of Technology.

[38] Yoo, Y. J., Hwang, D. H., & Sohn, D. S. (1999). Development of a subchannel analysis code MATRA applicable to PWRs and ALWRs. *Journal of the Korean Nuclear Society*, 31, 314-327.

[39] McClusky, H. L., Holloway, M. V., Conner, T. A., Beasley, D. E., Conner, M. E., & Smith, L. D. (2003). Mapping of the lateral flow field in typical subchannels of a support grid with vanes. *Journal of Fluids Engineering*, 125, 987-996.

[40] McClusky, H. L., Holloway, M. V., Beasley, D. E., & Conner, M. E. (2002). Development of swirling flow in a rod bundle subchannel. *Journal of Fluids Engineering*, 124, 747-755.

[41] Meyer, L. (2010). From discovery to recognition of periodic large scale vortices in rod bundles a source of natural mixing between subchannels—a review. *Nuclear Engineering and Design*, 240, 1575-1588.

[42] Frank, T., Reiterer, F., & Lifante, C. (2011). *Investigation of the PWR subchannel void distribution benchmark (OECD/NRC PSBT benchmark) using ANSYS CFD*. Paper presented at the International Topical Meeting on Nuclear Reactor Thermal Hydraulics, Toronto, ON, Canada.

[43] Roelofs, F., Gopala, V. R., Chandra, L, Viellieber, M., & Class, A. (2012). Simulating fuel assemblies with low resolution CFD approaches. *Nuclear Engineering and Design*, 250, 548-559.

[44] Baudry, C., Guingo, M., Douce, A., Laviéville, J., Mimouni, S., & Boucker, M. (2012). Numerical study of the steady-state subchannel test-case with NEPTUNE_CFD for the OECD/NRC NUPEC PSBT benchmark. *Science and Technology of Nuclear Installations*, 2012, 1-11.

[45] Conner, M. E., Baglietto, E., & Elmahdi, A. M. (2010). CFD methodology and validation for single-phase flow in PWR fuel assemblies. *Nuclear Engineering and Design*, 240, 2088-2095.

[46] Smith, B. L., Song, C. H., Chang, S. K., Lee, J. R., & Kim, J. W. (2013). *Report of the OECD/NEA-KAERI rod bundle CFD benchmark exercise* (Report No. NEA/CSNI/R(2013)5). Nuclear Energy Agency.

[47] Cho, S., Moon, S. K., Chun, S. Y., Kim, Y. S., & Baek, W. P. (2007). Spacer grid effects during a reflood in an annulus flow channel. *Journal of Nuclear Science and Technology*, 44, 967-976.

[48] Ylönen, A. T. (2013). *High-resolution flow structure measurements in a rod bundle* (Doctoral dissertation). Swiss Federal Institute of Technology in Zurich.

[49] Rubin, A., Schoedel, A., Avramova, M., Utsuno, H., Bajorek, S., & Velazquez-Lozada, A. (2010). *OECD/NRC benchmark based on NUPEC PWR subchannel and bundle tests (PSBT), volume I: experimental database and final problem specifications* (Report No. NES/NSC/DOC(2010)1). United States Nuclear Regulatory Commission, Nuclear Energy Agency.

[50] STAR-CCM+ v11.04 User Manual, CD-adapco (2016).

[51] Hochreiter, L. E., Cheung, F. B., Lin, T. F., McLaughlin, Jr., D. M., Spring, J. P., Kutzler, P. M., & Ergun, S. (2014). *Rod bundle heat transfer facility – steady-state steam cooling experiments* (Report No. NUREG/CR-7152). United States Nuclear Regulatory Commission.

[52] Karoutas, Z. E., Xu, Y., Smith III, L, D., Joffre, P. F., & Sung, Y. (2015). *Use of CFD to predict critical heat flux in rod bundles*. Westinghouse Electric Company.

[53] Xu, Y., Sung, Y., & Tatli, E. (2015). *CFD evaluation of OECD PSBT geometry effects based on fluid temperature measurements*. Paper presented at the International Topical Meeting on Nuclear Reactor Thermal Hydraulics, Chicago, IL, USA.

[54] Dittus, F. W., & Boelter, L, M. K. (1930). Heat transfer in automobile radiators of the tubular type. *Publications in Engineering 2*, University of California, Berkeley, 443-461.

[55] Bhaskaran, R., & Collins, L. (2012). *Introduction to CFD Basics* (Course notes for MAE 5230). Cornell University.

[56] Wallis, G. (1969). *One-Dimensional Two-Phase Flow*. McGraw-Hill.

[57] Churchill, S. W. (1977). Friction-factor equation spans all fluid-flow regimes. *Chemical Engineering*, 84, 91-92.

[58] Zigrang, D. J., & Sylvester, N. D. (1985). A review of explicit friction factor equations. *Journal of Energy Resources Technology*, 107, 280-283.

[59] Shiralkar, B. S., & Radcliffe, D. W. (1971). An experimental and analytical study of the synthesis of grid spacer loss coefficients (Report No. NEDE-13181). General Electric.

[60] Marek, J., & Rehme, K. (1979). Heat transfer in smooth and roughened rod bundles near spacer grids. Fluid Flow and Heat Transfer over Rod or Tube Bundles, ASME, 163-170.

[61] Incropera, F. P., DeWitt, D. P., Bergman, T. L., & Lavine, A. S. (2007). Fundamentals of heat and mass transfer (Sixth edition). John Wiley & Sons, Inc., Hoboken, New Jersey.

[62] Todreas, N. E., & Kazimi, M. S. (1990). *Nuclear systems I: thermal hydraulic fundamentals*. Taylor & Francis Group, New York, New York.

[63] Winterton, R. H. S. (1998). Where did the Dittus and Boelter equation come from? *International Journal of Heat and Mass Transfer*, 41, 809-810.

[64] Mills, A. F. (1962). Experimental investigation of turbulent heat transfer in the entrance region of a circular conduit. *Journal of Mechanical Engineering Science*, 4, 63-77.

[65] Avramova, M. (2011). *CTF/STAR-CD off-line coupling for simulation of cross-flow caused by mixing vane spacers in rod bundles*. Paper presented at the International Conference on Mathematics and Computational Methods Applied to Nuclear Science and Engineering, Rio de Janeiro, Brazil.

[66] Serre, G., Chandesris, M., Bestion, D. (2013). *Modelling the heat transfer enhancement by grids in rod-bundle using a turbulence model in the CATHARE-3 code*. Paper presented at the International Topical Meeting on Nuclear Reactor Thermal-Hydraulics, Pisa, Italy.

[67] Hochreiter, L., Ivanov, K., Utsuno, H., Kasahar, F., Neykov, B., & Aydogan, F. (2006). *NUPEC BWR full-size fine-mesh bundle test (BFBT) benchmark*. Technical report, Nuclear Energy Agency.

[68] Karoutas, Z., Sung, Y, Chang, Y., Kogan, G., & Joffre, P. (2002). *Subcooled boiling data from rod bundles*. Technical report, Electric Power Research Institute.

[69] Roache, P. J. (1994). Perspective: A Method for Uniform Reporting of Grid Refinement Studies, *Journal of Fluids Engineering*, 116, 405-413.

[70] Richardson, L. F. (1927). *The Deferred Approach to the Limit*, Transactions of the Royal Society of London, Series A, 226, 299-361.

Appendix A

CTF data-files

Spacer grid-directed crossflow model data-files for CTF

Data-files from CFD simulation results are needed for the spacer grid-directed cross-flow simulations. If the CTF input deck parameter IXFLOW is set to either 1 or 3, the *dirct_data.inp* data-file as well as the *xflow_data* file are required for the CTF simulation.

The *dirct_data.inp* file contains information in two columns; the first is the CTF gap number, and the second relates to the direction of the lateral fluid flow over the gap. A value of 1.0 indicates flow from the lower-numbered subchannel to the higher-numbered subchannel. Conversely, a value of -1.0 indicates flow from a higher-numbered subchannel to a lower-numbered subchannel. A value of 0.0 indicates that this gap does not experience spacer grid-driven cross-flow. The example file below has been abridged, and shows the layout for a CTF model featuring 60 subchannel connection gaps.

dirct_data.inp

```
  1    0.0
  2    0.0
  3    0.0
  4    0.0
  5    0.0
...    ...
 56    1.0
 57    1.0
 58   -1.0
```

```
 59  -1.0
 60  -1.0
```

The second data-file required when CTF's directed cross-flow model is enabled, *xflow_data*, stores the calculated lateral convection factors as a function of axial distance and vane angle. The first line of relevant data provides the total number of axial locations for which lateral convection data are supplied, and then the number of angles for which data are provided. The following line contains the index for the data, which can be grouped for various spacer grid geometries. The next line read by CTF contains each of the spacer grid vane angles, in degrees. Then, columns of information correspond to the axial locations (in meters) and the lateral convection factors grouped by vane angle. The following example file has been truncated in the axial dimension. It provides information for four different vane angles, of 10°, 20°, 30°, and 40°. The first line also indicates that information is provided for 260 axial levels.

xflow_data

```
*************************************************
* 2D table for lateral cross-flow
*************************************************
     260   4     0     0
*
  1
*
          10.      20.      30.      40.
0.00   0.0000   0.0000   0.0000   0.0000
0.23   0.0001   0.0001   0.0001   0.0001
0.24   0.0001   0.0001   0.0001   0.0001
0.25   0.0001   0.0001   0.0001   0.0001
0.26   0.0001   0.0001   0.0001   0.0001
 ...      ...      ...      ...      ...
2.96   0.0238   0.0509   0.0596   0.0638
2.97   0.0238   0.0509   0.0596   0.0638
2.98   0.0238   0.0509   0.0596   0.0638
2.99   0.0238   0.0509   0.0596   0.0638
3.00   0.0238   0.0509   0.0596   0.0638
```

Spacer grid-enhanced turbulent mixing model data-file for CTF

The data-file needed for the spacer grid-enhanced turbulent mixing simulations, *sg_mult_data*, is required if the CTF input deck parameter IXFLOW is set to either 2 or 3.

The *sg_mult_data* file holds the values for the turbulent mixing multiplier grouped by vane angle and axial position. The first line of information provides CTF with the number of axial levels as well as the number of angles for which turbulent mixing multipliers are supplied. The next line of data provides the index for the set of turbulent mixing data. The following line provides the spacer grid vane angles, in degrees, for which data are provided. The turbulent mixing multipliers are then supplied in columns, sorted by axial distance and grouped by vane angle. The following sample for the *sg_mult_data* file contains information for 105 axial distances and 2 spacer grid mixing vane angles; 0° and 15°. The file has been abridged in the axial dimension.

sg_mult_data

```
*****************************************************
* 2D table for the turbulent mixing multiplier
*****************************************************
     105   2    0    0
*
  1
*
           0.0    15.0
0.0000  1.0000  1.0032
0.7824  1.0000  1.1260
0.8124  1.0000  4.0587
0.8424  1.0000  2.7668
   ...     ...     ...
3.9144  1.0000  2.7668
3.9444  1.0000  1.7056
3.9744  1.0000  1.1480
```

Spacer grid-enhanced heat transfer coefficient model data-file for CTF

The data-file required for modelling enhanced heat transfer due to spacer grids, *htc_mult_data*, is necessary when the user sets the CTF input deck parameter IXFLOW to 4.

The *htc_mult_data* file contains the values for the heat transfer coefficient multipliers grouped by rod, surface index, and axial location. The first line of information from the data-file relays information on the number of rods, number of surfaces per rod, and the number of axial locations per rod to CTF. The first table provides the information for the first rod, grouped in columns for each surface of the rod and sorted by axial location of the multiplier. Additional tables are present until the number of rods have been supplied. The following sample *htc_mult_data* file specifies multiplier for 2 rods, with 4 surfaces per rod and 10 axial positions per rod. The values for the second rod are abridged in the axial dimension.

htc_mult_data

```
************************************************
* 2D tables for HTC multiplier data
************************************************
*  Rods   Surfs   Axial
      2       4      10
*
* Rod 1
*  z       S1       S2       S3       S4
0.00  0.0000  0.0000  0.0000  0.0000
0.23  0.0001  0.0001  0.0001  0.0001
0.24  0.0001  0.0001  0.0001  0.0001
0.25  0.0001  0.0001  0.0001  0.0001
0.26  0.0001  0.0001  0.0001  0.0001
0.27  0.0002  0.0002  0.0002  0.0002
0.28  0.0002  0.0002  0.0002  0.0002
0.29  0.0001  0.0001  0.0001  0.0001
0.30  0.0001  0.0001  0.0001  0.0001
* Rod 2
*  z       S1       S2       S3       S4
0.00  0.0012  0.0026  0.0033  0.0039
...      ...      ...      ...      ...
0.30  0.0630  0.1327  0.2086  0.2620
```